Advances in Polymer Science 265

Sabine Ludwigs *Editor*

P3HT Revisited – from Molecular Scale to Solar Cell Devices

Springer

265
Advances in Polymer Science

Aims and Scope

The series Advances in Polymer Science presents critical reviews of the present and future trends in polymer and biopolymer science. It covers all areas of research in polymer and biopolymer science including chemistry, physical chemistry, physics, material science.

The thematic volumes are addressed to scientists, whether at universities or in industry, who wish to keep abreast of the important advances in the covered topics.

Advances in Polymer Science enjoys a longstanding tradition and good reputation in its community. Each volume is dedicated to a current topic, and each review critically surveys one aspect of that topic, to place it within the context of the volume. The volumes typically summarize the significant developments of the last 5 to 10 years and discuss them critically, presenting selected examples, explaining and illustrating the important principles, and bringing together many important references of primary literature. On that basis, future research directions in the area can be discussed. Advances in Polymer Science volumes thus are important references for every polymer scientist, as well as for other scientists interested in polymer science - as an introduction to a neighboring field, or as a compilation of detailed information for the specialist.

Review articles for the individual volumes are invited by the volume editors. Single contributions can be specially commissioned.

Readership: Polymer scientists, or scientists in related fields interested in polymer and biopolymer science, at universities or in industry, graduate students.

Special offer:
For all clients with a standing order we offer the electronic form of Advances in Polymer Science free of charge.

More information about this series at
http://www.springer.com/series/12

Sabine Ludwigs
Editor

P3HT Revisited – from Molecular Scale to Solar Cell Devices

With contributions by

D. Andrienko · M. Brinkmann · K. Daoulas · D. Djurado · L. Hartmann · N. Kayunkid · S. Ludwigs · C. K. Luscombe · A. J. Moulé · D. Neher · C. Poelking · P. Sista · K. Tremel · A. Troisi · S. T. Turner · J. Zaumseil

Springer

Editor
Sabine Ludwigs
IPOC-Functional Polymers
Institute of Polymer Chemistry
University of Stuttgart
Stuttgart
Germany

ISSN 0065-3195 ISSN 1436-5030 (electronic)
ISBN 978-3-662-45144-1 ISBN 978-3-662-45145-8 (eBook)
DOI 10.1007/978-3-662-45145-8
Springer Heidelberg New York Dordrecht London

Library of Congress Control Number: 2014955368

Printed on acid-free paper

Springer is part of Springer Science+Business Media (www.springer.com)

Preface

It is my great pleasure to present our book "P3HT Revisited – from Molecular Scale to Solar Cell Devices" in the Springer series *Advances in Polymer Science*. The book deals with poly(3-hexylthiophene), P3HT, which was first synthesized in the early 1990s and has become the work-horse or "fruit fly" (see chapter by Andrienko and coworkers, "Morphology and Charge Transport in P3HT: A Theorist's Perspective") of the opto-electronic community. The choice of authors – with backgrounds and expertise in polymer synthesis, structure analysis, polymer crystallization and morphology, transistor and solar cell device preparation and characterization, and polymer theory – is representative of the large community of scientists that have worked and are *still* working on this fascinating conjugated semicrystalline polymer. As highlighted by Moulé et al. (see chapter "P3HT-Based Solar Cells: Structural Properties and Photovoltaic Performance"), the research activity on P3HT is enormous, as demonstrated by the large number of articles published each year on this topic.

The book is structured as follows: The first chapter gives an overview of historic and modern routes for P3HT synthesis. The second and third chapters focus on the morphology of P3HT, which is dominated by its semicrystalline nature. The fourth chapter is devoted to field-effect transistors based on P3HT and other polythiophene polymers with high mobilities. A theorist's perspective on morphology and charge transport is given in the fifth chapter. The sixth chapter contains an introduction to and review on P3HT bulk heterojunction solar cells in combination with the fullerene derivative phenyl-C61-butyric acid methyl ester (PCBM).

Summarizing, we have tried to draw a consistent picture of P3HT at different length scales ranging from the molecular scale over the mesoscopic scale to the device level. The P3HT structure on the molecular and mesoscopic scale has been correlated with its optical, electrochemical, electronic, and opto-electronic properties, which provide the basis for its performance in transistor and solar cell devices.

Last, but not least, I express my sincere thanks to all the authors of this book for their contributions and to Dr. Tobias Wassermann and his team for their support.

Stuttgart, Germany — Sabine Ludwigs

Contents

Adv Polym Sci (2014) 265: 1–38
DOI: 10.1007/12_2014_278

Published online: 4 July 2014

Progress in the Synthesis of Poly (3-hexylthiophene)

Prakash Sista and Christine K. Luscombe

Abstract Polythiophene synthesis has undergone a multitude of changes, starting from the initial methods of acid-catalyzed polymerizations with low yields of oligomeric polythiophenes to modern methods using transition metal-based catalysts that allow controlled synthesis of poly(alkylthiophene)s with high molecular weight and regioregularity. The discovery of the opto-electronic properties of conjugated polymers played a major role in this development. Further improvements such as externally initiated polymerization not only enabled the synthesis of polymers that are almost 100% regioregular, but also gave the capability for in situ synthesis of these polymers on substrates, which increases their applicability in opto-electronic devices. This chapter summarizes developments in the methodology of polythiophene synthesis.

Keywords Controlled molecular weight · Externally initated polymerization · Poly(3-hexylthiophene) · Poly(alkylthiophene) · Polythiophene · Quasi-living polymerization · Regioregularity · Star-shaped P3HT

Contents

P. Sista and C.K. Luscombe (✉)
Department of Materials Science and Engineering, University of Washington, Seattle, WA 98195-2120, USA
e-mail: luscombe@uw.edu

Abbreviations

acac	Acetylacetonate
Ar	Aryl
Bn	Benzyl
bpy	2,2′-Bipyridyl
Bu	Butyl
cat	Catalyst
cod	1,5-Cyclooctadiene
Cp	Cyclopentadienyl
dppb	Bis(diphenylphosphino)benzene
dppe	Bis(diphenylphosphino)ethane
dppf	Bis(diphenylphosphino)ferrocene
dppp	Bis(diphenylphosphino)propane
Et	Ethyl
HF	Hydrofluoric acid
ITO	Indium tin oxide
LDA	Lithium diisopropylamide
Me	Methyl
NBS	*N*-Bromosuccinimide
NCS	*N*-Chlorosuccinimide
P3AT	Poly(3-alkylthiophene)
P3HT	Poly(3-hexylthiophene)
P3MT	Poly(3-methylthiophene)
PDI	Polydispersity index
Ph	Phenyl
PPh_3	Triphenylphosphine
TFA	Trifluoroacetic acid
THF	Tetrahydrofuran

1 Introduction

Conjugated polymers have garnered significant research attention since the discovery of highly conductive polyacetylene by Shirakawa. The semiconducting properties of these materials and their solution processability raised visions of production of flexible electronic devices using roll-to-roll processing technologies at low cost. Further advantages of conjugated polymers, such as their light weight and corrosion resistance as compared to inorganic semiconductors, promoted

extensive research attention. Of all the classes of conjugated polymers, polythiophenes play an important role. The environmental stability of polythiophene and its derivatives furthered research interest in these materials [1]. With the advances in synthetic methodologies, polythiophenes and specifically poly (3-hexylthiophene) (P3HT) became frontrunners in the research on conjugated polymers. P3HT has found application in various organic electronic devices such as solar cells, field-effect transistors, light-emitting diodes, and many others. P3HT has been the model polymer for various fundamental studies relating to charge transport and film morphology due to its ease of synthesis and good opto-electronic properties. The significance of polythiophenes is demonstrated by the number of reviews and books written on the progress made in the synthesis of these polymers and in gaining control of their properties [2–20].

3-Hexylthiophene, being an unsymmetrical monomer, gives rise to regioisomers during the early stages of its polymerization. Depending on the relative ratio of these regioisomers, the resultant polymers have different regioregularities. With the development of sophisticated characterization tools for solid-state packing of the polymer, a clear understanding has emerged for the relation between solid-state packing and opto-electronic properties. Reports relating the effects of regiospecificity of the polymerization and of the conjugation length of the synthesized polymer to its electronic properties have highlighted the need for development of synthetic techniques for precise regiochemical control during the polymerization reaction [21–30]. The development of synthetic techniques and the control achieved over the polymerization are discussed in this text.

1.1 Initial Synthetic Methods for Polythiophenes

Early work on thiophenes dates back to 1883, when thiophene was extracted from coal-tar and its properties were studied [31]. Acid-catalyzed polymerization of thiophene was reported to yield insoluble oligomers [32]. It was further shown that oligomers of thiophene can be synthesized by reaction with 100% orthophosphoric acid, Lewis acids, montmorillonite clay, and silica–alumina catalysts [33–40]. Electrochemical oxidation was also employed for the synthesis of polythiophenes [41]. It was observed that the polythiophenes synthesized by the above-mentioned methods had both 2,5-couplings and 2,4-couplings, with the former being more predominant. However, all the methods described above were only successful in the synthesis of oligomers containing three to five repeating units.

Discovery of the high electrical conductivity of polyacetylene films on doping with I_2 promoted significant interest in the synthesis of various conjugated polymer families [42]. The first successful synthesis of polythiophenes with many repeating units was achieved by the Yamamoto group [43]. They generated a mono-Grignard by reaction between 2,5-dibromothiophene and magnesium metal at 1:1 molar ratio and polymerized this active monomer using a transition metal catalyst [$NiCl_2$(bpy)] to obtain a polythiophene powder. The polymer obtained displayed a much higher

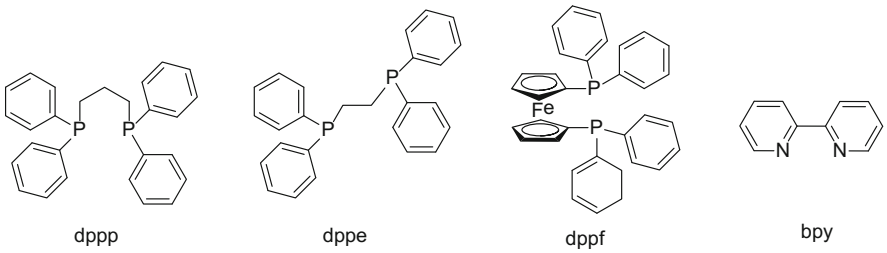

Fig. 1 Structures of some of the common ligands used in transition metal catalysts; *dppp*-bis (diphenylphosphino)propane, *dppe*-bis(diphenylphosphino)ethane, *dppf*-bis(diphenylphosphino) ferrocene, *bpy*-2,2′-bipyridyl

molecular weight ($M_n = 1{,}370$ g/mol) than polymers from previous attempts by other groups. However, a major fraction of the polymer was insoluble. The Dudek group also followed a similar procedure using the more soluble $Ni(acac)_2$, with a similar result [44]. The Kumada cross-coupling reaction [45–47] adopted in both these syntheses predominantly yields 2,5-coupling. Further optimization of conditions such as ligands on the catalyst [48–53] (Fig. 1) and variation of metal [51, 52], solvent [49, 51], reaction temperature [48–50], and halogen attached to thiophene [49–51, 54, 55] led to improvements in the chemical synthesis of polythiophenes. Alternative synthetic routes such as oxidative coupling of dilithiothiophenes [56], oxidative polymerization [57], and electrochemical polymerization [58, 59] have also been explored (Scheme 1). However, the soluble fractions of the resultant polymers from all these synthetic methods had low molecular weights.

1.2 Poly(3-alkylthiophenes)

During studies on the optimization of polythiophene synthesis, the Yamamoto group discovered that polymers obtained from 2,5-dibromo-3-methylthiophene are more soluble than unsubstituted polythiophenes and also yield higher molecular weights [48]. They speculated that the increase in solubility was due to the alkyl substitution at the β-position of the thiophene ring. This study enabled the spectral study of the synthesized polythiophenes in chloroform solution. Other groups subsequently reported synthesis of poly(3-methylthiophenes) and their properties [1, 52, 60–62]. All these polymers had improved solubilities compared to polythiophenes, but the molecular weights of the synthesized polymers were low. Jen, Elsenbaumer and coworkers synthesized a series of poly(3-alkylthiophene)s (P3ATs) with varying alkyl chain lengths (methyl, ethyl, butyl, and octyl) and obtained highly soluble and environmentally stable polymers [63–65]. The molecular weights of the synthesized polymers were in the range of 3,000–8,000 g/mol. Subsequently, other groups also reported the synthesis of P3ATs by oxidative [66] and electrochemical [67, 68] polymerization.

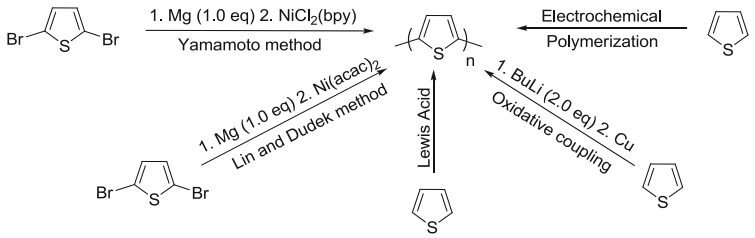

Scheme 1 Different synthetic schemes for the preparation of polythiophene [43, 44, 56–59].

Typical chemical polymerization of 3-alkylthiophenes involved the Kumada cross-coupling reaction of 2,5-diiodo-3-alkylthiophene in the presence of nickel catalysts. The first step of the reaction involved the formation of a Grignard reagent by the reaction of the 2,5-diiodo-3-alkylthiophene with one equivalent of magnesium. The asymmetry of the 3-alkylthiophene monomers leads to the formation of two isomers during the metal insertion reaction. The presence of these isomers gives rise to polymeric structures with different regioregularities, thereby leading to differences in the opto-electronic properties of the synthesized polymers. The regioisomerism and its influence on the opto-electronic properties of the polymers will be discussed in the next section.

2 Regioregularity in Poly(3-alkylthiophenes)

Yamamoto group first predicted the presence of regioisomers during the polymerization of the unsymmetrical monomer 3-methylthiophene [48]. In their analysis, they used the splitting of the methyl peak in the aliphatic region of the ^{1}H NMR spectrum of poly(3-methylthiophene) to explain the presence of different regioisomers during polymerization. In the unsymmetrical 3-alkylthiophenes, the α-carbon (2-position) between the sulfur atom and the alkyl chain is labeled as the 'head' position (H) and the α-carbon (5-position) is labeled the 'tail' position (T) (Fig. 2). When the Grignard is formed from 2,5-dibromothiophene, two different isomers 2-bromo-5-bromomagnesio-3-hexylthiophene and 5-bromo-2-bromomagnesio-3-hexylthiophene are produced. During the formation of dimers, three different regioisomers can be obtained: head–head (HH), head–tail (HT), and tail–tail (TT). Four different regioisomeric triads HH–TH, HH–TT, TT–HT, and HT–HT can be obtained during coupling. The HT–HT isomer is the regioregular isomer and the other three isomers are regioirregular. In a fully regioregular polymer chain (all couplings are HT couplings), the polymer is fully conjugated with the backbone remaining planar due to the sp^2 hybridized carbons in the thiophene ring. This planarity enables efficient π-stacking interactions between adjacent polymer chains. On the other hand, the presence of a HH or a TT coupling induces steric repulsion between the alkyl chains of subsequent thiophene units

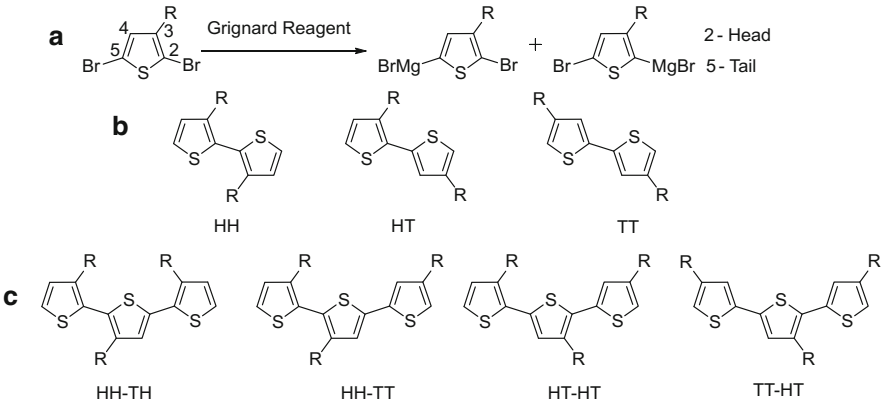

Fig. 2 (**a**) Numbering of the carbon atoms on the thiophene ring, indicating the head and tail positions on the ring and the isomers obtained on reaction with a Grignard reagent. (**b**) Structures of possible couplings in the dimers of 3-alkylthiophene rings. (**c**) Structures of the four possible regioisomeric triads of 3-alkylthiophene

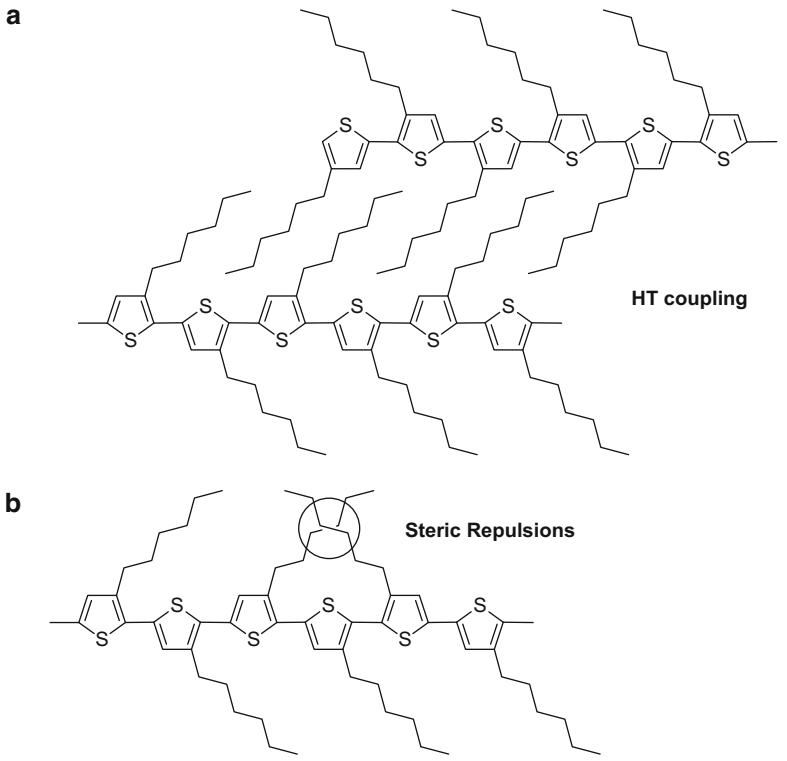

Fig. 3 Structures showing (**a**) the solid-state packing efficiency of HT-coupled P3HT and (**b**) steric repulsions in regioirregular P3HT that disrupt the solid-state packing

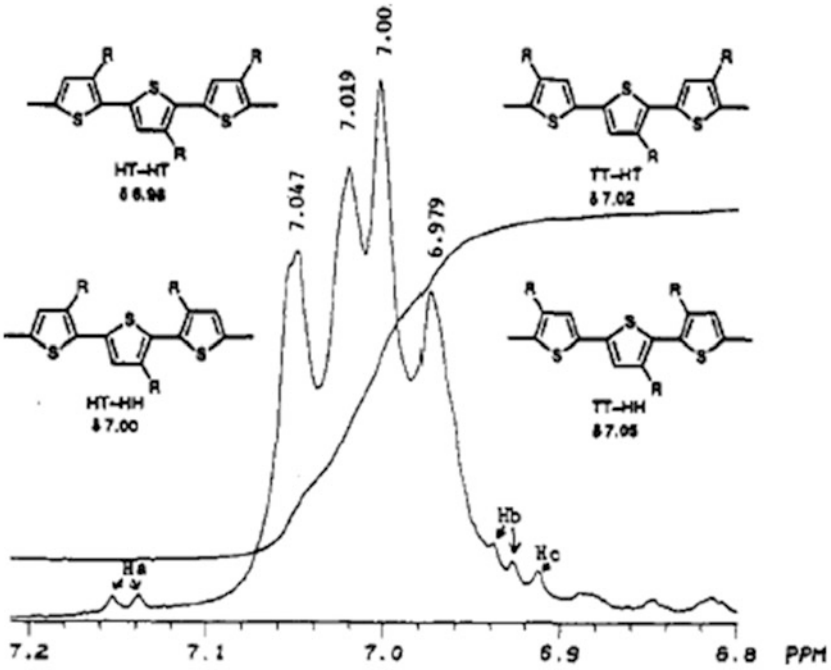

Fig. 4 ^{1}H NMR peak assignment for HT–HT (6.98 ppm), HT–HH (7.00 ppm), TT–HT (7.02 ppm), and TT–HH (7.05 ppm) coupling [76]. Reprinted with permission from Chen and Rieke [76]. Copyright (1992) American Chemical Society

(Fig. 3). This repulsion leads to dihedral twists in the polymer backbone, thereby reducing the packing efficacy of the polymer chains and leading to inferior opto-electronic properties compared with the regioregular counterpart [69–73].

The differences in the chemical environment of the aromatic proton at the 4-position of the thiophene ring in the regioisomeric triads shown in Fig. 2 lead to different chemical shifts in the ^{1}H NMR spectrum. The Wudl group synthesized regiochemically defined poly(3,3′-dihexyl-2,2′-bithiophene) using oxidative and electrochemical polymerization of 3,3′-dihexyl-2,2′-bithiophene. A careful comparison of the ^{1}H and ^{13}C NMR spectra of poly(3,3′-dihexyl-2,2′-bithiophene) with P3HT enabled estimation of the chemical shifts of the regioisomers [74]. Further studies enabled the exact elucidation of the chemical shifts for each of the aromatic protons in the regioisomers [75]. It was established that the aromatic protons involved in HT–HT coupling are observed at 6.98 ppm in the ^{1}H NMR spectrum of P3HT whereas those involved in HT–HH are found at 7.00 ppm, TT–HT at 7.02 ppm, and TT–HH 7.05 ppm (Fig. 4) [76]. This enabled quantification of the percentage composition of the different couplings present in a P3HT molecule.

3 Synthesis of Regioregular Poly(3-alkylthiophene)

The first chemical synthesis of regioregular poly(3-alkylthiophene) (P3AT), consisting predominantly of HT couplings, was reported by McCullough and coworkers [77, 78]. In this reaction, the 5-position of 2-bromo-3-alkylthiophene was lithiated using lithium diisopropylamine (LDA) at −40°C. This was followed by a transmetallation of the lithium to magnesium with $MgBr_2{\cdot}Et_2O$ to obtain 2-bromo-5-bromomagnesio-3-alkylthiophene, which was then polymerized by Kumada cross-coupling using Ni(dppp)Cl_2 as the catalyst (Scheme 2). The synthesized poly(3-dodecylthiophene) had a weight-averaged molecular weight (M_w) of 16 kg/mol with a high regioregularity (91% HT coupling) and high electrical conductivity (up to 10^5 S/m). This synthetic method is also known as McCullough method. The reaction was later improved by replacing $MgBr_2$ with $ZnCl_2$ for the transmetallation reaction, due to the higher solubility of $ZnCl_2$ at −78°C [79]. In the same year as McCullough's first report on regioregular P3AT synthesis, Chen and Rieke also reported an alternative method for obtaining highly regioregular P3ATs [76]. Rieke's method involved the reaction of 2,5-dibromo-3-hexylthiophene with highly reactive zinc to obtain the isomers 2-bromo-5-bromozincio-3-hexylthiophene and 2-bromozincio-5-bromo-3-hexylthiophene in 9:1 molar ratio. This mixture was polymerized by the use of the Negishi coupling reaction with Ni(dppe)Cl_2 (0.2 mol%) as the catalyst (Scheme 2). Regioregular P3HT (~98.5% HT coupled) with a molecular weight of about 15 kg/mol was obtained in quantitative yield (Scheme 2). ^{1}H NMR spectrum of the polymer revealed the HT–HT coupling peak at 6.98 ppm (Fig. 5). Further optimizations showed that the regioselectivity of the oxidative addition reaction can be improved by performing the experiment at cryogenic temperatures (−78°C) [80]. The use of Pd or Ni(0) catalysts produced polymers with higher incidence of HH coupling (>30% HH coupling) [80]. The use of 2-bromo-5-iodo-3-hexylthiophene also improves the regioselectivity of oxidative addition by affording 2-bromo-5-iodozincio-3-hexylthiophene exclusively [80].

The McCullough method and the Rieke method were significant breakthroughs in the progress of synthesis of regioregular P3ATs with good thermal and electronic properties. However, the cryogenic temperatures adopted in both methods made them not so ideal for large scale synthesis. In 1999, McCullough discovered a simple and convenient route for the synthesis of highly regioregular P3ATs by the use of Grignard metathesis [81]. This method involves the reaction of 2,5-dibromothiophene with a Grignard reagent in tetrahydrofuran (THF) at reflux conditions to generate the regioisomers 2-bromo-5-bromomagnesio-3-alkylthiophene and 5-bromo-2-bromomagnesio-3-alkylthiophene, which are then polymerized in situ using Ni(dppp)Cl_2 to obtain regioregular P3AT (Scheme 3). The synthesized poly(3-dodecylthiophene) had a number-averaged molecular weight (M_n) of 20–35 kg/mol with a polydispersity index (PDI) of 1.2–1.5 and a high regioregularity (>99% HT couplings). A reasonable regioselectivity was observed, with the ratio of the regioisomers 2-bromo-5-bromomagnesio-3-alkylthiophene and

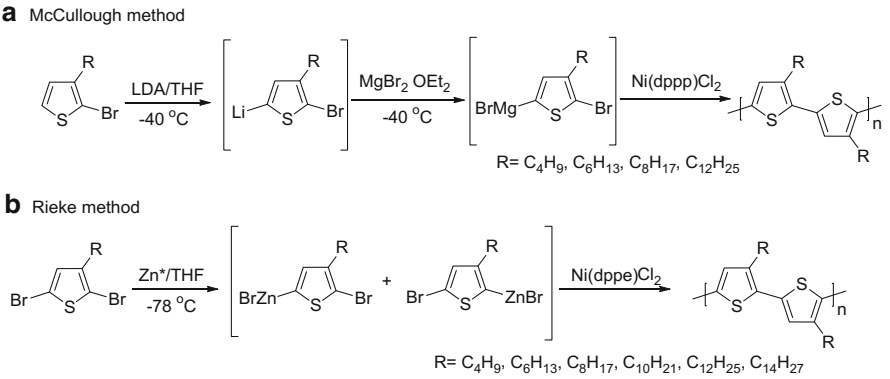

Scheme 2 McCullough method and Rieke method for the synthesis of regioregular P3AT

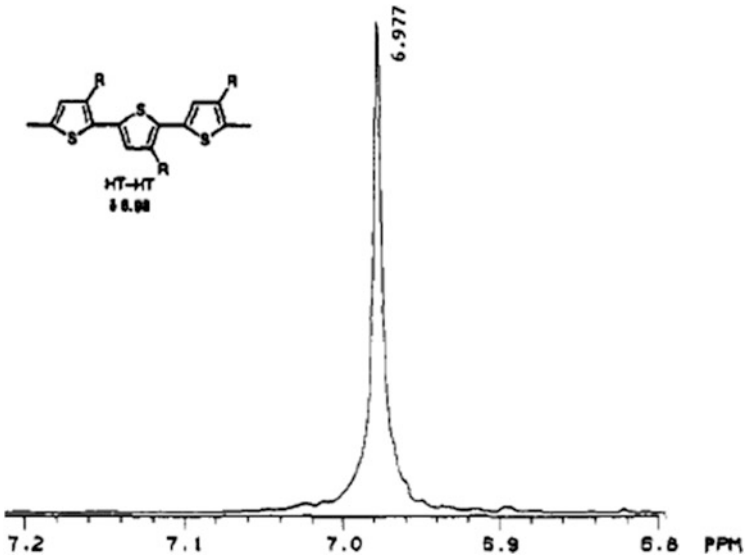

Fig. 5 [1]H NMR spectrum of the aromatic region of highly regioregular P3HT [76]. Reprinted with permission from Chen and Rieke [76]. Copyright (1992) American Chemical Society

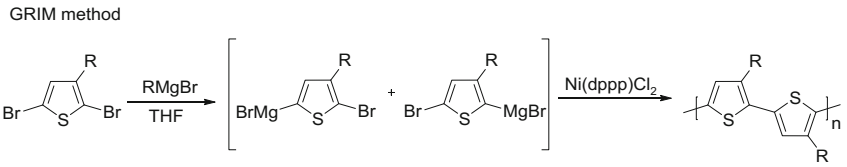

Scheme 3 GRIM method for the synthesis of regioregular P3ATs

5-bromo-2-bromomagnesio-3-alkylthiophene being 4:1, indicating a preferential magnesium–bromine exchange reaction at the 5-position of the thiophene ring. Further optimization of this method involved changes in the reaction temperature and changing the monomer to 2-bromo-5-iodo-3-alkylthiophene for a preferential Grignard reaction at the 5-position of the thiophene ring [82].

3.1 Other Synthetic Methods

With the advent of the Grignard metathesis polymerization method, the synthesis of regioregular P3ATs could be performed at room temperatures and without the use of highly activated metallic zinc. There were many other attempts at producing highly regioregular P3ATs. Andersson and coworkers reported a regioselective polymerization of 3-(4-octylphenyl)thiophene by a controlled oxidation using $FeCl_3$ as the catalyst [83, 84]. They reported a slow addition of $FeCl_3$ slurry to control the ratio of Fe^{3+} to Fe^{2+} in the polymerization mixture and thereby the regioselectivity of the polymerization [83, 84]. The synthesized polymer had a M_n of 23 kg/mol with a regioregularity of 94%. They proposed that the polymerization reaction initiates by the formation of a radical cation on thiophene and that chain propagation proceeds through the carbocation [84]. However, the regioselectivity obtained by poly[3-(alkylphenyl)thiophene] could not be achieved for P3ATs with the same method [83, 84]. Oxidative polymerization was also attempted on 3-(4-butylphenyl)thiophene using $VO(acac)_2$ catalyst [85]. After 24 h of reaction, the soluble fraction had M_n ranging between 3 and 10 kg/mol, with regioregularities between 72 and 90%. Telechelic regioregular P3HTs were synthesized by Stille coupling polymerization of 2-iodo-3-hexyl-5-(tributylstannyl)thiophene in the presence of Pd(0) catalyst. The prepolymer was synthesized in THF and quenched in methanol. Soxhlet extractions were performed on the prepolymer to remove the low molecular weight fractions. The fraction obtained from hexane extraction was further polymerized in toluene at reflux conditions to obtain a high molecular weight polymer. The final polymer had a M_n of 16 kg/mol with a PDI of 1.2 and 96% HT couplings [86]. Given the environmental stability of the trialkylstannyl end group, Stille coupling polymerization was also employed by other groups to obtain P3ATs with reasonable molecular weights and high regioregularity [87, 88]. Suzuki coupling polymerization was also employed for the synthesis of P3ATs [89, 90]. [1′,3′-(2′,2′-Dimethylpropylene)]-2-iodo-3-octyl-5-thienylboronate was polymerized in the presence of $Pd(OAc)_2$ to obtain poly(3-octylthiophene) with M_w of 27 kg/mol, PDI of 1.5, and 96–97% HT couplings [89]. Other palladium-based catalysts were also used for the synthesis of P3HT [91–93]. Continuous flow methods have also been used for the synthesis of P3HT [94].

Direct (hetero)arylation polymerization (DHAP) is also used for the synthesis of polythiophenes [95–98]. In this method, oxidative coupling occurs between an aromatic group that contains a leaving group and an unsubstituted aromatic ring. The unsubstituted aromatic ring undergoes C–H activation leading to an oxidative

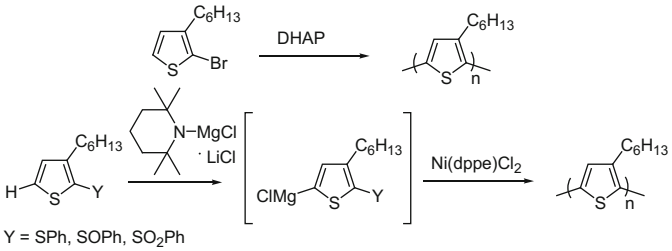

Scheme 4 Direct (hetero)arylation polymerization (*DHAP*) [99] and polymerization by C–S bond cleavage [100]

coupling reaction between the two aromatic rings [99] (Scheme 4). The Hermann–Beller catalyst *trans*-bis-(acetato)bis[*o*-(di-*o*-tolylphosphino)benzyl]dipalladium (II) or $Pd(OAc)_2$ are generally used to catalyze this reaction. This reaction is performed at high temperatures, leading to lower regioregularities and the possibility of 2,4-couplings [96–98]. However, the advantage of avoiding monomer functionalization makes this method more versatile. Further exploration of reaction conditions is required for the synthesis of polymers with high regioregularities and controlled molecular weights with low PDIs.

Mori's group recently reported the polycondensation of thiophenes by C–S bond cleavage [100]. In this method, 2-(phenylsulfonyl)-3-hexylthiophene is reacted with a Knochel–Hauser base to generate 5-chloromagnesio-2-(phenylsulfonyl)-3-hexylthiophene, which on reaction with a nickel catalyst such as $Ni(dppe)Cl_2$ generates P3HT (Scheme 4). The substituents at the 2-position of thiophene can be sulfides, sulfoxides, or sulfones. The presence of an electron-withdrawing group at the 2-position increases the acidity of the proton at the 5-position, thereby only mild conditions are required for the deprotonation reaction. The polydispersities of the polymers obtained vary between 1.3 and 2.3 depending on the conditions employed.

4 Mechanism of Grignard Metathesis

Understanding the mechanism of polymerization plays an important role in the synthesis of novel polymer architectures and in extending the method to different monomers. Extensive work has been carried out in order to understand the mechanism of polymerization by Ni catalysts. Initial work on Grignard coupling reactions between halothiophenes and aryl Grignard reagents in the presence of Ni-phosphine catalysts was undertaken by the groups of Masse [101] and Kumada [45–47]. Kumada predicted transmetallation (reaction of Grignard reagent with nickel catalyst) to be the first step in the catalytic cycle. Yamamoto and coworkers predicted the mechanism for both polythiophenes and P3ATs with Ni(0) catalyst [102, 103]. According to their mechanistic pathway, there are three steps in the polymerization that are repeated multiple times: (1) oxidative addition of the

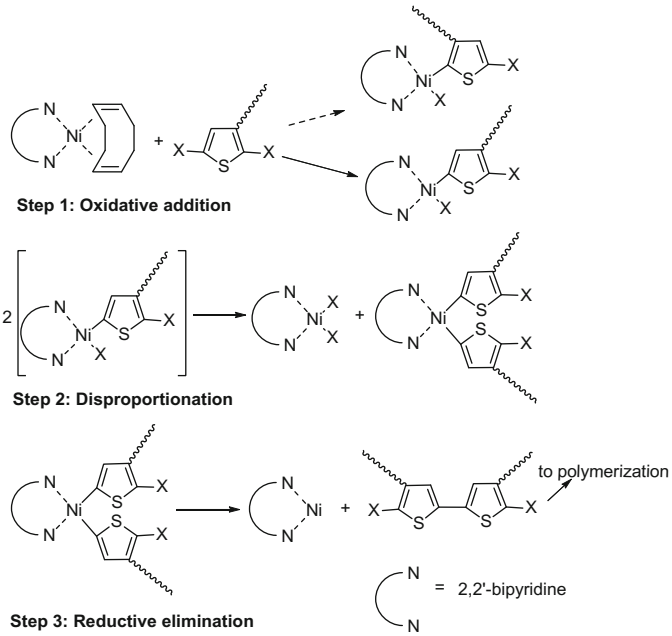

Scheme 5 Mechanism of P3AT synthesis using Ni(cod)(bpy) catalyst, as proposed by Yamamoto [103]. Reprinted from Miyazaki and Yamamoto [103], Copyright (1994) with permission from Elsevier

2,5-dihalo-3-alkylthiophene to the Ni(cod)(bpy) complex to form Ni(bpy)RX; (2) disproportionation of the oxidative addition product to form Ni(bpy)R_2 and Ni(bpy)X_2; and (3) reductive elimination to form the dimer R_2. The cycle of these three steps is repeated on the dimer to add subsequent monomeric units to form a polymeric chain (Scheme 5).

The synthesis of P3ATs by Grignard metathesis (GRIM) involves a polycondensation reaction in the presence of a Ni(II) catalyst. Early attempts at the synthesis of P3ATs by GRIM produced polymers with large PDIs and uncontrolled molecular weight, ascertaining the belief that GRIM undergoes a step-growth mechanism just like any other polycondensation reaction. In 2004, Yokozawa's group showed evidence that the synthesis involves a chain-growth mechanism [104, 105]. They obtained kinetic data for the polymerization reaction and showed that the value of M_n obtained during the reaction was directly proportional to the feed ratio of monomer to catalyst. Yokozawa and colleagues observed that the increase in molecular weight of the polymer was directly proportional to the consumption of monomer. The plot of monomer conversion versus time also indicated a large monomer conversion in the initial stages of the reaction followed by a saturation in the conversion [104]. All this evidence indicated the presence of a chain-growth mechanism for the polymerization by GRIM. Yokozawa showed that it is possible to synthesize P3HT with a controlled molecular weight and narrow PDI (about 1.15) [105].

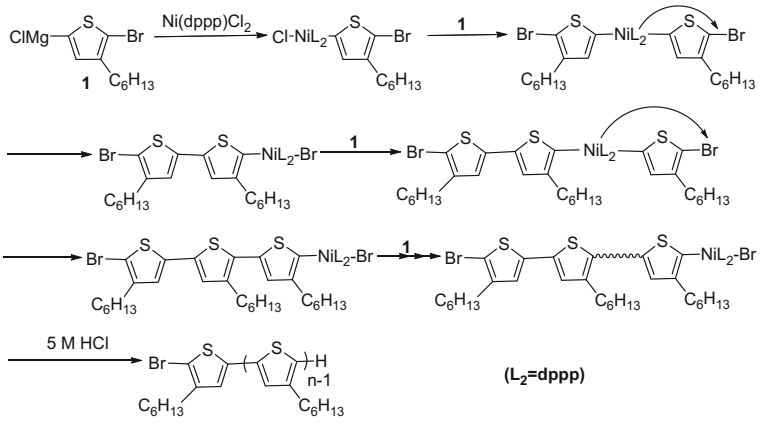

Scheme 6 Mechanism of chain-growth polymerization of 2-bromo-5-chloromagnesio-3-hexylthiophene using Ni(dppp)Cl_2 catalyst, as proposed by Yokozawa [106]. Reprinted with permission from Miyakoshi et al. [106]. Copyright (2005) American Chemical Society

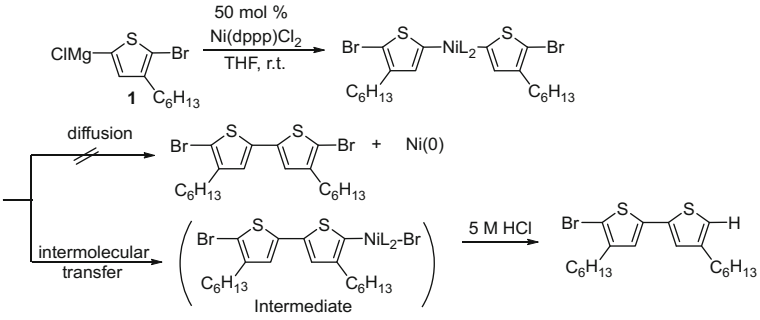

Scheme 7 Evidence of intramolecular catalyst transfer [106]. Reprinted with permission from Miyakoshi et al. [106]. Copyright (2005) American Chemical Society

Yokozawa proposed that the chain-growth mechanism by GRIM is through a catalyst transfer mechanism (Scheme 6) [106]. His proposed mechanism also involves a transmetallation reaction as the first step in the polymerization, generating a Ni(0) that is bound to two thiophene molecules. A coupling reaction between the two thiophene units is followed by an intramolecular transfer of the Ni(0) across the thiophene unit (Scheme 7). This intramolecular transfer was confirmed by addition of 50 mol% of Ni(dppp)Cl_2 to 2-bromo-5-chloromagnesio-3-hexylthiophene and the subsequent quenching of the reaction mixture in 5 M HCl. Gas chromatography coupled with mass spectrometry (GC/MS) of the products confirmed almost exclusive presence of 4,4′-dihexyl-5-bromo-2, 2′-bithiophene. The TT regioisomer was confirmed by heteronuclear multiple-bond correlation spectroscopy (HMBC) NMR. This intramolecular transfer is also termed ‘ring walking’ by many researchers [107–109]. The catalytic cycle

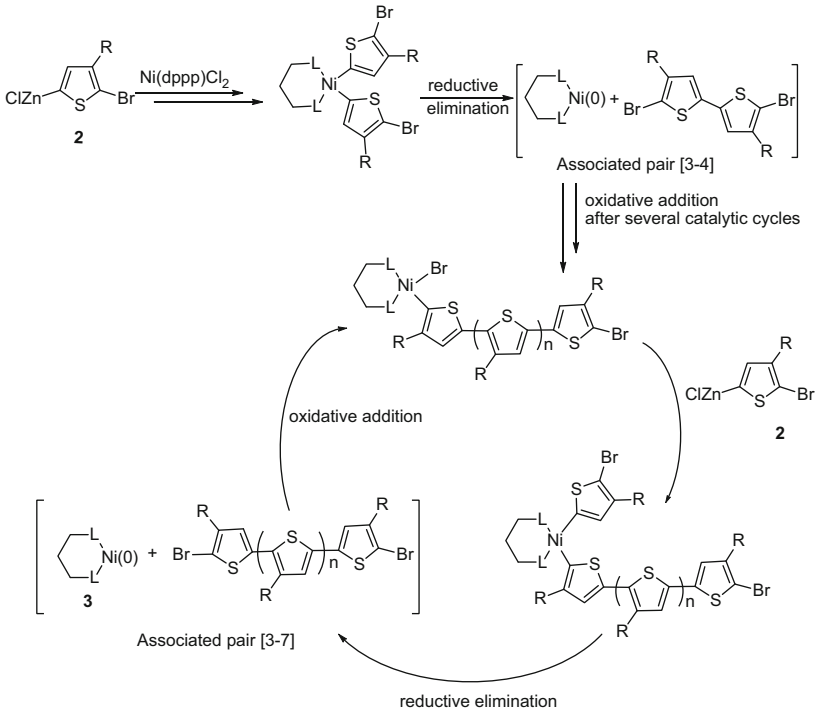

Scheme 8 Chain-growth mechanism of Grignard metathesis polymerization proposed by the McCullough group [110]. Reprinted with permissions from Sheina et al. [110]. Copyright (2004) American Chemical Society

continues with further transmetallation followed by an intramolecular chain transfer reaction. Quenching the polymerization reaction with 5 M HCl afforded a polymer with Br/H endgroups, which was confirmed by matrix-assisted laser desorption ionization–time of flight (MALDI-TOF) MS. The presence of only Br/H end groups and the absence of polymer chains terminated by Br/Br or H/H indicated that the attached NiL_2 group does not fall off the growing polymer chain. To further prove that the propagating group is the Ni complex, Yokozawa and colleagues added ArMgCl to the polymerization mixture to observe an Ar/Ar-terminated polymer chain (if the MgCl group is involved in the transfer, a H/Ar-terminated polymer chain should be observed) upon quenching the polymerization. They also predicted that the chain growth proceeds in only one direction, with only one NiL_2 group involved with one polymer chain. They termed the polymerization a catalyst transfer polycondensation reaction, which was later named the Kumada catalyst transfer polycondensation (KCTP).

Shortly after Yokozawa's initial report, McCullough's group also reported evidence for a chain-growth mechanism for the McCullough method [110] as well as for the GRIM polymerization [111]. Their mechanism (Scheme 8) predicted that both polymerizations go through the two following steps: (1) transmetallation

reaction of two molecules of 2-bromo-5-chlorozincio-3-hexylthiophene or 2-bromo-5-chloromagnesio-3-hexylthiophene with a Ni(dppp)Cl_2 catalyst molecule and (2) reductive elimination to form TT coupled 5,5′-dibromo-4,4′-dihexylbithiophene and a Ni(0) complex. The Ni(0) and the dimer form an associated pair, which is a π-complex between the Ni catalyst and the growing polymer chain. The associated pair is involved in further oxidative addition reaction and monomer insertion, followed by another reductive elimination. This catalytic cycle continues by the addition of one monomeric unit each time until all the monomer is consumed. The main difference between the KCTP mechanism suggested by Yokozawa and McCullough's mechanism is that, in McCullough's method, the nickel group breaks off from the chain by reductive elimination and forms an associated pair with the polymer chain only to undergo further oxidative addition, whereas KCTP mechanism claims that the nickel group undergoes successive reductive elimination and oxidative addition, without the formation of an associated pair (by catalyst transfer). Both the mechanisms agree on the transmetallation step, thereby producing at least one TT coupling defect in the polymer chain. They both also predict that formation of the HH coupling product is not likely due to the steric hindrances involved. Boyd et al. prepared the reverse monomer (5-bromo-3-hexyl-2-iodothiophene) but did not observe polymerization or even dimer formation (even with 0.5 equivalents of Ni(dppp)Cl_2) [112], which supports the steric arguments of McCullough. The Kiriy group observed that the transmetallation step is crucial in the polymerization process and that further chain propagation is not favored if sterically hindered compounds are formed during the transmetallation step [113]. McCullough's group further established that GRIM polymerization was a quasi-living reaction [111] and that the polymerization was a first-order reaction with respect to Ni(dppp)Cl_2 catalyst. It was also demonstrated that the degree of polymerization could be precisely controlled by adjusting the ratio of monomer to initiator concentrations. The quasi-living nature of the polymerization meant that the polymer chains were still active towards the end of reaction and, hence, end-capping of the polymer chains or synthesis of block copolymers could be performed. End-capping of the polymer chains was carried out using an active reagent such as a Grignard reagent. The end-capping method allowed estimation of the average number of repeating units in the polymer chain by ^{1}H NMR peak integration.

(Note that gel permeation chromatography (GPC) overestimates the molecular weight of rod-like polymers such as P3HT. GPC generally measures the relative molecular weight of the polymers with respect to polystyrene standards. GPC measurements are based on the correlation of hydrodynamic volume of the polymer chains with their molecular weights and, hence, give an overestimated molecular weight for rod-like polymers such as P3HT [114]. A systematic comparison of molecular weights from ^{1}H NMR and GPC measurements by the Seferos group revealed that GPC overestimates the M_n values of P3HT as compared to ^{1}H NMR linearly by a factor of 1.3 for M_n of 6.5-23 kDa and nonlinearly for higher molecular weights [115]. On the other hand, MALDI-TOF MS can be used obtain the absolute molecular weights [116]). However, end-capping reactions are generally not

quantitative conversions, making estimation of the number of repeating units by NMR unreliable.

Synthesis of block copolymers could be performed by sequential addition of a second monomer to the 'living' polymer chain. This feature was exploited by many groups for the synthesis of a variety of block copolymers [111, 117–124]. Many researchers end-functionalized the P3HT chain with an end group [13, 108, 125–134] and later used the functionalization as a macroinititor for the synthesis of a second block using alternative techniques like anionic polymerization [129, 132, 133], reversible addition-fragmentation chain transfer (RAFT) [127], atom transfer radical polymerization (ATRP) [128], etc. [13, 108, 135]. This approach led to the synthesis of various block copolymers such as P3HT-*b*-PMMA [129] and P3HT-*b*-PBLG [130, 131], which would otherwise be not viable due to the non-involvement of the second block in GRIM. On the whole, GRIM is the most versatile technique for the synthesis of regioregular P3ATs.

Mechanistic studies by the McNeil group revealed that the rate-limiting step of GRIM polymerization is ligand dependent [136, 137]. They observed that when dppe is used as the ligand, the reductive elimination reaction is the rate-limiting step [136], whereas when dppp is used as the ligand, the transmetallation reaction is the rate-limiting step [137]. The Rawlins group observed that during the polymerization reaction, the nickel species diffuses from chain to chain, indicating a loss of chain ends, without a loss in control of molecular weight [138]. Kinetic isotope effect studies undertaken by Yoshikai et al. suggested that the transmetallation reaction is the first irreversible step in the reaction mechanism [92]. Varying the ligands attached to the catalyst was adopted by many research groups as an alternative strategy for expanding the scope of GRIM to different monomer systems [122, 139–145]. The McNeil group studied the synthesis of P3HT with dialkylphosphino nickel catalysts [139], whereas the Stefan group used the more soluble nickel-diimine catalyst [140]. Both groups observed a chain-growth polymerization mechanism.

The influence of additives such as LiCl on the mechanism of the reaction and quality of the end polymer was investigated by many groups [122, 137, 143, 146–151]. Knochel's group first observed that addition of LiCl salt during the magnesium–halogen exchange reaction increases the rate of the exchange reaction and also increases the yield of the metathesis reaction [146, 147]. It was understood that LiCl complexes with the Grignard reagent and breaks up the aggregates, thus increasing the reactivity of the Grignard reagent [150]. Further mechanistic studies revealed that addition of LiCl led to polymers with higher molecular weight and lower PDI [137, 148–151].

All three methods (McCullough method, Rieke method, and Grignard metathesis) are efficient in the synthesis of highly regioregular and narrow PDI polymers. However, the reaction mechanism of all three methods involves an initial TT coupling reaction that results in at least one regiodefect in the polymer chain. The end groups of the polymers in an efficient catalyst transfer reaction are H/Br. It has been observed that the presence of a bromine end group in the polymer chain lowers the opto-electronic properties of the polymer [152, 153]. Initiating the

polymerization from an external initiator would eliminate the TT regiodefect formed in the first step of the polymerization and also prevent the formation of Br terminal groups from the TT coupling reaction.

5 External Initiation of Polymerization

It has been well established that nickel catalyst allows the formation of highly regioregular P3HTs with well controlled molecular weight and PDIs. Initiating the polymerization from an external moiety should retain the quasi-living nature of GRIM/KCTP and, moreover, allow inclusion of an aromatic group that would preserve the aromaticity of the polymer backbone. The external initiation can be started using a small molecule initiator, a polymeric initiator, or one that contains a complex architecture.

The Kiriy group was the first to explore an external initiation polymerization by the preparation of a suitable initiator for the synthesis of P3HT [154]. They used Ar-Ni(PPh_3)$_2$-Br as an initiator (synthesized according to the oxidative addition reaction between bromobenzene or *o*-bromotoluene with Ni(PPh_3)$_4$ [155, 156]) for P3HT synthesis. This initiator molecule was then reacted with 2-bromo-5-chloromagnesio-3-hexylthiophene to generate P3HT, with 98% of chains having a phenyl end group [154]. The polymers displayed about 29 repeat units with a regioregularity reaching 85%. End-group analysis of the synthesized polymers revealed that the end groups were a mixture of Ph/H, Ph/Br, and H/H, indicating the presence of chain transfer or chain termination processes [107, 154]. Using the principles of chain-growth and step-growth polymerizations [157, 158], Kiriy and coworkers indicated that the underlying mechanism of the reaction is a chain-growth mechanism and not a step-growth mechanism [107]. The presence of chain transfer or chain termination processes would lower the livingness of the polymerization and would therefore make it difficult to achieve efficient synthesis of block copolymers and other polymer architectures. Kiriy and colleagues also synthesized polymer brushes by initiating the polymerization from surface-immobilized macroinitiators [154], which is explained in Sect. 5.2.

The Luscombe group further extended the work on initiator synthesis [159–161]. Doubina tried to replace the unstable, expensive, and carcinogenic Ni(PPh_3)$_4$ with an air-stable [162, 163] and inexpensive Ni(PPh_3)$_2$$Cl_2$ for the synthesis of Ar-Ni(PPh_3)$_2$-Br [159]. Two alternative methods were employed for the synthesis of the initiator Ar-Ni(PPh_3)$_2$-Br. First, Ni(PPh_3)$_4$ was produced in-situ by the reduction of Ni(PPh_3)$_2$$Cl_2$ with two equivalents of butyl lithium and in the presence of two equivalents of PPh_3. In a second method, bromo benzene was reacted with one equivalent of butyl lithium to generate an aryl lithium, which upon reaction with Ni(PPh_3)$_2$$Cl_2$ generated the initiator Ar-Ni(PPh_3)$_2$-Cl. The initiators produced by these two methods were utilized in an in-situ one-pot polymerization reaction. The initiator obtained by the first method could only produce polymers with a degree of polymerization (DP_n) of 50, indicating the presence of chain termination

and chain transfer reactions. The synthesized polymers contained 60% Ph/H terminal groups and when the initiator was replaced with Ar-Ni(PPh_3)$_2$-Cl the percentage of Ph/H terminal groups increased to 90%, indicating that chain growth is more efficient with Ar-Ni-(PPh_3)$_2$-Cl than with Ar-Ni(PPh_3)$_2$-Br. Doubina and coworkers also attempted simultaneous oxidative addition between Ni(cod)$_2$ and bromo benzene and ligand exchange reaction (with PPh_3, dppp, dppe and dppf) in a one-pot reaction (Scheme 9) [160]. The ligands dppp and dppe did not yield externally initiated polymers whereas the PPh_3 and dppf displayed high initiation efficiency (90% for PPh_3 and 83% for dppf). Both the polymers contained mixtures of Ph/H and Ph/Br end groups.

The Kiriy group extended the use of inexpensive Ni(PPh_3)$_2$Cl$_2$ by generating Ph-Ni(PPh_3)$_2$-Cl on reaction between Ph-MgCl and Ni(PPh_3)$_2$Cl$_2$ [166]. They also developed the initiators Ph-Ni(bpy)-Br and Ph-Ni(dppp)-Br (Scheme 9) [164]. The polymers obtained by using Ni(bpy)Cl$_2$ and Ph-Ni(bpy)-Br displayed good regioregularities; however, they had broad PDIs. The polymer obtained from Ph-Ni(bpy)-Br had a significant amount of Ph/Br and H/Br end groups. Ph-Ni (dppp)-Br and Ph-Ni(dppe)-Br were prepared by a ligand exchange reaction between Ph-Ni(bpy)-Br and dppp or dppe ligand. The polymers obtained from Ph-Ni(dppp)-Br as catalyst displayed high regioregularities and reasonably low PDIs. The molecular weight scalability was also good up to a DP_n of 100, with the presence of only Ph/H end groups (observed from NMR) indicating a good chain-growth polymerization procedure. Similar results were observed for Ph-Ni (dppe)-Br as the catalyst.

The Luscombe group synthesized Ph-Ni(dppp)-Cl and *o*-tolyl-Ni(dppp)-Cl by the oxidative addition between aryl chloride and Ni(PPh_3)$_4$, followed by a ligand exchange with dppp. When used as initiators, the two complexes produced fully regioregular P3HTs with PDIs of 1.1–1.2 (Scheme 9). Kinetic studies of the polymerization indicated that it is a chain-growth mechanism with only tolyl/H end groups for tolyl initiator, whereas the phenyl initiator displayed mostly Ph/H end groups with a small percentage of Ph/Br and H/Br also present (Fig. 6). The presence of polymer chains with Ph/Br end groups was attributed to the decreasing solubility of the polymer chain, whereas the H/H-terminated polymer chains were formed due to a small amount of Ni(dppp)$_2$ formed during the ligand exchange reaction. The more efficient initiation in the case of *o*-toluene indicates the importance of the methyl substituent in the *ortho* position to the Ni complex. Chatt [167] and Hidai [156] explained this phenomenon as electronic and steric stabilization of the Ni complex due to the *ortho* substituent; the *ortho* substituent holds the plane of the aryl group perpendicular to the plane of the Ni complex, thereby lowering the energy of the d_{xy} orbital (highest filled) of the Ni complex and by involving in π-backbonding to the π* orbital on the aryl group. The *ortho* substituent also sterically blocks the axial coordination site on the Ni atom and, hence, prevents the disruption of the geometry on the Ni complex.

Smeets and colleagues observed that Ar-Ni(PPh_3)$_2$-Cl gives only about 65% of Ar/H terminated polymers whereas about 95% Ar/H terminated polymers were observed by the addition of two equivalents of dppp ligands (addition of one

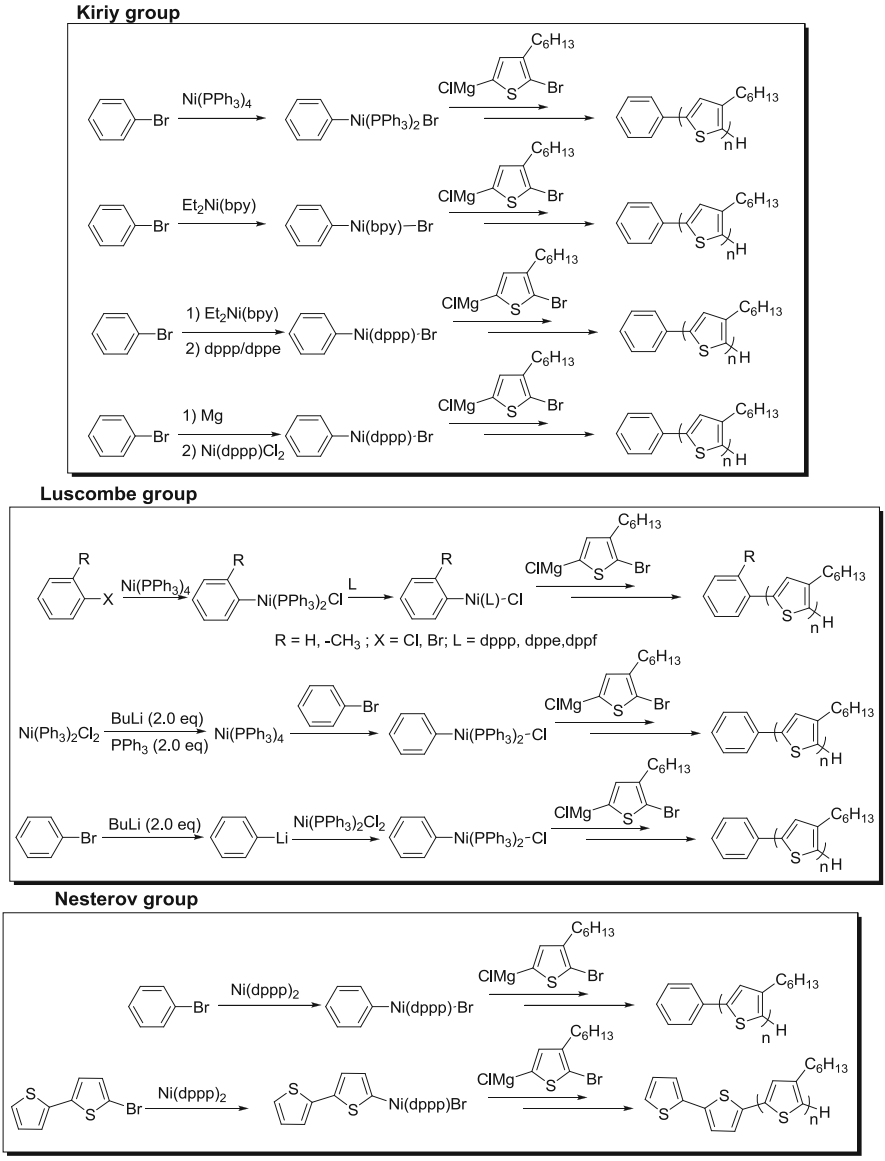

Scheme 9 External initiation of P3HT as used by the groups of Kiriy, Luscombe, and Nesterov [154, 159–161, 164, 165].

equivalent of dppp gave rise to only 85% Ar/H terminated polymers) [168]. All this research suggests that for an efficient external initiation polymerization reaction, the presence of a methyl substituent *ortho* to the Ni group on the aromatic ring of the initiator, the presence of a dppp ligand on the nickel atom, and a chloro substituent on the Ni atom increase the efficiency of polymerization.

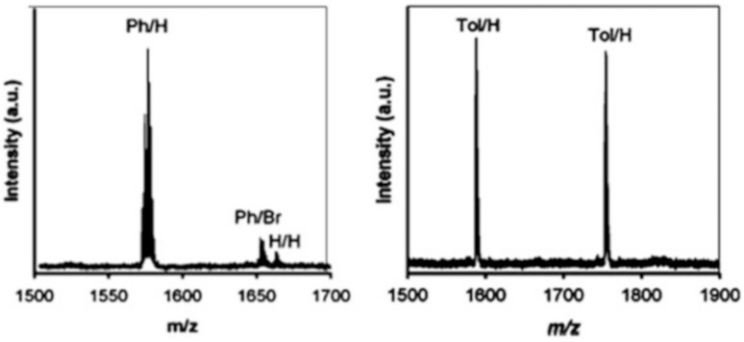

Fig. 6 MALDI-TOF MS of P3HT synthesized using Ph-Ni(dppp)-Cl (*left*) or *o*-tolyl-Ni(dppp)-Cl (*right*) as initiator [161]. Reprinted with permission from Bronstein and Luscombe [161]. Copyright (2009) American Chemical Society

The Nesterov group used a one-step method for the synthesis of the initiator. They reacted aryl halide with $Ni(dppp)_2$ to obtain the initiator Ar-Ni(dppp)-Cl in reasonably good yields (45–55%) [165]. Their method not only involved the one-step synthesis of Ar-Ni(dppp)-Cl initiator, but it also prevented the undesired presence of PPh_3 ligand, which may reduce the efficiency of the catalyst, promote disproportionation of the initiator, and also promote undesired aryl–aryl coupling. The authors claim that this procedure yields polymers that are defect-free and with 100% regioregularity. However, the polydispersities reported varied between 1.16 and 2.00.

5.1 Variation of Functional Groups That Can be Attached to the External Initiator

Efficient external initiation can pave the way to further functionalization and to varied polymer architectures. External initiation was attempted by different research groups with various functionalizations of the phenyl group (Fig. 7). Doubina et al. prepared a series of initiators by the addition of electron-donating and electron-withdrawing substituents on the phenyl ring to change the reactivity of oxidative addition reaction [159]. Although the rate and efficacy of the oxidative addition reaction is higher in the presence of an electron-withdrawing substituent [171], it was observed that the polymerization reaction is not very efficient. Very low amounts of initiator/H end groups have been observed for polymers synthesized from initiators with electron-withdrawing substituents on the phenyl ring, indicating a large number of chain transfer reactions. Similarly, the polymer obtained from 4-bromo anisole also displays very low amounts of initator/H end groups. Thus, it can be inferred that the polymerization of P3HT is more efficient on unfunctionalized phenyl rings in Ph-Ni$(PPh_3)_2$-Cl than on substituted phenyl rings.

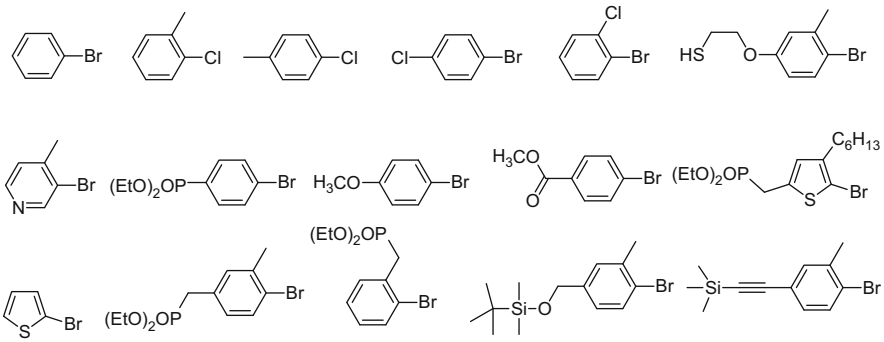

Fig. 7 Different functional groups explored for external initiation of polymerization [154, 159–161, 164, 168–170]

It was also observed that when *o*-chlorotoluene is used as the aryl halide, P3HT is produced only when PPh_3 is the ligand (but not with dppf), whereas *p*-chlorotoluene could not produce any polymer (with either of PPh_3 or dppf as the ligands). Doubina et al. further studied the steric effects on the polymerization by attaching phosphonate esters (which can be used to form efficient monolayers on metal oxides [172]) on the *ortho* and *para* positions of the phenyl ring [169]. The phosphonate ester, when substituted on the *para* position of the tolyl initiator, yielded about 94% HT couplings with a PDI of 1.2 and had up to 75% initiator/H end groups. The same substituent on the *para* position of the phenyl initiator did not yield any polymer, further emphasizing the advantage that the tolyl initiator has over the phenyl initiator [159, 169]. The polymer obtained from the *ortho*-substituted phosphonate ester contained only 37% initiator/H end groups, partly because of the incomplete oxidative addition reaction. The polymer obtained from (5-bromo-4-hexylthiophen-2-yl)methyl phosphonate initiator showed only 18% initiator/H end groups [169].

Smeets et al. synthesized *para*-siloxyl-substituted *o*-tolyl bromide and *para*-ethynyl-trimethyl silyl-substituted *o*-tolyl bromide, i.e., 1-bromo-2-methyl-4-({[(*t*-butyl) dimethylsilyl]oxy}methyl)benzene and 1-bromo-2-methyl-4-[2-(trimethylsilyl)-ethynyl]benzene (Fig. 7) [168]. The oxidative addition of these aryl halides with Ni $(PPh_3)_4$ followed by the addition of two equivalents of dppp ligand yielded 95% Ar/H-terminated polymer chains for the siloxyl substituent and about 80% Ar/H for the ethynyltrimethylsilyl substituent. These results, combined with Doubina's results [169] on *para*-substituted phosphonate esters, confirmed the importance of the presence of an *ortho* substituent position on the aromatic initiator, irrespective of the presence or absence of a substituent on the *para* position of the phenyl ring.

The presence of functional groups such as phosphonate ester, siloxane, and silanes on the initiating group helps in gaining an additional functionality to the polymer chain, such as the ability to attach to a surface, react with certain groups, etc. In the same context, the group of Koeckelberghs synthesized external initiator from 3-bromo-4-methylpyridine and other functional groups [170]. The polymers

obtained had polydispersities between 1.2 and 1.4 with the end groups for the majority of polymer chains being initiator/H and only a small quantity of initiator/Br observed. In Sect. 5.2, a few examples demonstrating the advantage of having functional group on the initiator are discussed.

5.2 *Initiation of Polymers from Surfaces*

One of the main advantages of external initiation of a polymerization is the ability to attach different functional groups on the initiator unit that can add an additional functionality to the polymer chain and interact with the external environment without disrupting the solid-state packing or the properties of the polymer.

The Kiriy group used the external initiation technique for the synthesis of polymer brushes by initiating the polymerization of 2-bromo-5-chloromagnesio-3-hexylthiophene using the macroinitiator PS-Ni(PPh_3)$_2$-Br, obtained by oxidative addition reaction between bromo-substituted polystyrene and Ni(PPh_3)$_4$. They immobilized the polystyrene on a glass substrate and initiated the polymerization, thereby obtaining polymer brushes of 40–70 nm thickness [154, 173]. The brushes exhibited the properties (solvatochromism and thermochromism) of highly regioregular P3HT. Kiriy and coworkers further extended this technique by grafting P3HT chains onto the block copolymer poly(4-vinylpyridine)-*b*-poly(4-iodostyrene) [174] and transformed the non-conductive surface of P4VP-*b*-PS(I) to a semiconductive surface. A low grafting density of one P3HT unit for every seven polystyrene units was observed. The grafted films displayed a smooth surface morphology. The grafted copolymer P4VP-*b*-PS(I)-*graft*-P3HT was also grown on silica particles (micron scale) (Fig. 8). Attempts to detach the grafted copolymer off the silica particles for the analysis of the P3HT chains were unsuccessful. Senkovsky et al. also grew P3HT chains on organosilicon nanoparticles [164]. Detachment of P3HT chains was successful by dissolution of the nanoparticles in HF. Analysis of the detached P3HT chains showed that the polymers had M_n of 43,000 g/mol. The group managed to grow densely grafted P3HT (with tethering density of 0.28 chains/nm^2), which increased the colloidal stability of the nanoparticles.

Sontag et al. explored the growth of polythiophene on gold surfaces by functionalizing the surface with a 6-(5-bromothiophen-2-yl)hexane-1-thiol [175]. The more reactive Ni(cod)(PPh_3)$_2$ complex was used for the oxidative addition with the bromo-end of the thiophene on the functionalized gold surface. The reactive Grignard species ClMg-Th-I was used for the growth of the polymer chain. Smooth polythiophene films of thickness ~14 nm could be grown and the sigma bonding of the films with the surface was confirmed by cyclic voltammetry (CV) and polarization-mode infrared reflection absorption spectroscopy (IRAS). The Locklin group further extended the surface initiation technique to indium tin oxide (ITO) and silica surfaces [148, 178–180]. Phosphonic acid derivatives were used for interaction with the ITO surface and for the formation of monolayers. Initiators were formed on these monolayers through the oxidative addition reaction

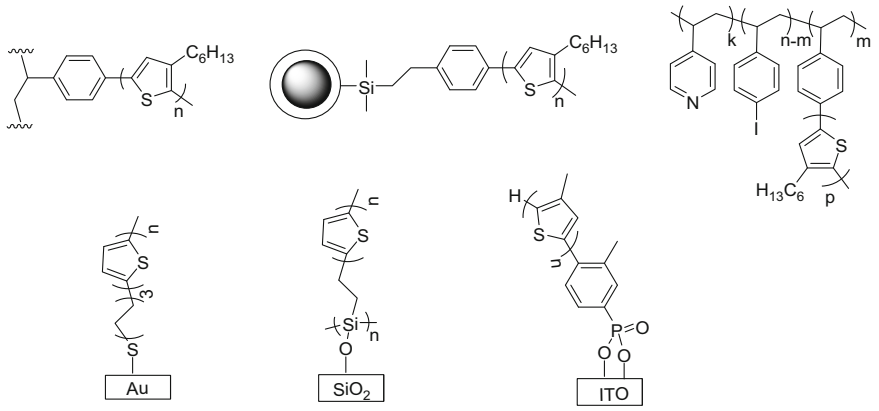

Fig. 8 Polymers grafted on to different surfaces [154, 164, 173–177]

with $Ni(cod)_2$ and ligand exchange with dppe, dppp, dppb, and bpy ligands [148]. The surface coverage decreased on ligand exchange due to disproportionation reactions [102, 105, 150, 169, 181–183], which can be lowered by the presence of a substituent *ortho* to the Ni complex on the initiator moiety [159, 168, 169]. The poly(3-methylthiophene) (P3MT) chains grown on these initiators exhibited uniform surface morphology on both silica and ITO, irrespective of the ligand used, with a surface thickness varying between 40 and 65 nm. It was shown that the use of a palladium catalyst for surface-initiated KCTP reduced the disproportionation reactions, thereby increasing the surface coverage [176]. The growth of polythiophenes on ITO surfaces has applications in the organic solar cell industry as a possible alternative for the commonly used conductive layer polyethylenedioxythiophene : polystyrenesulfonate (PEDOT:PSS), which is known to have some ill-effects on the ITO surface [184–186]. Doubina et al. functionalized the ITO surface with 4-chloro-3-methylbenzyl phosphonic acid and initiated the growth of P3MT using the initiation reactions discussed earlier [177]. Films with thicknesses up to 265 nm could be grown by controlling the monomer concentration in the solution. The films exhibited faster charge transfer kinetics upon doping, whereas the undoped films served as an electron blocking layer. These films offer tunable energy levels to facilitate charge transport in organic solar cells [148, 177]. Yang et al. further extended this work by fabricating bulk heterojunction (BHJ) solar cells of P3HT and PCBM utilizing the P3MT interlayer as a replacement for PEDOT:PSS [187]. They showed that the P3MT interlayer exhibits good transparency across the visible region as a function of film thickness and showed excellent stability in air, water, and organic solvents. The BHJ solar cells fabricated from P3HT:PCBM active layers displayed a power conversion efficiency (PCE) of 2.5%, whereas the devices with conventional structure using a PEDOT:PSS interfacial layer displayed a PCE of 3.2%. The substrates could also be reused after stripping off the cathode layer and the active layer [187]. This shows promise for further

exploration and optimization of the growth of P3MT layers on ITO surfaces for a more effective interlayer for organic solar cells.

5.3 *Exploration of Different Polymer Architectures Using External Initiation*

Multiarm or star-shaped polymer architectures have been explored for different coil-like polymers [188–190]. The Lin group reported star-shaped diblock copolymers of poly(acrylic acid) and P3HT and of polystyrene and P3HT by a combination of ATRP and GRIM [191–193]. Similarly, bottlebrush-shaped polymers were reported by Kilbey's group [194]. In this synthetic scheme, P3HT was first synthesized and the bromo end group was functionalized such that a norbornenyl-functionalized P3HT macromonomer was obtained, which was further polymerized by ring-opening metathesis polymerization (ROMP) [194]. Some other groups reported synthesis of diblock copolymers containing P3HT by a combination of GRIM with other living polymerization techniques [191, 195–197]. The Tang group synthesized an alternating copolymer of zinc-porphyrin with terthiophene and zinc-porphyrin with poly(3′-hexyl-2,2′-bithiophene) using the Stille coupling reaction [198]. They also used Stille coupling for the synthesis of star-shaped P3HT with porphyrin as the core [199]. Three-armed oligothiophene molecules have been synthesized by different groups [200, 201]. However, there were not many reports for conjugated polymers like P3HT until the advent of external initiation. A chain-growth, 'quasi-living' polymerization would provide higher control over the length of the arms of the polymer. The synthesis of these multiarm polymers can involve either an arm-first or a core-first approach. The arm-first approach involves the synthesis of a living polymeric chain and its end-functionalization with a multifunctional core, whereas the core-first approach involves building a multifunctional core from a small molecule and later grafting the polymer chains (simultaneous polymerization of multiple arms) from the core. The arm-first approach has steric and diffusion-controlled limitations involving reaction of the living polymer chain with the functional groups on the core. The core-first approach can be limited by insufficient initiation/grafting on polymer chains.

Different polymer architectures, such as two-armed (V-shaped), three-armed (Y-shaped), and star-shaped polymers, have been synthesized by both arm-first and core-first approaches. Wang et al. reported the synthesis of the first star-shaped P3HT [202]. They first synthesized a 5-bromothiophene-substituted dendritic polyphenylene core. This was followed by the synthesis of 2-bromo-5-(bromomagnesio)-3-hexylthiophene by the McCullough method and an in-situ simultaneous addition of Ni(dppp)Cl_2 catalyst and 5-bromothiophene-substituted dendritic core. The star-shaped polymer thus synthesized was compared with a linear P3HT molecule synthesized using the McCullough method. The differences in properties observed using multidetector size-exclusion chromatography (SEC),

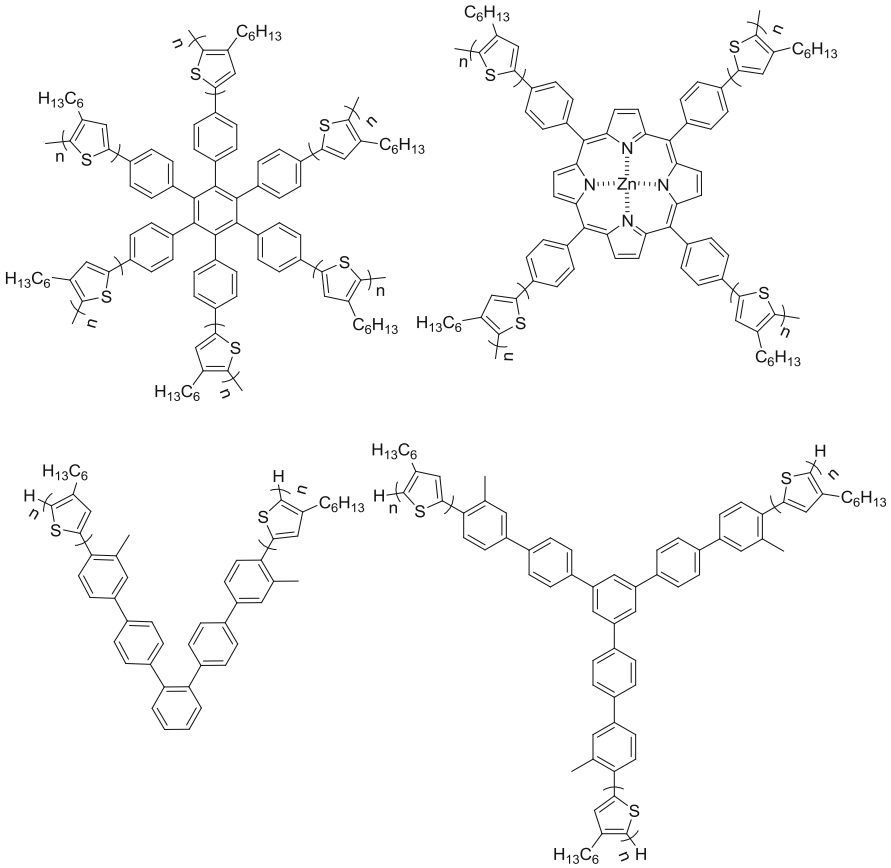

Fig. 9 Structures of the multiarmed P3HTs synthesized: six-armed star (*top left*), four-armed star (*top right*), two-armed V-shape (*bottom left*), and three-armed Y-shape (*bottom right*) [202, 210–213]

differential scanning calorimetry (DSC), and atom force microscopy (AFM) confirmed the presence of a star-shaped structure. Wang and coworkers further extended this methodology to synthesize star-shaped polymers in which a hyperbranched triphenylamine core was coupled with P3HT [203] or poly (3,4-ethylenedioxythiophene-didodecyloxybenzene) [204]. Similar reports of oligothiophenes decorated on dendrimers [205–208] and small organic molecules [209] have been reported.

The Kiriy group adopted a core-first synthetic approach for the synthesis of six-armed P3HT [210, 211]. The core was synthesized using the oxidative addition reaction of hexakis(4-bromophenyl)benzene with $Et_2Ni(bipy)$. Grafting P3HT chains on the initiator formed using GRIM gave rise to the six-armed P3HT with M_n of 8,000 kg/mol and PDI of 1.98. The presence of a hexaphenylbenzene core was confirmed by ^1H NMR analysis, and the surface morphology observed by AFM imaging was used to ascertain the star-shaped structure (Fig. 9).

However, it was difficult to ascertain whether the polymerization proceeded over all six arms.

Yuan et al. also adopted a core-first approach for the synthesis of V-shaped and three-armed (Y-shaped) P3HTs [212]. The benzene core was extended with a 4-phenyl-2-chlorotolyl group on each of the arms. Oxidative addition on the di- and tri-substituted cores using $Ni(cod)_2$ and PPh_3 was used , followed by ligand exchange with dppp. The synthesized polymers displayed molecular weights corresponding to the estimated DP_n with narrow PDIs of 1.10 and 1.15. There was excellent control over the chain-growth reaction, with nearly 100% core/H terminations for both V-shaped and Y-shaped polymers (Fig. 9). Although the length of the polymer chains averaged over all arms conformed to the estimated DP_n, the actual length of each of the arms or the uniformity of the chain lengths across all arms could not be estimated.

In a similar fashion, the group of Seferos adopted a core-first approach. They synthesized a bromine-functionalized zinc-porphyrin core [213]. An oxidative addition reaction on this core with $Ni(PPh_3)_4$ followed by a ligand exchange with dppp yielded a zinc-porphyrin initiator with four initiation sites. These four sites were utilized for the initiation of polymerization to obtain star-shaped polymers of P3HT and poly(3-hexylselenophene) (P3HS). GPC data on the polymerization indicated that pophyrin-$(P3HS)_4$ was isolated. However, it was not possible to ascertain the presence of polymer on all four arms nor the length of each of the arms [213]. However, this method shows good promise for controlled synthesis of novel polymer architectures.

6 Summary, Conclusions, and Outlook

The synthesis of polythiophenes has evolved from the initial methods yielding insoluble and intractable polymers to a good control over the number of repeating units and the regioregularity of the polymers. Moving forward from the insoluble polythiophenes, Yamamoto synthesized P3MTs that displayed a slight improvement in solubility and Elsenbaumer followed this by synthesizing P3ATs that were soluble. The improved solubility of the P3ATs led to the complete characterization of these polymers. However, the asymmetry of the 3-alkylthiophene ring contributed to the formation of four different regioisomeric triads (HH–TT, HT–HH, HT–HT, and TT–HT), of which HT–HT was the regioregular isomer and displayed good opto-electronic properties due to better solid-state packing of the polymer. Synthetic control for obtaining predominantly regioregular P3HT did not exist until the groups of McCullough and Rieke (in 1992) independently proposed synthetic schemes to obtain predominantly HT coupled (>95%) polymers. These methods, however, required cryogenic temperatures. In 1999, McCullough showed that highly regioregular P3ATs can be synthesized at ambient conditions using Grignard metathesis polymerization. The focus shifted towards understanding the mechanism of the polymerization. The groups of McCullough and Yokozawa showed

evidence that the polymerization goes through a chain-growth mechanism unlike other polycondensation reactions, with Yokozawa renaming the polymerization as the Kumada catalyst transfer polycondensation (KCTP). Mechanistic efforts into understanding the mechanism for obtaining absolute control were led by the groups of McCullough, Yokozawa, Kiriy, and McNeil. Kiriy proposed an external initiation method for growing P3HT grafts on polymers immobilized on surfaces. Further efforts at external initiation were led by the groups of Kiriy and Luscombe in attempts to obtain absolute control over the chain-growth mechanism for the synthesis of polymers with well-controlled molecular weights and narrow polydispersity indexes. The external initiation technique was further extended to initiation of polymerizations from surfaces such as gold, silica, and ITO. An environmentally stable P3MT layer was grown on ITO surfaces by the groups of Luscombe and Locklin and the latter further showed that this P3MT layer can probably replace the PEDOT:PSS interlayer in organic solar cells. The Kiriy and Luscombe groups took advantage of the robust chain-growth mechanism of GRIM/KCTP to synthesize star-shaped polymers using a core-first approach. Luscombe's group demonstrated that V-shaped and Y-shaped polymers could be synthesized with good control over molecular weights and narrow polydispersities. Further improvements in structure and functionality can be achieved by designing more complex architectures tuned for specific applications.

References

1. Tourillon G, Garnier F (1983) Stability of conducting polythiophene and derivatives. J Electrochem Soc 130:2042–2044
2. McCullough RD, Ewbank PC (1998) Regioregular, head-to-tail coupled poly (3-alkylthiophene) and its derivatives. In: Skotheim TA, Elsenbaumer RL, Reynolds JR (eds) Handbook of conducting polymers, 2nd edn, revised and expanded. Marcel Dekker, New York, pp 255-258
3. Jeffries-El M, McCullough RD (2007) Regioregular polythiophenes. In: Skotheim TA, Reynolds JR (eds) Handbook of conducting polymers, 3rd edn, Conjugated polymers processing and applications. CRC, Boca Raton, pp 1–49
4. McCullough RD (1999) The chemistry of conducting polythiophenes: from synthesis to self-assembly to intelligent materials. In: Fichou D (ed) Handbook of oligo- and polythiophenes. Wiley-VCH, Weinheim
5. Schopf G, Kossmehl G (1997) Polythiophenes – electrically conductive polymers. Adv Polym Sci 129:1–166
6. Ewbank PC, Stefan MC, Sauve G, McCullough RD (2009) In: Perepichka IF, Perepichka DF (eds) Handbook of thiophene-based materials: applications in organic electronics and photonics, vol 1: synthesis and theory. Wiley, West Sussex
7. McCullough RD (1998) The chemistry of conducting polythiophenes. Adv Mater 10:93–116
8. Perepichka IF, Perepichka DF, Meng H, Wudl F (2005) Light-emitting polythiophenes. Adv Mater 17:2281–2305
9. Roncali J (1992) Conjugated poly(thiophenes): synthesis, functionalization, and applications. Chem Rev 92:711–738
10. Roncali J (1997) Synthetic principles for bandgap control in linear π-conjugated systems. Chem Rev 97:173–205

11. Yamamoto T (2010) Molecular assembly and properties of polythiophenes. NPG Asia Mater 2:54–60
12. Miyakoshi R, Yokoyama A, Yokozawa T (2008) Development of catalyst-transfer condensation polymerization. Synthesis of π-conjugated polymers with controlled molecular weight and low polydispersity. J Polym Sci A Polym Chem 46:753–765
13. Stefan MC, Bhatt MP, Sista P, Magurudeniya HD (2012) Grignard metathesis (GRIM) polymerization for the synthesis of conjugated block copolymers containing regioregular poly(3-hexylthiophene). Polym Chem 3:1693–1701
14. Okamoto K, Luscombe CK (2011) Controlled polymerizations for the synthesis of semiconducting conjugated polymers. Polym Chem 2:2424–2434
15. Kiebooms R, Menon R, Lee K (2001) Synthesis, electrical and optical properties of conjugated polymers. In: Nalwa HS (ed) Handbook of advanced electronic and photonic materials and devices, vol 1: semiconductors. Academic, San Diego
16. Marrocchi A, Lanari D, Facchetti A, Vaccaro L (2012) Poly(3-hexylthiophene): synthetic methodologies and properties in bulk heterojunction solar cells. Energ Environ Sci 5:8457–8474
17. Bryan ZJ, McNeil AJ (2013) Conjugated polymer synthesis via catalyst-transfer polycondensation (CTP): mechanism, scope, and applications. Macromolecules 46:8395–8405
18. Yokozawa T, Ohta Y (2013) Scope of controlled synthesis via chain-growth condensation polymerization: from aromatic polyamides to π-conjugated polymers. Chem Commun 49:8281–8310
19. Sista P, Ghosh K, Martinez JS, Rocha RC (2014) Polythiophenes in biological applications. J Nanosci Nanotechnol 14:250–272
20. Bhatt MP, Magurudeniya HD, Rainbolt EA, Huang P, Dissanayake DS, Biewer MC, Stefan MC (2014) Poly(3-Hexylthiophene) nanostructured materials for organic electronics applications. J Nanosci Nanotechnol 14:1033–1050
21. Aiyar AR, Hong J-I, Reichmanis E (2012) Regioregularity and intrachain ordering: impact on the nanostructure and charge transport in two-dimensional assemblies of poly (3-hexylthiophene). Chem Mater 24:2845–2853
22. Barta P, Cacialli F, Friend RH, Salaneck WR, Zagorska M, Prori A (1999) On the influence of regioregularity on electronic and optical properties of poly(alkylthiophenes). Synthetic Met 101:296–297
23. Bouzzine SM, Bouzakraoui S, Hamidi M, Bouachrine M (2007) Impact of the torsion on the optoelectronic properties of poly(3-alkylthiophene): a spectroscopic and theoretical approaches. Asian J Chem 19:1651–1657
24. Mao H, Xu B, Holdcroft S (1993) Synthesis and structure–property relationships of regioirregular poly(3-hexylthiophenes). Macromolecules 26:1163–1169
25. Sirringhaus H, Brown PJ, Friend RH, Nielsen MM, Bechgaard K, Langeveld-Voss BMW, Spiering AJH, Janssen RAJ, Meijer EW, Herwig P, De LDM (1999) Two-dimensional charge transport in self-organized, high-mobility conjugated polymers. Nature 401:685–688
26. Chang J-F, Clark J, Zhao N, Sirringhaus H, Breiby DW, Andreasen JW, Nielsen MM, Giles M, Heeney M, McCulloch I (2006) Molecular-weight dependence of interchain polaron delocalization and exciton bandwidth in high-mobility conjugated polymers. Phys Rev B Condens Matter Mater Phys 74:115318
27. Zhang R, Li B, Iovu MC, Jeffries-El M, Sauve G, Cooper J, Jia S, Tristram-Nagle S, Smilgies DM, Lambeth DN, McCullough RD, Kowalewski T (2006) Nanostructure dependence of field-effect mobility in regioregular poly(3-hexylthiophene) thin film field effect transistors. J Am Chem Soc 128:3480–3481
28. Kline RJ, McGehee MD, Kadnikova EN, Liu J, Frechet JMJ (2003) Controlling the field-effect mobility of regioregular polythiophene by changing the molecular weight. Adv Mater 15:1519–1522

29. Zen A, Pflaum J, Hirschmann S, Zhuang W, Jaiser F, Asawapirom U, Rabe JP, Scherf U, Neher D (2004) Effect of molecular weight and annealing of poly(3-hexylthiophene)s on the performance of organic field-effect transistors. Adv Funct Mater 14:757–764
30. Kline RJ, McGehee MD, Kadnikova EN, Liu J, Frechet JMJ, Toney MF (2005) Dependence of regioregular poly(3-hexylthiophene) film morphology and field-effect mobility on molecular weight. Macromolecules 38:3312–3319
31. Meyer V (1883) Thiophene, a substance contained in coal-tar benzene. Chem Ber 16:1465–1478
32. Meyer V (1884) The thiophene and pyrroline groups. Chem Ber 16:2968–2975
33. Meisel SL, Johnson GC, Hartough HD (1950) Polymerization of thiophene and alkylthiophenes. J Am Chem Soc 72:1910–1912
34. Topchiev AV, Krentsel BA, Gol'dfarb YA (1959) Polymers of heterocycles. Izv Akad Nauk SSSR, Ser Khim 369
35. Strelko VV, Vysotskii ZZ (1964) Polymerization of thiophene on the surface of dehydratable silica gel. Sintez i Fiz-Khim Polimerov, Akad Nauk Ukr SSR, Inst Khim Vysokomolekul Soedin, Sb Statei 80–82
36. Armour M, Davies AG, Upadhyay J, Wassermann A (1967) Colored, electrically conducting polymers from furan, pyrrole, and thiophene. J Polym Sci A-1 Polym Chem 5:1527–1538
37. Ramsey JS, Kovacic P (1969) Polymerization of aromatic nuclei. XV. Polymerization of 2,5-di- and 2,3,5-trichlorothiophenes with aluminum chloride-cupric chloride. J Polym Sci A-1 Polym Chem 7:127–138
38. Curtis RF, Jones DM, Thomas WA (1971) The 'trimer' and 'pentamer' from the polymerization of thiophene by polyphosphoric acid. J Chem Soc C 1971:234–238
39. Huber LK (1971) Thiophene polymers and method of preparation. US patent 3,557,068
40. Louvar JJ (1971) Polymerization of heterocyclic compounds. US patent 3,574,072 A
41. Tourillon G, Garnier F (1982) New electrochemically generated organic conducting polymers. J Electroanal Chem Interfacial Electrochem 135:173–178
42. Chiang CK, Fincher CR Jr, Park YW, Heeger AJ, Shirakawa H, Louis EJ, Gau SC, MacDiarmid AG (1977) Electrical conductivity in doped polyacetylene. Phys Rev Lett 39:1098–1101
43. Yamamoto T, Sanechika K, Yamamoto A (1980) Preparation of thermostable and electric-conducting poly(2,5-thienylene). J Polym Sci Polym Lett Ed 18:9–12
44. Lin JWP, Dudek LP (1980) Synthesis and properties of poly(2,5-thienylene). J Polym Sci Polym Chem Ed 18:2869–2873
45. Tamao K, Sumitani K, Kumada M (1972) Selective carbon–carbon bond formation by cross-coupling of Grignard reagents with organic halides. Catalysis by nickel-phosphine complexes. J Amer Chem Soc 94:4374–4376
46. Tamao K, Sumitani K, Kiso Y, Zembayashi M, Fujioka A, Kodama S, Nakajima I, Minato A, Kumada M (1976) Nickel-phosphine complex-catalyzed Grignard coupling. I. Cross-coupling of alkyl, aryl, and alkenyl Grignard reagents with aryl and alkenyl halides: general scope and limitations. Bull Chem Soc Jpn 49:1958–1969
47. Tamao K, Kodama S, Nakajima I, Kumada M, Minato A, Suzuki K (1982) Nickel-phosphine complex-catalyzed Grignard coupling. II. Grignard coupling of heterocyclic compounds. Tetrahedron 38:3347–3354
48. Yamamoto T, Sanechika K, Yamamoto A (1983) Preparation and characterization of poly (thienylenes). Bull Chem Soc Jpn 56:1497–1502
49. Yamamoto T, Morita A, Miyazaki Y, Maruyama T, Wakayama H, Zhou ZH, Nakamura Y, Kanbara T, Sasaki S, Kubota K (1992) Preparation of π -conjugated poly(thiophene-2,5-diyl), poly(p-phenylene), and related polymers using zerovalent nickel complexes. Linear structure and properties of the π -conjugated polymers. Macromolecules 25:1214–1223
50. Yamamoto T, Maruyama T, Zhou ZH, Miyazaki Y, Kanbara T, Sanechika K (1991) New method using nickel(0) complex for preparation of poly(p-phenylene), poly(2,5-thienylene) and related π -conjugated polymers. Synthetic Met 41:345–348

51. Colon I, Kwiatkowski GT (1990) High-molecular-weight aromatic polymers by nickel coupling of aryl polychlorides. J Polym Sci A Polym Chem 28:367–383
52. Yamamoto T, Osakada K, Wakabayashi T, Yamamoto A (1985) Nickel and palladium catalyzed dehalogenating polycondensation of dihaloaromatic compounds with zinc. A new route to poly(2,5-thienylene)s and poly(1,4-phenylene). Makromol Chem Rapid Commun 6:671–674
53. Yamamoto T, Morita A, Maruyama T, Zhou ZH, Kanbara T, Sanechika K (1990) New method for the preparation of poly(2,5-thienylene), poly(p-phenylene), and related polymers. Polym J 22:187–190
54. Kobayashi M, Chen J, Chung TC, Moraes F, Heeger AJ, Wudl F (1984) Synthesis and properties of chemically coupled poly(thiophene). Synthetic Met 9:77–86
55. Hotz CZ, Kovacic P, Khoury IA (1983) Synthesis and properties of polythienylenes. J Polym Sci Polym Chem Ed 21:2617–2628
56. Berlin A, Pagani GA, Sannicolo F (1986) New synthetic routes to electroconductive polymers containing thiophene units. J Chem Soc Chem Commun 1986(22):1663–1664
57. Yoshino K, Hayashi S, Sugimoto R (1984) Preparation and properties of conducting heterocyclic polymer films by chemical method. Jpn J Appl Phys 23:899–900
58. Kaneto K, Kohno Y, Yoshino K, Inuishi Y (1983) Electrochemical preparation of a metallic polythiophene film. J Chem Soc Chem Commun 1983(7):382–383
59. Kaneto K, Yoshino K, Inuishi Y (1983) Electrical and optical properties of polythiophene prepared by electrochemical polymerization. Solid State Commun 46:389–391
60. Amer A, Zimmer H, Mulligan KJ, Mark HB Jr, Pons S, McAleer JF (1984) Polymerization of 3-methyl-2,5-dibromothiophene utilizing n-butyl lithium and copper(II) chloride. J Polym Sci Polym Lett Ed 22:77–82
61. Czerwinski A, Zimmer H, Chiem VP, Mark HB Jr (1985) The electrochemical deposition of conducting poly(3-methyl-2,5-thienylene) films from aqueous media. J Electrochem Soc 132:2669–2672
62. Yamamoto T, Sanechika K (1982) Preparation and properties of π-conjugated poly(3-methyl-2,5-thienylene). Chem Ind 301–302
63. Elsenbaumer RL, Jen KY, Oboodi R (1986) Processible and environmentally stable conducting polymers. Synthetic Met 15:169–174
64. Jen KY, Miller GG, Elsenbaumer RL (1986) Highly conducting, soluble, and environmentally-stable poly(3-alkylthiophenes). J Chem Soc Chem Commun 1986 (17):1346–1347
65. Jen KY, Oboodi R, Elsenbaumer RL (1985) Processible and environmentally stable conducting polymers. Polym Mater Sci Eng 53:79–83
66. Sugimoto R, Takeda S, Gu HB, Yoshino K (1986) Preparation of soluble polythiophene derivatives utilizing transition metal halides as catalysts and their property. Chem Express 1:635–638
67. Hotta S, Rughooputh SDDV, Heeger AJ, Wudl F (1987) Spectroscopic studies of soluble poly(3-alkylthienylenes). Macromolecules 20:212–215
68. Sato M, Tanaka S, Kaeriyama K (1986) Soluble conducting polythiophenes. J Chem Soc Chem Commun 1986(11):873–874
69. Adachi T, Brazard J, Ono RJ, Hanson B, Traub MC, Wu Z-Q, Li Z, Bolinger JC, Ganesan V, Bielawski CW, Vanden Bout DA, Barbara PF (2011) Regioregularity and single polythiophene chain conformation. J Phys Chem Lett 2:1400–1404
70. Brown PJ, Thomas DS, Kohler A, Wilson JS, Kim J-S, Ramsdale CM, Sirringhaus H, Friend RH (2003) Effect of interchain interactions on the absorption and emission of poly(3-hexylthiophene). Phys Rev B Condens Matter Mater Phys 67:064203
71. Jiang X, Osterbacka R, Korovyanko O, An CP, Horovitz B, Janssen RAJ, Vardeny ZV (2002) Spectroscopic studies of photoexcitations in regioregular and regiorandom polythiophene films. Adv Funct Mater 12:587–597

72. Mauer R, Kastler M, Laquai F (2010) The impact of polymer regioregularity on charge transport and efficiency of P3HT:PCBM photovoltaic devices. Adv Funct Mater 20:2085–2092
73. Kim Y, Cook S, Tuladhar SM, Choulis SA, Nelson J, Durrant JR, Bradley DDC, Giles M, McCulloch I, Ha C-S, Ree M (2006) A strong regioregularity effect in self-organizing conjugated polymer films and high-efficiency polythiophene:fullerene solar cells. Nat Mater 5:197–203
74. Maior RMS, Hinkelmann K, Eckert H, Wudl F (1990) Synthesis and characterization of two regiochemically defined poly(dialkylbithiophenes): a comparative study. Macromolecules 23:1268–1279
75. Sato M, Morii H (1991) Nuclear magnetic resonance studies on electrochemically prepared poly(3-dodecylthiophene). Macromolecules 24:1196–1200
76. Chen TA, Rieke RD (1992) The first regioregular head-to-tail poly(3-hexylthiophene-2,5-diyl) and a regiorandom isopolymer: nickel versus palladium catalysis of 2(5)-bromo-5(2)-(bromozincio)-3-hexylthiophene polymerization. J Am Chem Soc 114:10087–10088
77. McCullough RD, Lowe RD (1992) Enhanced electrical conductivity in regioselectively synthesized poly(3-alkylthiophenes). J Chem Soc Chem Commun 1992(1):70–72
78. McCullough RD, Lowe RD, Jayaraman M, Anderson DL (1993) Design, synthesis, and control of conducting polymer architectures: structurally homogeneous poly (3-alkylthiophenes). J Org Chem 58:904
79. Liu J, McCullough RD (2002) End group modification of regioregular polythiophene through postpolymerization functionalization. Macromolecules 35:9882–9889
80. Chen T-A, Wu X, Rieke RD (1995) Regiocontrolled synthesis of poly(3-alkylthiophenes) mediated by Rieke zinc: their characterization and solid-state properties. J Am Chem Soc 117:233
81. Loewe RS, Khersonsky SM, McCullough RD (1999) A simple method to prepare head-to-tail coupled, regioregular poly(3-alkylthiophenes) using Grignard metathesis. Adv Mater 11:250
82. Loewe RS, Ewbank PC, Liu J, Zhai L, McCullough RD (2001) Regioregular, head-to-tail coupled poly(3-alkylthiophenes) made easy by the GRIM method: investigation of the reaction and the origin of regioselectivity. Macromolecules 34:4324
83. Andersson MR, Mammo W, Olinga T, Svernsson M, Theander M, Inganas O (1999) Synthesis of regio-regular phenyl substituted polythiophenes with FeCl3. Synthetic Met 101:11–12
84. Andersson MR, Selse D, Berggren M, Jaervinen H, Hjertberg T, Inganaes O, Wennerstroem O, Oesterholm JE (1994) Regioselective polymerization of 3-(4-octylphenyl)thiophene with $FeCl_3$. Macromolecules 27:6503–6506
85. Hayakawa T, Fukukawa K-I, Morishima M, Takeuchi K, Asai M, Ando S, Ueda M (2001) Formation of regioregular head-to-tail poly[3-(4-butylphenyl)thiophene] by an oxidative coupling polymerization with vanadium acetylacetonate. J Polym Sci A Polym Chem 39:2287–2295
86. Iraqi A, Barker GW (1998) Synthesis and characterization of telechelic regioregular head-to-tail poly(3-alkylthiophenes). J Mater Chem 8:25–29
87. Marsella MJ, Carroll PJ, Swager TM (1995) Design of chemoresistive sensory materials: polythiophene-based pseudopolyrotaxanes. J Am Chem Soc 117:9832–9841
88. McCullough RD, Ewbank PC, Loewe RS (1997) Self-assembly and disassembly of regioregular, water soluble polythiophenes: chemoselective ionchromatic sensing in water. J Am Chem Soc 119:633–634
89. Guillerez S, Bidan G (1998) New convenient synthesis of highly regioregular poly (3-octylthiophene) based on the Suzuki coupling reaction. Synthetic Met 93:123–126
90. Yokozawa T, Suzuki R, Nojima M, Ohta Y, Yokoyama A (2011) Precision synthesis of poly (3-hexylthiophene) from catalyst-transfer Suzuki–Miyaura coupling polymerization. Macromol Rapid Commun 32:801–806

91. Bryan ZJ, Smith ML, McNeil AJ (2012) Chain-growth polymerization of aryl Grignards initiated by a stabilized NHC-Pd precatalyst. Macromol Rapid Commun 33:842–847
92. Yoshikai N, Matsuda H, Nakamura E (2008) Ligand exchange as the first irreversible step in the nickel-catalyzed cross-coupling reaction of Grignard reagents. J Am Chem Soc 130:15258–15259
93. Verswyvel M, Verstappen P, De CL, Verbiest T, Koeckelberghs G (2011) Development of a universal chain-growth polymerization protocol of conjugated polymers: toward a variety of all-conjugated block-copolymers. J Polym Sci A Polym Chem 49:5339–5349
94. Seyler H, Subbiah J, Jones DJ, Holmes AB, Wong WWH (2013) Controlled synthesis of poly (3-hexylthiophene) in continuous flow. Beilstein J Org Chem 9:1492–1500
95. Sevignon M, Papillon J, Schulz E, Lemaire M (1999) New synthetic method for the polymerization of alkylthiophenes. Tetrahedron Lett 40:5873–5876
96. Wang Q, Takita R, Kikuzaki Y, Ozawa F (2010) Palladium-catalyzed dehydrohalogenative polycondensation of 2-Bromo-3-hexylthiophene: an efficient approach to head-to-tail poly (3-hexylthiophene). J Am Chem Soc 132:11420–11421
97. Wang Q, Wakioka M, Ozawa F (2012) Synthesis of end-capped regioregular poly (3-hexylthiophene)s via direct arylation. Macromol Rapid Commun 33:1203–1207
98. Rudenko AE, Wiley CA, Stone SM, Tannaci JF, Thompson BC (2012) Semi-random P3HT analogs via direct arylation polymerization. J Polym Sci A Polym Chem 50:3691–3697
99. Mercier LG, Leclerc M (2013) Direct (hetero)arylation: a new tool for polymer chemists. Acc Chem Res 46:1597–1605
100. Tamba S, Fuji K, Nakamura K, Mori A (2014) Nickel(II)-catalyzed cross-coupling polycondensation of thiophenes via C–S bond cleavage. Organometallics 33:12–15
101. Corriu RJP, Masse JP (1972) Activation of Grignard reagents by transition-metal complexes. New and simple synthesis of trans-stilbenes and polyphenyls. J Chem Soc Chem Commun 1972(3):144a
102. Yamamoto T, Wakabayashi S, Osakada K (1992) Mechanism of carbon-carbon coupling reactions of aromatic halides, promoted by $Ni(COD)_2$ in the presence of 2,2′-bipyridine and triphenylphosphine, to give biaryls. J Organomet Chem 428:223–237
103. Miyazaki Y, Yamamoto T (1994) Characterization, properties and doping of poly (3-alkylthiophene-2,5-diyl)s, P3RThs (R=n-C6H13, n-C8H17, n-C12H25), prepared by using zero-valent nickel complex. Synthetic Met 64:69–76
104. Yokoyama A, Miyakoshi R, Yokozawa T (2004) Chain-growth polymerization for poly (3-hexylthiophene) with a defined molecular weight and a low polydispersity. Macromolecules 37:1169–1171
105. Miyakoshi R, Yokoyama A, Yokozawa T (2004) Synthesis of poly(3-hexylthiophene) with a narrower polydispersity. Macromol Rapid Commun 25:1663–1666
106. Miyakoshi R, Yokoyama A, Yokozawa T (2005) Catalyst-transfer polycondensation. mechanism of Ni-catalyzed chain-growth polymerization leading to well-defined poly (3-hexylthiophene). J Am Chem Soc 127:17542–17547
107. Beryozkina T, Senkovskyy V, Kaul E, Kiriy A (2008) Kumada catalyst-transfer polycondensation of thiophene-based oligomers: robustness of a chain-growth mechanism. Macromolecules 41:7817–7823
108. Kiriy A, Senkovskyy V, Sommer M (2011) Kumada catalyst-transfer polycondensation: mechanism, opportunities, and challenges. Macromol Rapid Commun 32:1503–1517
109. Tkachov R, Senkovskyy V, Komber H, Sommer J-U, Kiriy A (2010) Random catalyst walking along polymerized poly(3-hexylthiophene) chains in Kumada catalyst-transfer polycondensation. J Am Chem Soc 132:7803–7810
110. Sheina EE, Liu J, Iovu MC, Laird DW, McCullough RD (2004) Chain growth mechanism for regioregular nickel-initiated cross-coupling polymerizations. Macromolecules 37:3526–3528
111. Iovu MC, Sheina EE, Gil RR, McCullough RD (2005) Experimental evidence for the quasi-"living" nature of the grignard metathesis method for the synthesis of regioregular poly (3-alkylthiophenes). Macromolecules 38:8649–8656

112. Boyd SD, Jen AKY, Luscombe CK (2009) Steric stabilization effects in nickel-catalyzed regioregular poly(3-hexylthiophene) synthesis. Macromolecules 42:9387–9389
113. Tkachov R, Senkovskyy V, Komber H, Kiriy A (2011) Influence of alkyl substitution pattern on reactivity of thiophene-based monomers in Kumada catalyst-transfer polycondensation. Macromolecules 44:2006–2015
114. Holdcroft S (1991) Determination of molecular weights and Mark–Houwink constants for soluble electronically conducting polymers. J Polym Sci B Polym Phys 29:1585–1588
115. Wong M, Hollinger J, Kozycz LM, McCormick TM, Lu Y, Burns DC, Seferos DS (2012) An apparent size-exclusion quantification limit reveals a molecular weight limit in the synthesis of externally initiated polythiophenes. ACS Macro Lett 1:1266–1269
116. Liu J, Loewe RS, McCullough RD (1999) Employing MALDI-MS on poly(alkylthiophenes): analysis of molecular weights, molecular weight distributions, end-group structures, and end-group modifications. Macromolecules 32:5777–5785
117. Wu P-T, Ren G, Li C, Mezzenga R, Jenekhe SA (2009) Crystalline diblock conjugated copolymers: synthesis, self-assembly, and microphase separation of poly(3-butylthiophene)-b-poly(3-octylthiophene). Macromolecules 42:2317–2320
118. Van DBK, Cosemans I, Verbiest T, Koeckelberghs G (2010) Expression of supramolecular chirality in block copoly(thiophene)s. Macromolecules 43:3794–3800
119. Ho V, Boudouris BW, Segalman RA (2010) Tuning polythiophene crystallization through systematic side chain functionalization. Macromolecules 43:7895–7899
120. Zhang Y, Tajima K, Hashimoto K (2009) Nanostructure formation in poly(3-hexylthiophene-block-3-(2-ethylhexyl)thiophene)s. Macromolecules 42:7008–7015
121. Ohshimizu K, Ueda M (2008) Well-controlled synthesis of block copolythiophenes. Macromolecules 41:5289–5294
122. Javier AE, Varshney SR, McCullough RD (2010) Chain-growth synthesis of polyfluorenes with low polydispersities, block copolymers of fluorene, and end-capped polyfluorenes: toward new optoelectronic materials. Macromolecules 43:3233–3237
123. Hollinger J, Jahnke AA, Coombs N, Seferos DS (2010) Controlling phase separation and optical properties in conjugated polymers through selenophene-thiophene copolymerization. J Am Chem Soc 132:8546–8547
124. Locke JR, McNeil AJ (2010) Syntheses of gradient π-conjugated copolymers of thiophene. Macromolecules 43:8709–8710
125. Jeffries-El M, Sauve G, McCullough RD (2005) Facile synthesis of end-functionalized regioregular poly(3-alkylthiophene)s via modified Grignard metathesis reaction. Macromolecules 38:10346–10352
126. Jeffries-El M, Sauvé G, McCullough RD (2004) In-situ end-group functionalization of regioregular poly(3-alkylthiophene) using the Grignard metathesis polymerization method. Adv Mater 16:1017
127. Iovu MC, Craley CR, Jeffries-El M, Krankowski AB, Zhang R, Kowalewski T, McCullough RD (2007) Conducting regioregular polythiophene block copolymer nanofibrils synthesized by reversible addition fragmentation chain transfer polymerization (RAFT) and nitroxide mediated polymerization (NMP). Macromolecules 40:4733–4735
128. Iovu MC, Jeffries-El M, Sheina EE, Cooper JR, McCullough RD (2005) Regioregular poly (3-alkylthiophene) conducting block copolymers. Polymer 46:8582–8586
129. Moon HC, Anthonysamy A, Kim JK, Hirao A (2011) Facile synthetic route for well-defined poly(3-hexylthiophene)-block-poly(methyl methacrylate) copolymer by anionic coupling reaction. Macromolecules 44:1894–1899
130. Hundt N, Hoang Q, Nguyen H, Sista P, Hao J, Servello J, Palaniappan K, Alemseghed M, Biewer MC, Stefan MC (2011) Synthesis and characterization of a block copolymer containing regioregular poly(3-hexylthiophene) and poly(γ-benzyl-L-glutamate). Macromol Rapid Commun 32:302–308
131. Wu Z-Q, Ono RJ, Chen Z, Li Z, Bielawski CW (2011) Polythiophene-block-poly(γ-benzyl L-glutamate): synthesis and study of a new rod–rod block copolymer. Polym Chem 2:300–302

132. Iovu MC, Jeffries-El M, Zhang R, Kowalewski T, McCullough RD (2006) Conducting block copolymer nanowires containing regioregular poly(3-hexylthiophene) and polystyrene. J Macromol Sci A Pure Appl Chem 43:1991–2000
133. Dai C-A, Yen W-C, Lee Y-H, Ho C-C, Su W-F (2007) Facile synthesis of well-defined block copolymers containing regioregular poly(3-hexyl thiophene) via anionic macroinitiation method and their self-assembly behavior. J Am Chem Soc 129:11036–11038
134. Okamoto K, Luscombe CK (2014) Simple procedure for mono- and bis-end-functionalization of regioregular poly(3-hexylthiophene)s using chalcogens. Chem Commun. doi:10.1039/C3CC47560C
135. Zhao L, Feng C, Pang X, Jung J, Stefan MC, Sista P, Han R, Fang N, Lin Z (2013) Self-assembly of a conjugated triblock copolymer at the air–water interface. Soft Matter 9:8050–8056
136. Lanni EL, McNeil AJ (2009) Mechanistic studies on Ni(dppe)Cl2-catalyzed chain-growth polymerizations: evidence for rate-determining reductive elimination. J Am Chem Soc 131:16573–16579
137. Lanni EL, McNeil AJ (2010) Evidence for ligand-dependent mechanistic changes in nickel-catalyzed chain-growth polymerizations. Macromolecules 43:8039–8044
138. Achord BC, Rawlins JW (2009) Evidence of Ni(0) complex diffusion during grignard metathesis polymerization of 2,5-dibromo-3-hexylthiophene. Macromolecules 42:8634–8639
139. Lanni EL, Locke JR, Gleave CM, McNeil AJ (2011) Ligand-based steric effects in Ni-Catalyzed chain-growth polymerizations using bis(dialkylphosphino)ethanes. Macromolecules 44:5136–5145
140. Magurudeniya HD, Sista P, Westbrook JK, Ourso TE, Nguyen K, Maher MC, Alemseghed MG, Biewer MC, Stefan MC (2011) Nickel(II) α-diimine catalyst for Grignard metathesis (GRIM) polymerization. Macromol Rapid Commun 32:1748–1752
141. Tamba S, Shono K, Sugie A, Mori A (2011) C-H functionalization polycondensation of chlorothiophenes in the presence of nickel catalyst with stoichiometric or catalytically generated magnesium amide. J Am Chem Soc 133:9700–9703
142. Komber H, Senkovskyy V, Tkachov R, Johnson K, Kiriy A, Huck WTS, Sommer M (2011) Ring walking versus trapping of nickel(0) during Kumada catalyst transfer polycondensation using externally initiated electron-accepting thiophene-benzothiadiazole-thiophene precursors. Macromolecules 44:9164–9172
143. Stefan MC, Javier AE, Osaka I, McCullough RD (2009) Grignard metathesis method (GRIM): toward a universal method for the synthesis of conjugated polymers. Macromolecules 42:30–32
144. Sui A, Shi X, Wu S, Tian H, Geng Y, Wang F (2012) Controlled synthesis of polyfluorenes via Kumada catalyst transfer polycondensation with Ni(acac)2/dppp as the catalyst. Macromolecules 45:5436–5443
145. Bhatt MP, Magurudeniya HD, Sista P, Sheina EE, Jeffries-El M, Janesko BG, McCullough RD, Stefan MC (2013) Role of the transition metal in Grignard metathesis polymerization (GRIM) of 3-hexylthiophene. J Mater Chem A 1:12841–12849
146. Krasovskiy A, Knochel P (2004) A LiCl-mediated Br/Mg exchange reaction for the preparation of functionalized aryl- and heteroarylmagnesium compounds from organic bromides. Angew Chem Int Ed 43:3333–3336
147. Krasovskiy A, Krasovskaya V, Knochel P (2006) Mixed Mg/Li amides of the type R2NMgCl·LiCl as highly efficient bases for the regioselective generation of functionalized aryl and heteroaryl magnesium compounds. Angew Chem Int Ed 45:2958–2961
148. Sontag SK, Sheppard GR, Usselman NM, Marshall N, Locklin J (2011) Surface-confined nickel mediated cross-coupling reactions: characterization of initiator environment in Kumada catalyst-transfer polycondensation. Langmuir 27:12033–12041
149. Kochemba WM, Kilbey SM, Pickel DL (2012) End-group composition of poly (3-hexylthiophene)s prepared by in situ quenching of the Grignard metathesis

polymerization: influence of additives and reaction conditions. J Polym Sci A Polym Chem 50:2762–2769
150. Lohwasser RH, Thelakkat M (2011) Toward perfect control of end groups and polydispersity in poly(3-hexylthiophene) via catalyst transfer polymerization. Macromolecules 44:3388–3397
151. Wu S, Huang L, Tian H, Geng Y, Wang F (2011) LiCl-promoted chain growth Kumada catalyst-transfer polycondensation of the "reversed" thiophene monomer. Macromolecules 44:7558–7567
152. Kim JS, Lee Y, Lee JH, Park JH, Kim JK, Cho K (2010) High-efficiency organic solar cells based on end-functional-group-modified poly(3-hexylthiophene). Adv Mater 22:1355–1360
153. Kim Y, Cook S, Kirkpatrick J, Nelson J, Durrant JR, Bradley DDC, Giles M, Heeney M, Hamilton R, McCulloch I (2007) Effect of the end group of regioregular poly (3-hexylthiophene) polymers on the performance of polymer/fullerene solar cells. J Phys Chem C 111:8137–8141
154. Senkovskyy V, Khanduyeva N, Komber H, Oertel U, Stamm M, Kuckling D, Kiriy A (2007) Conductive polymer brushes of regioregular head-to-tail poly(3-alkylthiophenes) via catalyst-transfer surface-initiated polycondensation. J Am Chem Soc 129:6626–6632
155. Fahey DR (1970) Reaction of aryl and vinyl halides with nickel(O) complexes. J Am Chem Soc 92:402–404
156. Hidai M, Kashiwagi T, Ikeuchi T, Uchida Y (1971) Oxidative additions to nickel(0). Preparation and properties of a new series of arylnickel(II) complexes. J Organometal Chem 30:279–282
157. Carothers WH (1929) Polymerization and ring formation. I. Introduction to the general theory of condensation polymers. J Am Chem 51:2548–2559
158. Flory PJ (1953) Principles of polymer chemistry. Cornell University Press, New York
159. Doubina N, Ho A, Jen AKY, Luscombe CK (2009) Effect of initiators on the Kumada catalyst-transfer polycondensation reaction. Macromolecules 42:7670–7677
160. Doubina N, Stoddard M, Bronstein HA, Jen AKY, Luscombe CK (2009) The effects of binding ligand variation on the nickel catalyzed externally initiated polymerization of 2-bromo-3-hexyl-5-iodothiophene. Macromol Chem Phys 210:1966–1972
161. Bronstein HA, Luscombe CK (2009) Externally initiated regioregular P3HT with controlled molecular weight and narrow polydispersity. J Am Chem Soc 131:12894–12895
162. Saito S, Oh-tani S, Miyaura N (1997) Synthesis of Biaryls via a nickel(0)-catalyzed cross-coupling reaction of chloroarenes with arylboronic acids. J Org Chem 62:8024–8030
163. Wolfe JP, Buchwald SL (1997) Nickel-catalyzed amination of aryl chlorides. J Am Chem Soc 119:6054–6058
164. Senkovskyy V, Tkachov R, Beryozkina T, Komber H, Oertel U, Horecha M, Bocharova V, Stamm M, Gevorgyan SA, Krebs FC, Kiriy A (2009) "Hairy" poly(3-hexylthiophene) particles prepared via surface-initiated Kumada catalyst-transfer polycondensation. J Am Chem Soc 131:16445–16453
165. Chavez CA, Choi J, Nesterov EE (2014) One-step simple preparation of catalytic initiators for catalyst-transfer Kumada polymerization: synthesis of defect-free polythiophenes. Macromolecules 47:506–516
166. Senkovskyy V, Sommer M, Tkachov R, Komber H, Huck WTS, Kiriy A (2010) Convenient route to initiate Kumada catalyst-transfer polycondensation using Ni(dppe)Cl2 or Ni(dppp) Cl2 and sterically hindered Grignard compounds. Macromolecules 43:10157–10161
167. Chatt J, Shaw BL (1960) Alkyls and aryls of transition metals. III. Nickel(II) derivatives. J Chem Soc 1718–1729
168. Smeets A, Van den Bergh K, De Winter J, Gerbaux P, Verbiest T, Koeckelberghs G (2009) Incorporation of different end groups in conjugated polymers using functional nickel initiators. Macromolecules 42:7638–7641

169. Doubina N, Paniagua SA, Soldatova AV, Jen AKY, Marder SR, Luscombe CK (2011) Steric effects of the initiator substituent position on the externally initiated polymerization of 2-Bromo-5-iodo-3-hexylthiophene. Macromolecules 44:512–520
170. Monnaie F, Brullot W, Verbiest T, De Winter J, Gerbaux P, Smeets A, Koeckelberghs G (2013) Synthesis of end-group functionalized P3HT: general protocol for P3HT/nanoparticle hybrids. Macromolecules 46:8500–8508
171. Crabtree RH (2005) The organometallic chemistry of the transition metals, 4th edn. Wiley, Hoboken
172. Paramonov PB, Paniagua SA, Hotchkiss PJ, Jones SC, Armstrong NR, Marder SR, Bredas J-L (2008) Theoretical characterization of the indium tin oxide surface and of its binding sites for adsorption of phosphonic acid monolayers. Chem Mater 20:5131–5133
173. Khanduyeva N, Senkovskyy V, Beryozkina T, Bocharova V, Simon F, Nitschke M, Stamm M, Groetzschel R, Kiriy A (2008) Grafting of poly(3-hexylthiophene) from poly (4-bromostyrene) films by Kumada catalyst-transfer polycondensation: revealing of the composite films structure. Macromolecules 41:7383–7389
174. Khanduyeva N, Senkovskyy V, Beryozkina T, Horecha M, Stamm M, Uhrich C, Riede M, Leo K, Kiriy A (2009) Surface engineering using Kumada catalyst-transfer polycondensation (KCTP): preparation and structuring of poly(3-hexylthiophene)-based graft copolymer brushes. J Am Chem Soc 131:153–161
175. Sontag SK, Marshall N, Locklin J (2009) Formation of conjugated polymer brushes by surface-initiated catalyst-transfer polycondensation. Chem Commun 2009(23):3354–3356
176. Huddleston NE, Sontag SK, Bilbrey JA, Sheppard GR, Locklin J (2012) Palladium-mediated surface-initiated Kumada catalyst polycondensation: a facile route towards oriented conjugated polymers. Macromol Rapid Commun 33:2115–2120
177. Doubina N, Jenkins JL, Paniagua SA, Mazzio KA, MacDonald GA, Jen AKY, Armstrong NR, Marder SR, Luscombe CK (2012) Surface-initiated synthesis of poly (3-methylthiophene) from indium tin oxide and its electrochemical properties. Langmuir 28:1900–1908
178. Marshall N, Sontag SK, Locklin J (2011) Surface-initiated polymerization of conjugated polymers. Chem Commun 47:5681–5689
179. Marshall N, Sontag SK, Locklin J (2010) Substituted poly(p-phenylene) thin films via surface-initiated Kumada-type catalyst transfer polycondensation. Macromolecules 43:2137–2144
180. Orski SV, Fries KH, Sontag SK, Locklin J (2011) Fabrication of nanostructures using polymer brushes. J Mater Chem 21:14135–14149
181. Kim M, Hohman JN, Cao Y, Houk KN, Ma H, Jen AKY, Weiss PS (2011) Creating favorable geometries for directing organic photoreactions in alkanethiolate monolayers. Science 331:1312–1315
182. Chechik V, Crooks RM, Stirling CJM (2000) Reactions and reactivity in self-assembled monolayers. Adv Mater 12:1161–1171
183. Bilbrey JA, Sontag SK, Huddleston NE, Allen WD, Locklin J (2012) On the role of disproportionation energy in Kumada catalyst-transfer polycondensation. ACS Macro Lett 1:995–1000
184. Wong KW, Yip HL, Luo Y, Wong KY, Lau WM, Low KH, Chow HF, Gao ZQ, Yeung WL, Chang CC (2002) Blocking reactions between indium-tin oxide and poly(3,4-ethylene dioxythiophene):poly(styrene sulphonate) with a self-assembly monolayer. Appl Phys Lett 80:2788–2790
185. Yan H, Lee P, Armstrong NR, Graham A, Evmenenko GA, Dutta P, Marks TJ (2005) High-performance hole-transport layers for polymer light-emitting diodes. Implementation of organosiloxane cross-linking chemistry in polymeric electroluminescent devices. J Am Chem Soc 127:3172–3183
186. Ma H, Yip H-L, Huang F, Jen AKY (2010) Interface engineering for organic electronics. Adv Funct Mater 20:1371–1388

187. Yang L, Sontag SK, LaJoie TW, Li W, Huddleston NE, Locklin J, You W (2012) Surface-initiated poly(3-methylthiophene) as a hole-transport layer for polymer solar cells with high performance. ACS Appl Mater Interfaces 4:5069–5073
188. Hadjichristidis N, Pitsikalis M, Pispas S, Iatrou H (2001) Polymers with complex architecture by living anionic polymerization. Chem Rev 101:3747–3792
189. Gao H, Tsarevsky NV, Matyjaszewski K (2005) Synthesis of degradable Miktoarm star copolymers via atom transfer radical polymerization. Macromolecules 38:5995–6004
190. Voit BI, Lederer A (2009) Hyperbranched and highly branched polymer architectures-synthetic strategies and major characterization aspects. Chem Rev 109:5924–5973
191. Pang X-C, Zhao L, Feng C-W, Lin Z-Q (2011) Novel amphiphilic multiarm, starlike coil-rod diblock copolymers via a combination of click chemistry with living polymerization. Macromolecules 44:7176–7183
192. Pang X, Zhao L, Feng C, Wu R, Ma H, Lin Z (2013) Functional copolymer brushes composed of a hydrophobic backbone and densely grafted conjugated side chains via a combination of living polymerization with click chemistry. Polym Chem 4:2025–2032
193. Pang X, Feng C, Xu H, Han W, Xin X, Xia H, Qiu F, Lin Z (2014) Unimolecular micelles composed of inner coil-like blocks and outer rod-like blocks crafted by combination of living polymerization with click chemistry. Polym Chem 5:2747–2755
194. S-K A, Pickel DL, Kochemba WM, Chen J, Uhrig D, Hinestrosa JP, Carrillo J-M, Shao M, Do C, Messman JM, Brown WM, Sumpter BG, Kilbey SM II (2013) Poly(3-hexylthiophene) molecular bottlebrushes via ring-opening metathesis polymerization: macromolecular architecture enhanced aggregation. ACS Macro Lett 2:761–765
195. Han D, Tong X, Zhao Y (2012) Synthesis and characterization of six-arm star polystyrene-block-poly(3-hexylthiophene) copolymer by combination of atom transfer radical polymerization and click reaction. J Polym Sci A Polym Chem 50:4198–4205
196. Kim H-J, Lee YJ, Hwang SS, Choi DH, Yang H, Baek K-Y (2011) Synthesis of multiarmed poly(3-hexyl thiophene) star polymer with microgel core by GRIM and ATRP methods. J Polym Sci A Polym Chem 49:4221–4226
197. Sivula K, Ball ZT, Watanabe N, Frechet JMJ (2006) Amphiphilic diblock copolymer compatibilizers and their effect on the morphology and performance of polythiophene: fullerene solar cells. Adv Mater 18:206–210
198. Xiang N, Liu Y, Zhou W, Huang H, Guo X, Tan Z, Zhao B, Shen P, Tan S (2010) Synthesis and characterization of porphyrin-terthiophene and oligothiophene π-conjugated copolymers for polymer solar cells. Eur Polym J 46:1084–1092
199. Liu Y, Guo X, Xiang N, Zhao B, Huang H, Li H, Shen P, Tan S (2010) Synthesis and photovoltaic properties of polythiophene stars with porphyrin cores. J Mater Chem 20:1140–1146
200. Ponomarenko SA, Kirchmeyer S, Elschner A, Huisman B-H, Karbach A, Drechsler D (2003) Star-shaped oligothiophenes for solution-processible organic field-effect transistors. Adv Funct Mater 13:591–596
201. Vercelli B, Zotti G, Berlin A (2007) Star-shaped and linear terthiophene-thiol self-assembled monolayers as scaffolds for gold nanoparticles. Chem Mater 19:443–452
202. Wang F, Rauh RD, Rose TL (1997) An electrically conducting star polymer. J Am Chem Soc 119:11106–11107
203. Wang F, Wilson MS, Rauh RD, Schottland P, Reynolds JR (1999) Electroactive and conducting star-branched poly(3-hexylthiophene)s with a conjugated core. Macromolecules 32:4272–4278
204. Wang F, Wilson MS, Rauh RD, Schottland P, Thompson BC, Reynolds JR (2000) Electrochromic linear and star branched poly(3,4-ethylenedioxythiophene-didodecyloxybenzene) polymers. Macromolecules 33:2083–2091
205. Miller LL, Kunugi Y, Canavesi A, Rigaut S, Moorefield CN, Newkome GR (1998) "Vapoconductivity". Sorption of organic vapors causes large increases in the conductivity of a dendrimer. Chem Mater 10:1751–1754

206. Apperloo JJ, Janssen RAJ, Malenfant PRL, Groenendaal L, Frechet JMJ (2000) Redox states of well-defined π-conjugated oligothiophenes functionalized with poly(benzyl ether) dendrons. J Am Chem Soc 122:7042–7051
207. Wang F, Kon AB, Rauh RD (2000) Synthesis of a terminally functionalized bromothiophene polyphenylene dendrimer by a divergent method. Macromolecules 33:5300–5302
208. Sebastian R-M, Caminade A-M, Majoral J-P, Levillain E, Huchet L, Roncali J (2000) Electrogenerated poly(dendrimers) containing conjugated poly(thiophene) chains. Chem Commun 2000(6):507–508
209. Bras J, Guillerez S, Pepin-Donat B (2000) Preparation of conjugated gels of regioregular HT sexi(3-*n*-octylthiophene) and related star molecules. Chem Mater 12:2372–2384
210. Senkovskyy V, Beryozkina T, Bocharova V, Tkachov R, Komber H, Lederer A, Stamm M, Severin N, Rabe JP, Kiriy A (2010) A core-first preparation of poly(3-alkylthiophene) stars. Macromol Symp 291–292:17–25
211. Senkovskyy V, Beryozkina T, Komber H, Lederer A, Stamm M, Kiriy A (2008) Linear and star-shaped poly(3-hexylthiophene)s prepared by nickel bipyridyl-mediated Kumada catalyst transfer polycondensation (KCTP). Polym Prepr (Am Chem Soc, Div Polym Chem) 49:630–631
212. Yuan M, Okamoto K, Bronstein HA, Luscombe CK (2012) Constructing regioregular star poly(3-hexylthiophene) via externally initiated Kumada catalyst-transfer polycondensation. ACS Macro Lett 1:392–395
213. Li L, Hollinger J, Guerin G, Seferos DS (2012) Synthesis and network-like self-assembly of porphyrin-polyselenophene complexes. ChemPhysChem 13:4110–4115

Adv Polym Sci (2014) 265: 39–82
DOI: 10.1007/12_2014_288

Published online: 6 September 2014

Morphology of P3HT in Thin Films in Relation to Optical and Electrical Properties

Kim Tremel and Sabine Ludwigs

Abstract The search for renewable and environmentally friendly energy sources has made organic electronics an interesting field of research. Semiconducting polymers stand out because they offer cheap and easy processability at a large-scale from solution, combined with impressive optoelectronic properties. Polythiophenes, in particular poly(3-hexylthiophene) (P3HT), are the most prominent and investigated representatives of semiconducting polymers and have been applied in various devices such as solar cells and field-effect transistors. For this class of polymers, it has been well established that the morphology of the functional layer has a significant impact on the device performance. However, transport bottlenecks are hard to determine due to the complex semicrystalline microstructure, which is composed of a mixture of crystalline and amorphous domains. In order to gain a deeper understanding of the correlation between microstructure and functional properties, precise control of nucleation and growth of semicrystalline polymers such as P3HT is crucial. This article gives an overview of recent publications addressing the morphology and crystallization of regioregular P3HT, both in solution and thin film, and attempts to correlate these structural features to the functional (i.e. optical and electrical) properties of the polymer.

Keywords Absorption behavior • Charge transport • Crystallization • Nanostructure • Ordered nanostructure • Poly(3-hexylthiophene)

K. Tremel and S. Ludwigs (✉)
IPOC-Functional Polymers, Institute of Polymer Chemistry, University of Stuttgart, Pfaffenwaldring 55, 70569 Stuttgart, Germany
e-mail: sabine.ludwigs@ipoc.uni-stuttgart.de

Contents

1 Introduction

Semiconducting polymers have attracted a great deal of attention in the last decades because of their remarkable optoelectronic properties combined with low-cost solution processability [1–4]. One of the most prominent semiconducting polymers is poly(3-hexylthiophene) (P3HT), whose optoelectronic properties and device performance have been investigated extensively in numerous studies [1, 5–7]. Most of the fascinating properties of semiconducting polymers such as P3HT derive from their strong tendency to crystallize, because strong intermolecular interactions in well-ordered crystalline domains offer efficient charge transport pathways through the polymer layer on a macroscopic scale [8]. Polymer crystallization of flexible chains such as polyethylene (PE) has been described by numerous theories [9, 10]. As a result of different processing conditions, there is a great diversity of morphologies for these polymers, which have been widely explored and reviewed [11] during the last 50 years. Crystalline lamellae based on folded chains are unique for polymer crystals. Lamellae can further aggregate and form semicrystalline spherulites under static conditions, whereas an external field provokes anisotropic structures such as polymer fibrils [12, 13]. Precise control of crystallization conditions can allow the growth of single crystals [14, 15] formed of folded-chain lamellae, which are not only used for investigations of the crystallographic structure, but also for exploring crystallization kinetics. From an engineering point of view, the precise morphology is of great relevance because the mechanical properties strongly depend on the microstructure. Crystallization of conjugated polymers like P3HT is more complex due to the rigidity of the polymer backbone and the presence of side chains, which follow distinct crystallization kinetics [16]. A precise crystallization mechanism for conjugated polymers has not yet been fully established. The great advantage of a conjugated polymer backbone, however, is that it allows for functional properties with a characteristic absorption in the low-energy part of the spectrum and highly anisotropic charge transport. Hence, the exact morphology affects not only the mechanical but also the functional properties of the polymer layer and is therefore

crucial for device performance. For instance, charge transport is highly dependent on the order within the polymer layer at multiple length scales: On a local scale, charge transfer is affected by the extent of π-conjugation along the backbone as well as intermolecular chain contacts. On a macroscopic scale, the interconnectivity of crystalline grains plays a crucial role in the charge carrier mobility. Therefore, improving device performance requires precise control of morphology, and new methods to manipulate and control the polymer microstructure are continuously pursued. From a research point of view, gaining a detailed understanding of the correlation between morphology and functional properties is challenging and has been the focus of various publications [1, 17–20].

This chapter gives an overview of recent reports on the control of morphology of regioregular P3HT in thin films. Starting from a short introductory section about synthesis, energy levels, and optical properties in solution, we then discuss the preparation of one-dimensional (1D) fibers by controlled crystallization from solution. We then focus on P3HT thin films obtained by solution processing from good solvents, a procedure that is highly relevant for large-scale applications. The impact of molecular parameters and processing conditions on the semicrystalline morphology of P3HT on substrates is discussed in this context. The last part of the chapter deals with the manufacture of oriented structures of P3HT with long range order, with the clear perspective of understanding structure–function relations.

2 Regioregular Poly(3-hexylthiophene): Functional Properties

2.1 Materials

One of the first syntheses of unsubstituted polythiophenes with high conductivity after doping with iodine was reported in 1980 [21, 22]. However, due to the lack of processability of these polymers, alkyl chains were attached to the conjugated backbone to make the polymer soluble in common organic solvents and to allow deposition from solution. Because 3-alkylthiophene is an asymmetric monomer, there are three different regioisomers that vary in the relative orientation of the two thiophene rings when coupled between the 2- and 5-position: 2-2′ or head-to-head coupling (HH), 2-5′ or head-to-tail coupling (HT), and 5-5′or tail-to-tail coupling (TT).

As a result, polymers based on 3-alkylthiophene exhibit a different regiochemistry, which is illustrated in Fig. 1 for the example of P3HT. Polythiophenes containing a mixture of the different couplings are referred to as regioirregular or regiorandom. For polymers with irregular substituent distribution, the thiophene units twist away from planarity as a result of unfavorable HH coupling, which results in a drastic decrease in the conjugation length. In contrast, regioregular polythiophenes, which contain exclusively HT couplings, can adopt a

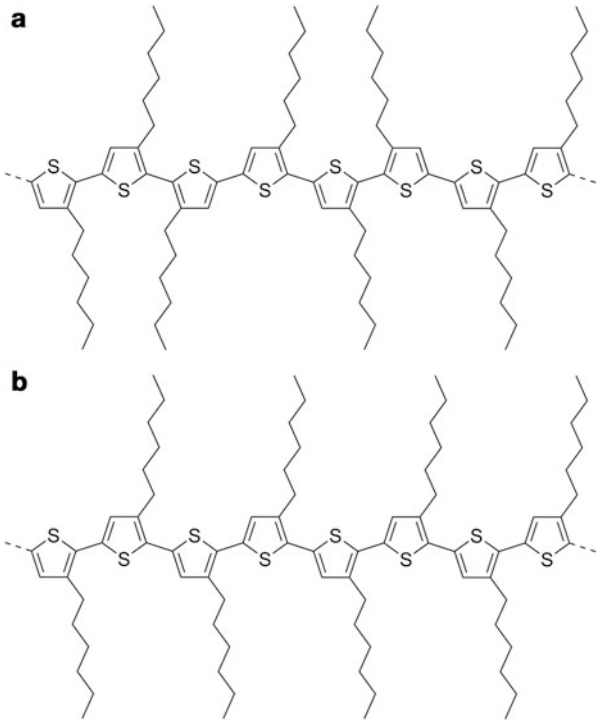

Fig. 1 Regioirregular (**a**) and regioregular (**b**) poly (3-hexylthiophene)

planar conformation of low energy with extended π-conjugation. This leads to highly desirable properties for device applications, such as effective charge transport and high absorption in the low energy part of the visible spectrum. In 1992, McCullough and Lowe described the first synthesis of regioregular P3HT via Ni-catalyzed Kumada cross-coupling [23, 24]. Using 3-alkylthiophene as the starting material, selective bromination to 2-bromo-3-alkylthiophene was followed by lithiation, transmetallation, and polymerization in the presence of nickel. In the same year, Chen and Rieke presented a second approach for the synthesis of regioregular P3HT via polycondensation of 2,5-dibromo-3-alkylthiophene using active zinc ("Rieke Zn") and nickel catalysis [25]. Both methods presented a breakthrough for polymer electronics, giving regioregular poly(3-alkylthiophene)s (P3ATs) with high conductivity. However, synthesis at a large scale was problematic because of the low temperatures necessary during reaction. This problem was overcome in 1999 by McCullough, who reported the synthesis of highly regioregular P3ATs by the Grignard metathesis reaction (GRIM), which allows synthesis at room temperature and at a large scale [26]. Recent progress on defect-free polythiophenes with controlled terminal groups has been accomplished by external initiation, developed and extended by Kiriy and Luscombe, respectively [27, 28]. A detailed review of synthetic routes for regioregular P3HT, including mechanistic details, can be found in the chapter by Sista and Luscombe in this book [29].

The literature we review in this chapter deals mainly with polymers that are made by the standard polymerization routes and that are commercially available. To obtain P3HT with different molecular weights, the method of Soxhlet extraction is quite common, first demonstrated for regioregular P3HT by Trznadel et al. [30]. Soxhlet extraction makes use of the different quality of solvents to separate P3HT into fractions of better defined molecular weight with narrow molecular weight distribution. Throughout this review we have tried to specify the molecular weight and polydispersity index of the samples studied in the cited publications to make the studies as comparable as possible.

2.2 Energy Levels from Electrochemical Measurements

P3HT is a classical semiconducting polymer that is nonconducting in the neutral state and becomes conducting upon doping. Figure 2a schematically shows the process of oxidation or p-doping to radical-cationic/polaron species and the reduction or n-doping to radical-anionic/polaron species by chemical or electrochemical doping.

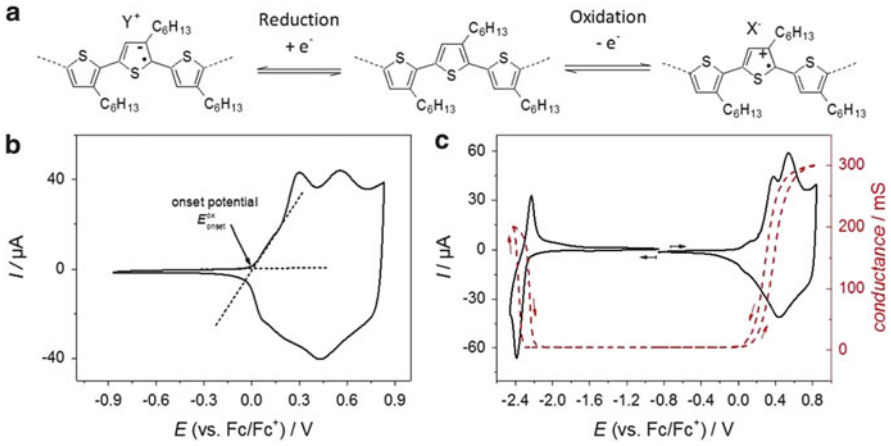

Fig. 2 (**a**) Molecular structure of the neutral (*middle*), reduced (*left*), and oxidized (*right*) forms of P3HT. The incorporation of counter ions (Y^+, X^-) from the supporting electrolyte during the electrochemical doping process ensures electroneutrality within the charged film. (**b**) Method for the determination of the oxidation onset potential value of P3HT from a cyclic voltammogram of a P3HT film deposited on a Pt working electrode; $v = 50$ mV/s, electrolyte: 0.1 M $TBAPF_6$/MeCN. The interception of the two tangents (*dashed lines*) at the initial slope of the peak current corresponds to E^{ox}_{onset}. (**c**) Cyclic voltammograms (*black*) including in-situ conductance measurements (*red*) of the reduction (n-doping) and oxidation (p-doping) of a P3HT film deposited on a Pt working electrode; $v = 20$ mV/s, electrolyte: 0.1 M $TBAPF_6$/MeCN; oxidation and reduction were recorded separately; *arrows* indicate scan direction. (Data measured by M. Goll and Dr. A. Ruff)

Determination of the energy levels is typically performed by electrochemistry, and cyclic voltammetry (CV) has been established as method of choice. The polymer is either dissolved in the supporting electrolyte or deposited on the working electrode. The measurements are usually performed with a three-electrode set-up that includes a working electrode, a reference electrode (for example Ag/AgCl), and a counter or auxiliary electrode. As electrolytes, acetonitrile (MeCN) or dichloromethane in the presence of conducting salts such as tetrabutylammonium hexafluorophosphate ($TBAPF_6$) are well-established. It is recommended to use ferrocene/ferrocenium (Fc/Fc^+) as external reference for each measurement to make electrochemical potentials comparable [31]. Detailed electrochemical characterization of P3HT films has been performed, for example, by Trznadel et al. [30] and Skompska et al. [32].

A typical reversible anodic oxidation cycle of a P3HT film is shown in Fig. 2b, in which the oxidation onset potential E^{ox}_{onset} is marked. It is assumed that the onset potential values in cyclic voltammograms correspond to the oxidation/reduction of the polymer chains with the largest conjugated π-system. Because the oxidation corresponds to the removal of electrons from the highest occupied molecular orbital (HOMO), and the reduction to adding electrons to the lowest occupied molecular orbital (LUMO), the onset oxidation and reduction potentials are closely related to the HOMO and LUMO energies. From the graph in Fig. 2c, an $E^{ox}_{onset} = 0.02\,V$ (versus Fc/Fc^+) and an $E^{red}_{onset} = -2.26\,V$ (versus Fc/Fc^+) can be determined for a P3HT film with a weight-averaged molecular weight (M_w) of 112 kg/mol and a polydispersity index (PDI) of 2.4. The graph also contains data on the in-situ conductance behavior of the P3HT film, which was measured in an electrolyte-gated transistor configuration (for the method of CV with in-situ conductance measurements see, for example, [33]). One can see that only upon doping (oxidation or reduction) does the otherwise nonconducting P3HT film become conducting.

From the onset potential values of the oxidation and reduction, the HOMO and LUMO levels, respectively, of the polymer can be calculated according to the following equations [34]:

$$E(\mathrm{HOMO}) = -\left(E^{ox}_{onset}(\mathrm{vs.}\ Fc/Fc^+) + 5.1\right)[\mathrm{eV}] \quad (1)$$

$$E(\mathrm{LUMO}) = -\left(E^{red}_{onset}(\mathrm{vs.}\ Fc/Fc^+) + 5.1\right)[\mathrm{eV}] \quad (2)$$

For the P3HT film in Fig. 2c, this leads to a HOMO level of −5.12 eV and a LUMO level of −2.84 eV. In the literature, a factor of 4.8 eV instead of 5.1 eV is often used, which dates back to a 1995 publication by Pommerehne and coworkers [35]. For a discussion of the validity of the approach of using onset potentials for HOMO/LUMO determination we refer to [33, 34].

From the HOMO and LUMO level, Eq. (3) can be used to estimate the electrochemical band gap, which is a critical quantity for polymer-based organic photovoltaics:

$$\text{band gap} = |E(\text{HOMO}) - E(\text{LUMO})| \quad (3)$$

The electrochemical band gap should not be confused with the optical band gap, which is typically derived from the onset of absorption in thin film absorption spectra. Optical spectra give information about the optical excitation of an electron from the ground to the first excited state, whereas electrochemical oxidation/reduction produces real charged species, i.e., cations and anions. A combination of HOMO determination by electrochemistry and LUMO determination by subtracting the optical band gap is not recommended.

Scharber et al. have proposed a relation between the HOMO of the polymer and the open circuit voltage V_{oc}, which was used to estimate the maximum efficiency of bulk-heterojunction solar cells for a number of material combinations, including P3HT and phenyl-C61-butyric acid methyl ester (PCBM) [36]. As an alternative to energy level determination with electrochemistry, the method of photoelectron spectroscopy can be used: Kahn and coworkers used a combination of direct and inverse photoemission spectroscopy complemented by near edge X-ray absorption fine structure (NEXAFS) for determination of the HOMO and LUMO energy levels and the energy gap between the LUMO of the acceptor and the HOMO of the donor [37].

2.3 *Optical Properties of P3HT Solutions*

P3HT is soluble in a variety of solvents, which enables easy and cheap processability from solution. Optical spectroscopy in solution gives information about the conjugation of isolated molecules, usually in the absence of interchain packing effects. In solution, P3HT exhibits one broad absorption peak without structural features, which is associated with isolated chains in a coiled conformation [38]. Both repulsive interactions between successive monomer units and interactions between the solvent and the side chains drive a dihedral twist of the polymer backbone in solution [17]. Barbara and coworkers studied the impact of regioregularity on the conformation of a single chain by means of single-molecule fluorescence excitation polarization spectroscopy [39]. Thereby, they observed more ordered conformations for regioregular chains, whereas the incorporation of HH and TT couplings resulted in a wider distribution of conformations due to unfavorable side chain interactions. This is reflected in the absorbance and fluorescence spectra of P3HT solutions of different regioregularity (shown in Fig. 3a). In chloroform solution, regioregular P3HT shows absorption and fluorescence maxima at 454 and 577 nm, respectively, whereas the peak maxima are blue-shifted to 420 and 572 nm in the case of regiorandom P3HT. This blue shift has been reported by several groups [40–42] and reflects a decreased conjugation length, which stems from a sterically driven twist of the backbone. For regioregular P3HT, the conjugation length of a single chain is further affected by the chain length. Figure 3b

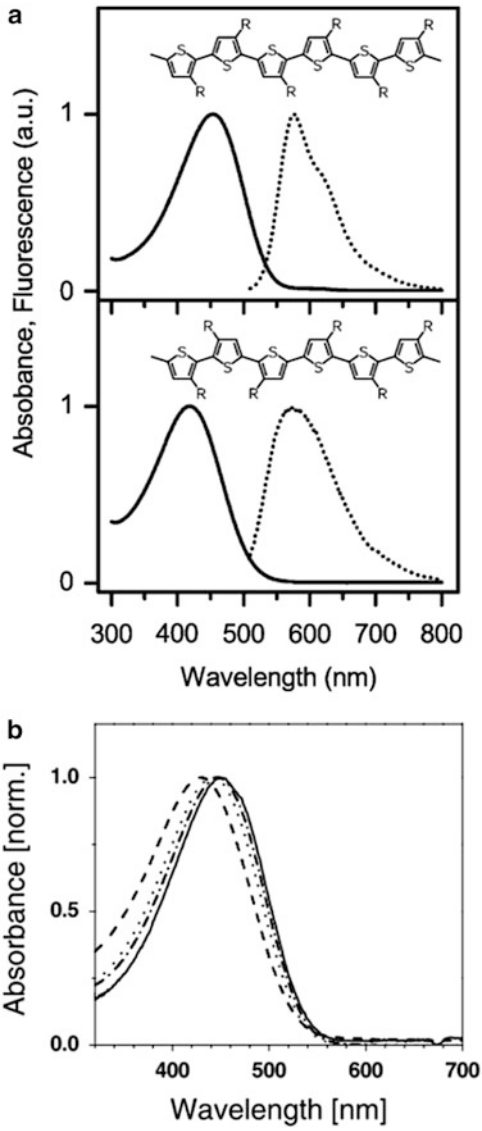

Fig. 3 (**a**) Absorbance (*solid line*) and fluorescence (*dotted line*) spectra of regioregular P3HT with 97% HT-HT coupling (*top*) and regiorandom P3HT with 64% HT-HT coupling (*bottom*) in chloroform solution [39]. (**b**) Absorbance of regioregular P3HT in chloroform solution as a function of molecular weight. The fractions were obtained by successive solvent extraction in ethyl acetate (*dashed line*), hexane (*dotted line*), dichloromethane (*dashed-dotted line*), and chloroform (*solid line*) [17]. (Reprinted with permission from Adachi et al. [39]. Copyright (2011) American Chemical Society. And reprinted with permission from Zen et al. [17]. Copyright (2004) Wiley-VCH)

shows solution spectra of regioregular P3HT in chloroform for four fractions of different molecular weight achieved by successive extraction in ethyl acetate, hexane, dichloromethane, and chloroform. The number-average molecular weight (M_n) of these fractions was 2.2 kg/mol (PDI = 1.43), 5.6 kg/mol (PDI = 1.18), 13.8 kg/mol (PDI = 1.48), and 19.0 kg/mol (PDI = 1.35). For regioregular P3HT, increasing the molecular weight leads to a slight bathochromic shift of the absorption maximum in solution, which results from an increase in the average conjugation length along the polymer backbone [17, 30].

The use of poor solvents or solvent mixtures can further allow aggregation and crystallization directly from solution, which is the subject of the following section. This aggregation is accompanied by a bathochromic shift of the absorption maxima and the appearance of a vibronic fine structure (see also Sect. 3). In the extreme case of solid-state spectra of P3HT films, these effects are even more pronounced, with the spectra also becoming more structured for high molecular weights (see Sect. 4.1.1).

3 Crystallization from Solution

The rigidity and planar conformation of the conjugated backbone of many semiconducting polymers such as regioregular P3HT allows efficient packing and crystallization. However, due to the difficulty of forming ordered crystalline structures from interpenetrating and entangled polymer chains of high rigidity, there are very few publications on single crystals of polymeric semiconductors [43]. Only recently has the growth of P3HT single crystals from solution using a self-seeding approach been reported [44]. The single crystalline nature of the deposited material and its identification as the form II polymorph was performed by Brinkmann via transmission electron microscopy coupled with electron diffraction (TEM/ED). For a more detailed crystal structure and polymorph discussion we refer to Sect. 4.1.2 and the article by Brinkmann et al. in this book [45].

Although insulating polymers such as PE crystallize in 2-dimensional (2D) lamellar sheets, conjugated polymers like P3HT typically form high aspect ratio, 1D nanocrystals (nanofibrils, nanowhiskers, nanofibers, and nanorods) [46]. Aggregation is driven by strong π–π interactions perpendicular to the conjugated backbone, as well as by hydrophobic interactions of the side chains.

In 1993, Ihn et al. were the first to report crystallization of P3HT nanocrystals from a dilute solution of a poor solvent [47]. Nanofibrils were grown from cyclohexanone (0.05%) by slow cooling of the solution from 50°C to room temperature (25°C/h). After deposition from solution on TEM grids, nanofibrils with a width of around 15 nm, a height of 5 nm, and a length of around 10 μm were evidenced by TEM. Figure 4a shows the bright-field image and the corresponding electron diffraction pattern of P3HT nanofibrils grown from cyclohexanone. A representative AFM height image of similar nanofibrils is given in Fig. 4b. The precise packing of the chains within the nanofibrils was determined by electron diffraction and X-ray analysis and is schematically presented in Fig. 4c. The polymer backbone packs normal to the long axis of the fibril (i.e., the π-stacking is oriented along the fibril direction), whereas the alkyl chains point perpendicular to the substrate. This arrangement is also referred to as edge-on orientation (see also Sect. 4.1.2). Although the height of the fibrils relates to only two or three layers of P3HT chains, the fibril length of around 10 μm demonstrates the strong packing tendency in the π-stacking direction. The fact that the (number) average contour length of the chains (around 65 nm), which was calculated on the basis of the (number) average

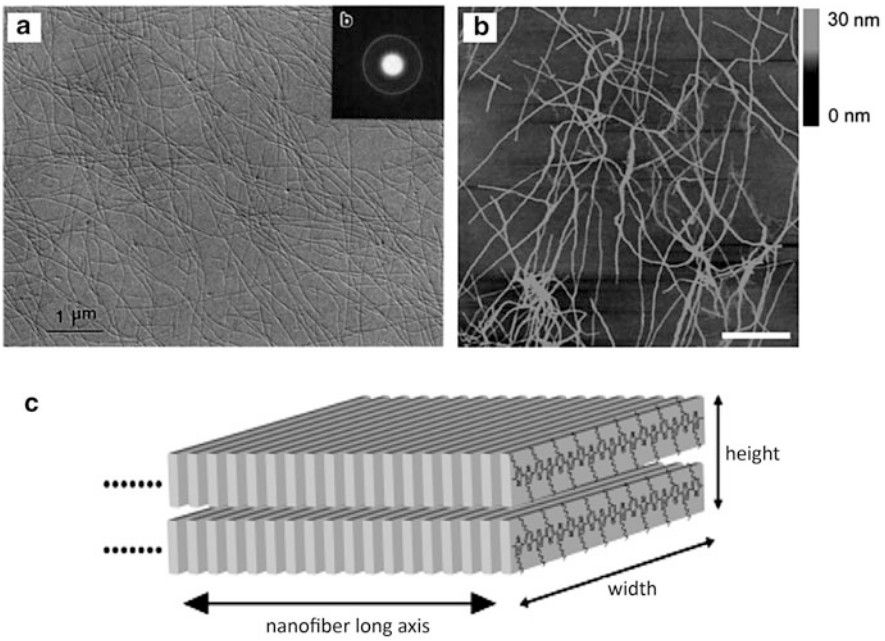

Fig. 4 (**a**) TEM image and the corresponding electron diffraction pattern (*inset*) of P3HT nanofibrils crystallized from cyclohexanone solution (0.05 wt%) [47]. (**b**) AFM height image of P3HT nanofibrils grown from a solution mixture of anisole and chloroform (4:1 vol%) and deposited on silicon wafers by spin-coating [48]. (**c**) Schematic representation showing the molecular orientation within a P3HT nanofibril [48]. (Reprinted with permission from Ihn et al. [47]. Copyright (1993) Wiley-VCH. And reprinted with permission from Samitsu et al. [48]. Copyright (2008) American Chemical Society)

molecular weight of 29 kg/mol, exceeds the width of the nanofibrils suggests that the chains fold back and forth in order to be incorporated into the nanostructures, a typical feature of semicrystalline polymers. Zhai and coworkers could further show that the fibril width increases with molecular weight, but saturates above a critical value of around 10 kg/mol (M_n) [49]. Below the critical molecular weight, nanofibrils are assumed to be formed by extended chains that span the width of the fibrils. Above the critical molecular weight, chain folding takes place and leads to a saturation of fibril width. The fold-length is dependent on the crystallization temperature in solution, which is characteristic of the crystallization of polymers.

Since the seminal work of Ihn et al. in 1993, a large number of publications have followed that deal with the structural and optical characterization of nanofibrils, but also address their performance in devices such as organic field-effect transistors (OFETs) and organic solar cells (OSCs) [47, 48, 50–53]. In general, two common approaches for P3AT nanofibril production are described in the literature [52]: (1) the whisker method and (2) the mixed solvent method. For both approaches, the growth of 1D nanocrystals is driven by strong π–π-interactions and unfavorable interactions between the solvent and polymer backbone under limited solubility.

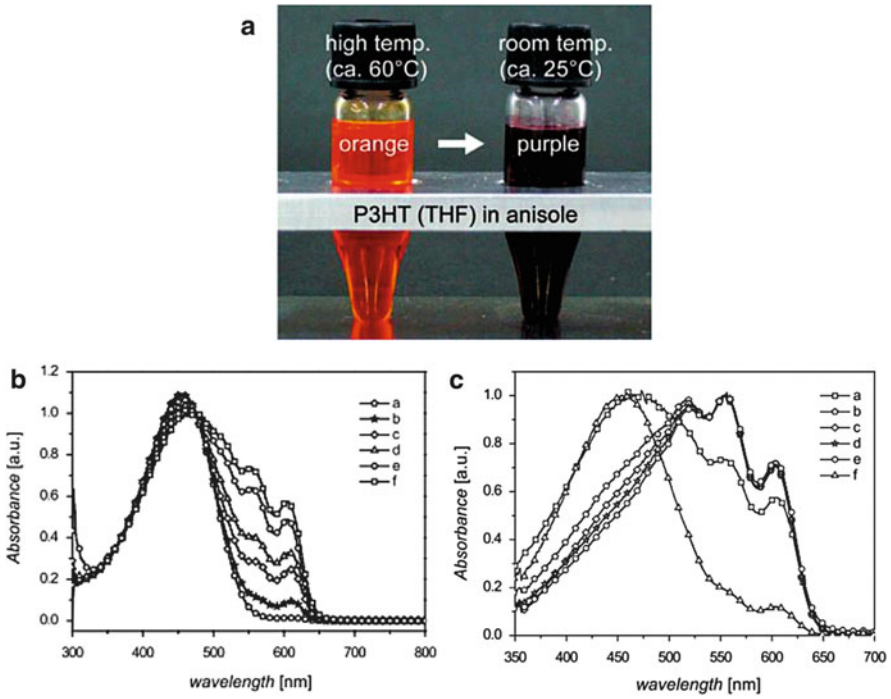

Fig. 5 (**a**) Photographic image of P3HT (Soxhlet-extracted from THF) in anisole (0.05 wt%) at 60°C (*left*) and room temperature (*right*) [48]. (**b**) Absorption spectra of P3HT in *p*-xylene (1 wt%) after dissolution at 80°C and subsequent cooling to room temperature at 20°C/h. Evolution of the solution was followed at room temperature, with the spectra being taken after (*a*) 2 h, (*b*) 4 h, (*c*) 6 h, (*d*) 21 h, (*e*) 28 h, and (*f*) 48 h [50]. (**c**) Absorption spectra of P3HT in *p*-xylene (1 wt%) (*a*) before centrifugation and filtration, (*b*) after the first centrifugation step, (*c*) after two centrifugation steps, (*d*) after five centrifugation steps, (*e*) after two centrifugation and one filtration steps, and (*f*) absorption spectrum of the collective filtrates [50]. (Reprinted with permission from Samitsu et al. [48]. Copyright (2008) American Chemical Society. And reprinted with permission from Berson et al. [50]. Copyright (2007) Wiley-VCH)

Using the whisker method introduced by Ihn et al. [47], Guillerez and coworkers followed the formation of P3HT nanofibrils in solution, prepared using a marginal solvent, by optical spectroscopy [50]. Aggregation in solution is accompanied by a drastic color transition from orange to purple/violet (see Fig. 5a), denoting a significant change in the physical conformation of the polymer chains, as reported by Ihn et al. and Samitsu et al. [47, 48]. This makes in-situ linear absorption spectroscopy an elegant and simple tool for monitoring aggregate formation in solution. Guillerez et al. reported crystal growth in *p*-xylene, which is a poor solvent for P3HT at room temperature, whereas complete dissolution of the polymer chains occurs at elevated temperature and gives rise to a single, broad absorption peak. The evolution of the solution spectrum after cooling to room temperature at a controlled rate is illustrated in Fig. 5b. After cooling, additional vibronic structures at

525, 555, and 610 nm gradually emerge, which is indicative of the formation of highly ordered structures. The appearance of an isosbestic point at 475 nm clearly suggests the presence of two different states in the polymer solution. This is explained by a transition of completely dissolved polymer chains into aggregated stacks without intermediate states.

A combination of centrifugation and filtration was used to isolate the fibers in the form of a crystalline powder that forms stable suspensions in *p*-xylene (1 wt%). The filtrate mainly comprised well-dissolved polymer chains, as can be seen from Fig. 5c. Size-exclusion chromatography further demonstrated that the nanofibrils were mainly composed of high molecular weight chains ($M_w \approx 46$ kg/mol, PDI = 2.3), whereas shorter chains remain dissolved in solution ($M_w \approx 38$ kg/mol, PDI = 2.8).

The mixed-solvent method is based on use of a combination of good and poor solvents [52, 54–56]. Thereby, unfavorable interactions between the polymer and the poor solvent drive the aggregation of chains into nanostructures. Kiriy et al. showed that highly aggregated 1D nanostructures of P3HT with a helical conformation of the backbone can be obtained by adding hexane to a solution of P3HT in $CHCl_3$. Hexane acts as a selective solvent for the side chains, but is a rather poor solvent for the conjugated backbone and, hence, favors π–π-interactions and aggregation [54]. In contrast, Sun et al. started with a solution of P3HT in a marginal solvent and demonstrated that, by adding small amounts of a good solvent, the crystallinity of nanofibrils could be improved as a result of an increased flexibility and organization of the chains within the aggregates [52]. Self-assembly can further be triggered by ultrasonication of the solvent mixture, as reported by Kim and coworkers [57].

Zhai and coworkers showed that P3HT nanofibrils can grow into highly ordered 2D nanoribbons, whose structure is shown in Fig. 6 [49]. However, this requires a well-defined nanofibril surface, which is present only in P3HT of low molecular weight for which chain folding is unlikely. Nanofibril growth was achieved by cooling a solution of P3HT in a marginal solvent from 90°C to room temperature. For $M_n > 10$ kg/mol, anisole (0.05 mg/mL) was used as a marginal solvent, whereas crystallization of low molecular weight P3HT ($M_n < 10$ kg/mol) required the use of a co-solvent of poor dissolving power (anisole/dimethylformamide (DMF), 1:2 vol%, 0.2 mg/mL) to reduce the solubility of the short chains. At first, crystallization from solution results in the formation of 1D nanofibrils, which then act as nucleating points for further growth along the [100] direction via alkyl chain interactions. For high molecular weight P3HT with M_n above a critical value of 10 kg/mol, chain folding results in nanofibrils with more defects, which prevents further growth of the nanofibrils into 2D nanoribbons.

A serious consequence of polymer crystallization in solution is gel formation, which is a severe issue regarding, for example, inkjet printing of polymeric semiconductors because gelation dramatically shortens the lifetime of electronic inks. The gelation mechanism has been intensively studied by Nandi and coworkers, who describe the gel formation of P3HT as a two-step process [58, 59]. In phase I, single isolated chains undergo a coil-to-rod transformation, and phase II involves the

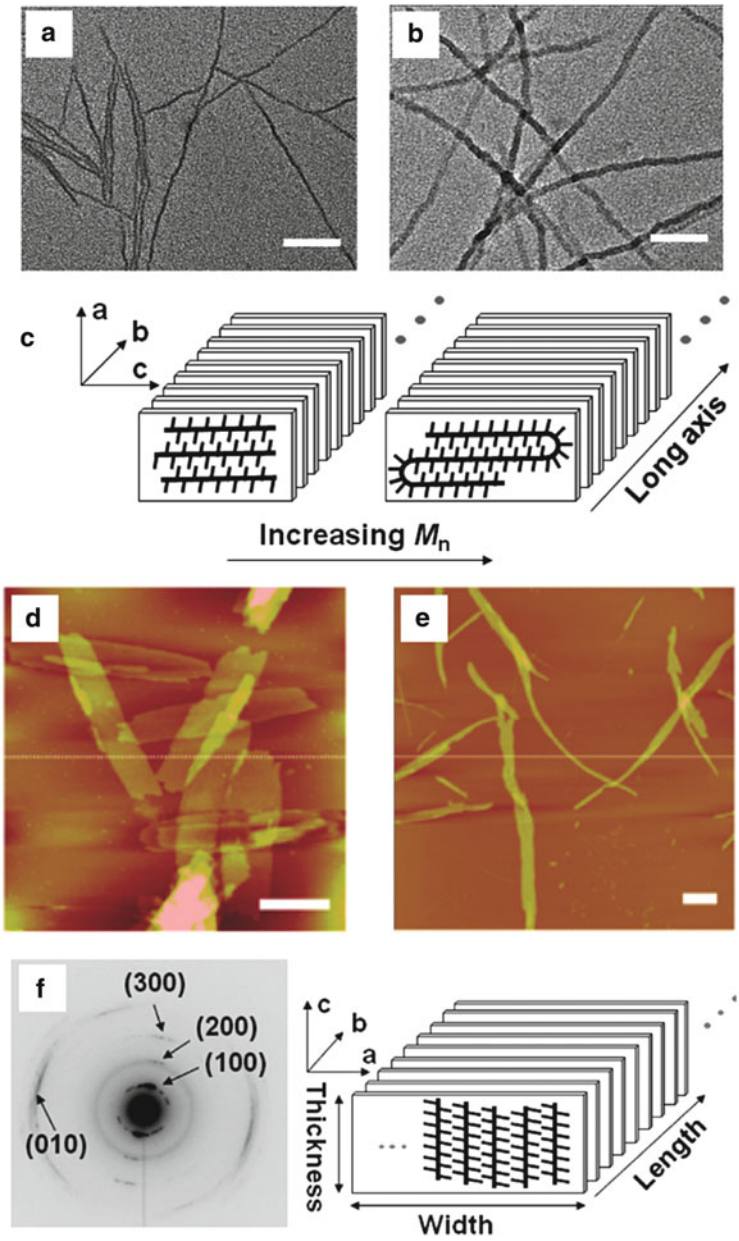

Fig. 6 (**a**, **b**) TEM images of P3HT fibrils grown from solution by the whisker method at 25°C: (**a**) $M_n = 6.0$ kg/mol, 0.2 mg/mL in DMF/anisole (2:1 vol%) and (**b**) $M_n = 15.6$ kg/mol 0.05 mg/mL in anisole [49]; *scale bars*: 100 nm. (**c**) Extended and folded polymer chains within the nanofibrils for $M_n < 10$ kg/mol and $M_n > 10$ kg/mol, respectively. (**d**, **e**) AFM phase images of P3HT nanoribbons prepared by the whisker method at 25°C and deposited on silicon wafers by spin-coating of (**d**)

crystallization of rods into fibrillar structures. Koppe et al. further assume that, after aggregation, ordered domains link to each other and form a gel, which results in an increase in viscosity (see Fig. 7) [51]. Aggregation and gelation occur most intensely and quickly for high molecular weight chains and can be delayed or even suppressed by "dilutants" such as PCBM and P3HT chains of low molecular weight. Furthermore, side chain length and regioregularity play a crucial role in the gelation process [58, 59].

For all the approaches described so far, crystal formation takes place in solution before the deposition of the polymer on a substrate. The deposition of pre-aggregated nanocrystals is typically achieved by means of drop-casting, spin-coating, or dip-coating. The performance of nanofibril-based films of polythiophenes has been intensely investigated in devices such as OFETs and OSCs [50, 52, 55, 57, 60–66]. Merlo and Frisbie reported hole mobilities of up to 0.06 cm^2/V s for single P3HT nanofibrils, demonstrating the high degree of order within the fibrils [60, 61]. Samitsu et al. further showed for P3AT of different side chain lengths that charge carrier transport in single fibrils is much more effective than between fibrils in a network, suggesting a transport barrier between adjacent fibrils (see Fig. 8) [63]. In contrast to thin films of P3AT cast from solutions prepared using a good solvent, nanofibril-based films exhibit hole mobilities that are relatively independent of the side chain length, which results from the high in-plane order of the chains within the fibrils (edge-on), whereas the molecular orientation in cast films is strongly affected by the alkyl chain length during solution-casting [53]. In bulk-heterojunction solar cells, P3HT nanofibrils yield high power conversion efficiencies of 3.9% [55] in combination with PCBM.

4 Thin Film Properties

Highly crystalline layers of P3HT can be obtained by pre-aggregation of nanofibrils in solution followed by deposition of the aggregated nanostructures on a substrate, which allows decoupling of crystallization from the film deposition process. However, device fabrication requires cheap and fast techniques to generate homogeneous films on a large scale. Consequently, controlled crystal formation in solution is difficult to implement for device fabrication. Deposition of conjugated polymers is typically pursued from solutions prepared using a good solvent like chloroform via various techniques such as spin-coating, doctor-blading, dip-coating, and inkjet-printing. In these fast processes, crystal formation takes place during drying of the

Fig. 6 (continued) $M_n = 6.0$ kg/mol, 0.2 mg/mL in DMF/anisole (2:1 vol%) and (**e**) $M_n = 10.2$ kg/mol, 0.05 mg/mL in anisole; *scale bars*: 500 nm. (**f**) Selected area electron diffraction of P3HT nanoribbons (10.2 kg/mol) corresponding to (**e**). Molecular arrangement within P3HT nanoribbons is shown on the *right*. (Reprinted with permission from Liu et al. [49]. Copyright (2009) American Chemical Society)

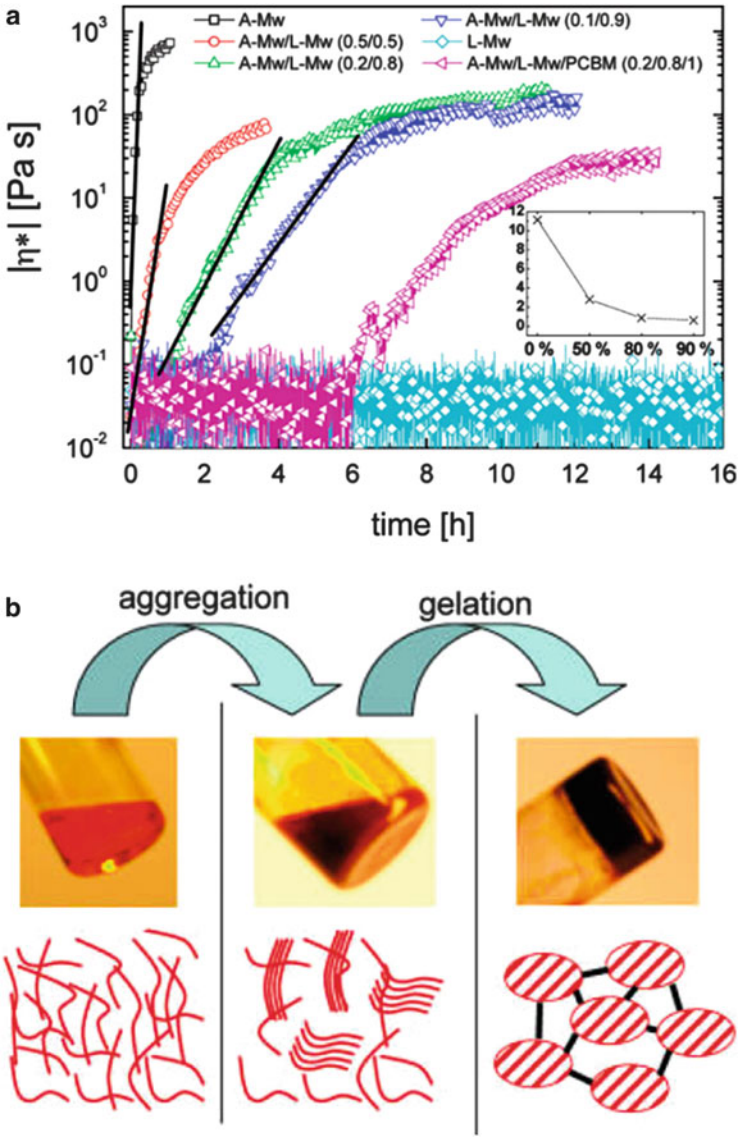

Fig. 7 (**a**) Rotational rheometer viscosity measurements of P3HT solutions in *o*-xylene (1 wt%) at 25°C for different molecular weight compositions obtained by mixing A-M_w ($M_w = 72.8$ kg/mol) and L-M_w ($M_w = 26.2$ kg/mol) in different proportions [51]. *Full lines* were generated by linear fits to the experimental viscosity evolution. *Inset*: the slope of the linear fits for increasing contents of L-M_w mixed with A-M_w (0, 50, 80, and 90 wt%). (**b**) Photographic images and sketches of the two-step process of polymer gelation for P3HT ($M_w = 72.8$ kg/mol) in *o*-xylene solution (1 wt%). (Reprinted with permission from Koppe et al. [51]. Copyright (2009) American Chemical Society)

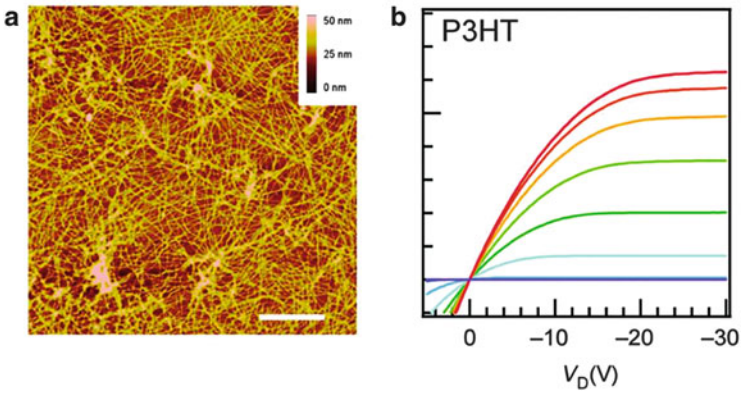

Fig. 8 A network of P3HT nanofibrils was grown from a solvent mixture of anisole and chloroform (4:1 vol%, 0.05 wt%) by slowly cooling the solution from 70°C to 20°C (25°C/h) [63]. The fibrils were deposited on transistor substrates by spin-coating. (**a**) AFM height image; *scale bar*: 1 μm. (**b**) Output characteristics of a nanofibril-based bottom gate, bottom contact transistor with V_G ranging from +5 V to −30 V (−5 V/step). (Reprinted with permission from Samitsu et al. [63]. Copyright (2010) American Chemical Society.)

film and therefore usually under nonequilibrium conditions. The microcrystalline morphology is strongly dependent on the film processing conditions, including the coating technique itself, but also on the choice of solvent and the nature of the substrate [5, 67–72]. In addition to the precise deposition conditions, the molecular parameters of the polymer (molecular weight and regioregularity) have a strong impact on the morphology [17, 18, 73–75].

In the following section, we review the influence of these different parameters on the thin film morphology, and also their impact on the functional properties in devices. The impact of thin film morphology on both the optical and electrical properties is discussed. The section is structured as follows: First, visual inspection of P3HT thin films is described, with absorption spectroscopy being an excellent tool for understanding intra- and interchain order in thin films. Then, the influence of molecular parameters and processing conditions on the mesoscopic and microcrystalline morphology is discussed. Some findings on the influence of morphology on charge transport are also included.

4.1 Preparation and Characterization of P3HT Films

4.1.1 Optical Properties of Thin Films

When P3HT films are deposited from solutions prepared using good solvents, significant color changes can be detected that range from orange to purple depending on the regioregularity and the molecular weight of the batch. Thin film

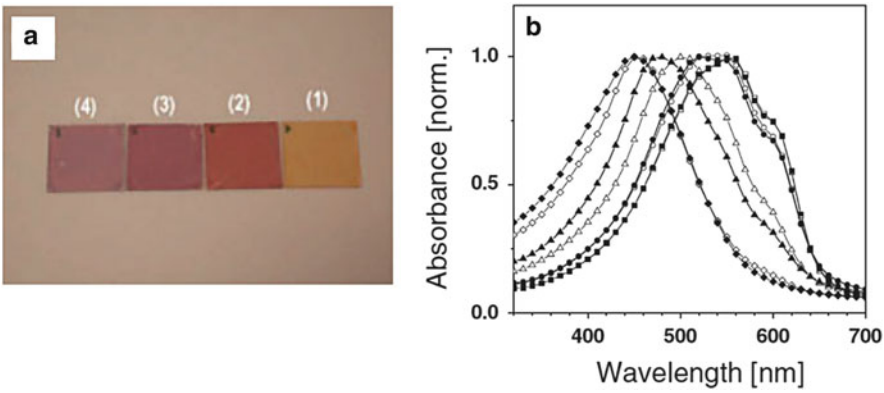

Fig. 9 Optical properties of P3HT thin films as a function of the molecular weight [17]: (**a**) Optical photographs of P3HT layers spin-cast from the ethyl acetate (*1*), hexane (*2*), dichloromethane (*3*), and chloroform (*4*) fractions. (**b**) Absorption spectra of P3HT thin films of the ethyl acetate (*open diamond, filled diamond*), *he*xane (*open triangle*, *filled triangle*), dichloromethane (*open circle*, *filled circle*), and chloroform (*open square*, *filled square*) fractions. *Open* and *filled symbols* correspond to as-cast and thermally annealed layers (5 min. at 150°C), respectively. (Reprinted with permission from Zen et al. [17]. Copyright (2004) Wiley-VCH)

spectra of regioirregular P3HT resemble the solution spectra of regioregular P3HT (shown in Fig. 3), consisting of a broad and almost featureless absorption band [76]. This observation is related to the fact that regioirregular P3HT forms mainly amorphous layers due to the weak tendency for intermolecular packing, which is impeded by the sterically driven twist of the backbone. Therefore, the physical conformation of the chains is similar to that of regioregular P3HT in the solution state. By contrast, film spectra of regioregular P3HT are significantly red-shifted and exhibit well-defined vibronic features in the low-energy part of the spectrum, which is attributed to the presence of π-stacked aggregates in which chain twisting is strongly constrained, leading to flat molecules with extended conjugation [76]. Additionally, the optical properties are strongly dependent on the molecular weight. This is illustrated in Fig. 9, which shows both photographs and absorption spectra of P3HT thin films of different molecular weight after solution-casting and thermal annealing, respectively [17]. The fact that the thin film spectrum of low molecular weight P3HT resembles the solution spectrum indicates that a large number of the chains adopt a twisted conformation in the solid state. Studies on thermochromism strengthen the interpretation that the variation in optical absorption is connected to the conformation of the polymer chain [17]. Heating a thin P3HT film of intermediate molecular weight (hexane fraction, $M_n = 5.6$ kg/mol) to 210°C leads to a strong color change from red to yellow/orange, most probably due to a twisting of the backbone. By contrast, little and almost no change is observed for high ($M_n = 19$ kg/mol) and low ($M_n = 2.2$ kg/mol) molecular weight P3HT, respectively.

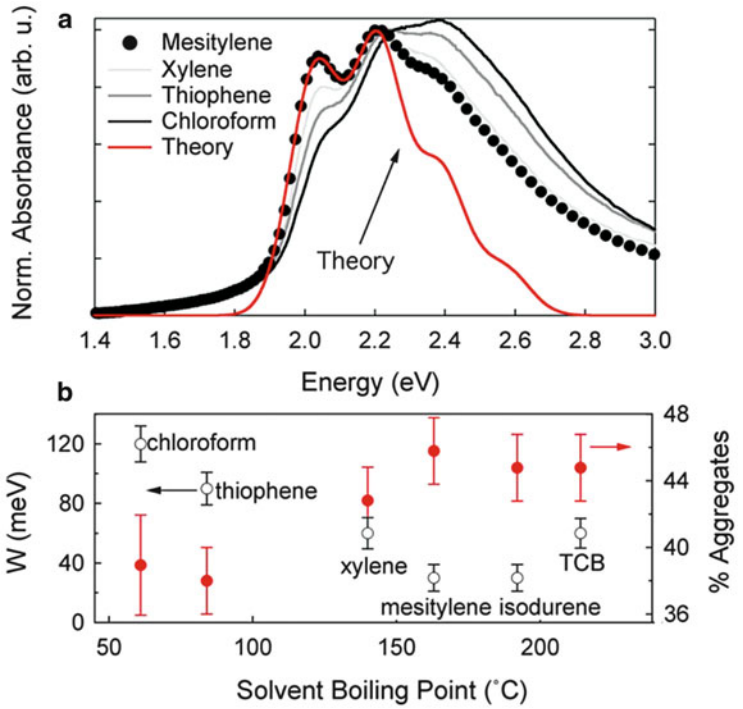

Fig. 10 (**a**) Normalized absorption spectra of P3HT films spin-coated from various solvents. A theoretical spectrum for mesitylene is depicted in *red* [78]. (**b**) Exciton bandwith (*W*) (*left axis*, open black symbols) and percentage of film that is formed of crystalline aggregates (*right axis*, red symbols) as a function of the casting solvent. (Reprinted with permission from Clark et al. [78]. Copyright (2009) American Institute of Physics)

Absorption spectroscopy is a good tool for determination of the degree of intra- and interchain order within P3HT thin films. A detailed and quantitative analysis of the absorption spectrum of regioregular P3HT was proposed by Spano and coworkers [6, 77, 78]. For a thin P3HT film, two parts of the absorption spectrum can be distinguished, as shown in Fig. 10a. The high energy part of the spectrum is attributed to disordered chains forming intrachain states, most probably related to chains in the amorphous part of the film, whereas the lower energy part denotes weakly interacting H-aggregates in crystalline regions of the layer. Two peaks can be identified in the lower energy part: A_{0-0} transition at 620 nm (2.0 eV) and A_{0-1} transition at 570 nm (2.2 eV). The free exciton bandwidth (*W*) within the crystalline domains is associated with the intensity ratio of the A_{0-0} and A_{0-1} peaks by the following equation:

$$\frac{A_{0-0}}{A_{0-1}} = \left(\frac{1 - 0.24W/E_p}{1 + 0.073W/E_p}\right)^2 \quad (4)$$

where E_p describes the energy of the main intramolecular vibration coupled to the electronic transition.

The Spano model provides an easy approach for estimating the aggregate content and intrachain order in P3HT thin films by simply exploiting the absorption spectrum, as shown in Fig. 10b. The model can be further used to follow crystallization of P3HT from solution, distinguishing between well-dissolved chains and chains incorporated in crystalline nanocrystals (compare with Sect. 3).

4.1.2 Mesoscale Morphology

Molecular Parameters

It is well established in the literature that the morphology of regioregular P3HT is highly affected by molecular parameters of the polymer such as molecular weight, regioregularity, and polydispersity [16–18, 73–75, 79–81]. In 2003, Fréchet and coworkers showed a clear correlation of the crystalline morphology and the molecular weight of poly(3-alkylthiophene)s, which is also accompanied by dramatic changes of the field-effect mobility [73].

Low molecular weight P3HT of $M_n < 10$ kg/mol forms well-defined nanorods whose widths show a linear increase with molecular weight and correspond well to the contour length of the chains (Fig. 11a) [75, 79]. This suggests that the nanorods are composed of extended chains, with the backbone being in the plane of the film and oriented perpendicular to the long axis of the nanorod. This structure is supported by X-ray diffraction (edge-on orientation; see end of this section). For higher molecular weights of $M_n > 10$ kg/mol, the periodicity of the nanofibrils saturates and less-defined, nodule-like morphologies appear (see Fig. 11b). Here, the contour length of the chains is much higher than the width of the nanofibrils. The linear increase in nanocrystal width with increasing molecular weight, followed by saturation (see Fig. 12), is attributed to chain folding [79].

Bending of P3AT chains in thin films was visualized by Mena-Osteritz and Grévin et al. after self-organization on highly oriented pyrolytic graphite (HOPG) via scanning tunneling microscopy [82, 83]. As a result of the relatively high stiffness of the conjugated backbone, chain folding is believed to induce stress on the stacking of the chains, which gives rise to decreased order and less-defined nanostructures in high molecular weight P3HT.

Regarding charge transport, by increasing the molecular weight M_n over one order of magnitude from around 4–36.5 kg/mol, the charge carrier mobility is observed to increase over almost four orders of magnitude, improving from 10^{-6} to 10^{-2} cm^2/V s [73]. Zen et al. propose that the field-effect mobility is highly affected by the crystallinity of the sample [17, 74]. Despite the high perfection of

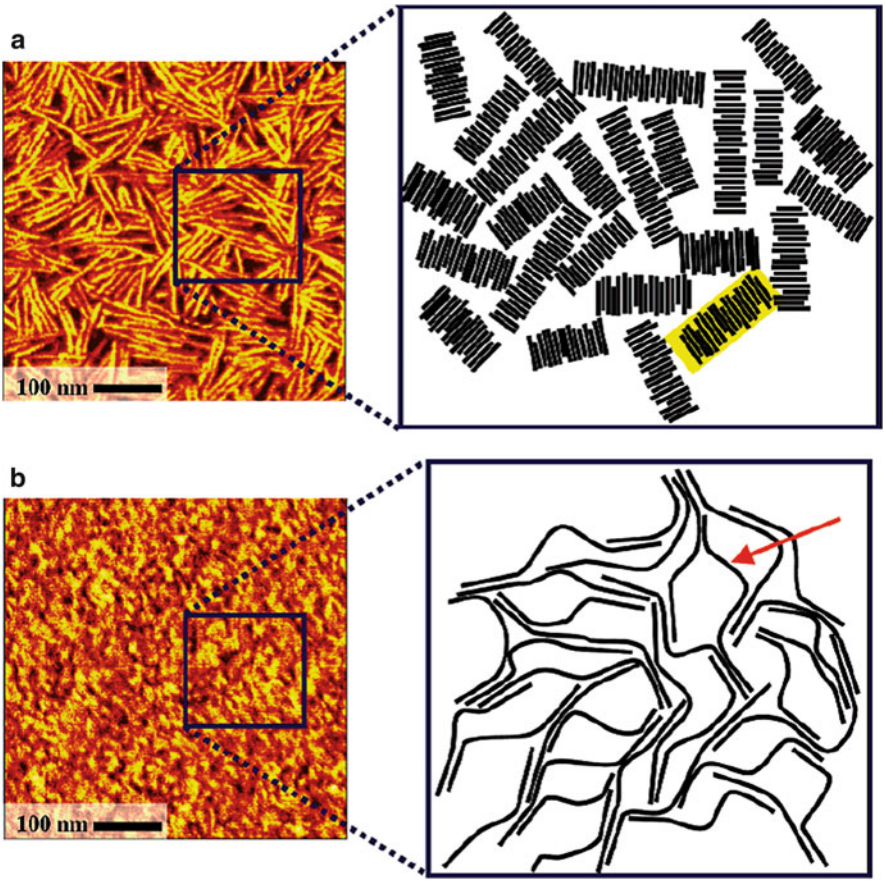

Fig. 11 Morphology of P3HT films directly after spin-coating: (**a**) Ribbons of a low molecular weight sample ($M_n < 4$ kg/mol) in an extended chain configuration [18]. (**b**) Less-defined morphology of a high molecular weight sample ($M_n > 30$ kg/mol) with tie molecules (marked by a *red arrow*) bridging crystalline domains. (Reprinted with permission from Kline et al. [18]. Copyright (2005) American Chemical Society)

the crystalline nanorods in low molecular weight P3HT, charge transport seems to be mainly determined by twisted chains in the amorphous matrix. In contrast, chains of high molecular weight adopt a planar chain conformation, enabling strong π–π-interactions and hence efficient charge transport. Kline et al. take into account that charges become trapped at grain boundaries between nanocrystals [18, 73]. In low molecular weight P3HT, the nanorods are poorly interconnected (as evidenced by AFM), which results in severe charge trapping. Longer chains can bridge the amorphous zones between the crystallites and soften the boundaries, leading to improved macroscopic charge transport. The presence of such interconnecting chains in high molecular weight P3HT, also referred to as tie-chains, is illustrated in Figs. 11 and 13. In general, the morphology of high molecular weight P3HT is

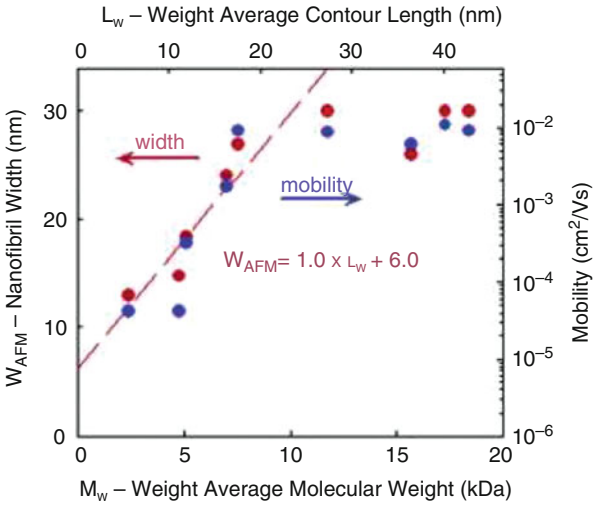

Fig. 12 Evolution of P3HT nanofibril width W_{AFM} and hole mobility μ as function of weight-average molecular weight M_{w} and weight-average contour length L_{w} [79]. Thin films were prepared by drop-casting from toluene (1 mg/mL). (Reprinted with permission from Zhang et al. [79]. Copyright (2006) American Chemical Society)

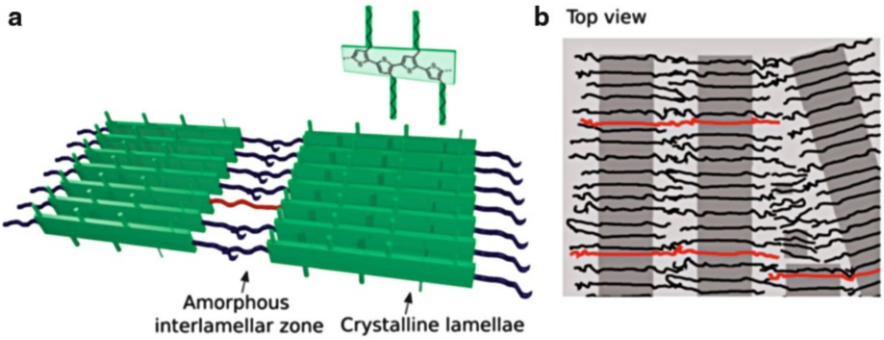

Fig. 13 Microstructure in P3HT thin films: (**a**) molecular arrangements of the polymer chains within the nanocrystalline lamellae, which are separated by amorphous domains; and (**b**) meso-scale morphology of P3HT consisting of crystalline lamellae (*dark grey*) separated by amorphous domains (*light grey*). Tie-chains connecting adjacent lamellae are shown in *red*. Image courtesy of Florian Fischer

composed of a mixture of ordered and amorphous regions. Crystalline lamellae formed of planar, stacked chain segments are separated by interlamellar amorphous domains comprising chain ends, chain folds, and long tie-chains, the latter interconnecting neighboring crystallites. Although little is known about the precise nature of these interconnections, qualitative considerations were proposed by

Salleo and coworkers in a recent publication [84]. On large length scales, polymer chains are flexible, whereas the backbone is rather rigid at the length scale of the persistence length. Therefore, the authors propose a weak bending of the polymer chains if the distance between adjacent crystallites is in the region of a few persistence lengths. These tie-chains with extended conjugation serve as an efficient charge transport pathway through disordered domains in high molecular weight P3HT.

Processing Conditions

Not only molecular parameters, but also the processing conditions strongly affect the thin film morphology. The literature on different deposition protocols and post-processing protocols is huge. In this section, we highlight some representative examples.

Typical solution deposition techniques are dip-coating, drop casting, and spin-coating, with the evaporation rate of the solvent increasing in the given order. The nanostructured morphology is most distinctive in the case of a slow drying of the film, when the polymer chains have sufficient time to self-assemble into nanocrystalline structures. Changes in the thin film morphology as a function of the solvent evaporation rate are illustrated in Fig. 14, which shows AFM images of P3HT films of four different molecular weights cast by three different methods under identical conditions. Dip-coating and spin-coating were performed from chloroform solution, whereas drop-cast films were obtained from a solvent mixture of chloroform and tetrahydrofurane (14:3, v/v). Fast solvent evaporation during spin-coating leads to rod-like structures only for low molecular weight samples, whereas layers of $M_n > 10$ kg/mol remain almost featureless. By contrast, slow solvent evaporation achieved by dip-coating results in well-defined nanostructures that are independent of the molecular weight. During the slow film drying process, the polymer chains can stack into ordered nanofibrils, even in the case of long chains. The impact of such a slow solvent evaporation achieved by dip-coating was further demonstrated by Heeger and coworkers, who studied charge transport in ultrathin dip-coated films with a thickness of a few nanometers [70]. The latter exhibit highly ordered structures, as evidenced by well-resolved bands in the optical absorption spectrum, which correlates with high mobilities reaching 0.2 cm^2/V s in accumulation mode.

In spin-coated layers, the microcrystalline order is typically low, especially when low boiling point solvents such as chloroform are used. Order can be significantly improved by using high boiling point solvents such as trichlorobenzene (TCB), as evidenced by X-ray diffraction and AFM [69]. This also causes a significant enhancement of the charge carrier mobility to 0.12 cm^2/V s, which is around one order of magnitude higher than for layers cast from chloroform. Another approach to slow solidification was demonstrated by Cho and coworkers, who reported the formation of highly ordered 1D nanofibrils via spin-coating in a solvent vapor atmosphere [85]. Spin-coating was carried out from chloroform, and the amount of chloroform within the spin-coating chamber determined the solvent

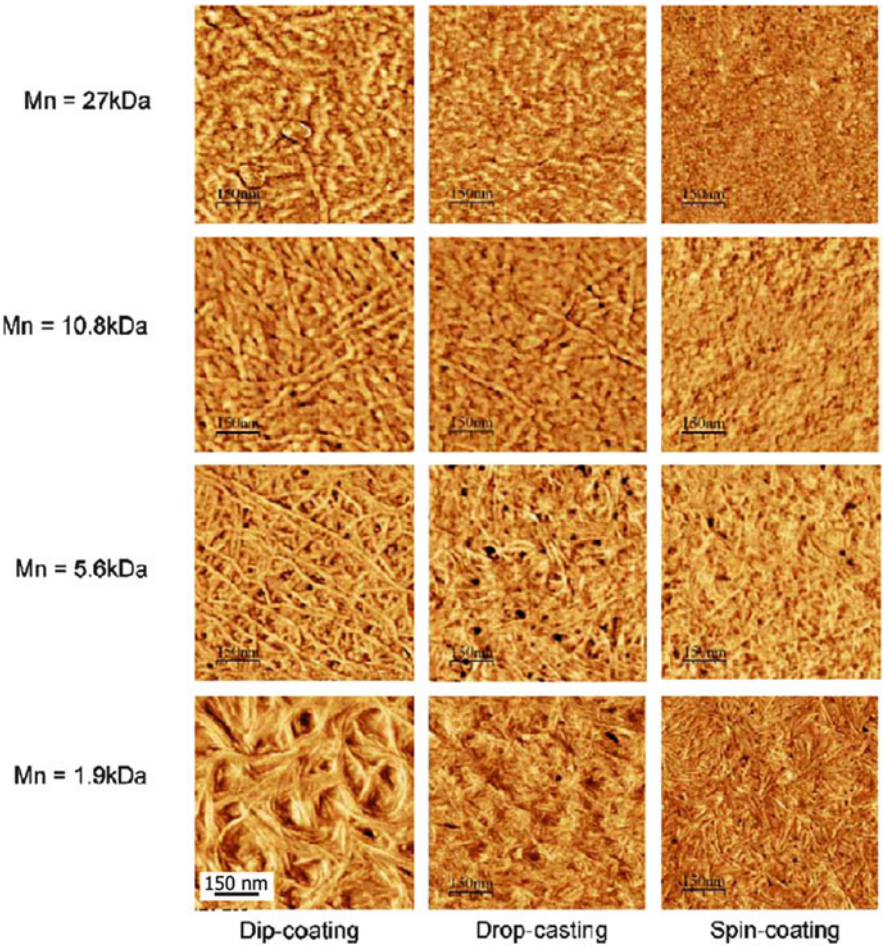

Fig. 14 AFM phase images of thin P3HT films of different molecular weight achieved by three different casting techniques [75]. (Reprinted from Verilhac et al. [75], Copyright (2006), with permission from Elsevier)

vapor pressure. Control of the solvent vapor pressure during solidification of the polymer enabled adjustment of the length of the resulting nanofibrils.

In 1996, Bao and coworkers compared the charge transport properties of P3HT layers deposited by spin-coating and drop-casting from different solvents [5]. Drop-cast films generally showed better charge transport, which was attributed to a higher degree of order achieved by the slow growth process of the film. However, the use of different solvents resulted in a significant scattering, and no clear evolution of the hole mobility as a function of the film drying time was found, which was related to differences in film quality. In order to achieve a better understanding of this behavior, a detailed structural investigation of drop-cast and spin-coated layers

from different solvents was accomplished in later years by Bao and coworkers [67, 68]. The fact that no clear correlation between the drying time and the field effect mobility could be found for drop-cast layers was attributed to the precise mesoscale morphology induced by different solvents, i.e., crystallinity, grain boundaries, branching of fibrils, and the degree of in-plane stacking. For further correlations between the charge carrier mobility and the processing conditions we refer to a recent review by Wuest and coworkers [86] and the article by Zaumseil in this book [87].

To summarize, the crucial parameters that affect hole mobility include: (1) the mesoscale morphology comprising the interconnectivity of crystalline domains and the presence of grain boundaries and (2) the <100> orientation distribution with respect to the substrate and, hence, the degree of in-plane π-stacking [67]. In the following section, studies on the orientation of the polymer chains with respect to the substrate are reviewed.

Texture and Orientation of Polymer Chains on Substrates

Before focusing on the texture of P3HT on substrates, research on structural models and the polymorphism into form I and form II is briefly mentioned.

From a crystallographic point of view, the *a*-axis corresponds to the (100) direction pointing in the direction of the alkyl chains, the *b*-axis (010) is the π–π-stacking direction, and the *c*-axis (001) corresponds to the direction along the polymer chain. Structural studies on P3ATs were initiated by Prosa in 1992, who also reported the presence of polymorphism into form I and II (see Fig. 15) [88, 89].

Prosa et al. initially reported an orthorhombic unit cell for form I [89]. In a later study, Tashiro et al. proposed other possible structures that are consistent with both experimental and simulated diffraction patterns [90]. Using electron diffraction, Brinkmann and Rannou found a monoclinic unit cell for form I P3HT [91]. This structure was challenged by Dudenko et al. [92]. Although it has not been possible to grow single crystals in form I (which makes the structure determination difficult),

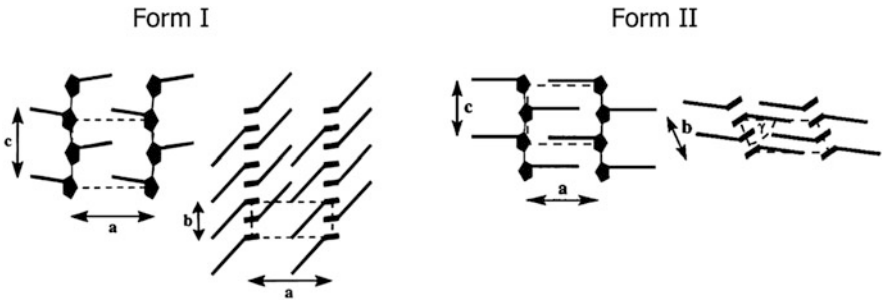

Fig. 15 Crystal structure of P3HT in form I and form II [88]. (Reprinted with permission from Prosa et al. [88]. Copyright (1996) American Chemical Society)

single crystals in form II were recently grown by a self-seeding approach from solution [44]. For a more in-depth discussion of the crystal structures we refer to [93] and Ref. [45] in this book.

Values of the degree of crystallinity are not usually discussed in the literature. This is because it is very difficult to determine the reference melting enthalpy ΔH_m of an ideal crystal of P3HT. A first value of 99 J/g was given by Malik and Nandi [94]. Only recently have optimized values of around 37 J/g been determined by DSC measurements and ^{13}C solid-state NMR measurements by Saalwächter and Thurn-Albrecht [16, 81], and values of around 50 J/g were found by Snyder and coworkers [95, 96]. Density measurements and correlations of the obtained densities to these melting enthalpies strongly suggest that values between 37 and 50 J/g seem to be correct [96].

Upon deposition from solution, two textures are mainly reported for P3HT thin films: edge-on and face-on. For an edge-on texture, the π-stacking is in the plane of the film, while the side chains point along the substrate normal (Fig. 16a). For a face-on texture, the polymer chains lie flat on the substrate with the π-stacking oriented along the substrate normal (Fig. 16b). In the literature, little is reported

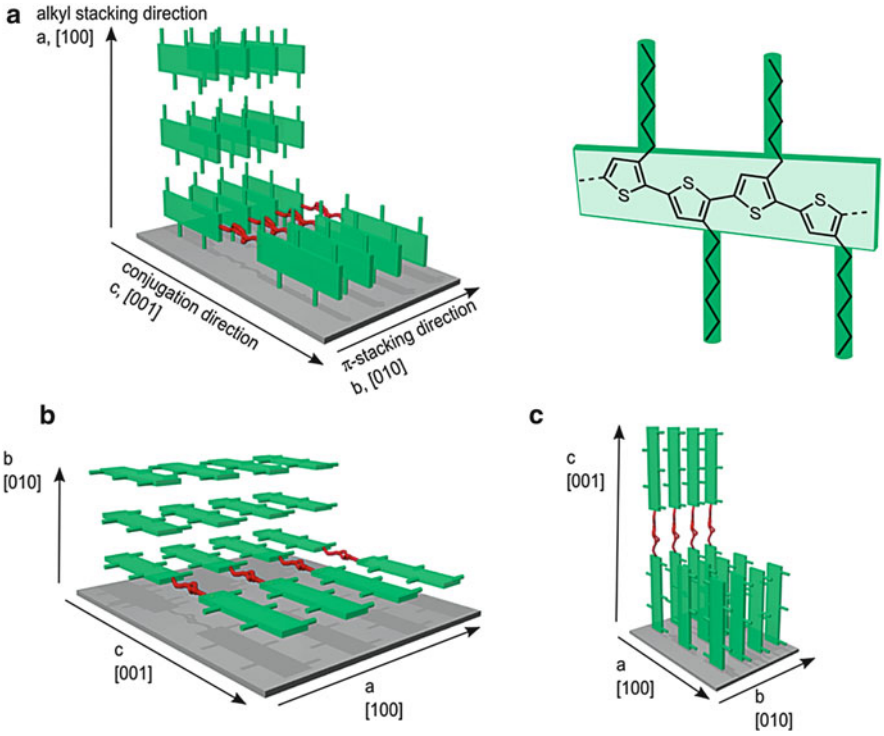

Fig. 16 Molecular orientation of P3HT in thin layers, with fast charge transport expected parallel to the chain axis and in the π-stacking direction, while the side chains act as barriers: (**a**) edge-on orientation, (**b**) face-on orientation, and (**c**) standing chains. Image courtesy of Florian Fischer

about standing chains of P3HT, where the polymer backbone stands vertically on the substrate (Fig. 16c) [97, 98]. The description of texture is not consistent in the literature, with some groups referring to the orientation of the chains and others denoting the orientation of crystalline grains with respect to the substrate. In this chapter, we refer to the molecular orientation of the polymer chains.

In general, the thermodynamically favored texture is assumed to be formed by edge-on oriented chains [1, 5, 68, 69]. This structure is obtained under conditions close to the equilibrium realized for slow casting methods such as drop-casting [1, 67, 68] and dip-coating, and by spin-coating from high boiling point solvents [69]. The face-on orientation is regarded as a kinetically trapped morphology, which is obtained by rapid drying of the layer [71]. This texture seems to be further favored for P3HT of low regioregularity [1] and for layers prepared under shear force, for instance via the friction transfer method [99] or mechanical rubbing [100] (see Sect. 4.2.1).

It is generally believed that fast charge transport occurs along the chain axis (*c*-axis) and in the π-stacking direction (*b*-axis), whereas the insulating side chains (*a*-axis) lead to charge barriers and low mobilities. Therefore, an edge-on orientation is highly desirable for OFETs since here high in-plane charge transport between the source and drain electrode is essential. The importance of molecular orientation for charge transport was first demonstrated by Sirringhaus and coworkers, who studied transistor properties for different textures [1]. In edge-on orientation, the field-effect mobility is more than 100 times higher than for chains in face-on orientation, which is attributed to the excellent charge transport along the chain axis and in the π-stacking direction.

The impact of the solvent evaporation rate on the texture was demonstrated by Bao and coworkers, who prepared P3HT layers from chloroform solution using two different methods, namely spin-coating and drop-casting (Fig. 17) [68]. In the slow drop-casting process, polymer chains have sufficient time to self-assemble into well-defined nanofibrils that are visible in AFM. In accordance with the morphology, the polymer chains adopt an edge-on orientation, as evidenced by grazing incidence X-ray diffraction (GIXRD) measurements. In stark contrast, AFM measurements of spin-cast layers show an almost featureless microstructure, while GIXRD reveals a predominant face-on texture.

DeLongchamp et al. studied the microstructure of P3HT spin-cast from chloroform for different spin speeds and found a remarkable change in the texture, which is shown in Fig. 18 [71]. With decreasing spin speed, a transition from mainly face-on to edge-on was observed. A reduction in spinning speed led to a slower evaporation of the solvent [101]. Therefore, this observation is in agreement with various reports in the literature showing that slow evaporation typically results in a higher degree of edge-on orientation [5, 70, 80, 102].

Besides the deposition conditions, the nature of the substrate can have a significant influence on the texture. Substrate treatment with self-assembled monolayers (SAMs) such as octadecyltrichlorosilane, hexamethyldisilazane, and γ-aminopropyltriethoxysilane results in an edge-on texture [72, 103–105]. By contrast, Chow and coworkers reported the formation of a face-on oriented P3HT

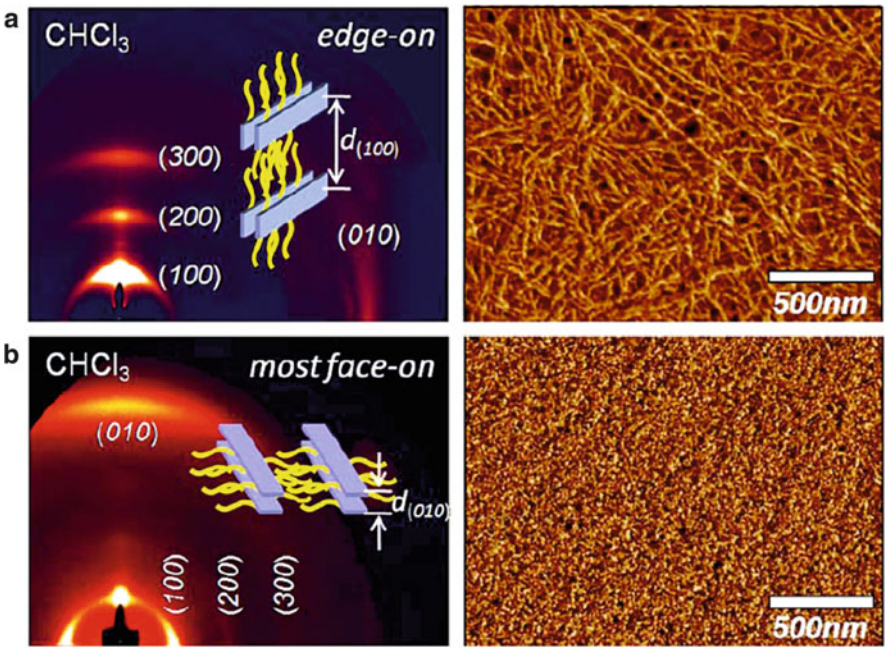

Fig. 17 Impact of processing conditions on the texture of P3HT [68]. GIXRD (*left*) and AFM measurements (*right*) of P3HT layers deposited from chloroform solution by (**a**) drop-casting and (**b**) spin-coating. (Reprinted with permission from Yang et al. [68]. Copyright (2007) American Institute of Physics)

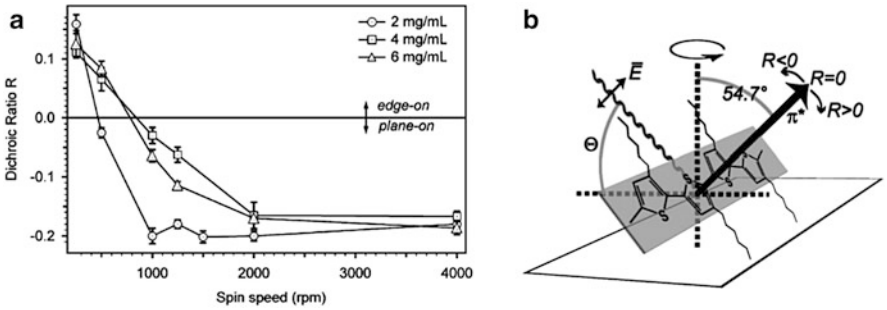

Fig. 18 (**a**) Results obtained by carbon K-edge NEXAFS measurements of P3HT films cast from chloroform for various spin speeds [71]. Positive values of the dichroic ratio *R* denote an edge-on orientation of the polymer backbone; negative values denote a face-on orientation ("plane-on"). (**b**) Chain orientation with respect to the substrate, with the π*-transition being perpendicular to the conjugated backbone. (Reprinted with permission from Delongchamp et al. [71]. Copyright (2005) American Chemical Society)

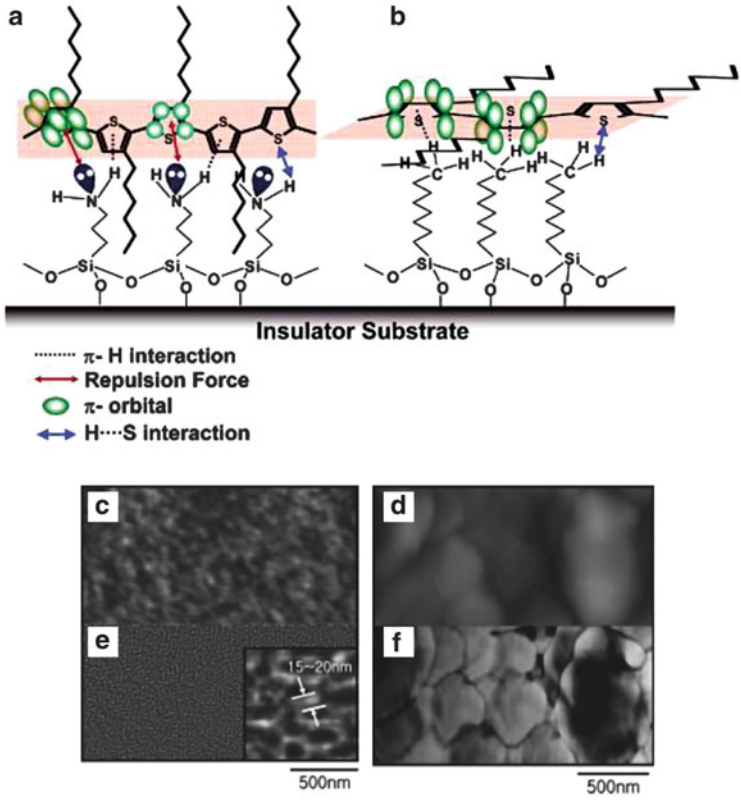

Fig. 19 Molecular orientation of P3HT on different surfaces with (**a**) edge-on and (**b**) face-on orientation [105]. (**c**) Height and (**e**) phase AFM images of P3HT on a NH_2-terminated SAM. (**d**) Height and (**f**) phase AFM images of P3HT on a CH_3-terminated SAM [104]. (Reprinted with permission from Kim et al. [105]. Copyright (2005) American Chemical Society. And reprinted with permission from Kim et al. [104]. (Copyright (2005) Wiley-VCH)

monolayer on substrates treated with octyltrichlorosilane [104, 105]. Figure 19 illustrates the variation in molecular orientation for different surfaces obtained by SAMs of different end-group functionalization. Thereby, the change in chain orientation is attributed to different interfacial interactions.

It should be noted that the orientation of the chains with respect to the substrate is not uniform throughout the film and is highly sensitive to the film thickness [103, 106]. For thick films in the range of a few hundreds of nanometers, π-stacked aggregates are randomly oriented and distributed in an amorphous matrix, whereas a preferential alignment of the chains is reported if the film thickness is in the range of the crystal size, i.e., below 25 nm. This is explained by a preferential pinning of the chains at the film–substrate interface, which results in a high degree of edge-on orientation in the first few layers of the film.

4.2 Inducing Order and Orientation in P3HT Thin Films

Due to the structural complexity of semicrystalline polymers such as P3HT, charge transport bottlenecks are difficult to determine. As opposed to small molecules, crystalline grains in conjugated polymers are usually too small to allow device fabrication within a single grain or across a single, isolated grain boundary. Therefore, typical macroscopic transport measurements based on field-effect transistors, for instance, average over a great number of randomly oriented crystals and grain boundaries. It remains extremely challenging to measure the impact of the structural anisotropy within a crystalline grain as well as the influence of grain boundaries of different orientation on charge transport. The main approach for overcoming this problem is to induce high in-plane orientation in thin polymer films. These highly anisotropic layers can serve as a tool for the study of optical and electronic properties along different structural and crystallographic directions. In addition, the introduction of controlled defects enables the probing of the impact of specific morphological features.

There are different approaches to the synthesis of highly ordered, anisotropic films. For homogeneous layers, anisotropy is mainly induced by controlling nucleation and growth processes and by methods based on shearing forces such as mechanical rubbing. In patterned thin films, confinement-induced orientation is exploited to obtain structural anisotropy. In the following section, different ideas on achieving structural anisotropy for homogeneous and patterned polymer layers and its impact on charge transport is discussed.

4.2.1 Order in Homogeneous Thin Films

Control of Nucleation and Growth

Epitaxial Crystallization

Epitaxial crystallization on orienting surfaces as one elegant method to induce order is thoroughly described by Brinkmann et al. [45]. We briefly highlight the main findings regarding the charge transport anisotropy of such films. Following the approach of directional epitaxial crystallization (DEC) adjusted by Brinkmann and Wittmann [107] and De Rosa et al. [108], Jimison et al. produced highly anisotropic layers of P3HT with fiber-like morphology after directional solidification on the crystallizable solvent 1,3,5-trichlorobenzene (TCB) (see Fig. 20) [19]. Thereby, the polymer backbone (c_{P3HT}) orients parallel to the long axis of the TCB needles (c_{TCB}), with the majority of chains adopting a face-on orientation (Fig. 20d). Transistor measurements in the *a*-*c*-plane of these anisotropic layers revealed a low charge transport barrier at grain boundaries parallel to the fiber axis compared with fiber-to-fiber grain boundaries. This result is explained by the relative grain orientation. Grain boundaries along the fiber separate crystallites in which all the chains orient along the fiber axis. In this geometry, it is likely that straight intergrain

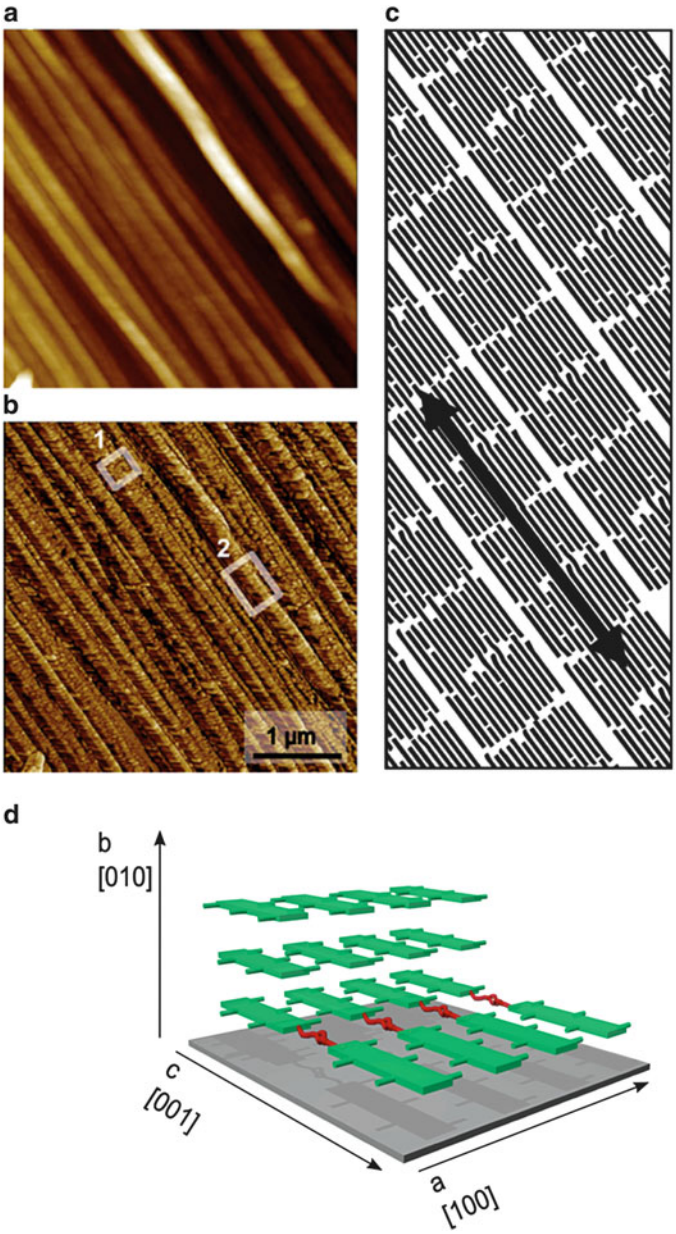

Fig. 20 AFM height (**a**) and phase (**b**) images of P3HT oriented via epitaxial directional crystallization [19]. A domain of equiaxed crystallites is highlighted in *box 1*, and a domain of elongated crystallites is marked by *box 2*. (**c**) Chain alignment within the fibers, with the chain axis being indicated by the *black arrow*. (**d**) Predominant face-on texture within the oriented fibers, allowing for charge transport measurements in the *a*-*c*-plane. (Reprinted with permission from Jimison et al. [19]. Copyright (2009) Wiley-VCH)

chains bridge the boundary and provide efficient charge transport pathways between crystalline grains in the fiber direction (see discussion on the concept of tie molecules in Sect. 4.1.2). By contrast, fiber-to-fiber grain boundaries only allow for intergrain chains with sharp bends and twists, which hamper charge transport. Charge transport along the fiber axis is around one order of magnitude higher than in the perpendicular direction.

Spherulite Growth

The order of P3HT thin films can be further realized via low nucleation densities obtained by controlled homogeneous nucleation and self-seeding. Conventional deposition techniques such as spin-coating usually result in a random orientation of the crystalline lamellae due to the high and uncontrolled nucleation. Spherulitic structures of classical, semicrystalline polymers such as polyethylene with low nucleation density are typically generated from the melt. However, melt-annealing of conjugated polymers is problematic due to the high melting temperatures and potential thermal degradation. Although spherulites for P3AT have not been observed after spin-coating and melt-annealing, Lu et al. and our group reported the formation of P3AT spherulites by solvent vapor annealing [20, 109–111]. Lu et al. reported on the transition of form I to form II in poly(3-butylthiophene)s associated with spherulite formation when thin films were treated with CS_2 vapor [110, 111]. A precise control of nucleation density and, hence, spherulite size for P3HT was achieved by us by introducing an approach based on the controlled swelling and subsequent deswelling in CS_2 vapor of well-defined pressure [20, 109]. Nucleation densities much smaller than those obtained after typical spin-casting conditions were achieved, resulting in spherulitic structures of 10–100 μm in diameter (see Fig. 21a). Thereby, the lamellar crystals composed of highly ordered, edge-on oriented chains exhibited common in-plane alignment over several tens of micrometers. Starting from a pre-cast film, swelling in solvent vapor atmosphere of sufficient pressure results in a complete dissolution of P3HT crystals present in the film after spin-coating. In this solution-like state, isolated chains adopt a flexible coil configuration that is reflected in a single broad peak at 465 nm in the absorption spectrum (illustrated in Fig. 21b). Recrystallization is induced by a controlled deswelling of the film to form a supersaturated solution, and can be followed in-situ by polarized optical microscopy (POM) and UV–vis absorption. Nucleation density is adjusted by controlling the degree of supercooling or by self-seeding, the latter approach relying on a small number of nuclei that remain in the solvent-swollen film and act as seeds in subsequent recrystallization. Following this methodology, nucleation densities over several orders of magnitude can be realized independently of crystal growth conditions.

By decreasing the nucleation density to such an extent that a single transistor can be placed in an ordered crystalline domain, charge transport measurements in the *b*-*c*-plane could be performed. For bottom gate, bottom contact transistors, average mobilities of $\mu_{II} = 0.07$ cm^2/V s and $\mu_{\perp} = 0.20$ cm^2/V s parallel (II) and perpendicular ($\perp$) to the spherulite growth direction were found, meaning that charge

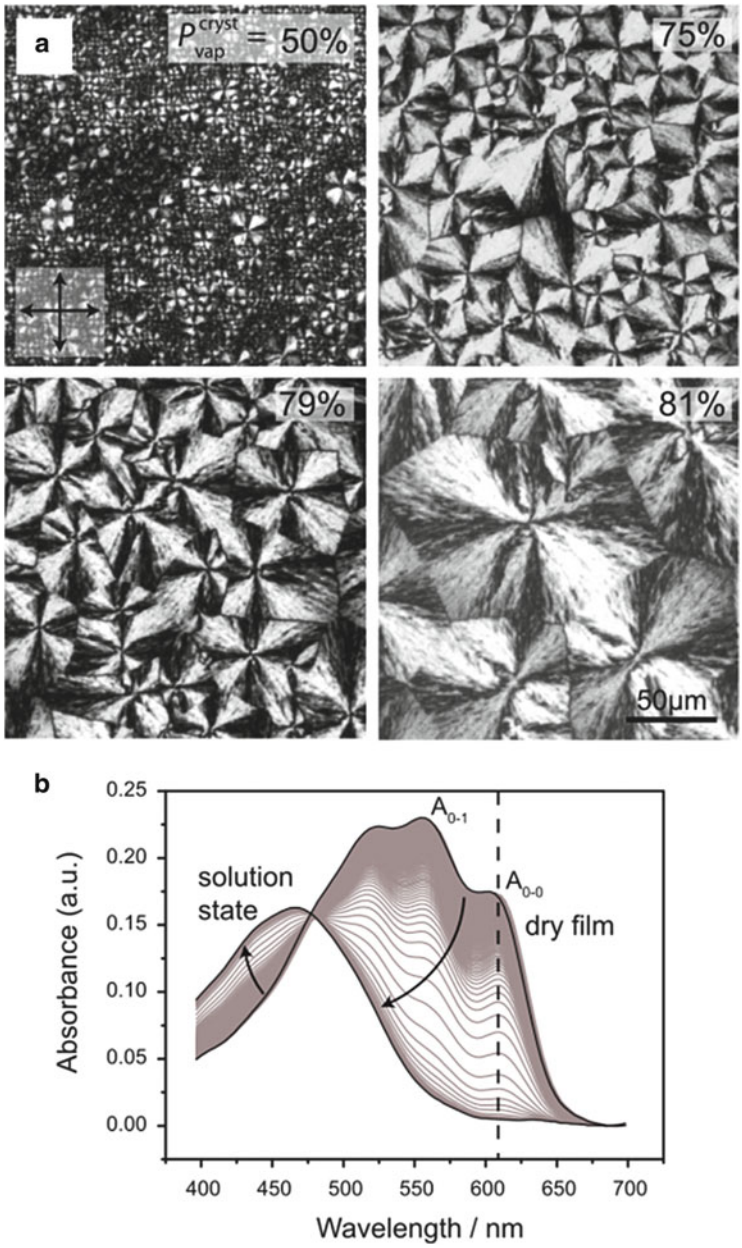

Fig. 21 (**a**) POM images of P3HT films crystallized at the denoted solvent vapor pressure P_{vap}^{cryst} for 30 min after primary swelling at 91% (CS_2 vapor) [109]. (**b**) In-situ absorption spectra of a P3HT film swollen in 90% CS_2 vapor. (Reprinted with permission from Crossland et al. [109]. Copyright (2011) Wiley-VCH)

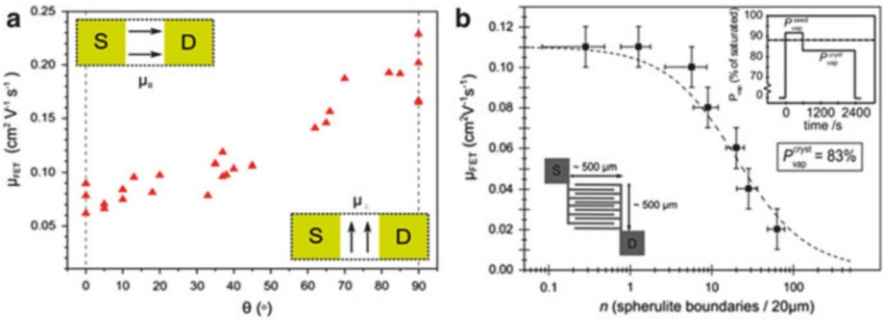

Fig. 22 (**a**) Mobility μ_{FET} within a spherulite as a function of the angle θ between the charge transport direction and the spherulite growth direction, the latter being equivalent to the π-stacking direction [20]. The *insets* demonstrate the spherulite growth direction within a transistor channel. (**b**) μ_{FET} measured in interdigitating transistor channels ($L = 20$ μm, $W = 10$ mm) as a function of the calculated number n of spherulite boundaries per 20 μm transistor channel. (Reprinted with permission from Crossland et al. [20]. Copyright (2012) Wiley-VCH.)

transport over macroscopic distances is around three times higher perpendicular to the crystalline lamellae than in π-stacking direction (Fig. 22). We attribute this observation to the presence of tie-molecules that bridge the amorphous regions between quasiparallel lamellae and therefore offer highly efficient transport pathways in the direction of the chain axis, despite the periodic appearance of amorphous zones. In contrast, a clear drop in the field-effect mobility is observed as soon as the number of nonaligned, interspherulite boundaries in the transistor channel exceeds one. There are two potential explanations for this observation: First, macroscopic charge transport might be impeded by a greater width of amorphous material in between adjacent spherulites compared with the amorphous, interlamellar regions within the spherulites. Second, tie-molecules are less likely to bridge nonaligned grain boundaries between adjacent spherulites than low-angle boundaries between quasiparallel lamellae. The latter interpretation (illustrated in Fig. 23) is in accordance with the model of Salleo and coworkers proposing that grain boundaries are not isotropic [112].

Mechanical Rubbing as Shearing Force

Shearing forces can further be used to induce alignment of the initially unoriented polymer chains in the solid state. The advantage of methods based on shearing forces is that they are independent of the applied substrate and, therefore, permit large-scale processing, which is crucial for device manufacture. In this regard, Nagamatsu et al. used the friction transfer method originally introduced by Wittmann and Smith [113] for orienting layers of poly(tetrafluoroethylene)s in order to produce highly anisotropic layers of P3HT [99]. Another method for orienting P3HT is mechanical rubbing, which is extensively used for the orientation

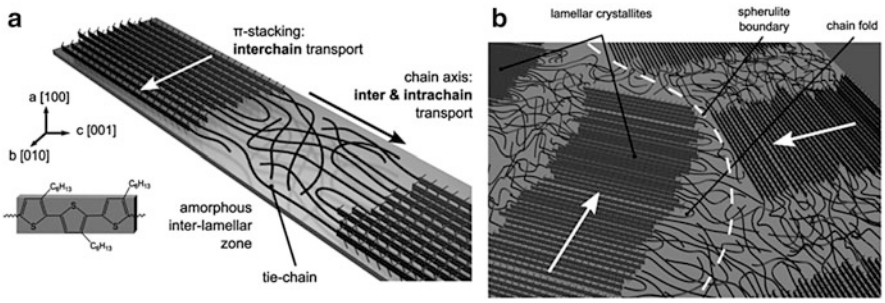

Fig. 23 (**a**) Quasiparallel lamellae composed of stacked aggregates (*solid rectangles*) that are separated by amorphous domains (*loose lines*) [20]. The chains adopt an edge-on orientation with the alkyl chains pointing normal to the substrate, which allows probing of the charge transport anisotropy in the *b*-*c*-plane. (**b**) Spherulite boundary where ordered domains meet. (Reprinted with permission from Crossland et al. [20]. Copyright (2012) Wiley-VCH)

of polyimide films applied as alignment layers in liquid crystal displays. Brinkmann and coworkers performed a detailed study on the orientation mechanism of P3HT by mechanical rubbing using a combination of TEM and polarized absorption spectroscopy [100]. In rubbed P3HT layers, the polymer backbone orients along the rubbing direction and the chains undergo a transition from edge-on to face-on, which was evidenced by electron diffraction (see Fig. 24a). After solution-casting, the ED pattern consists of a broad ring, which is assigned to the (020) reflection of the π-stacking (0.38 nm), indicating a preferential edge-on texture within isotropically oriented, crystalline domains. Rubbing (one or two cycles) of P3HT results in the appearance of arced (*h*00) reflections on the equator caused by the preferred in-plane orientation of the polymer backbone parallel to the rubbing direction. After four rubbing cycles, the (020) reflection is almost completely absent, while strongly arced (*h*00) reflections with $h = 1, 2, 3$ define the ED pattern. This observation demonstrates two points: (1) the degree of in-plane alignment of the polymer backbone parallel to the rubbing increases with increasing number of rubbing cycles and (2) rubbing causes the chains to undergo a transition from edge-on to face-on. Polarized absorption further confirms the optical anisotropy of rubbed layers of P3HT, estimated by the dichroic ratio at 550 nm (Fig. 24b). The degree of in-plane alignment is highly dependent on the molecular weight of the used sample, with the maximum alignment achieved for low molecular weights (Fig. 24c). This result is attributed to the presence of entanglements and chain folds for high molecular weight P3HT that impede chain reorientation and alignment of the pre-aggregated π-stacks. The effect of high temperature rubbing is currently being explored by Brinkmann and coworkers. The evolution of structural anisotropy as a function of molecular weight is reflected in a significant charge transport anisotropy in the *a*-*c*-plane, which is greatly increased for short chains of $M_w < 10$ kg/mol. Thereby, charge transport along the polymer chains is more than one order of magnitude higher than along the insulating side chains. This

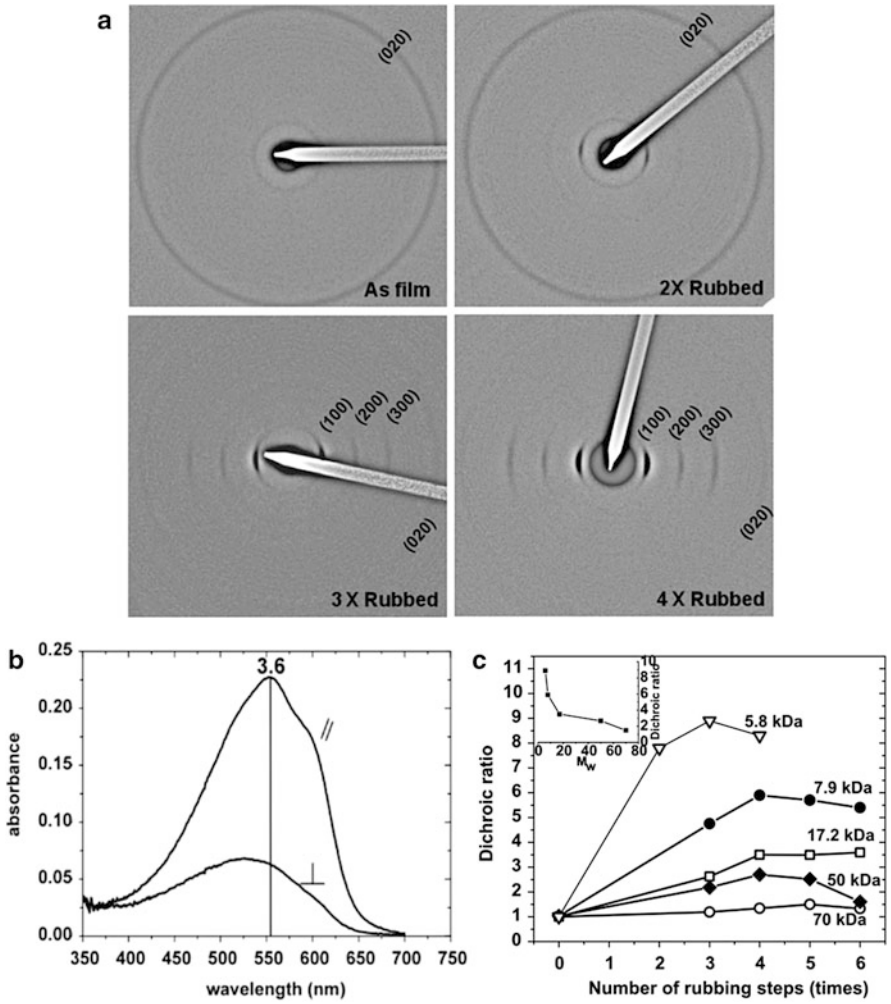

Fig. 24 (**a**) ED pattern of as-cast and rubbed layers of P3HT ($M_w = 17.2$ kg/mol) with increasing number of rubbing cycles [100]. For all patterns, the rubbing direction is oriented in the vertical direction. Each rubbing step is defined by a rubbing length of $l = 50$ cm. (**b**) Polarized absorption spectrum of a rubbed layer of P3HT ($M_w = 17.2$ kg/mol). The incident light is polarized parallel (II) and perpendicular ($\perp$) to the rubbing direction. (**c**) Evolution of the dichroic ratio measured at 550 nm as function of number of rubbing steps for different molecular weights ranging from 5.8 to 70 kg/mol. The *inset* displays the highest dichroic ratio measured for rubbed layers of P3HT of different molecular weight. (Reprinted with permission from Hartmann et al. [100]. Copyright (2011) Wiley-VCH)

observation is in agreement with results obtained by Heil et al., who focused on transistor measurements in rubbed layers of P3HT [114].

4.2.2 Order in Patterned Thin Films

Besides chain orientation, the shape of micro- and nanostructures plays a crucial role in device performance. For instance, bulk-heterojunction organic solar cells require phase separation of the donor and acceptor on the nanometer length scale in order to allow for efficient exciton separation into free charges. Within these phase-separated functional layers, charge transport to the respective electrodes is highly affected by both crystallinity and chain orientation. For applications, it is therefore essential to gain control of both the shape of nanostructures and the chain orientation within the nanostructures. Patterning of polymer layers in micro- or nanometer-sized structures is mainly achieved by lithographic methods, particularly nanoimprint lithography (NIL). In the standard NIL process, a rigid mold with nanostructured features is pressed into the polymer film at high pressure and enhanced temperature (above the glass transition temperature of the polymer). The mold is removed after cooling of the film below the T_g. The mechanism of chain orientation within confined geometries is complex and, according to Hu and Jonas, different factors must be considered [115]: reduced nucleation probability within cavities, graphoepitaxial alignment, rheological orientation, confinement, and pressure during the patterning process. It is not yet fully understood how each parameter affects a specific material.

NIL-induced orientation was first found for polyvinylidene fluoride (PVDF) and the liquid crystalline polymer poly(9,9-dioctylfluorene-*co*-benzothiadiazole) (F8BT) [116–118]. Structural anisotropy was also reported for P3HT after patterning by NIL. For instance, Cui et al. described strong optical birefringence for gratings of P3HT (700 nm periodicity) produced by NIL, most probably the result of stretching of chains in amorphous domains and reorientation of microcrystals [119]. A detailed investigation of the molecular orientation in nanostructures via GIXRD was given by Hu and coworkers and Ocko and coworkers [97, 120]. Hu and coworkers found that the molecular orientation is highly sensitive to the geometry of the nanostructures achieved via NIL. For both nanopillars and nanogratings, a vertical alignment of the backbone is found because the polymer chains orient along the flow during the imprinting process (see Fig. 25) [97]. In P3HT nanogratings, the π-stacking direction points along the grating axis. The orientation mechanism is explained by a combination of flow-induced chain alignment, attractive π–π interactions between neighboring chains, and hydrophobic interactions between the alkyl chains and the SAM-treated mold surface. By contrast, Ocko and coworkers reported a face-on orientation of chains in nanogrooves produced by NIL, while the polymer backbone preferentially aligns along the groove axis [120]. The variance of these results illustrates the importance of the mold geometry comprising the width and height of the nanostructures as well as the thickness of the residual layer, all parameters having a significant impact on the flow of material

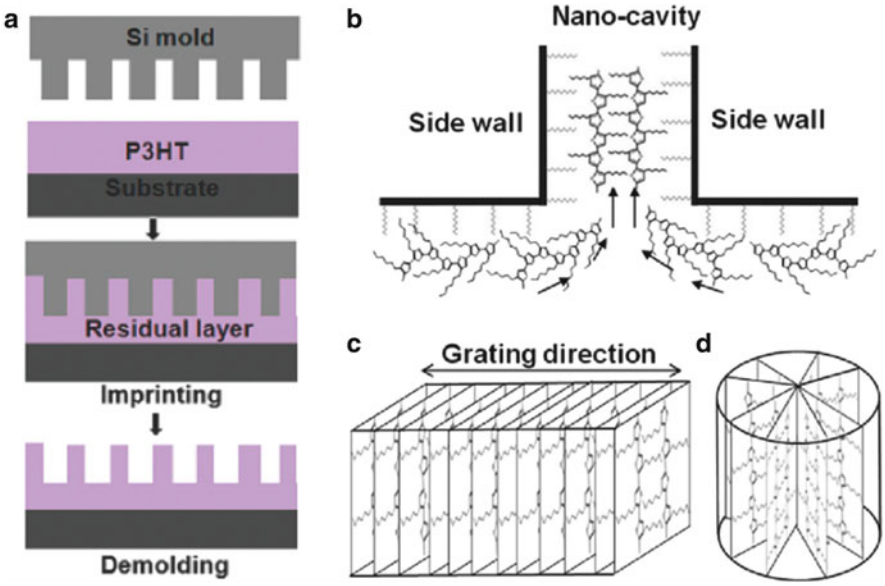

Fig. 25 Vertical chain alignment of P3HT within nanostructures produced by nanoimprint lithography (NIL) [97]: (**a**) the nanoimprinting process; (**b**) the chain alignment process induced by NIL, caused by both the material flow and interactions between the alkyl chains of the polymer chain and the hydrophobic surface of the mold cavities; and (**c**, **d**) ideal chain orientation within molds of different geometry, namely nanogratings (**c**) and nanopillars (**d**). (Reprinted with permission from Aryal et al. [97]. Copyright (2009) American Chemical Society)

during the imprinting process. On the basis of these results, Hu and coworkers proposed a more vertical orientation of chains in the case of high nanostructures with high aspect ratio, whereas the tendency of lying chains (face-on or edge-on) is stronger in flat nanostructures with a relatively thick residual layer [121]. This explanation is in agreement with results by McGehee and coworkers, who observed a clear correlation of structure size and molecular orientation in P3HT pillars of different diameter that were produced by filling anodic alumina films of different pore size with P3HT [122].

A development in NIL is the use of solvent vapor instead of temperature to assist lithography [123–125]. In solvent vapor, the viscosity of the polymer layer is significantly decreased, allowing the patterning of thermosensitive polymers at reduced pressures and temperatures. Line patterns of P3HT achieved by solvent vapor-assisted imprint lithography showed strong birefringence when crystallized under low nucleation density conditions in a well-defined solvent vapor atmosphere, as can be seen in Fig. 26a, b. The AFM image of a single P3HT line of around 500 nm in width (Fig. 26c) reveals a lamellar morphology that is indicative of a predominant edge-on texture, while the lamellae preferentially align parallel to the channel axis.

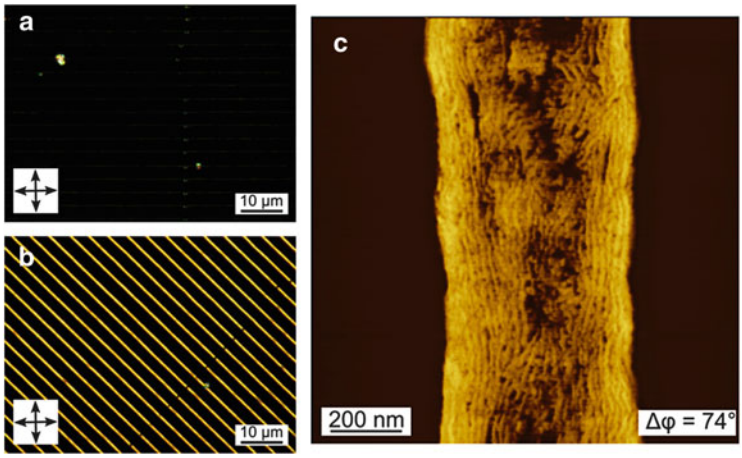

Fig. 26 Oriented films of P3HT prepared by solvent vapor-assisted nanoimprint lithography in a defined CS_2 atmosphere under low nucleation density conditions. (**a**, **b**) POM images of a P3HT line pattern with a periodicity of 3 µm showing strong optical birefringence in 0° (**a**) and 45° (**b**) orientation with respect to the crossed polarizers. (**c**) AFM phase image of a single P3HT line, showing confinement-induced orientation of the nanocrystalline lamellae along the channel axis

Nanostructured P3HT films with uniform molecular orientation show great potential for device application. Hu and coworkers reported the manufacture of OFETs and solar cells on the basis of P3HT nanogratings and observed enhanced device performance as a result of 3D chain alignment in the nanogratings [126]. For π-stacking along the grating and a vertical chain orientation [97], in-plane charge transport in OFETs is greatly enhanced along the grating direction and hence along the π-stacking (*b*-axis). Charge carrier mobilities of more than two orders of magnitude lower are found in the perpendicular direction (i.e., side chain direction, *a*-axis), demonstrating a significant charge transport anisotropy in the *a*-*b*-plane. Improved power conversion efficiencies for solar cells based on PCBM and P3HT nanogratings were found compared with bilayer and blend devices of the same material, which further depicts the increased order and interfacial area in the highly ordered P3HT nanostructures. Promising results have also been achieved for patterned solar cells prepared by solvent vapor-assisted imprint lithography [127–129].

Despite the power of NIL, there are further methods for obtaining highly ordered micro- or nanostructures. For example, we made use of a combination of template-directed dewetting and solvent vapor annealing to produce micrometer-sized P3HT structures of high order (Fig. 27) [130]. At first, solvent vapor-induced dewetting from topographically and chemically patterned transistor substrates allowed confining a fluid P3HT film into the micrometer-sized channels of a transistor. Recrystallization in confinement in controlled solvent vapor atmosphere permits low nucleation densities, leading to the oriented growth of the crystalline lamellae along the confining channel walls (see case A in Fig. 27). In this molecular

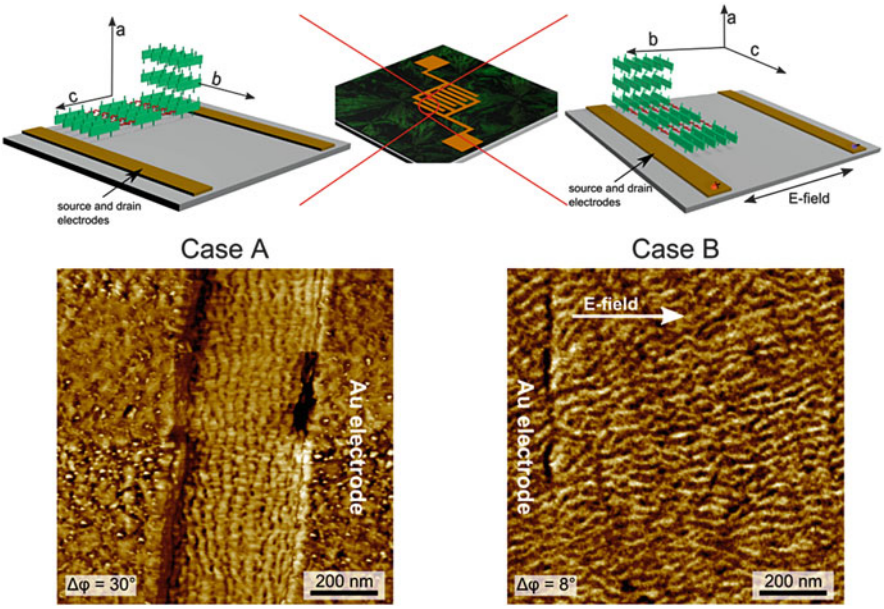

Fig. 27 Controlled dewetting process leading to highly ordered lamellae in edge-on orientation within the channels of a transistor [130]. Thereby, two different orientations of the lamellae with respect to the electrodes are obtained. P3HT films spin-coated on SAM-treated transistor substrates serve as initial state for the experiment. Solvent vapor annealing allows dewetting and subsequent recrystallization in confined structures. *Case A* and *B* demonstrate the molecular orientation within the channels for crystallization without and with applying an electric field between the source and drain electrodes, respectively. The corresponding AFM phase images shown below the sketches illustrate the in-plane alignment of the lamellae. (Reprinted with permission from Fischer et al. [130]. Copyright (2012) Royal Society of Chemistry)

orientation, charge transport between the confining electrodes is measured in the chain direction. In contrast, by applying an AC electric field between the confining electrodes during recrystallization, the crystalline lamellae are forced to align along the electric field lines. Here, charge transport measurements probe the mobility along the π-stacking direction (see case B in Fig. 27). Transistor measurements of these two different orientations illustrated in Fig. 27 revealed anisotropic charge transport in the *b*-*c*-plane only for high molecular weight P3HT ($M_w = 58.8$ kg/mol) with broad distribution (PDI = 1.9), with higher mobilities perpendicular to the lamellae axis and hence in the chain direction. In the case of lower molecular weights and PDIs ($M_w = 30.0$ kg/mol, PDI = 1.2), no charge transport anisotropy was detected. We assume that the existence of tie-molecules is less likely and, therefore, charge transport across interlamellar, amorphous domains is impeded by the necessity of intermolecular charge transfer.

5 Conclusions

It is well established that the molecular packing and mesoscale morphology of P3HT thin films play crucial roles in charge transport and device performance. However, due to the complex microstructure of P3HT, comprising a network of crystalline and amorphous domains, systematic investigation of the electrical bottlenecks remains challenging. Besides the molecular orientation, the mesoscale morphology is essential for charge transport, which is a complex multiscale process. Hence, different length scales must be considered. On a molecular scale, the charge carrier mobility is affected by intramolecular and intermolecular charge transport. The former is highly sensitive to the conformation of the chain and, hence, to potential defects along the backbone that reduce the conjugation length. The latter is defined by the strength of π–π interactions between adjacent chains. On a macroscopic scale, the charge transport is determined by the interconnectivity of the crystalline domains that are embedded in amorphous material. The introduction of order and orientation in P3HT thin films over large surface areas allows a better understanding of charge transport along different crystallographic directions and, hence, charge transport bottlenecks can be identified.

To summarize, the control and understanding of morphology from the molecular to the macroscopic scale is crucial for optical and electrical properties and therefore also for device applications. P3HT, which has been the working horse of the polymer electronic community for many years, can be regarded as a model semicrystalline polymer for more complicated, but also more efficient, polymers based on other repeating units, e.g., donor–acceptor polymers.

Acknowledgements Financial support is acknowledged from the DFG within IRTG-1642, SPP1355 and the Emmy Noether Programme. We thank F. Fischer, Dr. A. Ruff and M. Goll from our group for support with Figures 2, 13 and 16.

References

1. Sirringhaus H, Brown PJ, Friend RH, Nielsen MM, Bechgaard K, Langeveld-Voss BMW, Spiering AJH, Janssen RAJ, Meijer EW, Herwig P, de Leeuw DM (1999) Nature 401:685–688
2. Sirringhaus H, Kawase T, Friend RH, Shimoda T, Inbasekaran M, Wu W, Woo EP (2000) Science 290:2123–2126
3. Yan H, Chen Z, Zheng Y, Newman C, Quinn JR, Dötz F, Kastler M, Facchetti A (2009) Nature 457:679–686
4. He Z, Zhong C, Su S, Xu M, Wu H, Cao Y (2012) Nat Photon 6:591–595
5. Bao Z, Dodabalapur A, Lovinger AJ (1996) Appl Phys Lett 69:4108–4110
6. Spano FC (2005) J Chem Phys 122:234701
7. Kim Y, Cook S, Tuladhar SM, Choulis SA, Nelson J, Durrant JR, Bradley DDC, Giles M, McCulloch I, Ha C-S, Ree M (2006) Nat Mater 5:197–203
8. Salleo A (2007) Mater Today 10:38–45
9. Muthukumar M (2000) Eur Phys J E 3:199–202

10. Muthukumar M (2007) Shifting paradigms in polymer crystallization. In: Reiter G, Strobl GR (eds) Progress in understanding of polymer crystallization. Springer, Berlin/Heidelberg, p 1–18
11. Phillips PJ (1968) Rep Prog Phys 53:549–604
12. Keller A, Machin MJ (1967) J Macromol Sci B Phys 1:41–91
13. Brady JM, Thomas EL (1989) J Mater Sci 24:3311–3318
14. Till PH (1957) J Polym Sci 24:301–306
15. Young R, Bowden P (1973) J Mater Sci 8:1177–1184
16. Wu Z, Petzold A, Henze T, Thurn-Albrecht T, Lohwasser RH, Sommer M, Thelakkat M (2010) Macromolecules 43:4646–4653
17. Zen A, Pflaum J, Hirschmann S, Zhuang W, Jaiser F, Asawapirom U, Rabe JP, Scherf U, Neher D (2004) Adv Funct Mater 14:757–764
18. Kline RJ, McGehee MD, Kadnikova EN, Liu J, Fréchet JMJ, Toney MF (2005) Macromolecules 38:3312–3319
19. Jimison LH, Toney MF, McCulloch I, Heeney M, Salleo A (2009) Adv Mater 21:1568–1572
20. Crossland EJW, Tremel K, Fischer F, Rahimi K, Reiter G, Steiner U, Ludwigs S (2012) Adv Mater 24:839–844
21. Lin JW-P, Dudek LP (1980) J Polym Sci Polym Chem Ed 18:2869–2873
22. Yamamoto T, Sanechika K, Yamamoto A (2008) J Polym Sci Polym Lett Ed 18:2869–2873
23. McCullough RD, Lowe RD (1992) J Chem Soc Chem Commun 1992(1):70–72
24. Mccullough RD, Lowe RD, Jayaraman M, Anderson DL (1993) J Org Chem 58:904–912
25. Chen T-A, Rieke RD (1992) J Am Chem Soc 114:10087–10088
26. Loewe RS, Khersonsky SM, McCullough RD (1999) Adv Mater 11:250–253
27. Senkovskyy V, Khanduyeva N, Komber H, Oertel U, Stamm M, Kuckling D, Kiriy A (2007) J Am Chem Soc 129:6626–6632
28. Bronstein HA, Luscombe CK (2009) J Am Chem Soc 131:12894–12895
29. Sista P, Luscombe CK (2014) Progress in the synthesis of poly(3-hexylthiophene). (2014) Adv Polym Sci. doi:10.1007/12_2014_278
30. Trznadel M, Pron A, Zagorska M, Chrzaszcz R, Pielichowski J (1998) Macromolecules 31:5051–5058
31. Gritzner G, Kuta J (1984) Electrochim Acta 29:869–873
32. Skompska M, Szkurłat A (2001) Electrochim Acta 46:4007–4015
33. Heinze J, Frontana-Uribe BA, Ludwigs S (2010) Chem Rev 110:4724–4771
34. Cardona CM, Li W, Kaifer AE, Stockdale D, Bazan GC (2011) Adv Mater 23:2367–2371
35. Pommerehne J, Vestweber H, Guss W, Mahrt RF, Bässler H, Porsch M, Daub J (1995) Adv Mater 7:551–554
36. Scharber MC, Mühlbacher D, Koppe M, Denk P, Waldauf C, Heeger AJ, Brabec CJ (2006) Adv Mater 18:789–794
37. Guan Z-L, Kim JB, Wang H, Jaye C, Fischer DA, Loo Y-L, Kahn A (2010) Org Electron 11:1779–1785
38. Heffner GW, Pearson DS (1991) Macromolecules 24:6295–6299
39. Adachi T, Brazard J, Ono RJ, Hanson B, Traub MC, Wu Z-Q, Li Z, Bolinger JC, Ganesan V, Bielawski CW, Vanden Bout DA, Barbara PF (2011) J Phys Chem Lett 2:1400–1404
40. Chen T, Wu X, Rieke RD (1995) J Am Chem Soc 117:233–244
41. Mao H, Xu B, Holdcroft S (1993) Macromolecules 26:1163–1169
42. Xu B, Holdcroft S (1993) Macromolecules 26:4457–4460
43. Kim DH, Han JT, Park YD, Jang Y, Cho JH, Hwang M, Cho K (2006) Adv Mater 18:719–723
44. Rahimi K, Botiz I, Stingelin N, Kayunkid N, Sommer M, Koch FPV, Nguyen H, Coulembier O, Dubois P, Brinkmann M, Reiter G (2012) Angew Chem Int Ed 51:11131–11135
45. Brinkmann M, Hartmann L, Kayunkid N, Djurado D (2014) Understanding the structure and crystallization of regioregular poly(3-hexylthiophene) from the perspective of epitaxy. Adv Polym Sci. doi:10.1007/12_2014_280

46. Lim JA, Liu F, Ferdous S, Muthukumar M, Briseno AL (2010) Mater Today 13:14–24
47. Ihn KJ, Moulton J, Smith P (1993) J Polym Sci B Polym Phys 31:735–742
48. Samitsu S, Shimomura T, Heike S, Hashizume T, Ito K (2008) Macromolecules 41:8000–8010
49. Liu J, Arif M, Zou J, Khondaker SI, Zhai L (2009) Macromolecules 42:9390–9393
50. Berson S, De Bettignies R, Bailly S, Guillerez S (2007) Adv Funct Mater 17:1377–1384
51. Koppe M, Brabec CJ, Heiml S, Schausberger A, Duffy W, Heeney M, McCulloch I (2009) Macromolecules 42:4661–4666
52. Sun S, Salim T, Wong LH, Foo YL, Boey F, Lam YM (2011) J Mater Chem 21:377–386
53. Oosterbaan WD, Bolsée J-C, Gadisa A, Vrindts V, Bertho S, D'Haen J, Cleij TJ, Lutsen L, McNeill CR, Thomsen L, Manca JV, Vanderzande D (2010) Adv Funct Mater 20:792–802
54. Kiriy N, Jähne E, Adler H-J, Schneider M, Kiriy A, Gorodyska G, Minko S, Jehnichen D, Simon P, Fokin AA, Stamm M (2003) Nano Lett 3:707–712
55. Li L, Lu G, Yang X (2008) J Mater Chem 18:1984–1990
56. Park YD, Lee HS, Choi YJ, Kwak D, Cho JH, Lee S, Cho K (2009) Adv Funct Mater 19:1200–1206
57. Kim B, Kim M, Kim J (2010) ASC Nano 4:2160–2166
58. Malik S, Jana T, Nandi AK (2001) Macromolecules 34:275–282
59. Malik S, Nandi AK (2007) J Appl Polym Sci 103:2528–2537
60. Merlo JA, Frisbie CD (2003) J Polym Sci B Polym Phys 41:2674–2680
61. Merlo JA, Frisbie CD (2004) J Phys Chem B 108:19169–19179
62. Mas-Torrent M, Den Boer D, Durkut M, Hadley P, Schenning APHJ (2004) Nanotechnology 15:S265–S269
63. Samitsu S, Shimomura T, Heike S, Hashizume T, Ito K (2010) Macromolecules 43:7891–7894
64. Xin H, Kim FS, Jenekhe SA (2008) J Am Chem Soc 130:5424–5425
65. Xin H, Ren G, Kim FS, Jenekhe SA (2008) Chem Mater 20:6199–6207
66. Kim JS, Lee JH, Park JH, Shim C, Sim M, Cho K (2011) Adv Funct Mater 21:480–486
67. Yang H, Shin TJ, Yang L, Cho K, Ryu CY, Bao Z (2005) Adv Funct Mater 15:671–676
68. Yang H, LeFevre SW, Ryu CY, Bao Z (2007) Appl Phys Lett 90:172116
69. Chang J-F, Sun B, Breiby DW, Nielsen MM, Sölling TI, Giles M, McCulloch I, Sirringhaus H (2004) Chem Mater 16:4772–4776
70. Wang G, Swensen J, Moses D, Heeger AJ (2003) J Appl Phys 93:6137
71. Delongchamp DM, Vogel BM, Jung Y, Gurau MC, Richter CA, Kirillov OA, Obrzut J, Fischer DA, Sambasivan S, Richter LJ, Lin EK (2005) Chem Mater 17:5610–5612
72. Kline RJ, McGehee MD, Toney MF (2006) Nat Mater 5:222–228
73. Kline RJ, McGehee MD, Kadnikova EN, Liu J, Fréchet JMJ (2003) Adv Mater 15:1519–1522
74. Zen A, Saphiannikova M, Neher D, Grenzer J, Grigorian S, Pietsch U, Asawapirom U, Janietz S, Scherf U, Lieberwirth I, Wegner G (2006) Macromolecules 39:2162–2171
75. Verilhac J-M, LeBlevennec G, Djurado D, Rieutord F, Chouiki M, Travers J-P, Pron A (2006) Synth Met 156:815–823
76. Brown P, Thomas D, Köhler A, Wilson J, Kim J-S, Ramsdale C, Sirringhaus H, Friend R (2003) Phys Rev B 67:064203
77. Clark J, Silva C, Friend R, Spano F (2007) Phys Rev Lett 98:206406
78. Clark J, Chang J-F, Spano FC, Friend RH, Silva C (2009) Appl Phys Lett 94:163306
79. Zhang R, Li B, Iovu MC, Jeffries-El M, Sauvé G, Cooper J, Jia S, Tristram-Nagle S, Smilgies DM, Lambeth DN, McCullough RD, Kowalewski T (2006) J Am Chem Soc 128:3480–3481
80. Yang H, Shin TJ, Bao Z, Ryu CY (2007) J Polym Sci B Polym Phys 45:1303–1312
81. Pascui OF, Lohwasser R, Sommer M, Thelakkat M, Thurn-Albrecht T, Saalwächter K (2010) Macromolecules 43:9401–9410
82. Mena-Osteritz E (2002) Adv Mater 14:609–616
83. Grévin B, Rannou P, Payerne R, Pron A, Travers J-P (2003) Adv Mater 15:881–884

84. Noriega R, Rivnay J, Vandewal K, Koch FPV, Stingelin N, Smith P, Toney MF, Salleo A (2013) Nat Mater 12:1038–1044
85. Kim DH, Park YD, Jang Y, Kim S, Cho K (2005) Macromol Rapid Commun 26:834–839
86. Dang MT, Hirsch L, Wantz G, Wuest JD (2013) Chem Rev 113:3734–3765
87. Zaumseil J (2014) P3HT and other polythiophene field-effect transistors. Adv Polym Sci. doi:10.1007/12_2014_279
88. Prosa TJ, Winokur MJ, Mccullough RD (1996) Macromolecules 29:3654–3656
89. Prosa TJ, Winokur MJ, Moulton J, Smith P, Heeger AJ (1992) Macromolecules 25:4364–4372
90. Tashiro K, Kobayashi M, Kawai T, Yoshino K (1997) Polymer 38:2867–2879
91. Brinkmann M, Rannou P (2007) Adv Funct Mater 17:101–108
92. Dudenko D, Kiersnowski A, Shu J, Pisula W, Sebastiani D, Spiess HW, Hansen MR (2012) Angew Chem 51:11068–11072
93. Brinkmann M (2011) J Polym Sci B Polym Phys 49:1218–1233
94. Malik S, Nandi AK (2002) J Polym Sci B Polym Phys 40:2073–2085
95. Snyder CR, Henry JS, DeLongchamp DM (2011) Macromolecules 44:7088–7091
96. Lee CS, Dadmun MD (2014) Polymer 55:4–7
97. Aryal M, Trivedi K, Hu WW (2009) ACS Nano 3:3085–3090
98. Liu J, Sun Y, Gao X, Xing R, Zheng L, Wu S, Geng Y, Han Y (2011) Langmuir 27:4212–4219
99. Nagamatsu S, Takashima W, Kaneto K, Yoshida Y, Tanigaki N, Yase K, Omote K (2003) Macromolecules 36:5252–5257
100. Hartmann L, Tremel K, Uttiya S, Crossland E, Ludwigs S, Kayunkid N, Vergnat C, Brinkmann M (2011) Adv Funct Mater 21:4047–4057
101. Meyerhofer D (1978) J Appl Phys 49:3993
102. Aasmundtveit KE, Samuelsen EJ, Guldstein M, Steinsland C, Flornes O, Fagermo C, Seeberg TM, Pettersson LAA, Inganas O, Feidenhans'l R, Ferrer S (2000) Macromolecules 33:3120–3127
103. Joshi S, Grigorian S, Pietsch U, Pingel P, Zen A, Neher D, Scherf U (2008) Macromolecules 41:6800–6808
104. Kim DH, Park YD, Jang Y, Yang H, Kim YH, Han JI, Moon DG, Park S, Chang T, Chang C, Joo M, Ryu CY, Cho K (2005) Adv Funct Mater 15:77–82
105. Kim DH, Jang Y, Park YD, Cho K (2005) Langmuir 21:3203–3206
106. Joshi S, Pingel P, Grigorian S, Panzner T, Pietsch U, Neher D, Forster M, Scherf U (2009) Macromolecules 42:4651–4660
107. Brinkmann M, Wittmann J-C (2006) Adv Mater 18:860–863
108. De Rosa C, Park C, Thomas EL, Lotz B (2000) Nature 2145:433–437
109. Crossland EJW, Rahimi K, Reiter G, Steiner U, Ludwigs S (2011) Adv Funct Mater 21:518–524
110. Lu GH, Li LG, Yang XN (2007) Adv Mater 19:3594–3598
111. Lu G, Li L, Yang X (2008) Macromolecules 41:2062–2070
112. Street R, Northrup J, Salleo A (2005) Phys Rev B 71:165202
113. Wittmann JC, Smith P (1991) Nature 352:414–417
114. Heil H, Finnberg T, von Malm N, Schmechel R, von Seggern H (2003) J Appl Phys 93:1636
115. Hu Z, Jonas AM (2010) Soft Matter 6:21–28
116. Zheng Z, Yim K-H, Saifullah MSM, Welland ME, Friend RH, Kim J-S, Huck WTS (2007) Nano Lett 7:987–992
117. Hu Z, Baralia G, Bayot V, Gohy J-F, Jonas AM (2005) Nano Lett 5:1738–1743
118. Schmid S, Yim K, Chang M, Zheng Z, Huck W, Friend R, Kim J, Herz L (2008) Phys Rev B 77:115338
119. Cui D, Li H, Park H, Cheng X (2008) J Vac Sci Technol B Microelectron Nanometer Struct 26:2404

120. Hlaing H, Lu X, Hofmann T, Yager KG, Black CT, Ocko BM (2011) ACS Nano 5:7532–7538
121. Yang Y, Mielczarek K, Aryal M, Zakhidov A, Hu W (2012) ACS Nano 6:2877–2892
122. Coakley KM, Srinivasan BS, Ziebarth JM, Goh C, Liu Y, McGehee MD (2005) Adv Funct Mater 15:1927–1932
123. Voicu NE, Ludwigs S, Crossland EJW, Andrew P, Steiner U (2007) Adv Mater 19:757–761
124. Khang D-Y, Lee HH (2000) Appl Phys Lett 76:870
125. Lai KL, Hon MH, Leu IC (2011) J Micromech Microeng 21:075013
126. Zhou M, Aryal M, Mielczarek K, Zakhidov A, Hu W (2010) J Vac Sci Technol B Microelectron Nanometer Struct 28:C6M6
127. He X, Gao F, Tu G, Hasko D, Hüttner S, Steiner U, Greenham NC, Friend RH, Huck WTS (2010) Nano Lett 10:1302–1307
128. He X, Gao F, Tu G, Hasko DG, Hüttner S, Greenham NC, Steiner U, Friend RH, Huck WTS (2011) Adv Funct Mater 21:139–146
129. Park JY, Hendricks NR, Carter KR (2011) Langmuir 27:11251–11258
130. Fischer FSU, Tremel K, Sommer M, Crossland EJC, Ludwigs S (2012) Nanoscale 4:2138–2144

Adv Polym Sci (2014) 265: 83–106
DOI: 10.1007/12_2014_280

Published online: 9 July 2014

Understanding the Structure and Crystallization of Regioregular Poly (3-hexylthiophene) from the Perspective of Epitaxy

Martin Brinkmann, Lucia Hartmann, Navaphun Kayunkid, and David Djurado

Abstract Conjugated polymers form a remarkable class of macromolecules with fascinating electronic properties as well as structural features that make them very different from the more classical and flexible polyolefins. In thin films, the structure and the nanomorphology are two important parameters that control solid state properties such as charge transport. Due to the high anisotropy of electronic properties in conjugated polymers, it is essential to control both crystallization and domain orientation over large length scales. This review demonstrates that epitaxial growth is an original method for bringing macromolecules like regioregular poly(3-hexylthiophene) (P3HT) to a high level of order. Various orientation methods based on epitaxy are presented and the peculiar morphological and structural aspects of oriented P3HT, as analyzed by transmission electron microscopy (TEM), are described. The use of TEM on epitaxied layers is shown to shed some new light on the intriguing crystallization, structure, and growth of this key polymer for organic electronic applications.

M. Brinkmann (✉) and N. Kayunkid
Institut Charles Sadron, CNRS-Université de Strasbourg, 23 rue du loess, 67034 Strasbourg, France
e-mail: martin.brinkmann@ics-cnrs.unistra.fr

L. Hartmann
Institut Charles Sadron, CNRS-Université de Strasbourg, 23 rue du loess, 67034 Strasbourg, France

UMR SPrAM 5819 (CEA-CNRS-UJF) and SP2M, CEA Grenoble/INAC, 38054 Grenoble Cedex, France

D. Djurado
UMR SPrAM 5819 (CEA-CNRS-UJF) and SP2M, CEA Grenoble/INAC, 38054 Grenoble Cedex, France

Keywords Crystallization · Epitaxy · Poly(3-hexylthiophene) · Thin films · Transmission Electron Microscopy

Contents

1 Introduction

Plastic electronics has undergone increasing development over the last few decades and now appears as a major and challenging new research field. This is due in part to the ongoing efforts in the synthesis of new semiconducting polymers (SCPs) that show improved opto-electronic properties and are processable using low cost deposition methods (spin-coating, ink-jet printing, etc.) [1–8]. Interest in this field is also related to the increasing control of device manufacture and understanding of structure–property relationships [9–11]. Intrinsically, SCPs exhibit strongly anisotropic optical and electronic properties and, therefore, the control of both the polymer chain direction and the crystal orientation in thin films is essential [12, 13]. For instance, in the case of regioregular poly(3-hexylthiophene), preferential contact planes of crystallites on a substrate influence the charge transport properties and device performance to a large extent [12]. The 'edge-on' and 'face-on' orientations of the polymer backbones on a substrate [14–19] can favor charge transport along different directions to the substrate normal or to the orientation of an applied electric field [20]. From a device manufacture point of view, orientation of SCPs chains can be of high interest to channel charge carriers along one preferential direction and thus reduce parasitic current paths between adjacent OFETs in a dense array of transistors [2, 21–23]. Besides orientation, nanostructuring of conjugated polymers is another essential aspect that influences for instance photovoltaic activity in organic solar cells (OSC) based on a bulk heterojunction [24, 25]. This chapter presents the state-of-the-art concerning the structure and the morphology in highly oriented and/or nanostructured thin films of regioregular poly(3-alkylthiophene)s prepared by epitaxy. The first part of this contribution presents various examples of orientations obtained for polyolefins and P3HT as well as the corresponding structural investigations using TEM and X-ray diffraction methods. The second half of this chapter shows the interest of

epitaxial growth to address crystallization issues for P3HT. In particular, it presents recent results relative to (1) the structure determination of P3HT by electron diffraction analysis and (2) the impact of molecular weight (M_w) on the semicrystalline nanomorphology and structure of epitaxied P3HT thin films.

2 Epitaxy: Principle and Methods

2.1 Epitaxy of Semicrystalline Polymers: The Case of Polyolefins

Epitaxy can be defined as the directed growth of a crystalline or semicrystalline material on the surface of a crystalline substrate. As opposed to inorganic epitaxy, which implies covalent bonding between the overlayer and the substrate, the epitaxy of organic materials and polymers is governed by a subtle balance of weak noncovalent interactions that is often difficult to predict [26, 27]. As a general rule, the mutual orientation of the overlayer and the substrate can be described by a 2×2 matrix relating the two-dimensional (2D) lattices of both overlayer and substrate [26, 27]. One-dimensional (1D) epitaxy mechanisms, which imply lattice matching along a unique preferred direction of the substrate lattice, are also often encountered in the case of polymers, e.g., for polyethylene lamellae grown epitaxially on single-wall carbon nanotubes [28–30].

Polymer epitaxy on inorganic substrates was first reported in 1950 by Willems and by Fischer [31, 32] for polyolefins. Wittmann and colleagues performed systematic studies of polymer epitaxy in the early 1980s [33–35] using transmission electron microscopy (TEM). Epitaxy was recognized as a major driving force that could explain the efficiency of certain, albeit not all, aromatic crystals used as nucleating agents for polyolefins [33–35]. Moreover, TEM proved to be a unique tool for observing the characteristic structural and morphological features in epitaxied polymer films and uncovering the underlying crystallization and epitaxial growth mechanisms. The versatility of TEM lies in the possibility of operating the microscope in different and highly complementary modes, e.g., conventional bright field, electron diffraction, dark field, and high resolution (HR-TEM). Accordingly, complementary informations in real and reciprocal spaces can be combined for a precise understanding of structural issues at multiple length scales (molecular → mesoscopic), e.g., polymorphism, preferred orientation, and contact planes of polymer crystals and the dimensions of crystalline and amorphous domains. However, SCPs like most semicrystalline polymers are extremely beam sensitive, which implies that one must work with low electron doses so as to preserve the native structure of the polymer as much as possible, especially in HR-TEM [36, 37].

An instructive example of polyolefin epitaxy concerns the growth of polyethylene (PE) lamellae on aromatic crystals of *p*-terphenyl and anthracene. On these two

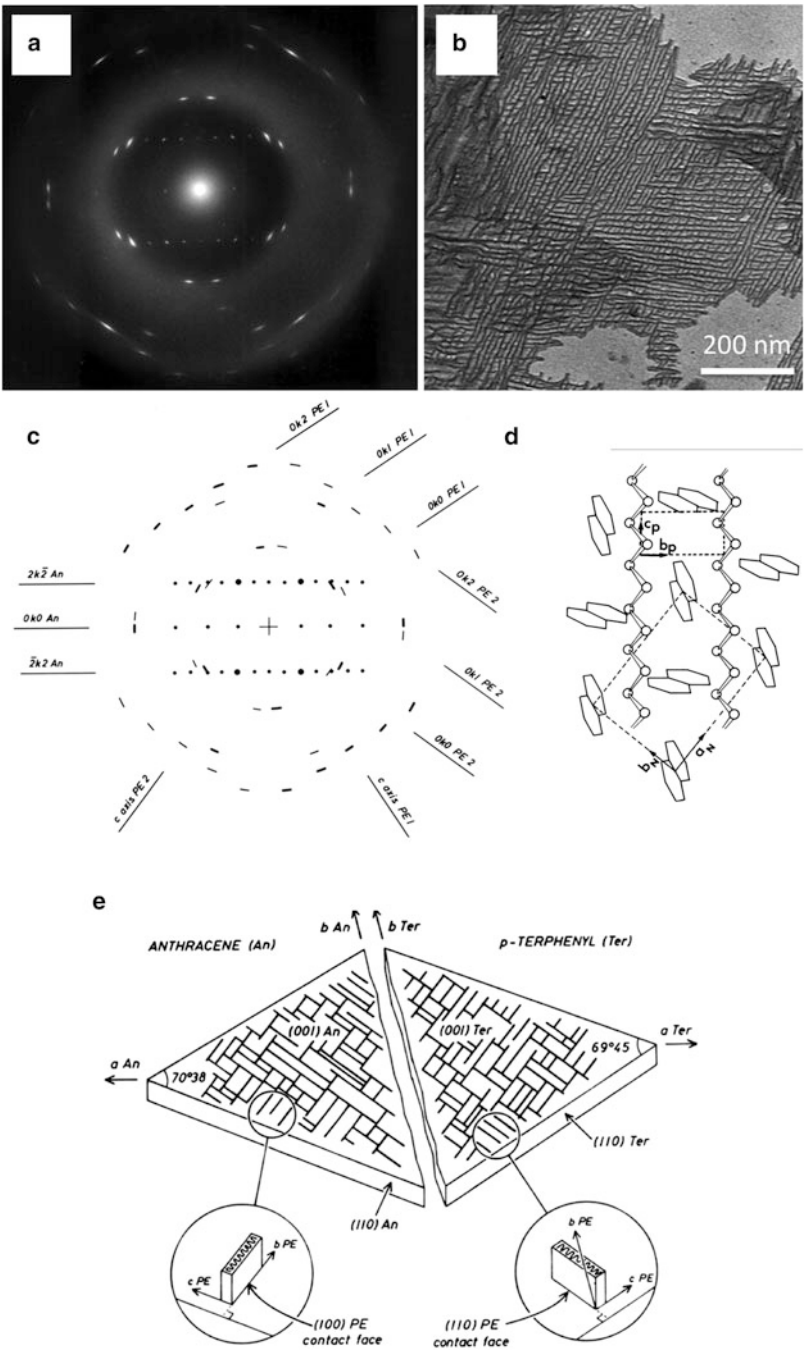

Fig. 1 (**a**) Electron diffraction pattern and (**b**) bright field showing a cross-hatched pattern of oriented crystalline lamellae of PE epitaxied on anthracene. (**c**) Schematic interpretation of the experimental ED pattern. (**d**) Orientation of PE chains on the surface of an anthracene crystal.

substrates, characteristic 2D matching between the PE and the substrate lattices was demonstrated. From a morphological point of view, epitaxial growth results in characteristic crosshatched patterns made of crystalline lamellae growing along specific in-plane directions. Figure 1a, b depicts the textured film morphologies and the electron diffraction pattern for epitaxied PE films grown on anthracene single crystal substrates. Figure 1c, d shows a schematic interpretation of the electron diffraction (ED) pattern and the orientation of PE chains on the anthracene crystal. The overall orientation of crystalline lamellae of PE in thin films epitaxied on anthracene and *p*-terphenyl is shown in Fig. 1e. For both substrates, 2D lattice matching between PE domains and the substrate was observed. This epitaxial condition explains the coexistence of two in-plane growth directions of crystalline PE lamellae on the $(0\ 0\ 1)_{An}$ surface of anthracene and the $(0\ 0\ 1)_{Ter}$ surface of *p*-terphenyl. Different substrate unit cell parameters lead to different contact planes of PE lamellae on *p*-terphenyl and anthracene, demonstrating that fine tuning of the contact plane of PE lamellae in a thin film can indeed be obtained by choosing the proper substrate for epitaxy.

2.2 *Epitaxy of Semiconducting Polymers on Aromatic Crystal Surfaces*

As seen in the case of PE, aromatic molecules (e.g., acenes) can be easily grown in the form of large single crystals and used as substrates for the epitaxial growth of lamellar polymer crystals. However, in contrast to most polyolefins, SCPs usually exhibit very high melting temperatures (240°C for P3HT), which restricts the choice of aromatic substrates. Single crystals of aromatic salts such as potassium-4-bromobenzoate (K-BrBz) or potassium acid phthalate (KAP) are well suited for the epitaxial orientation of P3HT because they can withstand very high annealing temperatures [38–41]. Preparation of the oriented layers involves first the growth of 10–100 μm single crystals from saturated solutions (see Fig. 2). These crystals are brought into contact with the polymer film, either by depositing a solution of single crystals onto the polymer film or by casting a polymer film on top of single crystals. Epitaxial crystallization of the polymer is enforced by isothermal annealing for several hours after a preliminary melting of the polymer film. Finally, the substrate material is removed by rinsing the films with water. Large areas of epitaxied conducting polymer films with a typical morphology that mimics the original shape of the substrate crystals (see Fig. 2b) are thus obtained.

Fig. 1 (continued) (**e**) Orientation of PE crystalline lamellae as observed on substrates of *p*-terphenyl and anthracene. Note the two different $(1\ 1\ 0)_{PE}$ and $(1\ 0\ 0)_{PE}$ contact planes of PE crystals on *p*-terphenyl and anthracene, respectively. (Reprinted with permission from [33] © 1981, J. Wiley and Sons and [35] © 1990, Elsevier)

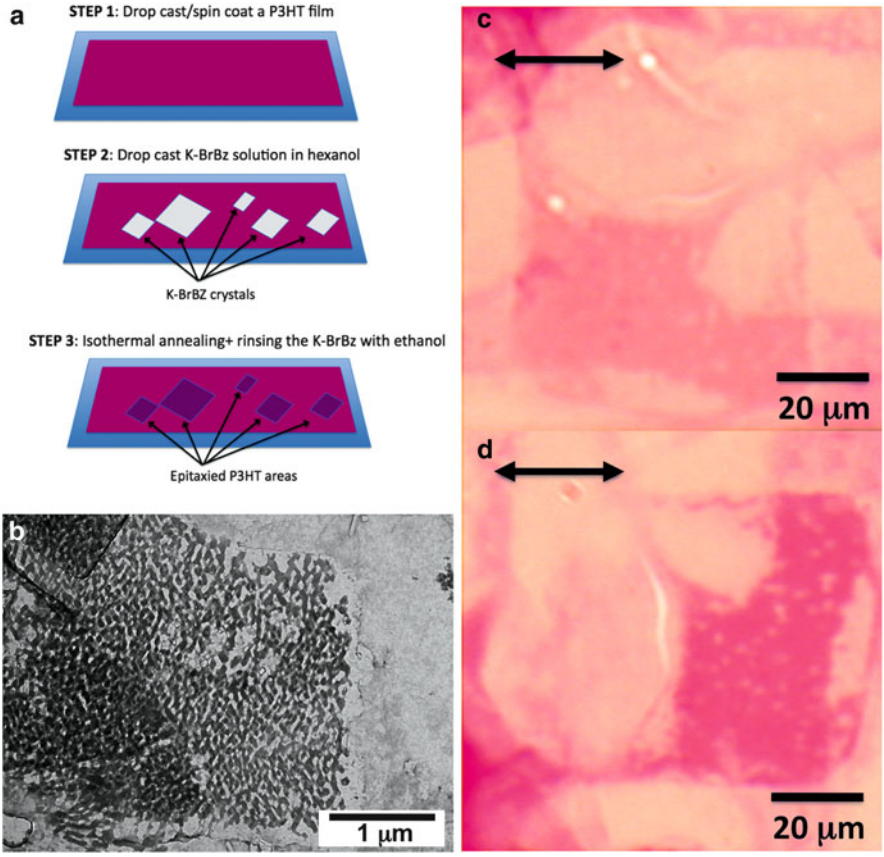

Fig. 2 (**a**) Three main steps of the oriented P3HT film preparation on aromatic salt crystals. (**b**) TEM-BF image showing an oriented and nanostructured P3HT film after removal of the K-BrBz substrate. The shape of the oriented P3HT film reproduces the initial rhombic-shaped K-BrBz crystal. (**c, d**) POM images of an oriented area of P3HT grown epitaxially on K-BrBz ($T = 180°C$). The remaining epitaxied P3HT area has the initial lozenge shape of the K-BrBz crystal. The epitaxied P3HT area shows a variation in the absorbance versus orientation of the incident light polarization (*double arrow*). (Reprinted with permission from [42] © 2010, American Chemical Society)

As illustrated in Fig. 3a, epitaxial growth of P3HT on K-BrBz leads to highly crystalline, oriented and nanotextured P3HT films that consist of a regular network of interconnected semicrystalline domains oriented along two preferential in-plane directions. The overall crystallinity and the level of in-plane orientation of the P3HT films are controlled by the temperature of isothermal crystallization (T_{iso}). Well-defined ED patterns with sharp reflections obtained for $T_{iso} = 180°C$ (see Fig. 3b) indicate that the crystalline domains grow with a unique $(1\,0\,0)_{P3HT}$ contact plane on the K-BrBz substrate ('edge-on' orientation of the conjugated backbone on the substrate). The P3HT chains are oriented along two preferred in-plane

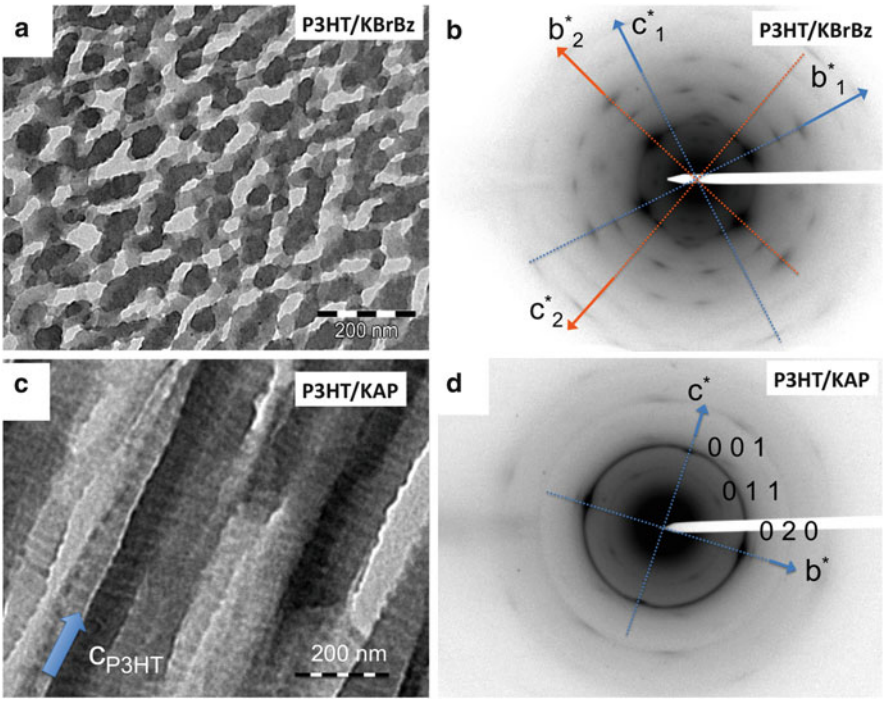

Fig. 3 TEM-BF images showing the oriented nanostructured patterns of P3HT formed on substrates of KBrBz (**a**, **b**) and KAP (**c**, **d**) after removal of the substrate. Note the unidirectional pattern obtained in the case of KAP versus the cross-hatched pattern on KBrBz due to a twofold in-plane orientation of P3HT domains, as indicated by the *blue* and *orange arrows*. (Adapted from [42] © 2010, American Chemical Society)

directions, namely the $[0 \pm 2\ 1]$ directions of K-BrBz. Preferred orientation of P3HT crystalline domains occurs at step edges of the substrate (see Fig. 4b) because of the matching between the layer period of P3HT, a_{P3HT}, and the terrace height of the K-BrBz substrate, $a_{K\text{-}BrBz}$, at the annealing temperature of 180°C ($a_{P3HT} = 1.75$ nm versus $a_{K\text{-}BrBz}/2 = 1.745$ nm) [42].

Accordingly, as illustrated in Fig. 4b, in the absence of a matching between in-plane unit cell parameters of the substrate and P3HT, it is a matching of unit cell parameters along the substrate normal that gives rise to this unique type of epitaxial growth of P3HT on K-BrBz. In addition to K-BrBz, epitaxial orientation of P3HT was also observed for substrates of potassium acid phthalate (KAP). This type of substrate was originally used for the alignment of a series of diactylenes by Thierry and coworkers [41]. As seen in Fig. 3c, d, orientation of P3HT is also achieved on substrates of KAP, leading to a unique (1 0 0) contact plane and a single in-plane orientation of the P3HT chain direction on the substrate. In contrast to K-BrBz, the films grown on KAP do not show a cross-hatched pattern but a periodic alternation of crystalline lamellae separated by amorphous interlamellar zones.

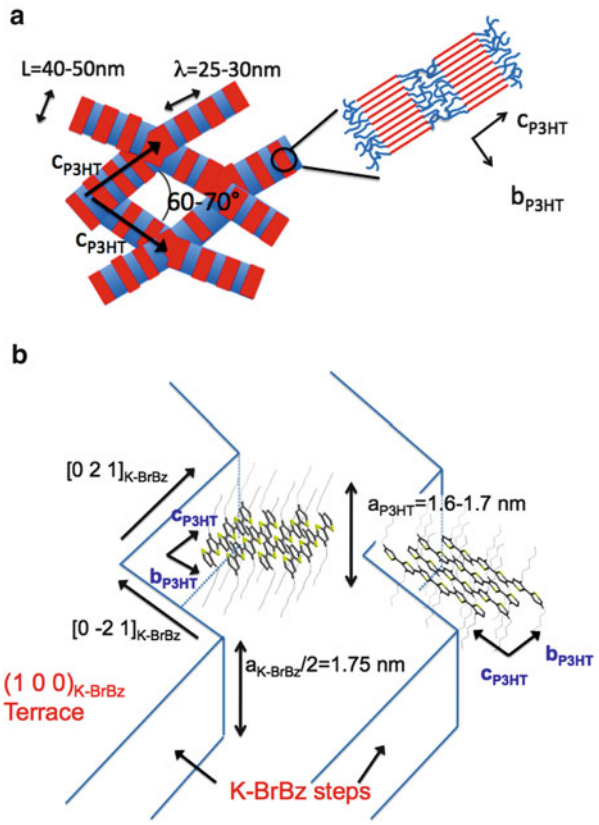

Fig. 4 (**a**) Nanomorphology and orientation of P3HT domains epitaxied on K-BrBz substrate. Crystalline zones are shown in *red* and amorphous interlamellar zones are colored in *blue*. (**b**) Preferential nucleation and orientation of P3HT domains at the step edges of a reconstructed K-BrBz substrate. The P3HT chains run parallel to the $[0\ 2\ 1]_{K\text{-}BrBz}$ or the $[0\ -2\ 1]_{K\text{-}BrBz}$ directions. The height of the π-stacked P3HT chains closely matches the observed step height of the K-BrBz substrate. (Reprinted with permission from [42] © 2010, American Chemical Society)

2.3 *Directional Epitaxial Crystallization*

One of the first examples of efficient epitaxial orientation of P3HT was obtained by directional epitaxial crystallization (DEC) in 1,3,5-trichlorobenzene (TCB) [43–51]. The originality of this orientation method lies in the use of a crystallizable aromatic solvent, in the present case TCB, which can successively play the role of solvent for the polymer and, once crystallized, the role of substrate for epitaxy. After orientation, TCB is readily removed by evaporation in vacuum, leaving large areas of highly oriented P3HT film. For P3HT with $M_w = 17$ kDa, the use of DEC produces oriented films with a high in-plane orientation of the chains. The ED pattern indicates fiber symmetry i.e. only the in-plane direction of the chains is well defined. However, to be able to prepare large-scale oriented domains, it was necessary to improve the original growth method [46]. Figure 5a describes and illustrates the various steps used to prepare P3HT films by the so-called slow-DEC method. In brief, the method achieves long range in-plane orientation of P3HT by using an orienting substrate of PTFE to guide the crystallization of TCB.

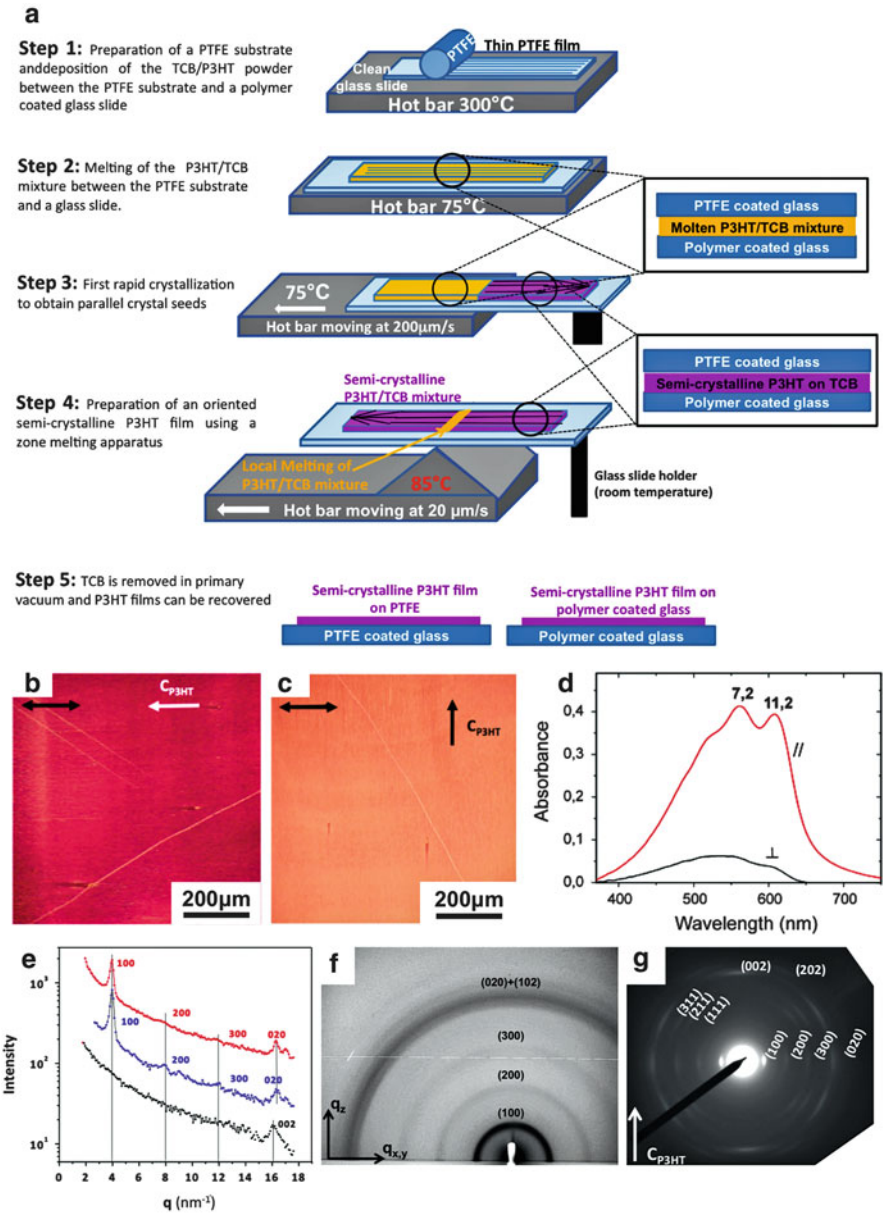

Fig. 5 (**a**) Different steps in the preparation of highly oriented P3HT films using the slow-DEC method. The use of a local zone melting moving at 20 µm/s in *step* 4 allows the growth of P3HT films with a high uniformity of in-plane orientation. (**b, c**) POM images of a P3HT thin film grown by DEC. Orientation of the incident light polarization is indicated by the *double arrows*; orientation of the P3HT chains, $\mathbf{c_{P3HT}}$, is indicated by *arrows*. (**d**) Polarized UV-visible absorption spectra of an epitaxied P3HT film. (**e**) X-ray line scans recorded in Bragg configuration of an epitaxied P3HT film ($M_w = 17.6$ kDa): *upper red curve* out-of-plane configuration; *central blue*

In addition, a zone melting technique is used to precisely control both the growth rate (typically 20 μm/s) and the in-plane orientation of TCB crystals and thus to achieve uniform surfaces of TCB crystals over several square centimeters, making the films suitable for the epitaxial growth of P3HT. The improvement of the overall in-plane orientation of the films leads to both the increase in the observed dichroic ratio in the UV–visible absorption spectra (in excess of 13) and a substantially narrowed angular spread of the in-plane orientation distribution of the P3HT crystals [46]. The improved in-plane orientation of the films grown by slow-DEC was particularly well observed by grazing incidence X-ray diffraction (GIXD), which probes the orientation over a surface of the order of 1 cm^2. Interestingly, by using GIXD, it was possible to distinguish the 0 0 2 from the 0 2 0 reflection (Fig. 5e) by changing the orientation of the incident X-ray beam with respect to the in-plane chain direction. This is usually not possible because in spin-coated P3HT films these two reflections overlap as they correspond to almost identical reticular distances (0.38 nm). The observation of a strong 0 0 2 reflection highlights the high crystallinity and 3D order observed in epitaxied layers.

Regarding the mechanism of orientation of P3HT on TCB, 1D epitaxy was observed for a 17 kDa sample [43] with the epitaxial conditions: $\mathbf{c_{P3HT}//c_{TCB}}$, $(0\ 1\ 0)_{P3HT}//(1\ 0\ 0)_{TCB}$ and $c_{P3HT}/2 \sim c_{TCB}$. In this case, the crystalline lamellae of P3HT grow perpendicular (i.e. edge-on) to the substrate of TCB (see Fig. 6). It is worth noting that the terms 'edge-on' and 'flat-on' are used hereafter to refer to the orientation of the crystalline lamellae on the substrate, not to the orientation of the π-conjugated skeleton on the substrate (the terms 'edge-on' and 'face-on' are used for the π-conjugated skeleton oriented perpendicular to and in the plane of the substrate, respectively).

Interestingly, the orientation of P3HT on TCB was found to depend on the molecular weight of the polymer. For a 7 kDa P3HT crystallizing with extended chains, two different types of orientation of the crystalline lamellae on TCB were evidenced. As well as edge-on lamellae, flat-lying P3HT lamellae consisting of 'standing' chains were also observed in BF (see Fig. 6). These lamellae are oriented in the plane of the substrate with $\mathbf{b_{P3HT}//c_{TCB}}$ and $(0\ 0\ 1)_{P3HT}//(1\ 0\ 0)_{TCB}$. This second population of oriented P3HT lamellae on TCB is also induced by 1D epitaxy of P3HT on TCB. Indeed, for this population of flat-on lamellae, we observe the epitaxial condition $b_{P3HT}/2 \sim c_{TCB}$ [43]. To conclude, directional epitaxial crystallization is a powerful method for aligning P3HT and other poly(3-alkylthiophene)s over large surfaces, provided that the growth of TCB is controlled, e.g., by a local zone melting (slow-DEC).

Fig. 5 (continued) curve GIXD with $\mathbf{q_i//c_{P3HT}}$; *lower black curve* $\mathbf{q_i} \perp \mathbf{c_{P3HT}}$ with $\mathbf{q_i}$ the vector of the incident X-ray beam. (**f**) 2D GIXD pattern recorded with the incident X -ray beam oriented 'parallel' to the chain direction. (**g**) TEM electron diffraction pattern. (Adapted with permission from [46] © 2012, Royal Society of Chemistry)

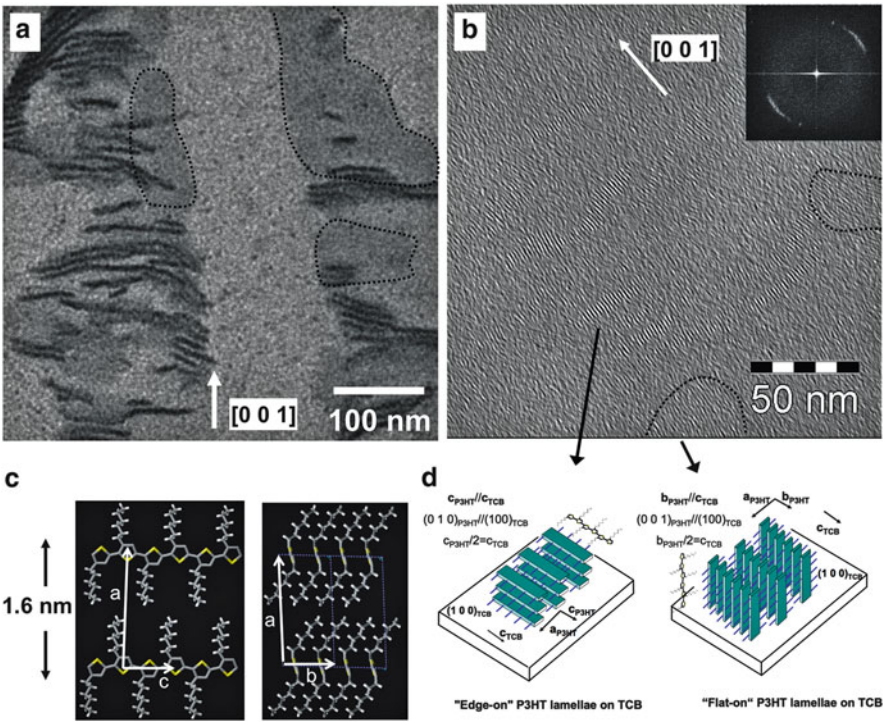

Fig. 6 (**a**) Underfocused TEM-BF image of a thin area of an oriented thin film of P3HT with $M_w = 7.3$ kDa grown by DEC. The flat-on lamellae have been delimitated by *dotted lines*. (**b**) Low-dose HR-TEM image. The flat-on lamellae have been identified by *dotted lines*. The average in-plane chain orientation is indicated by a *white arrow*. The *inset* corresponds to the fast Fourier transform. (**c**) Schematic projections of the chain packing of P3HT seen along the *b*- and *c*-axes.(**d**) Scheme showing the chain orientation in flat-on and edge-on lamellae seen in the HR-TEM image and giving the corresponding epitaxial conditions. (Reproduced with permission from [45] © 2009, American Chemical Society)

3 Epitaxy: An Interesting Insight into Structural and Morphological Aspects of P3HT

3.1 Structure Determination of Form I P3HT

The polymorphism of poly(3-alkylthiophene)s (P3ATs) was recognized early on by Prosa and others [52–57]. For the family of P3AT with $n = 3$ to 15 for the length of alkyl side chains, two characteristic layer periods have been observed. This indicates that P3ATs exist in two different crystal structures, called form I and form II, which differ mainly by the side chain packing. Structural models for both forms I and II have been proposed by several groups [52–61]. In general, the difficulty in

refining the crystal structure of a semicrystalline polymer lies in the limited size of single crystalline domains, which precludes the use of structural methods based on single crystal X-ray diffraction. As demonstrated in the work by Lotz and coworkers, electron diffraction in a TEM is a powerful alternative method for unraveling the structure of polyolefins [62–64] because it can be applied to micron-sized single crystalline domains. However, although numerous polyolefins can be grown in the form of lamellar single crystals, this is more difficult for P3ATs and has been reported only very recently for form II P3HT [61].

Accordingly, in the absence of single crystals of form I, the crystal structure of this polymorph was investigated by electron diffraction (ED) on highly oriented and crystalline films of P3HT (7.9 kDa) grown by slow-DEC [47]. A rotation-tilt sample holder is used in a TEM to acquire representative projections in reciprocal space, as shown in Fig. 7. The use of a rotation-tilt sample holder makes it possible to tilt the sample around well-defined directions, e.g., around the in-plane direction of the P3HT chains. The ED patterns were analyzed by a trial-and-error method to determine a structural model. Figure 8 depicts the resulting structure of form I P3HT. Of interest is the fact that this methodology makes it possible to determine the reflection rules (the systematic extinctions of some reflections), which are necessary to identify the space group of the crystal structure (P21/c in the present case). It is worth noting that space group identification is usually very difficult when only aligned fiber patterns are obtained and analyzed by X-ray diffraction.

The structural model of form I obtained by ED analysis is displayed in Fig. 8. It shows the following characteristic features: (1) the polythiophene backbone adopts a *trans* planar conformation, (2) *n*-hexyl side chains are not interdigitated, (3) the polythiophene backbones are separated by 0.38 nm along the *b*-axis with relatively short interatomic contacts of 0.34 nm between successive polythiophene backbones due to a tilting of the backbone plane to the stacking direction, and (4) the *n*-hexyl side chains are arranged in a rectangular subcell. Although this model accounts for a large number of characteristic features in the ED patterns, it needs further improvements from a crystallographic point of view. In particular, the use of an all-*trans* side chain conformation results in non-optimal torsional angles at the junction between the thiophene ring and the *n*-hexyl side chain. Further work to improve this model is currently in progress.

This structure has been recently challenged by a few alternative models. In particular, Hansen and coworkers determined a model using a combination of solid state NMR, X-ray diffraction and molecular modeling analysis on powders [65]. This model of form I proposes that the planes of the polythiophene backbones are perpendicular to the stacking direction (*b*-axis), resulting in the absence of short interchain contacts as observed in the model of Kayunkid et al. [47]. To explain the discrepancy between the two models, it was suggested that the structure in the DEC films may correspond to a different polymorph, i.e., form I′. However, the fiber pattern obtained for epitaxied P3HT films on TCB ($M_w = 17$ kDa) is identical to that reported by Tashiro et al. on stretch-oriented films, demonstrating that the

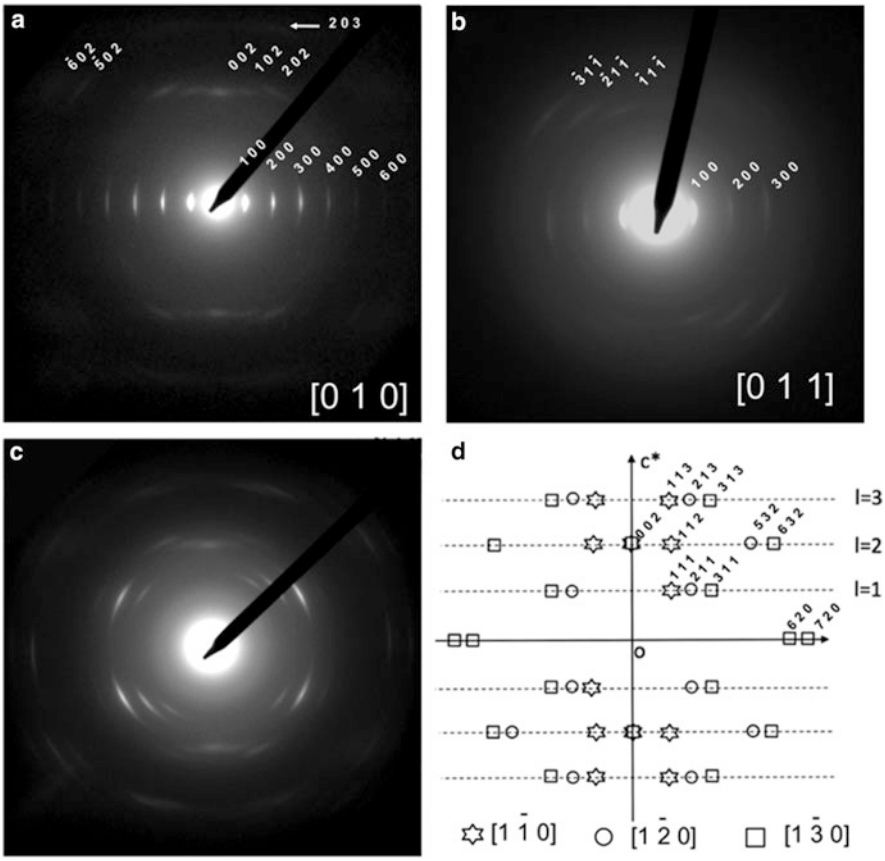

Fig. 7 Various ED patterns of an epitaxied thin film of P3HT corresponding to different zone axes: (**a**) [0 1 0] zone and (**b**) [0 1 1] zone. Note the asymmetry of the intensity of the $(-h\ 1\ -1)$ reflections ($h = 1, 2, 3$). (**c**) Superposition of ED patterns corresponding to [1 -1 0], [1 -2 0], and [1 -3 0] zones as illustrated in **d**. (**d**) The reflections arising from three nearby zones are identified by different *symbols*. (Reprinted with permission from [47] © 2010, American Chemical Society)

structure in the epitaxied films is not substrate-induced but corresponds indeed to form I [56, 57]. The two structural models of form I proposed by Dudenko et al. and Kayunkid et al. lead to significantly different ED patterns for the [0 1 0] and the [0 0 1] zones, as seen in Fig. 9. Overall, only the model by Kayunkid et al. gives satisfactory agreement with the experimental ED data. One of the most characteristic features of the [0 0 1] pattern is the asymmetry in the intensities of the (h 2 0) and (h 4 0) layer lines, which is not observed in the calculated pattern using the model of Dudenko et al. Furthermore, in the latter pattern, the intensity of the 1 0 1 reflection is strongly overestimated with respect to the experimental pattern.

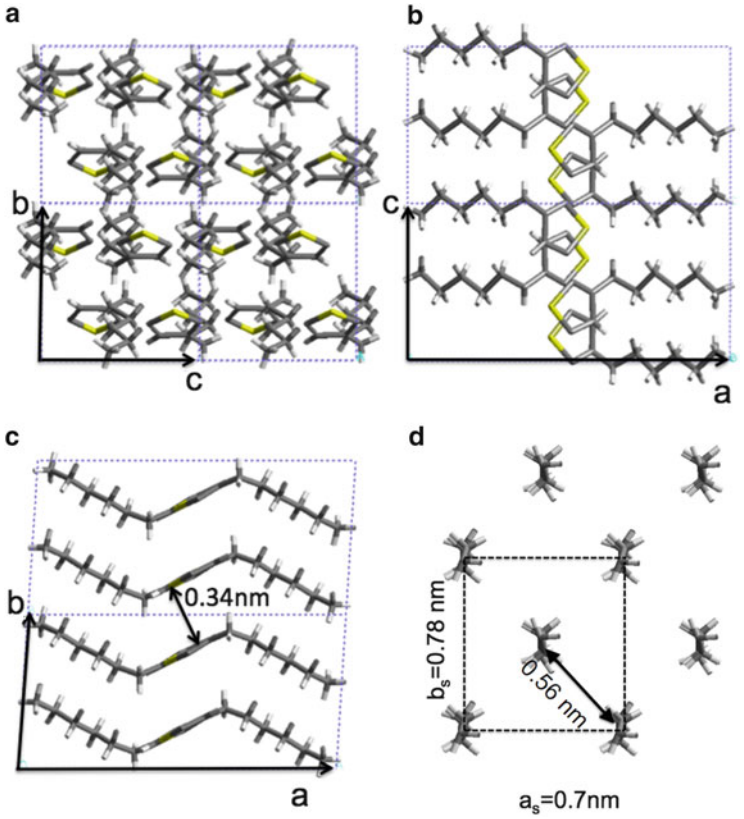

Fig. 8 (**a–c**) Projections of the P3HT crystal structure along the *a*-, *b*-, and *c*-axes of the unit cell. (**d**) Rectangular subcell accounting for the packing of the *n*-hexyl side chains in the crystal structure of P3HT. The view corresponds to the projection along the *n*-hexyl side chain direction (corresponding to the direction [1 2 0] in the unit cell of P3HT). (Reproduced with permission from [47] © 2010, American Chemical Society)

The strong differences observed in the models of form I obtained by two very different methodologies highlight the intrinsic difficulties of structure determination for polymers like P3HT. Although both methods present specific advantages, additional structural information is necessary to discriminate between them. In particular, it needs to be clarified to what extent the structure of form I observed for extended-chain crystals ($M_w < 10$ kDa) differs from that observed for folded-chain crystals ($M_w > 10$ kDa). As yet, a rather continuous variation of the unit cell parameters of form I P3HT with increasing M_w was reported for spin-coated thin films [66]. Therefore, it cannot be excluded that the packing of P3HT chains in form I is a function of molecular weight and could therefore evolve in a more or less continuous way between the two models shown in Fig. 9.

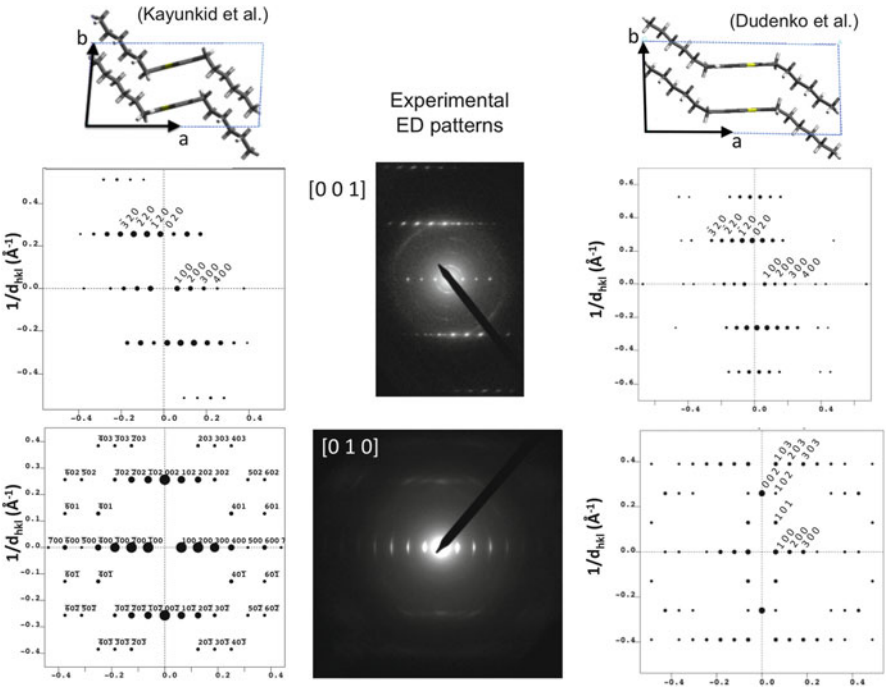

Fig. 9 Comparison of two structural models of form I P3HT as obtained by Dudenko et al. [65] (*right*) and Kayunkid et al. [47] (*left*) with the corresponding calculated ED patterns for the [0 0 1] and [0 1 0] zones. The experimental ED patterns for these two zones are shown in the *central column*. (Reproduced with permission from [47] © 2010, American Chemical Society)

3.2 Folded Chain Versus Extended Chain Crystallization

Macromolecular parameters like M_w and the regioregularity of P3HT are known to significantly affect charge transport properties in thin films [67, 68]. Various groups have investigated the correlations between the morphology observed by atomic force microscopy (AFM) in spin-coated films and the corresponding hole mobility in organic field-effect transistors (OFETs). It is reported that low-M_w P3HT forms well-defined nanofibrillar domains but exhibits poor hole mobility, whereas P3HT with $M_w \geq 20$ kDa yields thin films with poorly defined morphologies and significantly higher charge carrier mobilities. As a rationale, Kline proposed the existence of tie-chains linking successive crystalline domains via some poorly ordered amorphous zones [67]. With increasing M_w, one can expect an increasing proportion of such tie chains. Although AFM gave clear evidence for the formation of P3HT nanofibrils in thin films, the distinction between amorphous and crystalline domains was difficult [67]. Distinction was, however, possible by using TEM on epitaxied thin films [43, 44]. Therefore, by growing oriented films of P3HT by epitaxy, it is possible to investigate the influence of M_w on the semicrystalline

morphology and the crystallization of P3HT. Figure 10 shows the characteristic bright fields and GIXD 2D patterns recorded for two M_w fractions of P3HT ($M_w = 7.9$ kDa and $M_w = 50$ kDa). Oriented films prepared by slow-DEC show different structural and morphological features when the molecular weight of P3HT changes (see Fig. 10). The observed differences in morphology and structure as a function of M_w reflect different crystallization modes that are attributed to the presence or absence of chain folding and tie-chains.

All M_w fractions of P3HT give rise to oriented and periodic lamellar structures in films grown by epitaxy on TCB [43, 44]. In the TEM bright field (TEM-BF) images, a characteristic contrast is observed between crystalline domains and amorphous interlamellar zones (see Figs. 10 and 11). Therefore, one can observe the periodic alternation of crystalline (dark) and bright (amorphous) domains, i.e., the semicrystalline structure of the polymer. Additional differences between films of different M_ws are obtained by GIXD and ED. The effect of M_w on nanocrystal orientation is particularly well observed in the GIXD patterns when the incident X-ray beam is oriented parallel to the P3HT chain direction (see Fig. 10). For low-M_w P3HT, the GIXD 2D pattern reflects the coexistence of three populations of nanocrystals with (0 1 0), (0 0 1), and (0 1 1) contact planes. These three types of lamellae share the same in-plane orientation of their $\mathbf{a_{P3HT}}$ axis (direction of alkyl side chains), i.e., $\mathbf{a_{P3HT}} \perp \mathbf{c_{TCB}}$. For P3HT samples with a high M_w of 50 kDa that crystallize with folded chains, the GIXD pattern is very different and shows a sequence of (h 0 0) Scherrer rings. Such a pattern indicates that the epitaxied films for $M_w = 50$ kDa have a fiber-like symmetry, i.e., films consist of a variety of nanocrystals with different contact planes and a well-defined in-plane orientation of the P3HT chains enforced by 1D epitaxy on TCB.

Beside orientation of nanocrystals, M_w impacts strongly on the nanomorphology and in particular the semicrystalline structure of P3HT. In the original work by Brinkmann and Rannou on P3HT films grown by DEC [44], the total lamellar periodicity measured in the BF images is close to the length of the 'fully extended' chain for M_w ~6–8 kDa and it saturates to a value of ca. 27 ± 2 nm for $M_w \geq 17$ kDa. This behavior is due to a transition from an oligomeric-like system with fully extended chains in *all-trans* conformation to a semicrystalline system with a periodic alternation of crystalline lamellae separated by extended amorphous interlamellar zones harboring chain folds, chain ends, and tie molecules [43–45].

Incidentally, the total lamellar period L_{lam} in epitaxied P3HT films can exceed the value of 28 nm in films obtained by DEC if the growth of the films is performed at a 'slow' rate of 20 μm/s (slow-DEC) versus 1 mm/s for the original DEC method used by Brinkmann and Rannou [44]. Figure 12 shows the M_n-dependence of the total lamellar period (crystalline plus amorphous) L_{lam} measured in epitaxied films grown at 1 mm/s (DEC) and 20 μm/s (slow-DEC). In the regime of folded chain crystallization ($M_w > 10$ kDa), the slower growth rates result in longer lamellar periods for films of high-M_w P3HT. For instance, for $M_w = 50$ kDa ($M_n = 26$ kDa), $L_{lam} \sim 45$ nm can be observed versus 28 nm for films grown rapidly on a Koeffler bench [44]. Similar large lamellar periods were only observed in the case of spherullitic growth by swelling/deswelling of thin films by Crossland et al. [69] (see Tremel and Ludwigs [20]).

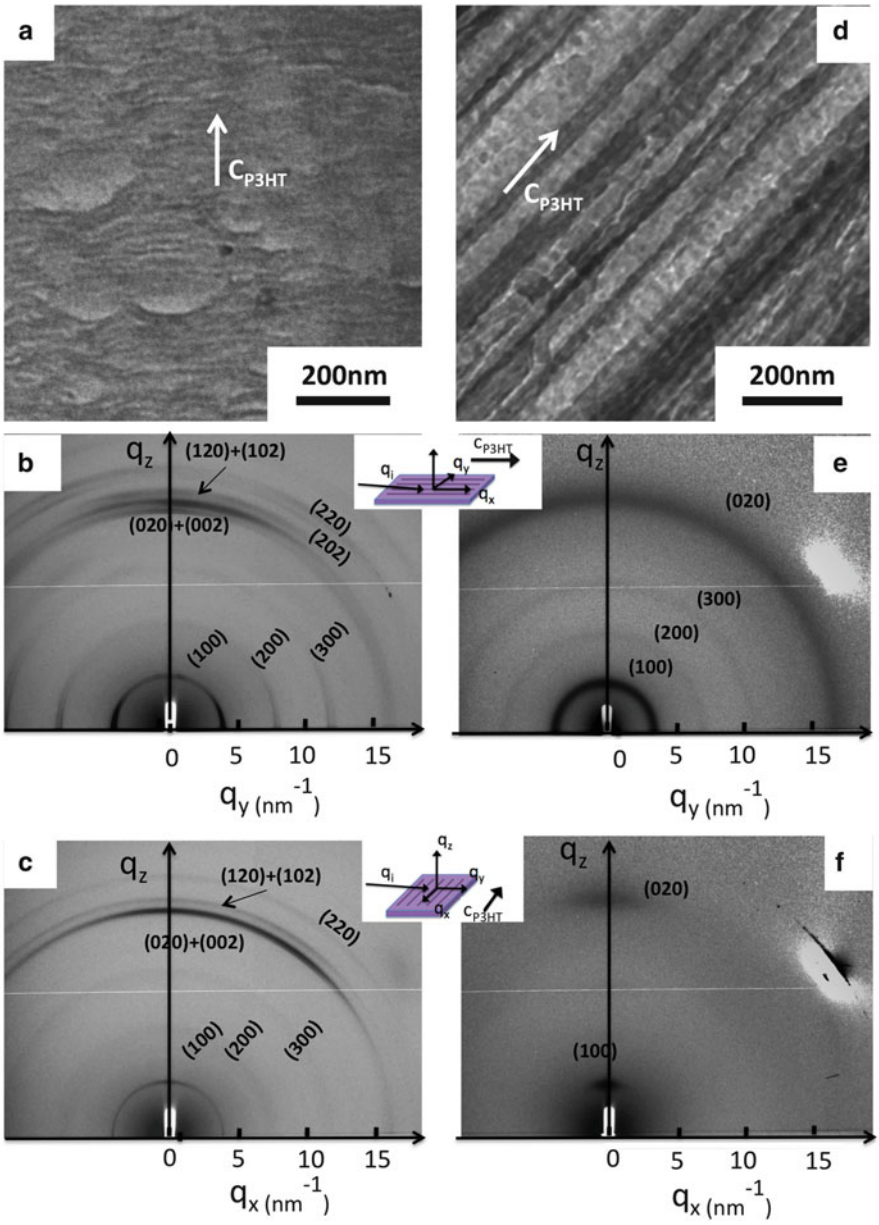

Fig. 10 TEM-BF images (**a**,**d**) and 2D GIXD patterns recorded with the incident q vector $\mathbf{q_i}$ oriented parallel (**b, e**) and perpendicular (**c, f**) to the P3HT chain direction $\mathbf{c_{P3HT}}$ for oriented P3HT films (20–50 nm thick) grown by slow-DEC: $M_w = 7.9$ kDa (**a**, **b**, **c**) and $M_w = 50$ kDa (**d**, **e**, **f**). The *insets* show the scattering GIXD configurations and the orientation of the incident beam with respect to the P3HT chain direction ($\mathbf{c_{P3HT}}$)

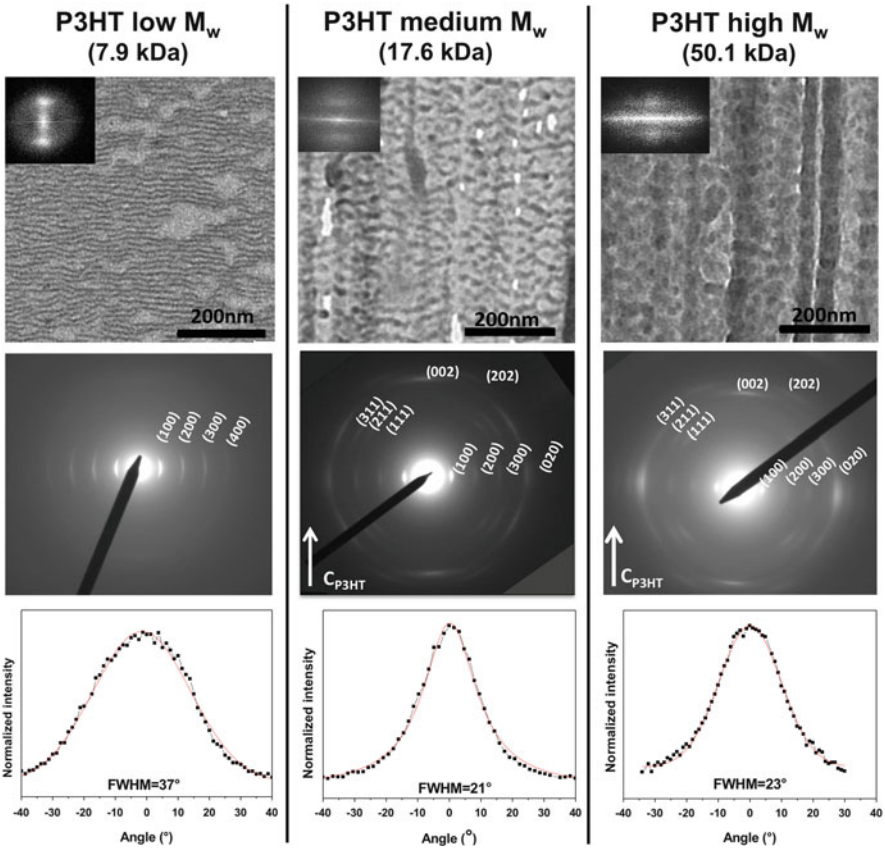

Fig. 11 Evolution of the lamellar morphology (*top row*), ED pattern (*middle row*), and azimuthal distribution of the (1 0 0) reflection (*bottom row*) obtained for epitaxied P3HT films grown by slow-DEC in TCB for three P3HT samples with different molecular weights. The *insets* in the *top* sequence correspond to the fast Fourier transform

Beside bright field and electron diffraction, Low dose HR-TEM was also used to show structural differences between various M_w fractions of P3HT. In HR-TEM images, a contrast is observed between the π-stacked polythiophene backbones and the layers of alkyl side chains. Therefore, it is possible to measure the average length of P3HT stems (chain segments) (L_c) along the chain direction $\mathbf{c_{P3HT}}$ and the number of unit cells along the side chain direction $\mathbf{a_{P3HT}}$ in P3HT nanocrystals. Figure 12 shows representative HR-TEM images of P3HT films grown by slow-DEC. Two main points can be noted with increasing M_w: (1) the average stem (chain) length (L_c) in the crystalline domains increases substantially from 6 to 16 nm, and (2) the lateral extension of the domains in the direction of the side chains (L_a) decreases from 25 to 13 stems. Apparently, in the regime of chain folding, the use of slow growth rates leads to longer stem lengths in the crystalline domains, suggesting that in most P3HT samples (spin-coated and drop-cast films),

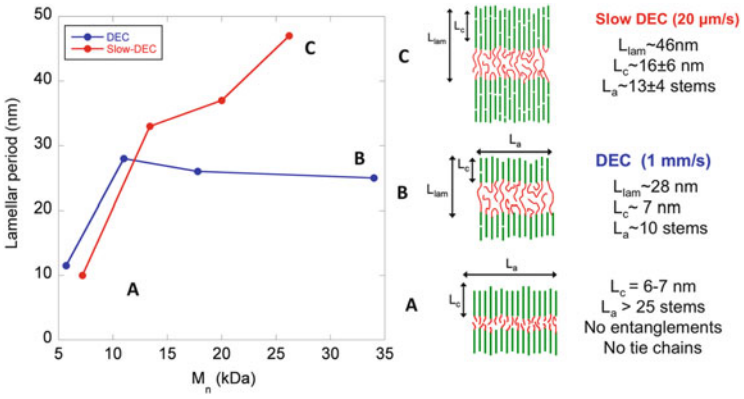

Fig. 12 *Left*: Evolution of the total lamellar period L_{lam} observed in the bright field for epitaxied P3HT films with different molecular weights and grown either by DEC on a Koeffler bench (fast growth) or by slow-DEC at 20 µm/s. *Right*: Evolution of the semicrystalline nanomorphology for P3HT films of low-M_w and high-M_w grown by DEC and slow-DEC. The dimensions of the crystalline domains are obtained from a statistical analysis of the HR-TEM images (see Fig. 13). *A*: regime of extended chain crystallization, *B*: regime of folded chain crystallization limited by the growth kinetics, and *C*: regime of folded chain crystallization observed for slow epitaxial growth (20 µm/s)

the observed total lamellar period is limited by both the growth kinetics and temperature.

Several factors may explain the different nanocrystal dimensions in low-M_w and high-M_w epitaxied films. First, the anisotropy of the crystal shape must reflect the folding ability of the chains, which is directly determined by the macromolecular parameters (average contour length, polydispersity index). The low-M_w P3HT used herein is rather monodisperse and crystallizes in extended form. Therefore, the epitaxial growth of low-M_w P3HT chains is not affected by chain folding. In other words, the growth of crystalline domains along the side chain direction ($\mathbf{a_{P3HT}}$ axis) implies only the sequential addition of new P3HT stems in that direction. For $M_w \geq 17$ kDa, folding as well as chain entanglements come into play and make the crystallization mechanism more complex. As demonstrated by Mena-Osteriz et al., a rather tight fold of a P3HT chain can be obtained by a sequence of about eight thiophene units in *cis* conformation leading to a fold radius of ~10 Å [70]. This implies that the position of the re-entrant chain is at least 20 Å away from the outgoing position along the $\mathbf{a_{P3HT}}$ direction and therefore does not occur at the expected position of the next neighbor P3HT stem in the crystal lattice (at 16.5 Å). This implies that tight folding is difficult in P3HT because the re-entrant chains exert stress on the crystalline lattice. It has been proposed that the increasing proportion of re-entrant chains in P3HT crystals could explain the expansion of the unit cell along $\mathbf{a_{P3HT}}$ observed in spin-coated and epitaxied films with increasing M_w [66].

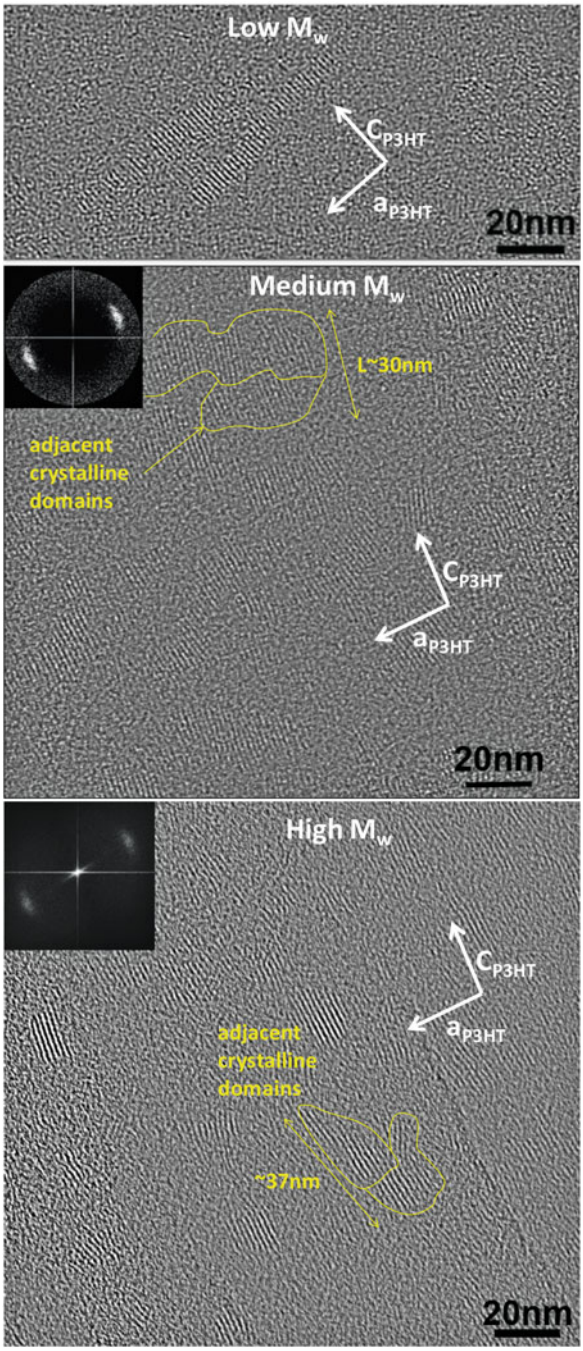

Fig. 13 Effect of increasing M_w on the shape of the crystalline domains of slow-DEC P3HT samples as observed by low dose HR-TEM. Low-M_w 7.9 kDa, medium M_w 17.6 kDa, and high-M_w 50.1 kDa. The *insets* correspond to the fast Fourier transforms of the HR-TEM images

Second, the growth of P3HT domains is certainly influenced by the diffusion kinetics of the chains on the TCB surface during slow-DEC. Diffusion of longer chains is likely to be more difficult on the TCB substrate as compared to oligomer-like chains. This may favor the growth of crystalline domains in the $\mathbf{a_{P3HT}}$ direction for short chains, resulting in domains with a high aspect ratio L_a/L_c.

Third, the polydispersity index of the low and high-M_w fractions differ notably. Low-M_w P3HT has a rather low polydispersity index (1.07) that explains the relative constant overall lamellar thickness (stem length) seen in the HR-TEM images. As opposed to this, high-M_w P3HT is more polydisperse (polydispersity index of ~2) and the stem length distribution is very broad. For high-M_w P3HT films, lamellae show a strong tapering as observed for instance in epitaxied films of polyfluorenes (PF2/6 and PFO) on oriented polytetrafluoroethylene (PTFE) [71]. For poly[9,9-bis(*n*-octyl)fluorene-2,7-diyl] (PFO), lamellar tapering was explained by segregation between short and long chains during crystallization. A similar effect may also occur in the case of P3HT for high-M_w samples, provided that the crystallization kinetics is slow enough.

As a concluding remark, HR-TEM at low dose is a valuable method for observing P3HT nanocrystals at the scale of crystalline stems. Important informations on the size and shape of the nanocrystals can be obtained. Recent results indicate that a similar analysis can also be performed on spin-coated P3AT films [72]. In particular, the influence of thermal annealing on the nanocrystal dimensions of various P3ATs (from *n*-pentyl to *n*-octyl side chains) was investigated as a function of the annealing temperature.

4 Conclusions and Outlook

This contribution has illustrated the versatility of epitaxial crystallization to generate highly crystalline and oriented films of P3HT. Different morphologies and nanotextured patterns can be obtained by the proper choice of substrates used for epitaxy, which often involves a 1D lattice matching, either in the plane (TCB, KAP) or along the normal to the substrate (K-BrBz). The role of macromolecular parameters on the crystallization of P3HT could also be unveiled. Electron diffraction, dark field, low dose HR-TEM imaging and GIXD provide highly complementary views of the P3HT structure and nanomorphology. In particular, the important role of the growth kinetics on the lamellar period and crystalline domain size was evidenced by using a slow-directional epitaxial crystallization method. Electron diffraction on epitaxied low-M_w P3HT proved to be a valuable approach for generating structural models of P3HT. Nevertheless, structural refinement of semiconducting polymers remains a difficult task and more quantitative analyses of ED patterns in conjunction with proper modeling tools will certainly allow the further improvement of existing models. Despite the fact that epitaxy is still difficult to transpose to large-scale device processing, the variety of results obtained by TEM and GIXD on epitaxied P3HT films illustrates the unique possibilities offered by this approach in revealing

structural details down to the molecular scale and in understanding the intrinsic crystallization mechanisms. New developments in the use of TEM to analyze the structure of SCPs are on the way. In particular, we recently showed the possibility of performing in-situ temperature-dependent experiments to follow structural transitions and reorientation processes in devices and correlating them with corresponding modifications in charge transport properties [73].

References

1. Heeger AJ (2001) Rev Mod Phys 73:681
2. James DI, Smith J, Heeney M, Anthopoulos TD, Salleo A, McCulloch I (2012) Organic semiconductor materials for transistors. In: Klauk H (ed) Organic electronics II: more materials and applications. Wiley-VCH, Weinheim, pp 1–26
3. Virkar AA, Mannsfeld S, Bao Z, Stingelin N (2010) Adv Mater 22:3857
4. Sirringhaus H, Kawase T, Friend RH, Shimoda T, Inbasekaran M, Wu W, Woo EP (2000) Science 290:2123
5. Friend RH, Gymer RW, Holmes AB, Burroughes JH, Marks RN, Taliani C, Bradley DDC, Dos Santos DA, Brédas JL, Lögdlund M, Salaneck WR (1999) Nature 397:121
6. Sirringhaus H, Brown PJ, Friend RH, Nielsen MM, Bechgaard K, Langeveld-Voss BMW, Spiering AJH, Janssen RAJ, Meijer EW, Herwig P, de Leeuw DM (1999) Nature 401:685
7. Nelson J (2002) Curr Opin Solid State Mater Sci 6:87
8. Brabec C, Scherff U, Diakonov V (2008) Organic photovoltaics. Wiley, Weinheim
9. Facchetti A (2010) Chem Mater 23:733
10. Himmelberger S, Dacuña J, Rivnay J, Jimison LH, McCarthy-Ward T, Heeney M, McCulloch I, Toney MF, Salleo A (2013) Adv Funct Mater 23:2091
11. Rivnay J, Mannsfeld SCB, Miller CE, Salleo A, Toney MF (2012) Chem Rev 112:5488
12. Lim JA, Liu F, Ferdous S, Muthukumar M, Briseno AL (2010) Mater Today 13:14
13. Brinkmann M (2011) J Polym Sci B 49:1218
14. Chang JF, Sun B, Breiby DW, Nielsen MN, Sölling TI, Giles M, McCulloch I, Sirringhaus H (2004) Chem Mater 16:4772
15. Rivnay J, Steyrleuthner R, Jimison LH, Casadei A, Chen Z, Toney MF, Facchetti A, Neher D, Salleo A (2011) Macromolecules 44:5246
16. Chabinyc ML, Toney MF, Kline RJ, McCulloch I, Heeney M (2007) J Am Chem Soc 129:3226
17. Yang H, Shine TJ, Yang L, Cho K, Ryu CY, Bao Z (2005) Adv Funct Mater 15:671
18. Yang H, LeFevre SW, Ryu C, Bao Z (2007) Appl Phys Lett 90:172116
19. Crossland EJW, Tremel K, Fischer F, Rahimi K, Reiter G, Steiner U, Ludwigs S (2012) Adv Mater 24:839
20. Tremel K, Ludwigs S (2014) Morphology of P3HT in thin films in relation to optical and electrical properties. Adv Polym Sci. doi:10.1007/12_2014_288
21. Jimison LH, Toney MF, McCulloch I, Heeney M, Salleo A (2009) Adv Mater 21:1568
22. Zheng Z, Yim KH, Saifullah MSM, Welland ME, Friend RH, Kim JS, Huck WTS (2007) Nano Lett 7:987
23. Lan YK, Huang CI (2009) J Phys Chem B 90:62117
24. Brabec CJ, Gowrisanker S, Halls JJM, Laird D, Jia S, Williams SP (2010) Adv Mater 22:3839
25. Peet J, Heeger AJ, Bazan GC (2009) Acc Chem Res 42:1700
26. Ward MD (2001) Chem Rev 101:1697
27. Hooks DE, Fritz T, Ward MD (2001) Adv Mater 13:227
28. Jiang S, Qian H, Liu W, Wang C, Wang Z, Yan S, Zhu D (2009) Macromolecules 42:9321

29. Bunk O, Nielsen MM, Sølling TI, van de Craats AM, Stutzmann N (2003) J Am Chem Soc 125:2252
30. Li L, Li CY, Ni C (2006) J Am Chem Soc 128:1692
31. Willems J (1955) Naturwissenschaften 42:176
32. Fischer EW (1958) Kolloid Z 159:108
33. Wittmann JC, Lotz B (1981) J Polym Sci Polym Phys 19:1837
34. Wittmann JC, Hodge AM, Lotz B (1983) J Polym Sci Polym Phys 21:2495
35. Wittmann JC, Lotz B (1990) Prog Polym Sci 15:909
36. Kobayashi T (1991) Organic crystals I: characterization. Springer, Berlin
37. Dorset DL (1995) Structural electron crystallography. Plenum, New York/London
38. Koutsky JA, Walton AG, Baer E (1967) Polym Lett 5:177
39. Rickert SE, Baer E (1978) J Mater Sci Lett 13:451
40. Kopp S, Wittmann JC, Lotz B (1994) Polymer 35:916
41. Da Costa V, Le Moigne J, Oswald L, Pham TA, Thierry A (1998) Macromolecules 31:1635
42. Brinkmann M, Contal C, Kayunkid N, Djuriç T, Resel R (2010) Macromolecules 43:7604
43. Brinkmann M, Wittmann JC (2006) Adv Mater 18:860
44. Brinkmann M, Rannou P (2007) Adv Funct Mater 17:101
45. Brinkmann M, Rannou P (2009) Macromolecules 42:1125
46. Roiban L, Hartmann L, Ersen O, Fiore A, Reiss P, Djurado D, Chandezon F, Legrand JF, Doyle S, Brinkmann M (2012) Nanoscale 4:7212
47. Kayunkid N, Uttiya S, Brinkmann M (2010) Macromolecules 43:4961
48. Brinkmann M (2007) Macromolecules 40:7532
49. Brinkmann M (2009) L'actualité Chim 326:31
50. Hartmann L, Tremel K, Uttiya S, Crossland E, Kayunkid N, Ludwigs S, Vergnat C, Brinkmann M (2011) Adv Funct Mater 21:4047
51. Brinkmann M, Gonthier E, Bogen S, Tremmel K, Ludwigs S, Hufnagel M, Sommer M (2012) ACS Nano 6:10319
52. Prosa TJ, Winokur MJ, Moulton J, Smith P, Heeger AJ (1992) Macromolecules 25:4364
53. Mardalen J, Samuelsen EJ, Gautum OR, Carlsen PH (1992) Synth Met 48:363
54. Prosa TJ, Winokur MJ, McCullough RD (1996) Macromolecules 29:3654
55. Meille SV, Romita V, Caronna T, Lovinger AJ, Castellani M, Belobrzeckaja L (1997) Macromolecules 30:7898
56. Tashiro K (1991) J Polym Sci Polym Phys 29:1223
57. Tashiro K, Kobayashi M, Kawai T, Yoshino K (1997) Polymer 38:2867
58. Lu G, Li L, Yang X (2007) Adv Mater 19:3594
59. Lu G, Li L, Yang W (2008) Macromolecules 41:2062
60. Buono A, Son NH, Raos G, Gila L, Cominetti A, Catellani M, Meille SV (2010) Macromolecules 43:6772
61. Rahimi K, Botiz I, Stingelin N, Kayunkid N, Sommer M, Koch F, Nguyen H, Coulembier O, Dubois P, Brinkmann M, Reiter G (2012) Angew Chem Int Ed 51:11131
62. Lotz B, Lovinger AJ, Cais RE (1988) Macromolecules 21:2375
63. Cartier L, Okihara T, Lotz B (1998) Macromolecules 31:3303–3310
64. Puiggali J, Ikada Y, Tsuji H, Cartier L, Okihara T, Lotz B (2000) Polymer 41:8921
65. Dudenko D, Kiersnowski A, Shu J, Pisula W, Sebastiani D, Spiess HW, Hansen MR (2012) Angew Chem Int Ed 51:11068
66. Zen A, Saphiannikova M, Neher D, Grenzer J, Grigorian S, Pietsch U, Asawapirom U, Janietz S, Scherf U, Lieberwirth I, Wegner G (2006) Macromolecules 39:2162
67. Kline RJ, McGehee MD, Kadnikova EN, Liu J, Fréchet JMJ, Toney MF (2005) Macromolecules 38:3312
68. Verilhac JM, LeBlevennec G, Djurado D, Rieutord F, Chouiki M, Travers JP, Pron A (2006) Synth Met 156:815
69. Crossland EJW, Rahimi K, Reiter G, Steiner U, Ludwigs S (2011) Adv Funct Mater 21:518

70. Mena-Osteriz E, Meyer A, Langeveld-Voss BMW, Janssen RAJ, Meijer EW, Bäuerle P (2000) Angew Chem Int Ed 39:2680
71. Brinkmann M, Charoenthai N, Traiphol R, Piyakulawat P, Wlosnewski J, Asawapirom U (2009) Macromolecules 42:8298
72. Salammal TS, Mikayelyan E, Grigorian S, Pietsch U, Koenen N, Scherf U, Kayunkid N, Brinkmann M (2012) Macromolecules 45:5575
73. Biniek L, Leclerc N, Bechara R, Heiser T, Brinkmann M (2013) Macromolecules 46:4014

Adv Polym Sci (2014) 265: 107–138
DOI: 10.1007/12_2014_279

Published online: 25 June 2014

P3HT and Other Polythiophene Field-Effect Transistors

Jana Zaumseil

Abstract Long before the potential of poly(3-hexylthiophene) (P3HT) in bulk-heterojunction solar cells was discovered, this conjugated polymer was one of the first and strongest contenders as a high mobility, solution-processable semiconductor for organic field-effect transistors (FETs). Many of the fundamental charge transport properties that were investigated for P3HT-FETs have informed subsequent studies of P3HT-based solar cells and the development of other high-mobility polythiophene-based polymers. Here we will give a brief overview of P3HT transistors, including the general working principles of polymer FETs and the various factors that influence device performance, such as regioregularity, molecular weight, solvents, chain alignment, and doping. Strategies for tuning the P3HT nano- and microstructure by using blends and copolymers and ways to reach the limits of charge transport in P3HT at high carrier densities will be discussed. Finally, we will survey some of the new polythiophene derivatives that have been developed over the last decade and may replace P3HT as the most popular polymer semiconductor.

Keywords Field-effect transistor · Mobility · Morphology · Poly(3-hexylthiophene) · Polymer · Polythiophene · Transport

Contents

J. Zaumseil (✉)
Department Materials Science and Engineering, Friedrich-Alexander-Universität Erlangen-Nürnberg, Martensstrasse 7, 91058 Erlangen, Germany
e-mail: jana.zaumseil@ww.uni-erlangen.de

1 Introduction

Long before the use of poly(3-hexylthiophene) (P3HT) in bulk-heterojunction solar cells was proposed, this conjugated polymer was one of the first and strongest contenders as a high mobility, solution-processable semiconductor for organic field-effect transistors (FETs). The first P3HT-FETs had already been reported in the late 1980s by Assadi et al. [1] and since the 1990s a large number of groups have worked on P3HT transistors, steadily improving their performance and deepening the understanding of the underlying physics [2–8]. Many of the fundamental charge transport properties investigated for P3HT-FETs have informed subsequent studies of P3HT-based solar cells and the development of other high-mobility polythiophene-based polymers. Here we will give a brief overview of P3HT-FETs, including the general working principles of polymer FETs, the various factors influencing device performance, and ways to reach the theoretical limits of charge transport in P3HT. Finally, we will discuss the new polythiophene derivatives that have been developed over the last decade and may replace P3HT as the most popular polymer semiconductor.

2 Transistor Structures and Working Principle

The basic function of a transistor is that of a switch and an amplifier. The amount of current flowing between two terminals is determined by a voltage applied to a third terminal, thus turning it on or off. This basic function makes transistors the fundamental building block of all logic circuits necessary for electronics. Thin film FETs generally consist of a semiconducting layer, which is separated from a gate electrode by a thin insulating gate dielectric. A source and a drain electrode of width W (channel width) separated by a distance L (channel length) are in direct contact with the semiconducting layer. The most commonly found geometries (in relation to the substrate) are the bottom contact/top gate (BC/TG, staggered), top contact/bottom gate (TC/BG), and bottom contact/bottom gate (BC/BG, coplanar) geometries (shown in Fig. 1a–c).

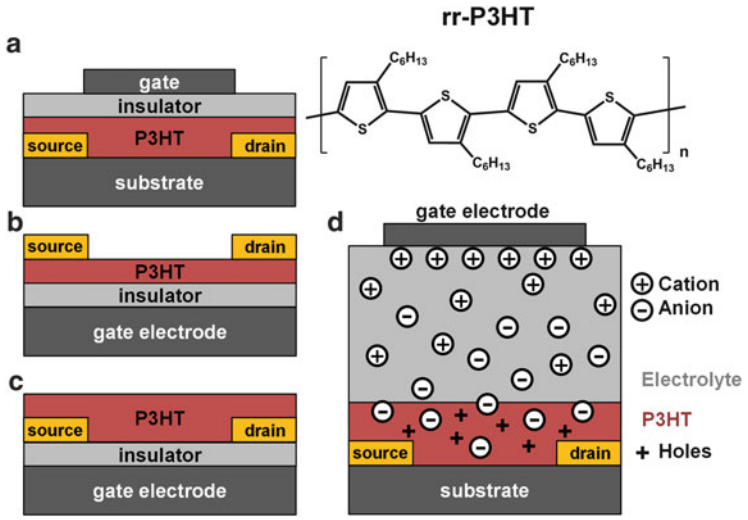

Fig. 1 Molecular structure of regioregular P3HT (*rr-P3HT*) and different transistor geometries: (**a**) bottom contact/top gate, (**b**) top contact/bottom gate, and (**c**) bottom contact/bottom gate. (**d**) Structure and working principle of electrolyte-gated, electrochemical transistors

Voltage is applied to the gate electrode (gate voltage, V_G) and the drain electrode (V_D). The source electrode is usually grounded ($V_S = 0$). The potential difference between source and drain is referred to as the source-drain voltage (V_{DS}). The source is the charge injecting electrode. When a positive gate voltage is applied with respect to the source, electrons are injected. When a negative gate voltage is applied, holes are injected. The applied gate voltage determines the amount of accumulated charges in the channel and thus the current flow between the source and the drain electrode (source-drain current, I_{DS}), which is the product of charge carrier density, mobility, and the lateral electric field. The number of accumulated charges in the channel is proportional to V_G and the areal capacitance C_i of the insulator. Note that charges only accumulate within a very short distance from the semiconductor–dielectric interface, usually within the first molecular layer. Not all induced charges are mobile and contribute to the current in an FET. Any existing deep trap states first have to be filled before the induced charges can become mobile. That is, a gate voltage higher than a so-called threshold voltage V_{Th} must be applied and thus the effective voltage for calculating the amount of mobile charges is $V_G - V_{Th}$. On the other hand, unintentional doping (e.g, by impurities) can cause charges to already be present in the channel when $V_G = 0$ and an opposite voltage has to be applied to turn the channel off. We will see that this is often the case for P3HT-FETs.

When a small source-drain voltage (i.e., a lateral electric field) is applied ($V_{DS} \ll V_G$), charges move from the injecting source to the drain electrode. A linear gradient of charge density forms and current flows. This is the linear regime, in

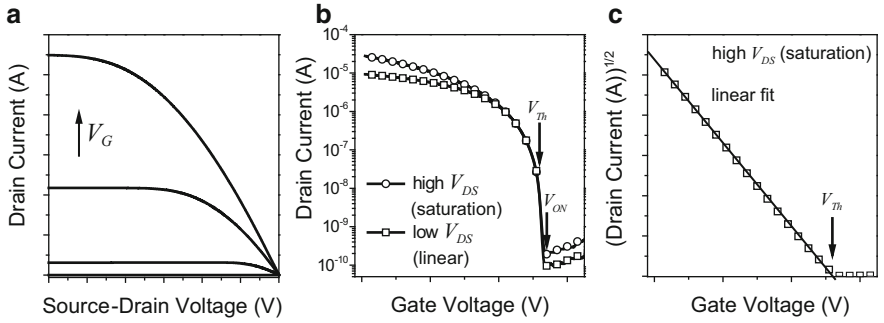

Fig. 2 (**a**) Output and (**b**) transfer characteristics of a near-ideal organic field-effect transistor in hole accumulation. (**c**) Extraction of mobility and threshold voltage from the square root plot of the saturation current

which the current flowing through the channel is directly proportional to V_{DS} and the charge carrier mobility μ_{lin} and can be described by:

$$I_{\mathrm{DS}}(\mathrm{lin}) = \frac{W}{L} \cdot C_{\mathrm{i}} \cdot \mu_{\mathrm{lin}} \cdot (V_{\mathrm{G}} - V_{\mathrm{Th}}) \cdot V_{\mathrm{DS}} \tag{1}$$

If the source-drain voltage is further increased, a point will be reached where $V_{\mathrm{DS}} = V_{\mathrm{G}} - V_{\mathrm{Th}}$. At this point the channel is 'pinched off.' That is, the local potential at the drain electrode is lower than the threshold voltage and a depletion region forms next to the drain. A space charge limited current can flow across this narrow depletion zone. Charge carriers are swept from the pinch-off point to the drain by the comparatively high electric field across the depletion region. Any additional increase in the source-drain voltage does not enhance the current substantially. The current saturates (see Fig. 2a). Hence, this regime is called the saturation regime. The saturation current $I_{\mathrm{DS}}(\mathrm{sat})$ is almost independent of V_{DS} and scales quadratically with the gate voltage and linearly with the saturation mobility (μ_{sat}) of the carriers:

$$I_{\mathrm{DS}}(\mathrm{sat}) = \frac{W}{2L} \cdot C_{\mathrm{i}} \cdot \mu_{\mathrm{sat}} \cdot (V_{\mathrm{G}} - V_{\mathrm{Th}})^2 \tag{2}$$

Equations (1) and (2) are often used to extract the charge carrier mobilities within the semiconducting layer and threshold voltages from the current–voltage characteristics (usually plotted as I_{DS} versus V_{G}; see Fig. 2b) of the respective FETs. Most popular in the current literature is the extraction of the saturation mobility from the slope of a plot of $\sqrt{I_{\mathrm{DS}}}$ versus V_{G} (see Fig. 2c). However, these often-applied equations are only strictly valid for idealized FETs in the gradual channel approximation with charge-carrier density (i.e., gate voltage)-independent mobilities and without any contact resistance. Very few FETs show such ideal behavior and care should be taken when extracting mobilities from non-ideal current–voltage

curves. For example, for almost all organic FETs, the threshold voltage extracted from the extrapolation of the linear regression of the square root of I_{DS} in the saturation regime to zero is not the same as the gate voltage, at which the current starts to increase. This point is called the onset voltage (V_{ON}) and is often quoted instead of the threshold voltage. More realistic models of charge transport in organic FETs, which take into account the dependence of mobility on charge carrier density or contact resistance, are also available [9, 10].

The carrier mobility ultimately determines the resistance of the channel at a given gate voltage and channel length, that is, how much current can go through the FET. This is important for current-driven light-emitting diodes in display pixels. It is also an important factor for the switching speed of any transistor and therefore for possible circuits. Clearly, the higher the mobility the better. For organic electronics, carrier mobilities between 0.1 and 1 $cm^2\ V^{-1}\ s^{-1}$ are considered to be the minimum for useful application and substantial efforts have been made over the last decade to increase the carrier mobility in organic semiconductors [11].

Another crucial parameter is the ratio of the on-current (at $V_G \gg V_{Th}$) to the off-current (at $V_G < V_{Th}$) in an FET. Even in the off-state of a transistor there is some current flow, called the 'off-current.' This results from various sources such as unintentional doping, the finite resistance of the semiconductor, and leakage to the gate electrode. The off-current should be as low as possible, whereas the on-current, when charges are accumulated, should be as high as possible. In traditional metal-oxide-semiconductor FETs (MOSFETs) this problem is solved by the pn-junction at the contacts [12]. In organic FETs, the bulk resistance of the undoped semiconductor largely determines the off-current. Depending on the intended application, on/off ratios of 10^6 to 10^9 are required.

The current–voltage characteristics of transistors are usually presented either as transfer curves, that is, the drain current is plotted versus the gate voltage for a constant source-drain voltage, or as output curves, that is, the drain current is plotted versus the source-drain voltage for a set of constant gate voltages (see Fig. 2). The output curves are instructive for determining the source-drain voltage range for which the linear and saturation regimes are valid. They can also indicate non-ohmic contact resistance, that is, the current does not increase linearly with low V_{DS} but exhibits a typical S-shaped curve. The transfer characteristics are most frequently presented in the literature and allow simple extraction of the on/off current ratio, onset voltages, and mobilities. Note that ideally both forward and reverse voltage sweeps should be plotted to estimate any charge trapping, which causes current hysteresis.

Charge accumulation and transport occur very close to the semiconductor–dielectric interface; hence, the surface of the dielectric and the order of the semiconductor directly at the interface have a large impact on device performance. This is especially important for P3HT as we will see in section 3.4. Consequently, the choice of device structure (e.g., bottom gate or top gate) is extremely important for the device performance. A popular, because convenient and easy to fabricate, structure is the bottom gate geometry with doped silicon as the gate electrode and thermally grown silicon dioxide as the gate dielectric. The silicon dioxide can be

easily functionalized with self-assembled monolayers of alkyl silanes to minimize the trap state density and change the surface energy, which influences the morphology of the polymer layer. Top contacts may be evaporated onto the semiconductor through a shadow mask. Bottom contacts are usually photolithographically patterned before the semiconductor is deposited. Even when the same electrode material (e.g., gold) is used, the injection properties and thus the contact resistance of top and bottom contact devices are different, which can affect the calculated mobilities. Also, although silicon substrates are convenient for basic research one should keep in mind that flexible polymer substrates and complex circuits require different processing techniques and materials, which can substantially affect device performance.

A new type of thin-film transistor, the electrolyte-gated transistor (EGT), has recently been introduced that allows low-voltage operation and high carrier densities [13, 14]. In these electrochemical transistors, the dielectric is replaced by an electrolyte with highly mobile anions and cations. The electrolyte is ionically conducting but electrically insulating. Typical examples of such electrolytes are blends of polyethylene oxide (PEO) with $LiClO_4$ [15], or imidazolium-based ionic liquids and iongels containing these ionic liquids [16, 17]. When a gate voltage is applied to such an electrolyte, the ions move according to their charge polarity. For example, in the case of a negative gate voltage, the cations move towards the gate electrode and the anions start to penetrate the semiconducting polymer (e.g., P3HT). In order to compensate for the extra negative charge in the polymer layer, holes are injected by the source electrode that can move through the channel to the drain (see Fig. 1d). Similar to the electrostatic accumulation regime in FETs, the source-drain current is modulated by the gate voltage, which determines the number of anions in the film. The advantage of electrolyte gating is the large amount of charge that can be accumulated in the channel at very low voltages. EGTs operate within a voltage range of less than 2 V and at high carrier densities (up to 10^{14} cm^{-2}) [18]. However, because the ions need to move in and out of the polymer layer, the switching speed of EGTs is slower than for traditional FETs. Also, the exact determination of carrier mobility in these devices is even less straightforward than for FETs with a dielectric of constant capacitance. The number of injected charges for these FETs must be determined by independent measurements of the displacement current at different gate voltage sweep rates [19] in order to extract a useful mobility number.

3 Improving and Understanding Device Performance of P3HT-FETs

The device performance of P3HT transistors depends sensitively on many factors that can be partially controlled through synthesis and processing. These factors influence the field-effect mobility, the threshold voltage, on/off current ratio, and

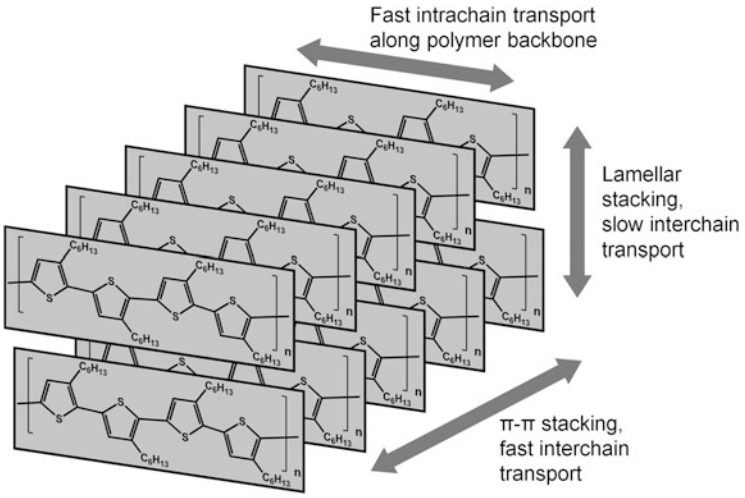

Fig. 3 Ordering of P3HT chains in crystalline aggregates and possible slow and fast charge transport directions

long-term stability of P3HT-FETs. Understanding the origin and impact of these parameters has led to substantial performance improvements in P3HT-FETs, from the first reports to today's state-of-the art devices. One of the most compelling properties of P3HT is its ability to form highly ordered π-stacks and side-chain lamella stacks (see Fig. 3). The interplay of orientation, length, and interconnectivity of these aggregates is crucial for charge transport in the plane of an FET channel and can be tuned to a large degree. Many device studies focus on the structure–property relationship, i.e., the relationship between crystallinity, size of aggregates, and carrier mobility in P3HT, which depends on a number of factors. In the following section we will discuss the most important factors and their effect on FET performance.

3.1 Regioregularity

The first P3HT-FETs demonstrated by Assadi et al. exhibited extremely low field-effect mobilities of 10^{-4} to 10^{-5} $cm^2\ V^{-1}\ s^{-1}$ [1], which would prohibit any useful application. The first major improvement in hole mobility was achieved by using highly regioregular head-to-tail P3HT (rr-P3HT) instead of the previously used regio-random P3HT [3]. This advance was made possible by a new synthetic route now known as the McCullough method, which enabled high yields of head-to-tail P3HT [20, 21] and the observation of improved ordering with a fixed stacking distance by X-ray diffraction [6]. Sirringhaus et al. subsequently showed that regioregular P3HT (>91% of head−tail attachment of side chains) formed lamellae

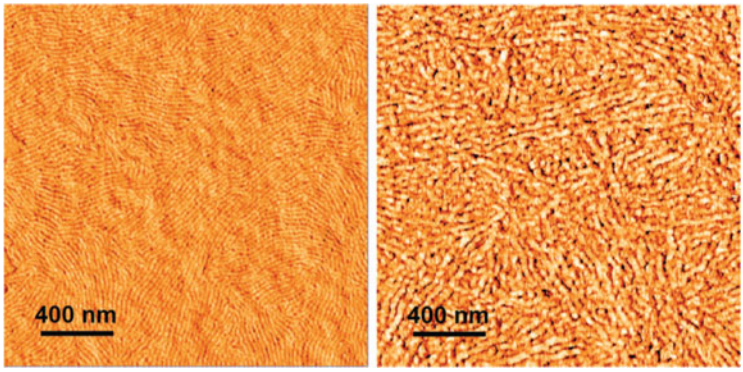

Fig. 4 AFM phase images of rr-P3HT thin films with low ($M_n = 12{,}000$ g/mol, *left*) and medium ($M_n = 21{,}000$ g/mol *right*) molecular weights. Reprinted with permission from Osaka and McCullough [23], copyright (2008) American Chemical Society

with strong π–π stacking and edge-on orientation with respect to the substrate, resulting in mobilities of up to 0.1 $cm^2\ V^{-1}\ s^{-1}$, whereas less regioregular P3HT (~80%) exhibited face-on orientation and low mobilities of about $2 \times 10^{-4}\ cm^2\ V^{-1}\ s^{-1}$ [4, 5]. High regioregularity leads to increased planarization of the polymer backbone and therefore increased conjugation length, which can be quantified by the ratio of the 0–0 and 0–1 peaks in the absorption spectrum [22]. This planarization also leads to nanofibrils, in which the P3HT chains form π–π stacks, that are easily observable by atomic force microscopy (AFM) (see Fig. 4) [23].

Nowadays it is common to use P3HT that is >95% head-to-tail regioregular and is readily commercially available. However, batch-to-batch variations are still a problem. Even small differences can result in large mobility changes, as shown by Aiyar et al. [24]. They compared two P3HT samples with similar molecular weight and polydispersity but different regioregularities (94% versus >98%) and found an order of magnitude higher mobilities for the more regioregular P3HT for all deposition conditions. By excluding all tail-to-tail defects (i.e., 100% head-to-tail regioregularity) Kohn et al. [25] demonstrated that it is possible to obtain samples with very high crystallinity (70%), which is only limited by the polydispersity of the P3HT chains and should enable clear correlations between the P3HT structure and carrier mobility.

3.2 Molecular Weight

The molecular weight (M_W) has a profound effect on most of the physical properties of any polymer. The charge carrier mobility in P3HT is no exception. The hole mobility in P3HT-FETs increases by several orders of magnitude (from 10^{-5} to

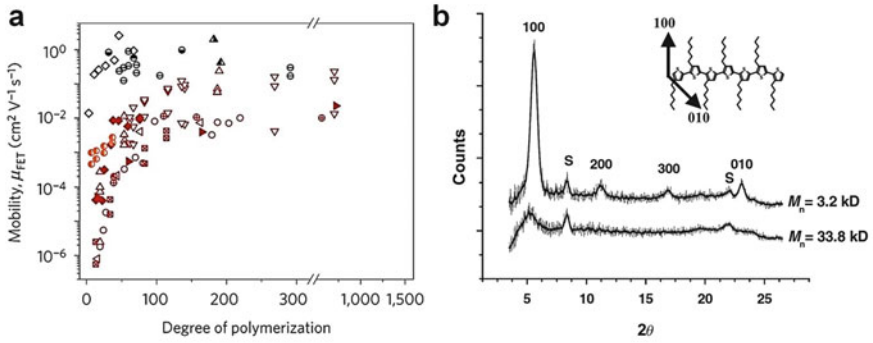

Fig. 5 (**a**) Field-effect mobility versus degree of polymerization (i.e., molecular weight) for various semiconducting polymers (*red symbols* indicate results for P3HT). Reprinted by permission from Macmillan Publishers Ltd: Nature Materials [8], copyright 2013. (**b**) X-ray diffraction analysis of high and low molecular weight P3HT thin films. Reprinted with permission from Kline et al. [25], Wiley-VCH Verlag GmbH & Co. KGaA, Weinheim, copyright 2003

0.1 $cm^2\ V^{-1}\ s^{-1}$) within a relatively narrow range of molecular weights (2–50 kg/mol) and then saturates [26–31]. Similar behavior can be found for other polythiophenes [32] and indeed many other semiconducting polymers [33], as shown in Fig. 5a. The observation of improved mobility with regioregularity and thus crystallinity of the P3HT suggested that crystallinity is the crucial factor for mobility. However, high molecular weight P3HT films are less crystalline than those of low molecular weight P3HT, as indicated by diminished X-ray diffraction peaks from the obtained films (see Fig. 5b) [26].

The formation of crystalline P3HT nanofibrils and their width increases with M_W but only up to 10 kg/mol [29]. As the molecular weight increases further, the overall crystallinity actually decreases while the hole mobility improves further. Clearly, for efficient charge transport over several micrometers the short but well-ordered nanofibrils (width <30 nm) cannot be solely responsible. Transmission electron microscopy (TEM) studies suggest that although the average crystallinity is lower for high molecular weight polymers, the connectivity between the crystalline lamellae is enhanced through so-called tie molecules that span the gap between the crystalline regions [34]. This notion explains why the mobility increases with molecular weight but not why it saturates for higher degrees of polymerization.

Noriega et al. concluded from the vast amount of literature on this topic that paracrystallinity and aggregate formation govern charge transport [8]. Paracrystallinity is a measure of the structural disorder in an imperfect crystal as random fluctuations in lattice spacing. It can be determined from the shape and breadth of X-ray diffraction peaks [35]. For a perfect crystal, the paracrystallinity factor g would be 0%, whereas 10% paracrystallinity would be representative of a strongly disordered lattice. Large paracrystalline disorder leads to deep tails of electronic states extending into the bandgap of the semiconductor and thus to higher thermal activation energies for transport and lower mobility. The paracrystallinity

parameters of P3HT thin films actually increase with molecular weight from about 3 to 7% and saturate at around the same molecular weight as the mobility. This suggests that for long polymer chains, which guarantee good connectivity between the P3HT aggregates, the paracrystallinity starts to limit charge transport and therefore carrier mobility.

3.3 Solvents, Deposition Conditions, and Post-deposition Treatment

The order and crystallinity of P3HT also depend on the film deposition conditions. Spincoating, dip-coating, and dropcasting are the most popular techniques for research. In general, slow evaporation of the solvent improves aggregation/crystallinity and thus mobility. Dropcast films tend to show superior performance over spincoated samples. A detailed study by Chang et al. showed that the use of high boiling point solvents such as trichlorobenzene instead of chloroform for spincoating P3HT led to higher crystallinity and, consequently, improvement in mobility by a factor of ten from 0.012 to 0.12 $cm^2\ V^{-1}\ s^{-1}$ for medium molecular weight P3HT (see Fig. 6) [36]. Interestingly, the dependence of the transconductance and thus the mobility on gate voltage also changed with the boiling point of the solvent. Clark et al. showed that this behavior can be correlated with the free exciton bandwidth of the P3HT aggregates, as determined from simple absorption measurements [37]. Within the multiple trapping and release model [38], a shallow distribution of localized states (i.e., narrow exciton bandwidth as seen for films spincoated from high boiling point solvent) leads to a weakly gate voltage-dependent mobility, whereas a broad distribution of localized states (i.e., also broad exciton bandwidth in films spincoated from low boiling point solvents) results in strongly gate voltage-dependent mobilities.

The spin speed also has an effect on the orientation of the P3HT chains within a spincoated film and thus on the obtained mobility because it affects the drying time. DeLongchamp et al. showed that fast spinning speeds (4,000 rpm) resulted in more plane-on orientation [determined by near-edge X-ray absorption fine structure (NEXAFS) spectroscopy] and lower mobilities, whereas low spinning speeds (250 rpm) led to edge-on orientation and higher mobilities for P3HT thin films deposited from chloroform [39].

Dropcasting is another way to ensure pre-aggregation of the polymer chains in solution and thus preferential ordering during a slow drying process. Film crystallinity as determined by AFM and X-ray diffraction is generally higher than for spincoated films [40]. Lowering the temperature during dropcasting enhances crystallinity further [41]. However, dropcast films tend to be less uniform than spincoated films. They usually show a coffee-stain effect. Similarly, long drying times and more uniform films over large areas can be obtained by doctor-blading and wire bar-coating of polymer solutions [42, 43].

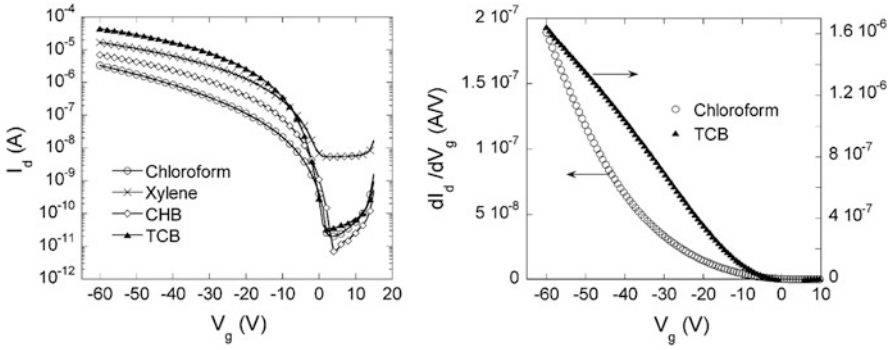

Fig. 6 *Left*: Transfer characteristics (saturation regime, $V_{DS} = -60$ V) of bottom gate/bottom contact transistors with P3HT spincoated onto HMDS-treated SiO_2 from different boiling point solvents [chloroform, xylene, cyclohexylbenzene (*CHB*) and trichlorobenzene (*TCB*)]. *Right*: Transconductance dI_{DS}/dV_G (at $V_{DS} = -60$ V) of devices spincoated from chloroform and trichlorobenzene, indicating gate voltage-dependent mobility. Reprinted with permission from Chang et al. [35], copyright (2004), American Chemical Society

For the fabrication of circuits, the semiconductor has to be patterned and neither spincasting nor dropcasting are appropriate for large scale production. Various printing techniques such as flexography, offset, gravure, screen, inkjet, or aerosol-jet printing are used [44, 45]. Each of these techniques allows for different minimum feature sizes and requires P3HT ink formulations with different viscosities, resulting in different P3HT film morphologies. For example, inkjet printing and aerosol-jet printing produce relatively rough and disordered films [46, 47]. So far, no clear correlation between the applied printing technique for P3HT thin films and device performance has been established.

In addition to the deposition technique, the preparation of the P3HT solution has an effect on the microstructure and final hole mobility within the polymer layer. Mild ultrasonication of the P3HT solution for several minutes before spincasting enhances the mobility, especially for high molecular weight P3HTs [48–50]. In a comprehensive study of microstructure and transport properties of P3HT films spincast from ultrasonicated solutions, Zhao et al. reported a 20-fold increase in field-effect mobility (from 5×10^{-4} to 0.01 $cm^2\ V^{-1}\ s^{-1}$) of high M_W (68 kDa) P3HT films spincoated from toluene after 6 min of ultrasonication compared to untreated solutions [50]. On the other hand low M_W (35 kDa) P3HT films produced in the same way showed only a slight decrease in mobility with sonication time. The observed mobility enhancement appears to be a result of the disentanglement of the P3HT chains during sonication. Entanglements are more frequent in high M_W polymers and thus the effect can be expected to be larger than for lower molecular weight polymers. Ultrasonication facilitates free movement and disentanglement of the chains, which can then form ordered aggregates more efficiently. Consequently, the lamellar thickness of the high molecular weight P3HT film increased from 14.9 to 19.3 nm with ultrasonication time, as shown by TEM. Furthermore, absorption spectra indicated an increase in the fraction of P3HT molecules involved in

aggregates from 55 to 59%. The reduction of entanglements should also reduce disorder within the π-stacks and thus lead to improved interchain transport and higher mobilities.

As shown above, aggregates are crucial for obtaining high mobility P3HT films. Another way of promoting the creation of ordered aggregates during film formation is by adding poor solvents with a higher boiling point than the main solvent to a P3HT solution. The lower volatility of the poor solvent leads to longer drying times, which again promote controlled aggregation. This was demonstrated by Park et al. who added acetonitrile (0–10%, boiling point 81°C) to solutions of P3HT in chloroform (boiling point 61°C) [51]. Absorption spectra of the mixed solutions started to show aggregation-related red-shifts and characteristic vibronic features for acetonitrile volume fractions of 17%. The crystallinity of spincast films increased. However, the maximum field-effect mobility of 0.015 $cm^2\ V^{-1}\ s^{-1}$ was found for films spincast from solutions of 1 wt% P3HT in chloroform with only 3.3 vol% acetonitrile. Higher volume fractions of acetonitrile led to precipitation and, thus, inhomogeneous films and worse FET performance. For low concentrations of acetonitrile in the precursor solution, aggregation started during the evaporation process as the volume fraction of the non-solvent increased. This also explains why adding acetonitrile to high boiling point, good solvent solutions like dichlorobenzene (boiling point 174°C) and chlorobenzene (boiling point 132°C) did not show any improvement in crystallinity or mobility.

Chang et al. added acetone, which has a lower boiling point (56°C), to chloroform solutions of P3HT and observed an increase in hole mobility from 0.0043 to 0.017 $cm^2\ V^{-1}\ s^{-1}$ for 2 vol% of acetone [52]. Absorption spectra of the solutions showed no sign of aggregation, whereas absorption spectra of the spincast films started to show peaks associated with π–π stacking in P3HT aggregates. Also, the grazing incidence X-ray diffraction of spincoated films showed an increase of the (100) peak intensity, associated with lamellar packing along the crystallographic direction perpendicular to the polymer backbone. Chloroform and acetone form a pressure-minimum (temperature-maximum) azeotrope at about 68 vol% of chloroform and 32 vol% of acetone, with a boiling point of 64.7°C [53]. Hence, during the drying process the concentration of the non-solvent acetone increased gradually up to that volume fraction and aggregate formation was facilitated. This led to the observed increase in field-effect mobilities without any additional post-deposition treatment.

The pre-aggregation can be driven to its extreme (i.e., formation of P3HT nanowires) by cooling a solution of a moderate solvent (e.g., 1,2-dichlorobenzene) [54–58] or by templating their growth from solution by carbon nanotubes [59, 60]. These nanowires can be several micrometers long and 10–20 nm wide. They show a high degree of order but transport can only occur along the π–π stacking direction. FETs based on single P3HT nanowires show reasonable mobilities of about 0.02 $cm^2\ V^{-1}\ s^{-1}$ [61, 62], whereas networks of nanowires generally show lower overall mobilities due to the limited fill-factor and necessary nanowire-to-nanowire contacts. The lower mobility in P3HT nanowires compared to the highest possible mobilities in P3HT thin films indicates that transport along the π–π stacking direction is slower than along the polymer backbone.

For some polymers, post-deposition treatment is necessary or at least beneficial to reach maximum field-effect mobilities. This is for example the case for PBTTT (structure **P2**, see Fig. 11). After annealing within the liquid-crystal mesophase, this polymer forms large crystalline areas and the hole mobility increases to 0.7 $cm^2\ V^{-1}\ s^{-1}$ [113]. For P3HT, simple annealing up to 150°C does not lead to substantial improvement in the film morphology or hole mobility [63]. Prolonged annealing above 160°C even leads to performance degradation [64]. However, moderate annealing in inert atmosphere or under vacuum increases the on/off ratio and shifts the onset voltage to more negative values (depending on the initial preparation conditions) due to the removal of oxygen from the film [47, 63]. In order to substantially increase the crystallinity of a preformed P3HT film, solvent–vapor annealing or controlled solvent swelling and deswelling is required. Carbon disulfide (CS_2) is a good solvent for swelling polythiophene thin films under controlled vapor pressure [65–67]. Within a swollen P3HT film the majority of polymer chains adopt coil-like configurations and no indication for aggregates is found. When the CS_2 vapor pressure is reduced, the film deswells and recrystallization can take place under controlled conditions. Using this technique, Crossland et al. were able to tune nucleation density and grow large P3HT spherulites with diameters of up to 100 μm [65]. Field-effect transistors produced with these recrystallized P3HT films showed high hole mobilities (up to 0.11 $cm^2\ V^{-1}\ s^{-1}$), which decreased with the number of spherulite boundaries within the channel [68].

In summary, the order and microstructure of P3HT thin films is extremely sensitive to the solvents used, deposition conditions, and post-deposition treatment. This can pose a problem for reproducibility but also enables wide tunability of transport properties with the same polymer. Hence, careful control of all processing parameters and complementary characterization techniques are crucial before drawing any conclusions from device characteristics.

3.4 Dielectric Interface

In addition to regioregularity, molecular weight, and the solution deposition conditions of P3HT, the surface treatment of the dielectric has been found to be extremely important for the orientation, crystallinity, and ultimately the carrier mobility of P3HT thin films. As mentioned above, the typical device structure used for studies on charge transport in P3HT is the bottom gate/top contact geometry with doped silicon as the gate electrode and thermally grown SiO_2 as the gate dielectric. Clean, untreated SiO_2 surfaces are terminated by –OH groups and are thus very hydrophilic. These surface groups as well as adsorbed water can act as charge traps [69, 70]. For most organic semiconductors, either solution-processed or vapor-deposited, the passivation of the SiO_2 surface with hexamethyldisilazane (HMDS) or self-assembled monolayers of alkylsilanes improves device performance with respect to both mobility and threshold voltage [71, 72]. By modifying

the end groups of the self-assembled monolayer (e.g., –CN, –F versus CH_3) and thus the surface dipole, it is possible to shift the threshold voltage and alter the orientation of organic molecules at the interface [73].

Early studies on P3HT employed HMDS-treated SiO_2 surfaces and found substantial enhancement of mobility compared to bare SiO_2 [4, 5]. This was attributed to the promotion of edge-on orientation and thus π–π stacking of the P3HT molecules. Subsequent experiments showed that using alkylsilanes, in particular octadecyltrichlorosilane (OTS), significantly improved the crystallinity and order of P3HT close to the interface [74–76]. Modern X-ray characterization techniques such as WAXS, SAXS, NEXAFS, etc. played an important role in analyzing the buried P3HT interface in these devices [77]. Overall, it has emerged that self-assembled monolayers such as OTS are crucial for the nucleation of P3HT crystallites at the dielectric surface where charge transport takes place. Kline et al. first showed that for low molecular weight P3HT, surface treatment with OTS instead of HMDS increased mobility by orders of magnitude and explained this by improved edge-on orientation and thus more shallow-angle grain boundaries between crystallites. The effect was less pronounced for high molecular weight P3HT [75]. Jimison et al. later found that the crystallinity of spincoated P3HT films was actually lower at the surface than in the bulk, whether the surface was treated or not. However, the interaction of the alkyl chains of the polymer with those of the OTS apparently promoted nucleation and thus the density of interface-nucleated crystallites was 20 times larger than on bare SiO_2, leading to higher carrier mobilities [76].

It is important to realize that these results are to a large degree specific to the particular bottom gate device structure. The mobility in top-gated FETs, which are common in flexible electronics, depends on the roughness of the P3HT surface and the microstructure of the film at the top surface. Spincoating or printing a gate dielectric on top also means that the semiconductor film is exposed to another solvent. Even if an orthogonal solvent is chosen that does not dissolve the P3HT, it may swell the film and thus alter its structure. In addition, the dielectric constant of the dielectric plays a role and influences the charge carrier mobility due to dipolar disorder and the associated broadening of the density of states [78, 79].

3.5 Alignment and Grain Boundaries

Detailed control and characterization of the microstructure in P3HT thin films enables inference as to the nature of charge transport in this conjugated polymer. Early studies had suggested that the π–π stacking in P3HT is responsible for fast charge transport [5]. Although this is true, because interchain transport ultimately limits the overall mobility in P3HT thin films, the π–π stacking direction is not the direction of highest mobility. According to theoretical calculations [80, 81], the fastest charge transport should still be that along the polymer backbone (i.e., the intrachain transport), as is the case for many other conjugated polymers [82, 83]. In

order to verify this notion experimentally, a number of transport measurements on P3HT films with predetermined alignment were carried out. The earliest study of charge transport in aligned P3HT on friction-transferred polytetrafluoroethylene (PTFE) by Amundson et al. indicated in-plane anisotropy of the mobility [84], but the roughness of the PTFE alignment layer and its impact on mobility did not allow for a clear distinction of the origin of the mobility differences. Later, Jimison et al. investigated the influence of grain boundaries on transport in aligned P3HT using a directional crystallization technique to form films with an anisotropic fiber structure containing crystalline regions that were separated by disordered grain boundaries [85]. The polymer chains within crystallites were oriented parallel to the fiber axis. Top-contact FETs with charge transport either parallel or perpendicular to the fiber direction showed mobilities that were an order of magnitude higher along the fibers than across. Jimison et al. concluded that the effective device mobility was dominated by the mobility in the grain boundaries and, thus, the observed mobility anisotropy in the aligned P3HT films was mainly due to different grain-boundary orientations. That is, holes crossed the grain boundaries along the fiber direction much more easily than the boundaries across fibers. Along a fiber, the different crystallites can be bridged by tie molecules, which maintain connectivity. This is not possible for crystallites in neighboring fibers. Efficient π–π-overlap is also not likely due to disorder at the fiber edge. Thus, not just the number of grain boundaries but also their placement and relative orientation are important for maximizing the overall charge transport.

A convenient way of aligning P3HT thin films without introducing defects and independent of the substrate is the application of strain by stretching a pre-cast film on a rubbery (polydimethylsiloxane, PDMS) substrate before transferring it onto the FET substrate. This was demonstrated by O'Connor et al. [86]. The crystalline parts of the films aligned in the direction of applied strain. The degree of alignment increased proportionally with strain while the amorphous regions remained highly disordered. In short-channel (5 μm) FETs, the mobility increased by almost a factor of 2 in the direction of strain but decreased by a factor of 4–5 perpendicular to it, reaching a maximum ratio of 9 at a strain of 100%. Importantly, the strained films exhibited an increasing amount of plane-on orientation instead of the usually observed edge-on orientation, which enables transport along the π–π stacking direction. In agreement with theory, these results suggest that transport along the polymer backbone is fastest, followed by transport in the π–π stacking direction and side-chain stacking direction.

This direction dependence was further corroborated by studies of mobility anisotropy within P3HT films without the influence of grain boundaries. Crossland et al. [68] grew large spherulites (diameters > 100 μm) of P3HT by controlled solvent swelling with carbon disulfide and deposited arrays of electrodes on top., This arrangement enabled FET measurements for various angles with respect to the radial spherulite growth direction. Mobilities were again higher along the polymer backbones than along the π–π stacking direction despite periodic amorphous interlamellar interruptions. Fisher et al. tested this further by producing aligned films of P3HT with different molecular weights by applying an electric field during

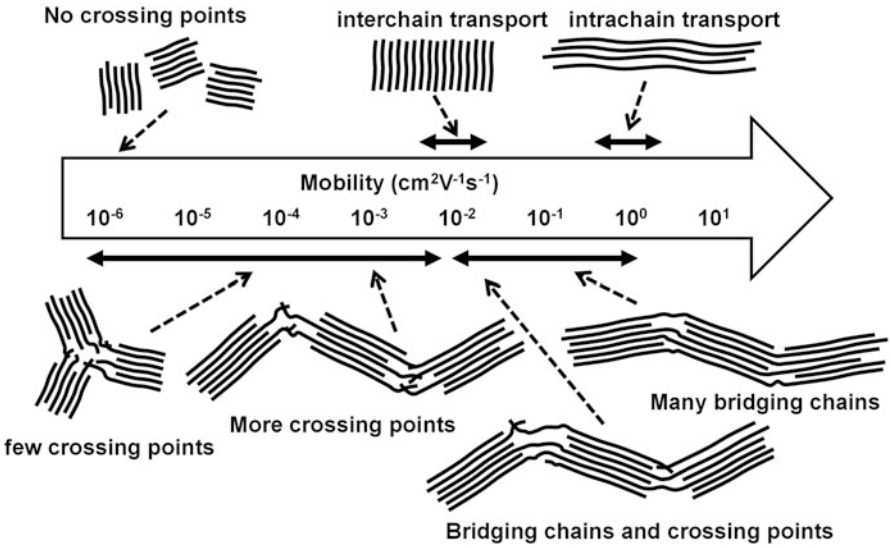

Fig. 7 Possible arrangements of long and short P3HT polymer chains and related hole mobilities, as suggested in Lan and Huang [79]

recrystallization and by low nucleation density recrystallization under confinement [87]. In the former case, charge transport takes place along the polymer chains and across low-angle boundaries between lamellae. In the latter case, charges have to move in the π–π stacking direction. Interestingly, only for high molecular weight samples a significantly higher mobility (~0.01 $cm^2\ V^{-1}\ s^{-1}$) along the polymer backbones (i.e., perpendicular to the π–π stacking direction) compared to the π–π stacking direction (~0.003 $cm^2\ V^{-1}\ s^{-1}$) was observed. Because transport along the backbone direction is ultimately limited by the boundaries between adjacent lamellae, long polymer chains are more likely to act as tie molecules connecting the two lamellae. In samples with low molecular weight this is less likely and the mobility is limited even compared to transport in the π–π stacking direction, which is slower but does not require tie molecules.

Similar differences between intrachain and interchain transport were also found for the related π-stacked polythiophene poly{2,5-bis(3-alkylthiophen-2-yl)thieno [3,2-b]thiophene} (PBTTT; **P2** in Fig. 11) [88]. Here, the mobilities along the chains in well-ordered ribbons formed by zone casting ranged from 0.13 to 0.2 $cm^2\ V^{-1}\ s^{-1}$ versus 0.026 to 0.06 $cm^2\ V^{-1}\ s^{-1}$ perpendicular to the chains, i.e., in the π–π stacking direction. The obtained ratio was not as high as expected, probably due to limitation of the mobility along the chains by disordered grain boundaries.

The following picture of charge transport in semicrystalline P3HT and similar polythiophenes emerges, as summarized by Lan et al. and shown in Fig. 7 [80]. The fastest transport is intrachain transport along the polymer backbone. For optimal transport, the polymer backbone should be strongly planarized to allow for long

conjugation lengths. However, as the channel of a transistor is much longer than a single polymer chain, interchain hopping is necessary for macroscopic transport. This is facilitated by tie molecules that bridge adjacent crystallites. For optimal bridging the boundary angle should be low, leading to mobility anisotropy in aligned semicrystalline films. The need for tie molecules also explains the increase in mobility with molecular weight, although P3HT films with lower molecular weight show higher crystallinity and lower paracrystalline disorder than high molecular weight films. The well-ordered crystalline regions are not connected to each other and hence transport is strongly inhibited. Charge transport along the π–π stacking direction is slower than perpendicular to it but faster than in the side-chain stacking direction, in which long alkyl chains and minimal orbital overlap hinder charge transfer.

In summary, obtaining maximum hole mobilities in P3HT transistors requires long, well-planarized and π–π-stacked polymer chains that are well connected via tie molecules at shallow angles. High crystallinity is no guarantee for high mobility; instead, the connectivity of crystalline domains plays a major role in macroscopic charge transport.

3.6 Blends and Copolymers

In contradiction to what one might expect, mixing P3HT with insulating polymers can actually improve the carrier mobility and stability of P3HT-FETs substantially. In the simplest case, the air stability of the device is improved by forming an encapsulation layer of the insulating polymer on top of the P3HT. However, through judicious choice of polymer and processing conditions it is possible to affect the P3HT morphology in a way that leads to higher hole mobilities despite an excess of the insulating polymer. This was first demonstrated by Goffri et al. for blends of P3HT and semicrystalline isotactic polystyrene or polyethylene [89]. The blends were processed in a way that allowed the P3HT to crystallize first (e.g., by casting from a hot solution onto a hot substrate), followed by crystallization of the semicrystalline insulating polymer. This propelled the already solidified P3HT to the surface and interface of the film with the substrate. The resulting vertically stratified structure creates continuous films of P3HT at the dielectric interface. Even at blend compositions as low as 3 wt% of P3HT this procedure led to FETs with hole mobilities of 0.01 $cm^2\ V^{-1}\ s^{-1}$. In addition, these blend devices were self-encapsulating and thus more air-stable than pure P3HT-FETs. In other cases, the formation of crystalline nanofibrils within an insulating matrix is observed by TEM and AFM (e.g., for P3HT/PS blends in dichloromethane and poly (3-butylthiophene)/PS in 1,2-dichlorobenzene) [56, 90]. Even at low volume fractions they can maintain continuous pathways for charge transport and mobilities ranging from 0.006 to 0.014 $cm^2\ V^{-1}\ s^{-1}$.

Although blends can show intriguing phase separation behavior, control over the micro- and nanostructure of such films is limited. Predetermining the film's

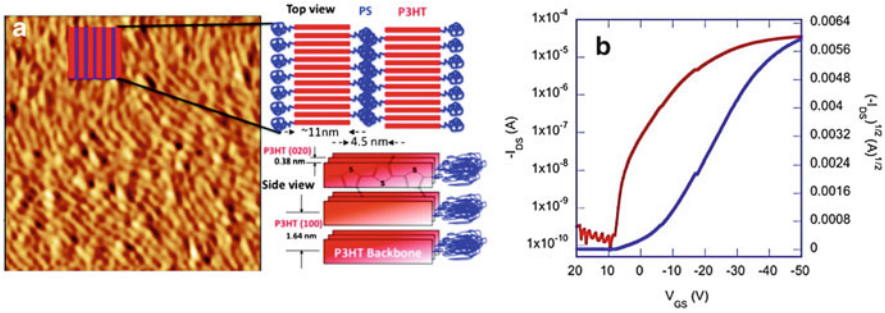

Fig. 8 (**a**) AFM images (500 × 500 nm) of the lamellar structure of a PS-*b*-P3HT copolymer film with schematic illustration of the lamellar nanostructure. (**b**) Transfer characteristics of a bottom contact field-effect transistor with 85 wt% P3HT. Reprinted with permission from Yu et al. [92]. Copyright (2011) American Chemical Society

morphology by the molecular structure of the components would be very beneficial. This is the goal for designing block copolymers of P3HT and insulating polymers of different kinds that phase-separate on the nanoscale. Variation in the length of the different blocks leads to different equilibrium morphologies (e.g., lamellar or cylindrical) [91], which could be utilized for devices. Two different types of diblock copolymers can be distinguished: rod–coil copolymers, which have an amorphous insulating block [92–94], and crystalline diblock copolymers, in which the insulating polymer is also semicrystalline and adds another driving force for ordering [95–98]. Depending on the employed synthetic route, either the P3HT length or the length of the insulating part can be varied. Unfortunately, many of these synthetically challenging and therefore expensive block copolymers do not show significantly higher mobilities than their pure rr-P3HT counterparts and are certainly far from reaching the high mobilities necessary for most applications. In the best cases, the mobilities remained similar and the threshold voltage and on/off current ratio were improved. For example, films of P3HT-polyethylene copolymers that were processed from hot solutions similar to blends of the same composition resulted in high mobility (0.01–0.1 $cm^2\ V^{-1}\ s^{-1}$) FETs with good on/off ratios (~10^5). Again, crystallization of the polyethylene block probably caused the pre-crystallized P3HT segments to form a low-percolation-threshold co-continuous structure [97]. Yu et al. synthesized polystyrene-*block*-poly(3-hexylthiophene) (PS-*b*-P3HT) block copolymers with fixed polystyrene coil length [93]. Thin films of these copolymers showed a lamellar structure after spincoating from trichlorobenzene and thermal annealing (shown in Fig. 8). The best mobilities (~0.08 $cm^2\ V^{-1}\ s^{-1}$) were found for a diblock copolymer with a relatively high P3HT content of 85 wt% compared to the pure rr-P3HT (~0.046 $cm^2\ V^{-1}\ s^{-1}$). Importantly, the on/off ratio was substantially increased from 8×10^3 to 10^5 and long-term stability was also improved.

The device characteristics of blends and copolymers of P3HT and insulating polymers are striking, especially because the formation of co-continuous transport paths within such a matrix has been unclear. Lu et al. could show that moderate

doping by oxygen or other p-dopants like F4-TCNQ is necessary to obtain high mobilities and good on/off ratios in such devices [7]. Blends of 5 wt% P3HT and polystyrene that were processed under strict exclusion of oxygen and annealed under vacuum initially showed almost no charge transport. The devices improved after moderate doping by storing the devices in a nitrogen glovebox with an oxygen concentration at the parts per million level. Mobilities reached 0.1–0.2 $cm^2 V^{-1} s^{-1}$ and on/off ratios of 10^6 were accomplished. Similar behavior was found for other thiophene-based polymers and for doping with F4-TCNQ. Lu et al. argued that the specific morphology of the P3HT network was crucial for this performance improvement. Most of the semiconductor formed a poorly interconnected network of nanometer-sized crystallites at the top surface, while parts of this network penetrated the insulating matrix closer to the gate dielectric in a bottom gate/top contact configuration. In the doped state, the network paths penetrating into the matrix were depleted when a positive voltage was applied and thus interrupted charge transport. This led to low off-currents. When a negative voltage was applied, holes accumulated in those parts and the entire network became conducting. The FET was in its on-state. In the undoped state, charge accumulation occurred first in the network parts close to the gate, leaving the larger parts on the top surface screened. They were thus dominated by trap states and were essentially non-conducting. The high mobilities could be explained by good interchain order of the P3HT, as indicated by a strong 0–0 vibronic transition in the absorption spectrum and narrow (020) X-Ray diffraction peaks. Given the excellent performance and stability of these devices containing only small amounts of semiconducting polymer, they are very interesting for various applications. A simple circuit of a unipolar inverter based on two blend FETs was fabricated and showed good switching behavior, with gains as high as 60. Thus, simple blends instead of complicated and expensive copolymers might ultimately push the performance of P3HT-FETs beyond the current limits.

3.7 Doping and On/Off Ratio

As already mentioned above, one of the major problems of P3HT-based FETs is the low on/off ratio due to unintentional doping. A low off-current is important for almost all electronic applications. For example, transistors that drive pixels should have an on/off ratio of 10^9 to achieve maximum contrast. For digital logic, a low off-current reduces unwanted power dissipation. The high off-currents in P3HT transistors are due to p-doping of the films by oxygen. The additional positive charge carriers have to be compensated by the gate voltage, which leads to positive turn-on voltages in many P3HT-FETs. Also, the influence of the gate field extends only few nanometers into the channel, whereas the whole P3HT film is doped. This results in high bulk conductance and thus high off-currents (see Fig. 9).

Early on, the p-doping of P3HT by oxygen was attributed to the formation of a reversible P3HT:O_2 charge transfer complex [100]. Interestingly, doping of P3HT

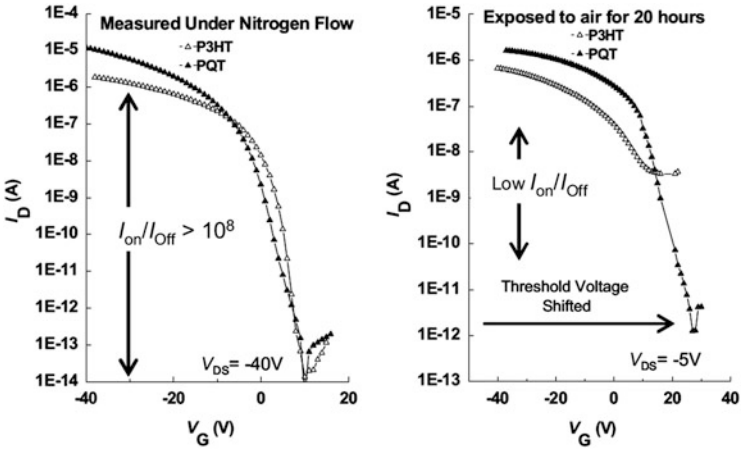

Fig. 9 Transfer characteristics of FETs fabricated with PQT (*filled triangles*) and P3HT (*empty triangles*) as semiconductors and measured under nitrogen flow (*left*). The same devices were exposed to air for 20 h (*right*). Reprinted with permission from Arias et al. [103], Wiley-VCH Verlag GmbH & Co. KGaA, Weinheim, copyright 2006

is very slow in the dark even under atmospheric oxygen pressure but very fast when accompanied by illumination with near-infrared or visible light. Liao et al. investigated the kinetics of doping and de-doping of P3HT under various conditions [101]. They found that even in a moderate vacuum with very low oxygen background pressure doping occurs within minutes under illumination. Because it is very difficult to exclude all oxygen during commercial fabrication processes, this would pose a significant problem for the application of P3HT in any commercial devices, although de-doping in the dark and under vacuum is possible. At room temperature this is a slow process, but can be significantly enhanced by annealing close to the glass transition temperature of P3HT in a vacuum. The type of substrate/dielectric and the porosity of the P3HT film also play a role [102]. Non-polar interfaces are preferable in order to slow down doping.

Sperlich et al. investigated the species formed during exposure of P3HT to oxygen and light using electron paramagnetic resonance (EPR), photoluminescence (PL), and PL-detected magnetic resonance (PLDMR) [103]. They confirmed the formation of a positive polaron and a negative charge transfer complex after excitation of the P3HT to the first excited singlet state, which then reacts with oxygen. This process is fast compared to the same reaction in the dark. However, the authors also found irreversible photooxidation, which is the result of the reaction of the excited P3HT triplet with oxygen. This process only occurs under intense visible light illumination or UV exposure and leads to degradation of the P3HT. This photooxidation cannot be reversed by applying a vacuum.

Although the unintentional p-doping of P3HT is mostly reversible, it constitutes a problem for device operation and several approaches to make FETs less sensitive to oxygen have been pursued. One way is to modify the chemical structure of the

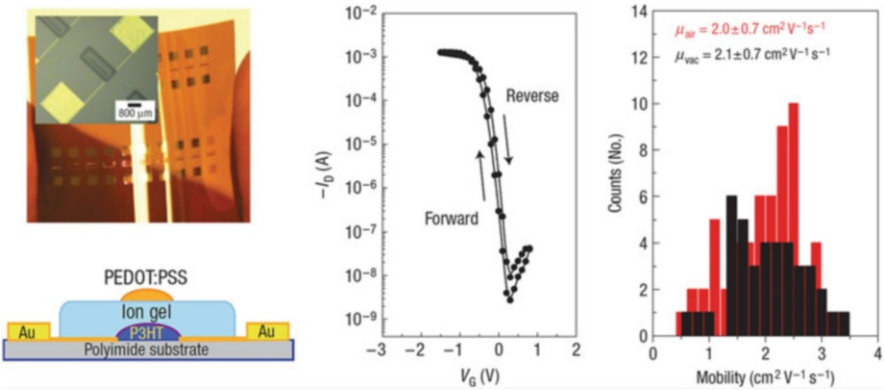

Fig. 10 From *left* to *right*: Optical micrograph, schematic illustration, transfer characteristics, and mobility distribution of electrolyte-gated P3HT transistors with high charge carrier mobilities. Reprinted by permission from Macmillan Publishers Ltd: Nature Materials [17], copyright 2008

polythiophene to increase the ionization potential, as in the dialkylated quaterthiophene PQT (**P1** in Fig. 11). Another method is self-encapsulation, as shown in Fig. 9 [99, 104]. For self-encapsulation, the P3HT is mixed with another polymer (e.g., polymethylmethacrylate, PMMA) in solution and phase separates vertically during spincoating on octyltrichlorosilane-treated substrates. The PMMA forms an encapsulation layer on top, which enables stable operation of P3HT-FETs with high on/off ratios in air as well as additional encapsulation with inorganic layers without damaging the semiconductor. Here also, blends of P3HT and insulating polymers may solve both mobility and stability issues and thus enable future application in circuits that have to operate in ambient conditions over long periods of time.

3.8 Electrochemical Doping

Electrolyte gating allows for the accumulation of very high charge carrier densities in organic FETs and operation at very low voltages. As shown by Tanase et al., the carrier mobility in polymers depends strongly on the induced charge carrier density. This is commonly found for P3HT as well [9]. By using electrolyte gating Xia et al. examined the hole mobility in P3HT for carrier densities up to 4×10^{14} cm^{-2} [18]. They found an increase in mobility from 0.005 to 1.2 cm^2 V^{-1} s^{-1} and higher (see Fig. 10) [17]. The high mobilities, low operating voltages, and the fact that the necessary electrolytes can be printed in the form of iongels enable the production of fully printed, flexible circuits (e.g., inverters, ring-oscillators, and D flip-flop circuits) based on P3HT-EGTs with good performance and fast switching times [17, 47, 105]. Due to the efficient gating by penetration of ions into the P3HT and thus compensation of unintentional doping, the on/off ratios of P3HT-EGT are very good (10^6) and threshold voltages are around zero even when the devices are printed in air [47].

The high carrier densities that are possible with electrolyte gating raise the question of what happens if the carrier density is increased close to one charge per monomer unit in the P3HT chain. Would an insulator-to-metal transition be possible? Wang et al. demonstrated a stable Hall effect in electrolyte-gated P3HT films [106], which was possible due to a crossover from a strongly non-adiabatic, variable range hopping regime to an adiabatic, diffusive, band-like transport regime at three-dimensional hole densities of up to 10^{21} cm^{-3}, corresponding to 0.2 holes per thiophene ring. However, probably due to doping-induced disorder at these high hole densities, carrier wavefunction delocalization and Coulomb gap collapse and thus insulator-to-metal transition did not occur. Nevertheless, this experiment shows the potential of studying charge transport in P3HT at the limits of carrier density and thus examining the fundamental properties of conjugated polymers.

4 New Polythiophene Derivatives for FETs

Although interest in P3HT as a model system is still strong, many new versions of thiophene-based semiconducting polymers have been developed over the past decade. The main design criteria were stability against oxygen doping, large area ordering, solution-processability, and high carrier mobility. To achieve these properties, the number, length, and position of alkyl side chains was varied and fused thiophene moieties and electron-deficient comonomer units were introduced. The resulting new materials can reach hole mobilities of up to 10 $cm^2\ V^{-1}\ s^{-1}$ in some cases [107, 108] and can be used to study structure–property relationships. Detailed synthetic approaches and molecular designs have been discussed in a number of reviews [23, 109–112]; here we will only present a few examples of polythiophene derivatives that are particularly promising for FET applications.

Improving the air stability of polythiophenes is crucial for their applicability in commercial devices. To achieve this, the position of the highest occupied molecular orbital (HOMO) energy level has to be shifted further away from the vacuum level, i.e., the ionization potential has to be increased to values larger than −4.9 eV. One possible method is to reduce the coplanarity of the system and thus the conjugation length, although this will also reduce π–π stacking and carrier mobility. The ionization potential also depends on the electron density of the conjugated system. Introducing electron-withdrawing groups to the conjugated system or reducing the density of electron-donating groups will therefore shift the HOMO level further away from the vacuum level. The first advance in this direction was reported by Ong et al., who developed dialkylated quaterthiophene polymers (usually named PQT; **P1** in Fig. 11) [104]. Two thiophene units separate the alkyl-bearing units and prevent them from interfering with each other. The favorable orientation of the alkyl chains and their low density lead to close π–π stacking and mobilities as high a 0.14 $cm^2\ V^{-1}\ s^{-1}$. The central thiophene units

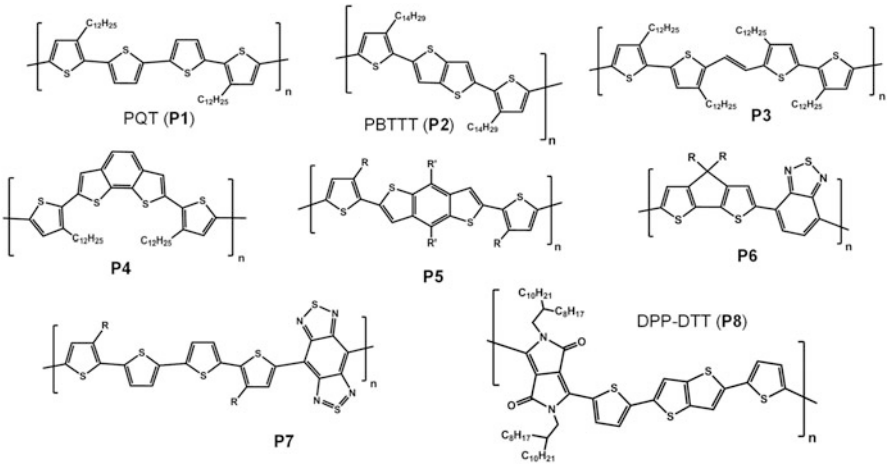

Fig. 11 Examples of polythiophenes and polythiophene copolymers with modified ionization potential or higher charge carrier mobility than P3HT

allow for enough rotational freedom to reduce the conjugation length and therefore increase the ionization potential by 0.1 eV, which makes PQT significantly more air-stable than P3HT (see Fig. 9) [99]. However, this rotational freedom also reduces overall ordering, which led McCullough and coworkers to introduce a fused thieno[3,2-b]thiophene unit [113]. The thienothiophene units are quite rigid and planarize the backbone, which is advantageous for π–π stacking and intra- and intermolecular charge transport. FETs based on these so-called PBTTTs (**P2** in Fig. 11) can reach mobilities of up to 0.72 $cm^2\ V^{-1}\ s^{-1}$ after annealing into the mesophase, which induces very large crystalline domains with extended nanoribbons. Due to the higher ionization potential of −5.1 eV, PBTTTs are also relatively stable in air. Transport along the PBTTT backbone is typically 3–5 times faster than in the π–π stacking direction, as shown for zone-cast films with large and aligned nanoribbon domains [88]. Extending the PQT approach, Kim et al. showed that tetraalkylated PQT with a central vinylene group inserted between two head-to-head oriented thiophene units (**P3** in Fig. 11) experiences less steric repulsion [114]. The vinylene group decreased the band gap and increased the degree of planarity. However, long dodecyl side chains were necessary to provide solubility. After annealing at 200°C the films were highly crystalline. Top-gate FETs showed hole mobilities of up to 1 $cm^2\ V^{-1}\ s^{-1}$ and better air-stability than P3HT.

Müllen and coworkers demonstrated that the incorporation of the benzo [2,1-b;3,4-b′]dithiophene unit into a polythiophene (**P4** in Fig. 11, with $R = n\text{-}C_{12}H_{25}$) had several advantageous effects [115]. First, the ionization potential increased, making the polymer more air-stable. Second, the extended π-system ensured good stacking properties. Placing solubilizing alkyl side chains only on

the neighboring thiophene units led to a slight curvature of the polymer backbone. This modification increased solubility (in dichlorobenzene) and avoided very strong aggregation, which would impede ordered film formation. The hole mobility of such an optimized conjugated polymer was >0.1 $cm^2\ V^{-1}\ s^{-1}$ without any special annealing or processing conditions. The linear isomer (**P5** in Fig. 11, with $R' = H$, $R = n\text{-}C_{12}H_{25}$) also packed very tightly, but here the π–π-interactions were too strong and led to precipitation during processing and thus low uniformity of the thin films. The resulting field-effect mobilities were ten times lower than those of the curved **P4**. Pan et al. showed that addition of alkyl side chains to the central, linear benzo[1,2-b:4,5-b′]dithiophene unit (**P5**, with $R' = R = n\text{-}C_6H_{13}$ or $R' = R = n\text{-}C_{10}H_{21}$) enabled good solubility in 1,2-dichlorobenzene and gave highly ordered films with mobilities of 0.25 and 0.4 $cm^2\ V^{-1}\ s^{-1}$, respectively, and high on/off ratios of 10^6, combined with good air-stability [109, 116, 117].

The cyclopentadithiophenes (CPDT) are another class of promising fused thiophene-based materials. In CPDTs, the bridging carbon atom with the alkyl substituents is sp^3-hybridized and does not participate in the delocalization along the polymer backbone. Films of CPDT homopolymers showed a disordered, amorphous structure and only low (10^{-4} $cm^2\ V^{-1}\ s^{-1}$) mobilities [118]. In contrast, copolymers of CPDT with the electron-withdrawing group 2,1,3-benzothiadiazole (BT) (CPDT-BT; **P6** in Fig. 11, with $R = n\text{-}C_{16}H_{33}$) exhibited much higher mobilities [119], which could be increased up to 3.3 $cm^2\ V^{-1}\ s^{-1}$ by optimized processing [120, 121].

The high mobilities of the CPDT-BT copolymers renewed interest in thiophene copolymers with electron-deficient comonomers. Fan et al. synthesized a copolymer of the highly electron-withdrawing benzobisthiadiazole (BBT) and dialkylated quaterthiophene (**P7** in Fig. 11, with R = 2-octyldodecyl). This polymer packed with a very short π–π stacking distance of 3.5 Å and exhibited an average hole mobility of 1.8 $cm^2\ V^{-1}\ s^{-1}$ after annealing at 280°C [122]. Due to its donor–acceptor structure, the bandgap of this polymer is quite small (0.7 eV) and the lowest unoccupied molecular orbital (LUMO) is low enough to enable electron injection and thus ambipolar charge transport.

All these examples show that, although P3HT is no longer in the race as a high-mobility semiconducting polymer, the structural motifs of thiophenes and fused thiophenes are still important as building blocks for the next generation of polymer semiconductors. Even the current record holders with hole mobilities of up to 10 $cm^2\ V^{-1}\ s^{-1}$ that are based on the acceptor moiety *N*-alkyl diketopyrrolo-pyrrole (DPP) are copolymers with several thiophene units (e.g., P-29-DPPDBTE[107]) or dithienylthieno[3,2-b]thiophene (DPP-DTT[106]; **P8** in Fig. 11). The high mobilities of these polymers are not based on high crystallinity but on a morphology with small length-scale, short contacts interconnected by polymer backbones that allow one-dimensional transport. These short contacts are enhanced by dipolar interactions between neighboring backbones, as for example in DPP copolymers, in which the polar pyrrole units drive aggregation through noncovalent interactions [123].

5 Conclusions

Despite its long history, the intricacies and complexities of charge transport in P3HT field-effect transistors still fascinate scientists. Over the last few years a more complete picture of the relationship between film morphology and charge carrier mobility has emerged thanks to advanced characterization and processing techniques. At the same time, it has become obvious that the maximum mobilities of P3HT are fundamentally limited and so new high-mobility thiophene-based polymers have entered the race towards the application of polymer transistors in organic electronics. Although P3HT may no longer be the prime candidate for application in circuits, the many possible variations in morphology (depending on molecular structure and processing) and their impact on carrier mobility in thin films will continue to give insights into the fundamental principles of charge transport in conjugated polymers.

References

1. Assadi A, Svensson C, Willander M, Inganas O (1988) Field-effect mobility of poly (3-hexylthiophene). Appl Phys Lett 53:195–197
2. Paloheimo J, Kuivalainen P, Stubb H, Vuorimaa E, Yli-Lahti P (1990) Molecular field-effect transistors using conducting polymer Langmuir–Blodgett films. Appl Phys Lett 56:1157–1159
3. Bao Z, Dodabalapur A, Lovinger AJ (1996) Soluble and processable regioregular poly (3-hexylthiophene) for thin film field-effect transistor applications with high mobility. Appl Phys Lett 69:4108–4110
4. Sirringhaus H, Tessler N, Friend RH (1998) Integrated optoelectronic devices based on conjugated polymers. Science 280:1741–1744
5. Sirringhaus H, Brown PJ, Friend RH, Nielsen MM, Bechgaard K, Langeveld-Voss BMW, Spiering AJH, Janssen RAJ, Meijer EW, Herwig P et al (1999) Two-dimensional charge transport in self-organized, high-mobility conjugated polymers. Nature 401:685–688
6. McCullough RD, Tristram-Nagle S, Williams SP, Lowe RD, Jayaraman M (1993) Self-orienting head-to-tail poly(3-alkylthiophenes): new insights on structure–property relationships in conducting polymers. J Am Chem Soc 115:4910–4911
7. Lu G, Blakesley J, Himmelberger S, Pingel P, Frisch J, Lieberwirth I, Salzmann I, Oehzelt M, Di Pietro R, Salleo A et al (2013) Moderate doping leads to high performance of semiconductor/insulator polymer blend transistors. Nat Commun 4:1588
8. Noriega R, Rivnay J, Vandewal K, Koch FPV, Stingelin N, Smith P, Toney MF, Salleo A (2013) A general relationship between disorder, aggregation and charge transport in conjugated polymers. Nat Mater 12:1038–1044
9. Tanase C, Meijer EJ, Blom PWM, de Leeuw DM (2003) Unification of the hole transport in polymeric field-effect transistors and light-emitting diodes. Phys Rev Lett 91:216601
10. Natali D, Fumagalli L, Sampietro M (2007) Modeling of organic thin film transistors: effect of contact resistances. J Appl Phys 101:014501–014512
11. Gelinck G, Heremans P, Nomoto K, Anthopoulos TD (2010) Organic transistors in optical displays and microelectronic applications. Adv Mater 22:3778–3798
12. Sze SM (2002) Semiconductor devices – physics and technology, 2nd edn. Wiley, New York

13. Panzer MJ, Frisbie CD (2008) Exploiting ionic coupling in electronic devices: electrolyte-gated organic field-effect transistors. Adv Mater 20:3177–3180
14. Kim SH, Hong K, Xie W, Lee KH, Zhang S, Lodge TP, Frisbie CD (2012) Electrolyte-gated transistors for organic and printed electronics. Adv Mater 25:1822–1846
15. Panzer MJ, Frisbie CD (2006) High carrier density and metallic conductivity in poly (3-hexylthiophene) achieved by electrostatic charge injection. Adv Funct Mater 16:1051–1056
16. Lee J, Panzer MJ, He Y, Lodge TP, Frisbie CD (2007) Ion gel gated polymer thin-film transistors. J Am Chem Soc 129:4532–4533
17. Cho JH, Lee J, Xia Y, Kim B, He YY, Renn MJ, Lodge TP, Frisbie CD (2008) Printable ion-gel gate dielectrics for low-voltage polymer thin-film transistors on plastic. Nat Mat 7:900–906
18. Xia Y, Cho JH, Lee J, Ruden PP, Frisbie CD (2009) Comparison of the mobility-carrier density relation in polymer and single-crystal organic transistors employing vacuum and liquid gate dielectrics. Adv Mater 21:2174–2179
19. Xie W, Frisbie CD (2011) Organic electrical double layer transistors based on rubrene single crystals: examining transport at high surface charge densities above 1013 cm^{-2}. J Phys Chem C 115:14360–14368
20. McCullough RD, Lowe RD (1992) Enhanced electrical conductivity in regioselectively synthesized poly(3-alkylthiophenes). J Chem Soc Chem Commun 1992(1):70–72
21. McCullough RD, Lowe RD, Jayaraman M, Anderson DL (1993) Design, synthesis, and control of conducting polymer architectures: structurally homogeneous poly (3-alkylthiophenes). J Org Chem 58:904–912
22. Clark J, Silva C, Friend RH, Spano FC (2007) Role of intermolecular coupling in the photophysics of disordered organic semiconductors: aggregate emission in regioregular polythiophene. Phys Rev Lett 98:206406
23. Osaka I, McCullough RD (2008) Advances in molecular design and synthesis of regioregular polythiophenes. Acc Chem Res 41:1202–1214
24. Aiyar AR, Hong J-I, Reichmanis E (2012) Regioregularity and intrachain ordering: impact on the nanostructure and charge transport in two-dimensional assemblies of poly (3-hexylthiophene). Chem Mat 24:2845–2853
25. Kohn P, Huettner S, Komber H, Senkovskyy V, Tkachov R, Kiriy A, Friend RH, Steiner U, Huck WTS, Sommer J-U, Sommer M (2012) On the role of single regiodefects and polydispersity in regioregular poly(3-hexylthiophene): defect distribution, synthesis of defect-free chains, and a simple model for the determination of crystallinity. J Am Chem Soc 134 (10):4790–4805
26. Kline RJ, McGehee MD, Kadnikova EN, Liu JS, Frechet JMJ (2003) Controlling the field-effect mobility of regioregular polythiophene by changing the molecular weight. Adv Mater 15:1519–1522
27. Chang JF, Clark J, Zhao N, Sirringhaus H, Breiby DW, Andreasen JW, Nielsen MM, Giles M, Heeney M, McCulloch I (2006) Molecular-weight dependence of interchain polaron delocalization and exciton bandwidth in high-mobility conjugated polymers. Phys Rev B 74:115318
28. Zen A, Pflaum J, Hirschmann S, Zhuang W, Jaiser F, Asawapirom U, Rabe JP, Scherf U, Neher D (2004) Effect of molecular weight and annealing of poly(3-hexylthiophene)S on the performance of organic field-effect transistors. Adv Funct Mater 14:757–764
29. Zhang R, Li B, Iovu MC, Jeffries-El M, Sauvé G, Cooper J, Jia S, Tristram-Nagle S, Smilgies DM, Lambeth DN et al (2006) Nanostructure dependence of field-effect mobility in regioregular poly(3-hexylthiophene) thin film field effect transistors. J Am Chem Soc 128:3480–3481
30. Kline RJ, McGehee MD, Kadnikova EN, Liu JS, Frechet JMJ, Toney MF (2005) Dependence of regioregular poly(3-hexylthiophene) film morphology and field-effect mobility on molecular weight. Macromolecules 38:3312–3319

31. Virkar AA, Mannsfeld S, Bao Z, Stingelin N (2010) Organic semiconductor growth and morphology considerations for organic thin-film transistors. Adv Mater 22:3857–3875
32. Verilhac J-M, Pokrop R, LeBlevennec G, Kulszewicz-Bajer I, Buga K, Zagorska M, Sadki S, Pron A (2006) Molecular weight dependent charge carrier mobility in poly(3,3″-dioctyl-2,2′:5′,2″-terthiophene). J Phys Chem B 110:13305–13309
33. Donley CL, Zaumseil J, Andreasen JW, Nielsen MM, Sirringhaus H, Friend RH, Kim JS (2005) Effects of packing structure on the optoelectronic and charge transport properties in poly(9,9-Di-N-octylfluorene-Alt-benzothiadiazole). J Am Chem Soc 127:12890–12899
34. Brinkmann M, Rannou P (2009) Molecular weight dependence of chain packing and semicrystalline structure in oriented films of regioregular poly(3-hexylthiophene) revealed by high-resolution transmission electron microscopy. Macromolecules 42:1125–1130
35. Rivnay J, Noriega R, Kline RJ, Salleo A, Toney MF (2011) Quantitative analysis of lattice disorder and crystallite size in organic semiconductor thin films. Phys Rev B 84:045203
36. Chang J-F, Sun B, Breiby DW, Nielsen MM, Sölling TI, Giles M, McCulloch I, Sirringhaus H (2004) Enhanced mobility of poly(3-hexylthiophene) transistors by spin-coating from high-boiling-point solvents. Chem Mat 16:4772–4776
37. Clark J, Chang J-F, Spano FC, Friend RH, Silva C (2009) Determining exciton bandwidth and film microstructure in polythiophene films using linear absorption spectroscopy. Appl Phys Lett 94:163306
38. Salleo A, Chen TW, Volkel AR, Wu Y, Liu P, Ong BS, Street RA (2004) Intrinsic hole mobility and trapping in a regioregular poly(thiophene). Phys Rev B 70:115311
39. DeLongchamp DM, Vogel BM, Jung Y, Gurau MC, Richter CA, Kirillov OA, Obrzut J, Fischer DA, Sambasivan S, Richter LJ et al (2005) Variations in semiconducting polymer microstructure and hole mobility with spin-coating speed. Chem Mat 17:5610–5612
40. Yang H, Shin TJ, Yang L, Cho K, Ryu CY, Bao Z (2005) Effect of mesoscale crystalline structure on the field-effect mobility of regioregular poly(3-hexyl thiophene) in thin-film transistors. Adv Funct Mater 15:671–676
41. Salammal Shabi T, Grigorian S, Brinkmann M, Pietsch U, Koenen N, Kayunkid N, Scherf U (2012) Enhancement in crystallinity of poly(3-hexylthiophene) thin films prepared by low-temperature drop casting. J Appl Polym Sci 125:2335–2341
42. Krebs FC (2009) Fabrication and processing of polymer solar cells: a review of printing and coating techniques. Sol Energ Mater Sol Cell 93:394–412
43. Khim D, Han H, Baeg K-J, Kim J, Kwak S-W, Kim D-Y, Noh Y-Y (2013) Simple bar-coating process for large-area, high-performance organic field-effect transistors and ambipolar complementary integrated circuits. Adv Mater 25:4302–4308
44. Sondergaard R, Hosel M, Angmo D, Larsen-Olsen TT, Krebs FC (2012) Roll-to-roll fabrication of polymer solar cells. Mater Today 15:36–49
45. Søndergaard RR, Hösel M, Krebs FC (2013) Roll-to-roll fabrication of large area functional organic materials. J Polym Sci B 51:16–34
46. Wong L-Y, Png R-Q, Silva FBS, Chua L-L, Repaka DVM, Shi-Chen, Gao X-Y, Ke L, Chua S-J, Wee ATS et al (2010) Interplay of processing, morphological order, and charge-carrier mobility in polythiophene thin films deposited by different methods: comparison of spin-cast, drop-cast, and inkjet-printed films. Langmuir 26:15494–15507
47. Kim SH, Hong K, Lee KH, Frisbie CD (2013) Performance and stability of aerosol-Jet-printed electrolyte-gated transistors based on poly(3-hexylthiophene). ACS Appl Mater Interfaces 5:6580–6585
48. Aiyar AR, Hong J-I, Nambiar R, Collard DM, Reichmanis E (2011) Tunable crystallinity in regioregular poly(3-hexylthiophene) thin films and its impact on field effect mobility. Adv Funct Mater 21:2652–2659
49. Aiyar AR, Hong J-I, Izumi J, Choi D, Kleinhenz N, Reichmanis E (2013) Ultrasound-induced ordering in poly(3-hexylthiophene): role of molecular and process parameters on morphology and charge transport. ACS Appl Mater Interfaces 5:2368–2377

50. Zhao K, Khan HU, Li R, Su Y, Amassian A (2013) Entanglement of conjugated polymer chains influences molecular self-assembly and carrier transport. Adv Funct Mater 23:6024–6035
51. Park YD, Lee HS, Choi YJ, Kwak D, Cho JH, Lee S, Cho K (2009) Solubility-induced ordered polythiophene precursors for high-performance organic thin-film transistors. Adv Funct Mater 19:1200–1206
52. Chang M, Choi D, Fu B, Reichmanis E (2013) Solvent based hydrogen bonding: impact on poly(3-hexylthiophene) nanoscale morphology and charge transport characteristics. Acs Nano 7:5402–5413
53. Lide DR (ed) (1994) CRC handbook of chemistry and physics, 75th edn. CRC, Boca Raton
54. Lu G, Tang H, Qu Y, Li L, Yang X (2007) Enhanced electrical conductivity of highly crystalline polythiophene/insulating-polymer composite. Macromolecules 40:6579–6584
55. Oh JY, Shin M, Lee TI, Jang WS, Min Y, Myoung J-M, Baik HK, Jeong U (2012) Self-seeded growth of poly(3-hexylthiophene) (P3ht) nanofibrils by a cycle of cooling and heating in solutions. Macromolecules 45:7504–7513
56. Qiu L, Lee WH, Wang X, Kim JS, Lim JA, Kwak D, Lee S, Cho K (2009) Organic thin-film transistors based on polythiophene nanowires embedded in insulating polymer. Adv Mater 21:1349–1353
57. Jo SB, Lee WH, Qiu L, Cho K (2012) Polymer blends with semiconducting nanowires for organic electronics. J Mater Chem 22:4244–4260
58. Wu P-T, Xin H, Kim FS, Ren G, Jenekhe SA (2009) Regioregular poly(3-pentylthiophene): synthesis, self-assembly of nanowires, high-mobility field-effect transistors, and efficient photovoltaic cells. Macromolecules 42:8817–8826
59. Liu J, Zou J, Zhai L (2009) Bottom-up assembly of poly(3-hexylthiophene) on carbon nanotubes: 2d building blocks for nanoscale circuits. Macromol Rapid Commun 30:1387–1391
60. Sarker BK, Liu J, Zhai L, Khondaker SI (2011) Fabrication of organic field effect transistor by directly grown poly(3 hexylthiophene) crystalline nanowires on carbon nanotube aligned array electrode. ACS Appl Mater Interfaces 3:1180–1185
61. Merlo JA, Frisbie CD (2003) Field effect conductance of conducting polymer nanofibers. J Polym Sci B 41:2674–2680
62. Merlo JA, Frisbie CD (2004) Field effect transport and trapping in regioregular polythiophene nanofibers. J Phys Chem B 108:19169–19179
63. Wang GM, Swensen J, Moses D, Heeger AJ (2003) Increased mobility from regioregular poly(3-hexylthiophene) field-effect transistors. J Appl Phys 93:6137–6141
64. Cho S, Lee K, Yuen J, Wang G, Moses D, Heeger AJ, Surin M, Lazzaroni R (2006) Thermal annealing-induced enhancement of the field-effect mobility of regioregular poly (3-hexylthiophene) films. J Appl Phys 100:114503–114506
65. Crossland EJW, Rahimi K, Reiter G, Steiner U, Ludwigs S (2011) Systematic control of nucleation density in poly(3-hexylthiophene) thin films. Adv Funct Mater 21:518–524
66. Lu GH, Li LG, Yang XN (2007) Achieving perpendicular alignment of rigid polythiophene backbones to the substrate by using solvent-vapor treatment. Adv Mater 19:3594–3598
67. Wang H, Liu J, Xu Y, Han Y (2013) Fibrillar morphology of derivatives of poly (3-alkylthiophene)S by solvent vapor annealing: effects of conformational transition and conjugate length. J Phys Chem B 117:5996–6006
68. Crossland EJW, Tremel K, Fischer F, Rahimi K, Reiter G, Steiner U, Ludwigs S (2012) Anisotropic charge transport in spherulitic poly(3-hexylthiophene) films. Adv Mater 24:839–844
69. Chua LL, Zaumseil J, Chang JF, Ou ECW, Ho PKH, Sirringhaus H, Friend RH (2005) General observation of N-type field-effect behaviour in organic semiconductors. Nature 434:194–199

70. Aguirre CM, Levesque PL, Paillet M, Lapointe F, St-Antoine BC, Desjardins P, Martel R (2009) The role of the oxygen/water redox couple in suppressing electron conduction in field-effect transistors. Adv Mater 21:3087–3091
71. Lim SC, Kim SH, Lee JH, Kim MK, Kim DJ, Zyung T (2005) Surface-treatment effects on organic thin-film transistors. Synth Met 148:75–79
72. Ito Y, Virkar AA, Mannsfeld S, Oh JH, Toney M, Locklin J, Bao Z (2009) Crystalline ultrasmooth self-assembled monolayers of alkylsilanes for organic field-effect transistors. J Am Chem Soc 131:9396–9404
73. Kobayashi S, Nishikawa T, Takenobu T, Mori S, Shimoda T, Mitani T, Shimotani H, Yoshimoto N, Ogawa S, Iwasa Y (2004) Control of carrier density by self-assembled monolayers in organic field-effect transistors. Nat Mater 3:317–322
74. Kim DH, Park YD, Jang Y, Yang H, Kim YH, Han JI, Moon DG, Park S, Chang T, Chang C et al (2005) Enhancement of field-effect mobility due to surface-mediated molecular ordering in regioregular polythiophene thin film transistors. Adv Funct Mater 15:77–82
75. Kline RJ, McGehee MD, Toney MF (2006) Highly oriented crystals at the buried interface in polythiophene thin-film transistors. Nat Mater 5:222–228
76. Jimison LH, Himmelberger S, Duong DT, Rivnay J, Toney MF, Salleo A (2013) Vertical confinement and interface effects on the microstructure and charge transport of P3ht thin films. J Polym Sci B 51:611–620
77. Rivnay J, Mannsfeld SCB, Miller CE, Salleo A, Toney MF (2012) Quantitative determination of organic semiconductor microstructure from the molecular to device scale. Chem Rev 112:5488–5519
78. Veres J, Ogier SD, Leeming SW, Cupertino DC, Khaffaf SM (2003) Low-K insulators as the choice of dielectrics in organic field- effect transistors. Adv Funct Mater 13:199–204
79. Veres J, Ogier S, Lloyd G, de Leeuw D (2004) Gate insulators in organic field-effect transistors. Chem Mat 16:4543–4555
80. Lan Y-K, Huang C-I (2009) Charge mobility and transport behavior in the ordered and disordered states of the regioregular poly(3-hexylthiophene). J Phys Chem B 113:14555–14564
81. Lan Y-K, Yang CH, Yang H-C (2010) Theoretical investigations of electronic structure and charge transport properties in polythiophene-based organic field-effect transistors. Polym Int 59:16–21
82. Sirringhaus H, Wilson RJ, Friend RH, Inbasekaran M, Wu W, Woo EP, Grell M, Bradley DDC (2000) Mobility enhancement in conjugated polymer field-effect transistors through chain alignment in a liquid-crystalline phase. Appl Phys Lett 77:406–408
83. Zaumseil J, Groves C, Winfield JM, Greenham NC, Sirringhaus H (2008) Electron-hole recombination in uniaxially aligned semiconducting polymers. Adv Funct Mater 18:3630–3637
84. Amundson KR, Sapjeta BJ, Lovinger AJ, Bao ZN (2002) An in-plane anisotropic organic semiconductor based upon poly(3-hexyl thiophene). Thin Solid Films 414:143–149
85. Jimison LH, Toney MF, McCulloch I, Heeney M, Salleo A (2009) Charge-transport anisotropy due to grain boundaries in directionally crystallized thin films of regioregular poly (3-hexylthiophene). Adv Mater 21:1568–1572
86. O'Connor B, Kline RJ, Conrad BR, Richter LJ, Gundlach D, Toney MF, DeLongchamp DM (2011) Anisotropic structure and charge transport in highly strain-aligned regioregular poly (3-hexylthiophene). Adv Funct Mater 21:3697–3705
87. Fischer FSU, Tremel K, Sommer M, Crossland EJC, Ludwigs S (2012) Directed crystallization of poly(3-hexylthiophene) in micrometre channels under confinement and in electric fields. Nanoscale 4:2138–2144
88. Lee MJ, Gupta D, Zhao N, Heeney M, McCulloch I, Sirringhaus H (2011) Anisotropy of charge transport in a uniaxially aligned and chain-extended, high-mobility, conjugated polymer semiconductor. Adv Funct Mater 21:932–940

89. Goffri S, Muller C, Stingelin-Stutzmann N, Breiby DW, Radano CP, Andreasen JW, Thompson R, Janssen RAJ, Nielsen MM, Smith P et al (2006) Multicomponent semiconducting polymer systems with low crystallization-induced percolation threshold. Nat Mater 5:950–956
90. Kim FS, Jenekhe SA (2012) Charge transport in poly(3-butylthiophene) nanowires and their nanocomposites with an insulating polymer. Macromolecules 45:7514–7519
91. Kim HC, Park SM, Hinsberg WD (2010) Block copolymer based nanostructures: materials, processes, and applications to electronics. Chem Rev 110:146–177
92. Liu J, Haynes D, Balliet C, Zhang R, Kowalewski T, McCullough RD (2012) Self encapsulated poly(3-hexylthiophene)-poly(fluorinated alkyl methacrylate) rod-coil block copolymers with high field effect mobilities on bare Sio2. Adv Funct Mater 22:1024–1032
93. Yu X, Xiao K, Chen J, Lavrik NV, Hong K, Sumpter BG, Geohegan DB (2011) High-performance field-effect transistors based on polystyrene-B-poly(3-hexylthiophene) diblock copolymers. Acs Nano 5:3559–3567
94. Sauvé G, McCullough RD (2007) High field-effect mobilities for diblock copolymers of poly (3-hexylthiophene) and poly(methyl acrylate). Adv Mater 19:1822–1825
95. Lee J-Y, Lin C-J, Lo C-T, Tsai J-C, Chen W-C (2013) Synthesis, morphology, and field-effect transistor characteristics of crystalline diblock copolymers consisted of poly (3-hexylthiophene) and syndiotactic polypropylene. Macromolecules 46:3005–3014
96. Lin J-C, Lee W-Y, Kuo C-C, Li C, Mezzenga R, Chen W-C (2012) Synthesis, morphology, and field-effect transistor characteristics of new crystalline–crystalline diblock copolymers of poly(3-hexylthiophene-block-steryl acrylate). J Polym Sci A Polym Chem 50:686–695
97. Müller C, Goffri S, Breiby DW, Andreasen JW, Chanzy HD, Janssen RAJ, Nielsen MM, Radano CP, Sirringhaus H, Smith P et al (2007) Tough, semiconducting polyethylene-poly (3-hexylthiophene) diblock copolymers. Adv Funct Mater 17:2674–2679
98. Radano CP, Scherman OA, Stingelin-Stutzmann N, Müller C, Breiby DW, Smith P, Janssen RAJ, Meijer EW (2005) Crystalline–crystalline block copolymers of regioregular poly (3-hexylthiophene) and polyethylene by ring-opening metathesis polymerization. J Am Chem Soc 127:12502–12503
99. Arias AC, Endicott F, Street RA (2006) Surface-induced self-encapsulation of polymer thin-film transistors. Adv Mater 18:2900–2904
100. Abdou MSA, Orfino FP, Son Y, Holdcroft S (1997) Interaction of oxygen with conjugated polymers: charge transfer complex formation with poly(3-alkylthiophenes). J Am Chem Soc 119:4518–4524
101. Liao H-H, Yang C-M, Liu C-C, Horng S-F, Meng H-F, Shy J-T (2008) Dynamics and reversibility of oxygen doping and De-doping for conjugated polymer. J Appl Phys 103:104506–104508
102. Liu C-C, Yang C-M, Liu W-H, Liao H-H, Horng S-F, Meng H-F (2009) Interface effect of oxygen doping in polythiophene. Synth Met 159:1131–1134
103. Sperlich A, Kraus H, Deibel C, Blok H, Schmidt J, Dyakonov V (2011) Reversible and irreversible interactions of poly(3-hexylthiophene) with oxygen studied by spin-sensitive methods. J Phys Chem B 115:13513–13518
104. Ong BS, Wu YL, Liu P, Gardner S (2004) High-performance semiconducting polythiophenes for organic thin-film transistors. J Am Chem Soc 126:3378–3379
105. Xia Y, Zhang W, Ha M, Cho JH, Renn MJ, Kim CH, Frisbie CD (2010) Printed sub-2V gel-electrolyte-gated polymer transistors and circuits. Adv Funct Mater 20:587–594
106. Wang S, Ha M, Manno M, Daniel Frisbie C, Leighton C (2012) Hopping transport and the hall effect near the insulator–metal transition in electrochemically gated poly (3-hexylthiophene) transistors. Nat Commun 3:1210
107. Li J, Zhao Y, Tan HS, Guo Y, Di C-A, Yu G, Liu Y, Lin M, Lim SH, Zhou Y et al (2012) A stable solution-processed polymer semiconductor with record high-mobility for printed transistors. Sci Rep 2:754

108. Kang I, Yun H-J, Chung DS, Kwon S-K, Kim Y-H (2013) Record high hole mobility in polymer semiconductors via side-chain engineering. J Am Chem Soc 135:14896–14899
109. Ong BS, Wu Y, Li Y, Liu P, Pan H (2008) Thiophene polymer semiconductors for organic thin-film transistors. Chemistry 14:4766–4778
110. McCulloch I, Heeney M, Chabinyc ML, DeLongchamp D, Kline RJ, Cölle M, Duffy W, Fischer D, Gundlach D, Hamadani B et al (2009) Semiconducting thienothiophene copolymers: design, synthesis, morphology, and performance in thin-film organic transistors. Adv Mater 21:1091–1109
111. Nielsen CB, McCulloch I (2013) Recent advances in transistor performance of polythiophenes. Prog Polym Sci 38:2053–2069
112. McCulloch I, Holliday S, Donaghey J (2014) Advances in charge carrier mobilities of semiconducting polymers used in organic transistors. Chem Mater 26:647-663
113. McCulloch I, Heeney M, Bailey C, Genevicius K, MacDonald I, Shkunov M, Sparrowe D, Tierney S, Wagner R, Zhang W et al (2006) Liquid-crystalline semiconducting polymers with high charge-carrier mobility. Nat Mater 5:328–333
114. Kim J, Lim B, Baeg K-J, Noh Y-Y, Khim D, Jeong H-G, Yun J-M, Kim D-Y (2011) Highly soluble poly(thienylenevinylene) derivatives with charge-carrier mobility exceeding 1 cm^2 v^{-1} s^{-1}. Chem Mat 23:4663–4665
115. Rieger R, Beckmann D, Pisula W, Steffen W, Kastler M, Müllen K (2010) Rational optimization of benzo[2,1-B;3,4-B′]dithiophene-containing polymers for organic field-effect transistors. Adv Mater 22:83–86
116. Pan H, Li Y, Wu Y, Liu P, Ong BS, Zhu S, Xu G (2007) Low-temperature, solution-processed, high-mobility polymer semiconductors for thin-film transistors. J Am Chem Soc 129:4112–4113
117. Pan H, Wu Y, Li Y, Liu P, Ong BS, Zhu S, Xu G (2007) Benzodithiophene copolymer – a low-temperature, solution-processed high-performance semiconductor for thin-film transistors. Adv Funct Mater 17:3574–3579
118. Horie M, Majewski LA, Fearn MJ, Yu C-Y, Luo Y, Song A, Saunders BR, Turner ML (2010) Cyclopentadithiophene based polymers-a comparison of optical, electrochemical and organic field-effect transistor characteristics. J Mater Chem 20:4347–4355
119. Zhang M, Tsao HN, Pisula W, Yang C, Mishra AK, Müllen K (2007) Field-effect transistors based on a benzothiadiazole–cyclopentadithiophene copolymer. J Am Chem Soc 129:3472–3473
120. Tsao HN, Cho D, Andreasen JW, Rouhanipour A, Breiby DW, Pisula W, Müllen K (2009) The influence of morphology on high-performance polymer field-effect transistors. Adv Mater 21:209–212
121. Tsao HN, Cho DM, Park I, Hansen MR, Mavrinskiy A, Yoon DY, Graf R, Pisula W, Spiess HW, Müllen K (2011) Ultrahigh mobility in polymer field-effect transistors by design. J Am Chem Soc 133:2605–2612
122. Fan J, Yuen JD, Cui W, Seifter J, Mohebbi AR, Wang M, Zhou H, Heeger A, Wudl F (2012) High-hole-mobility field-effect transistors based on Co-benzobisthiadiazole-quaterthiophene. Adv Mater 24:6164–6168
123. Zhang X, Richter LJ, DeLongchamp DM, Kline RJ, Hammond MR, McCulloch I, Heeney M, Ashraf RS, Smith JN, Anthopoulos TD et al (2011) Molecular packing of high-mobility diketo pyrrolo-pyrrole polymer semiconductors with branched alkyl side chains. J Am Chem Soc 133:15073–15084

Adv Polym Sci (2014) 265: 139–180
DOI: 10.1007/12_2014_277

Published online: 29 July 2014

Morphology and Charge Transport in P3HT: A Theorist's Perspective

Carl Poelking, Kostas Daoulas, Alessandro Troisi, and Denis Andrienko

Abstract Poly(3-hexylthiophene) (P3HT) is the fruit fly among polymeric organic semiconductors. It has complex self-assembling and electronic properties and yet lacks the synthetic challenges that characterize advanced donor–acceptor-type polymers. P3HT can be used both in solar cells and in field-effect transistors. Its morphological, conductive, and optical properties have been characterized in detail using virtually any and every experimental technique available, whereas the contributions of theory and simulation to a rationalization of these properties have so far been modest. The purpose of this review is to take a snapshot of these results and, more importantly, outline directions that still require substantial method development.

Keywords Charge transport · Morphology · Organic semiconductors · P3HT

Contents

C. Poelking and D. Andrienko (✉)
Max Planck Institute for Polymer Research, Ackermannweg 10, 55128 Mainz, Germany
e-mail: carl.poelking@mpip-mainz.mpg.de; denis.andrienko@mpip-mainz.mpg.de

K. Daoulas
Max Planck Institute for Polymer Research, Ackermannweg 10, 55128 Mainz, Germany

InnovationLab GmbH, 69115 Heidelberg, Germany
e-mail: daoulas@mpip-mainz.mpg.de

A. Troisi
Department of Chemistry and Centre for Scientific Computing, University of Warwick, Coventry CV4 7AL, UK
e-mail: a.troisi@warwick.ac.uk

1 Introduction

Thiophene-based conjugated polymers have accompanied, if not originated, the interest in conductive polymer materials and their application in organic field-effect transistors (OFETs) and organic photovoltaic (OPV) devices [1]. The most studied representative of this class of materials is poly(3-hexyl-thiophene) (P3HT) with its regioregular (head-to-tail) isomer (see Fig. 1), as first synthesized by Rick McCullough in 1992 [2]. Polythiophenes, however, were already an intensely studied class of conjugated polymers, a rudimentary description of the compound being published as early as 1883 [3]. The first polymerization reactions with high yield and small concentrations of synthesis impurities were reported in 1980 [4, 5]. These compounds were essentially not processable due to the strong interaction of the conjugated backbones. In 1986, Elsenbaumer reported the synthesis of easily processable poly(alkyl-thiophenes) (PATs) [6]. Solution-processed into thin films, these materials could exhibit reasonable conductivities limited, however, by the disorder that results from a regiorandom attachment of the side chains to the thiophene monomers. It was the synthesis of regioregular (rr) P3ATs [2] that eventually paved the way for applications in devices such as OFETs and OPV cells. Here, we recapitulate key experimental results relevant to polymorphism, formation of self-assembled nanostructures, and charge transport in rr-P3HT. An extended overview is provided in the rest of the contributions of this volume, various books, and monographs (e.g., [7])

Like many conjugated polymers, P3HT is a polymorph, i.e., forms different crystal structures depending on processing conditions. The most frequently observed are so-called forms I and II [8], which differ by the side chain conformation and interdigitation, inclination of conjugated backbones with respect to the stacking direction, and the shift of successive (along the π-stacking direction) polymer chains [9]. Form I, which is observed after annealing, is the structure

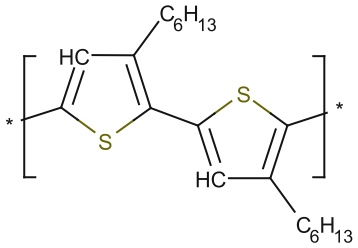

Fig. 1 Regioregular poly(3-hexyl-thiophene) (P3HT)

encountered in most studies dealing with OFETs and OPVs. It has a monoclinic unit-cell (for bulk P3HT samples X-ray diffraction, XRD, provides $a = 1.60$ nm, $b = 0.78$ nm, and $c = 0.78$ nm [10]). Polymorph II has been found to have a significantly smaller unit cell dimension along the a-axis and has thus been assumed to have interdigitated alkyl groups [8], which distinguishes it from form I. Upon heating, form II irreversibly transforms into form I. This phase transition is accompanied by a change in unit-cell dimensions, with interlayer spacings increasing and intrastack distances decreasing. A similar first-order phase transition has been described recently in a combined infrared-spectroscopy and wide-angle XRD study for a non-interdigitated metastable polymorph that transforms into the stable form I, hence establishing a third polymorph, I′ [11, 12]. Simulated unit cells of polymorphs I and I′ are shown in Fig. 2.

On a mesoscale, crystallization from supercooled solutions in poor solvents can lead to the formation of secondary structures, notably nanofibers, with a width of tens of nanometers and length of several micrometers [14].

Charge transport in P3HT has been studied with the aim of relating regioregularity, molecular weight and, hence, morphology to hole mobility, and thus to the efficiency of P3HT/methanofullerene (PCBM) bulk heterojunction solar cells, for which the power conversion efficiency was reported to be 4.4% as early as 2005 [15]. Hole mobilities of 10^{-5} cm^2/V s (10^{-4} cm^2/V s) were measured for 94% (98%) regioregular P3HT using the time-of-flight (TOF) technique [16]. Dispersive transients of the regiorandom P3HT indicated that the polymer is conductive, yet its mobility could not be extracted from TOF measurements due to sizeable disorder. The mobility temperature dependence, analyzed using the Gaussian disorder model (GDM), suggested an energetic disorder of around 50–60 meV. Both hole and electron TOF mobilities were reported to be independent of the molecular weight up to 20 kDa, and then decreased by an order of magnitude as molecular weight increased to 120 kDa [17]. The reported zero-field mobilities for shorter chains were of the order of 10^{-4} cm^2/V s. A GDM-fitted energetic disorder of 71(54) meV was extracted for short (long) chains.

Meanwhile, field-effect mobilities ranging around $\mu \sim 10^{-5}$ cm^2/V s were reported for the very first OFET device that used polythiophene for the semiconducting channel [18]. By choosing rr-P3HT, μ could be increased by three orders of magnitude [19]. OFET mobilities of ~0.1 cm^2/V s were measured as a function of the molecular weight after spin-casting from higher boiling point solvents [20]. The field-effect mobility was found to increase with molecular weight in spite of reduced crystallinity. This was attributed to either better interconnectivity of the

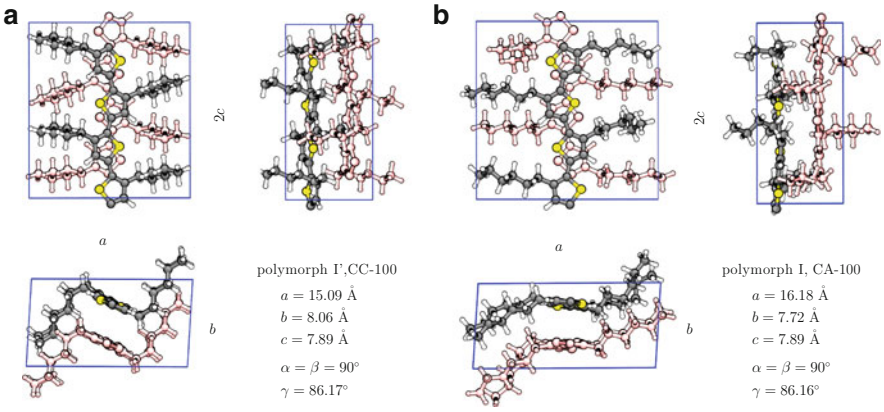

Fig. 2 Unit cells of polymorphs I′ (**a**) and I (**b**) as obtained from molecular dynamics simulations. To highlight the backbone and side chain packing, we use C for crystalline and A for amorphous states, i.e., CA-100 corresponds to a system with a crystalline arrangement of backbones, amorphous packing of side-chains, and regioregularity of 100%. CC-100 corresponds to a system with crystalline side chains and 100% regioregularity. Adapted with permission from Poelking et al. [13]. Copyright (2013) American Chemical Society

polymer network [21] or smaller intrachain ring torsions present in high molecular weight molecules [22].

Transistor hole mobilities have even been reported for individual P3HT nanofibers [14, 23, 24]. Along the fiber, this mobility was as high as 0.06 cm^2/V s. An energetic disorder of 108 meV was extracted from temperature-dependent measurements.

Stimulated by this multitude of experimental investigations, a number of theoretical studies have been conducted to rationalize the wide spectrum of mobilities obtained for a single compound and link the transport characteristics to the self-assembly properties, morphology, and electronic structure of P3HT. The controversy started when examining conformations of a single isolated chain: the thiophene dimer was reported to adopt a twisted backbone conformation [25], whereas increasing the oligomer length resulted in a planarized backbone. The situation with oligomer assemblies is even more involved; indeed, we still do not know the order of crystalline polymorphs on the energy axis, cannot quantify the density of defects in a crystalline morphology, or quantify the relative volume fractions of crystalline and amorphous phases. We do not really understand what exactly limits charge transport in ordered lamellar systems: is it large energetic disorder or small electronic couplings? Why is the hole transport strongly dispersive even though the reported energetic disorder is moderate? How does regioregularity contribute to morphological ordering, density of states, and electronic couplings? In which ways does molecular weight impact mobility? Our goal is to summarize approaches and answers to some of these questions from a theoretical perspective and to provide an outlook for the remaining questions.

2 Morphology

The theoretical and computational toolbox used to study self-assembling properties of conjugated polymers is very versatile: On the highest level of resolution, it includes accurate quantum chemical calculations capable of predicting the properties of isolated oligomers and dimers, normally without side chains. Less computationally demanding density functional methods can deal with much longer oligomers (10–20 repeat units), including side chains, and are often used to compare ground state energies of experimentally proposed arrangements of atoms in a unit cell. To assess crystalline packing modes at ambient conditions and during annealing, as well as to study amorphous melts and longer chain lengths, classical force fields have been parametrized. To access even longer length and time scales (micrometers, microseconds), coarse-grained models have been developed to study amorphous melts and liquid-crystalline phases of P3HT.

The ultimate goal of these simulations is to self-assemble the polymer in silico, i.e., to predict its polymorphs as well as the degree of disorder in the kinetically trapped molecular arrangements. The honest assessment is that we are fairly far from achieving this goal. The main obstacles are insufficient accuracy of methods at a specific level of resolution, long simulation times required to study self-assembly, and uncontrolled error propagation from one level to another, e.g., when parameterizing force fields based on quantum chemical calculations, or developing coarse-grained models using force-field-generated reference data.

We will provide a summary of simulation results, starting with single-molecule properties and then expanding to molecular arrangements of P3HT in crystals, melts, and finally binary mixtures with PCBM, a typical acceptor used in organic solar cells.

2.1 Single Molecules

Ab initio methods have been extensively used to analyze conformations of the conjugated backbone and side-chain orientations with respect to the plane of conjugation [25]. Here, the extended π-conjugated system flattens the backbone, whereas nonbonded interactions between consecutive repeat units (i.e., steric repulsions between hydrogen atoms, Coulomb interactions, and van der Waals interactions) often tend to distort its planarity. For P3HT, both planar [26] and nonplanar stable geometries have been reported, depending on the side-chain orientation [27]. At the B3LYP/6-31+G level of density functional theory (DFT), the nonplanar backbone has an energy of ~0.03 eV lower (per monomer) than the planar backbone (evaluated in a 10-mer) [28]. This indicates that chain conformations in the bulk are predominantly determined by interchain van der Waals and Coulomb interactions, a conclusion also drawn from calculations of molecular dimers [29].

Because typical energy differences between planar and nonplanar conformations are in the order of tens of millielectronvolts, which is the accuracy threshold of density functional methods, one is forced to use more accurate (and computationally demanding) quantum-chemical methods. However, the ground-state twist angle between repeat units has been found to depend on the oligomer length, saturating at about ten repeat units. Furthermore, torsional potentials are correlated up to the second-nearest-neighbor rings [30], thus making geometry predictions a formidable task even for isolated oligomers [31].

2.2 *Crystalline Oligothiophenes*

Both density functional and force-field calculations have been used to study crystalline P3HT mesophases. Density functional calculations have been primarily used to establish whether experimentally reported crystal structures correspond to well-defined energy minima [32–35]. Using a van-der-Waals-corrected generalized gradient approximation (GGA) functional, Dag and Wang concluded that the crystal with shifted backbones (i.e., with one of the thiophene layers shifted along the chain direction by the thiophene–thiophene distance) and side chains rotated around the torsion angle is the most stable of three studied structures [36]. Xie et al. reached the conclusion that a structural motif without this registry shift and without rotation of the side chains, but instead with a small backbone tilt, has the lowest potential energy [34]. Similar to the situation with a single isolated chain, typical energy differences between different packing motives are in the order of 10 meV per unit cell and, hence, theoretical methods are at their accuracy limits, making it difficult to rank different molecular arrangements. Also, unit-cell optimizations are performed at zero Kelvin, meaning that entropic effects, notably the chain excluded volume, are ignored.

To study larger systems and longer timescales, various flavors of P3HT force fields were developed. In the majority of cases, parameters of an existing force field were refined in order to reproduce the torsional potential between thiophene units and electrostatic potential around an isolated oligomer [13, 37]. The parametrization has been subsequently refined to account for the change in the backbone potential with oligomer length [13, 26, 28, 38–40]. To this end, atomistic simulations have been used to analyze proposed packing arrangements of three P3HT polymorphs (phases I, I′, and II; see Fig. 2), and to scrutinize the effect of regioregularity on paracrystalline, dynamic, and static nematic order parameters [13]. Molecular dynamics simulations suggest that the most stable P3HT polymorph has planar thiophene backbones shifted by one thiophene ring with respect to each other. Hexyl side chains are twisted away from the backbone in a *trans* fashion, resulting in a non-interdigitated packing structure, although stable structures with interdigitated side chains were also reported [41]. Force-field-based estimates of the mass density (1.05 g cm^{-3}), melting temperature (490 K), and surface tension (32 mN/m) all agree with the reported experimental values

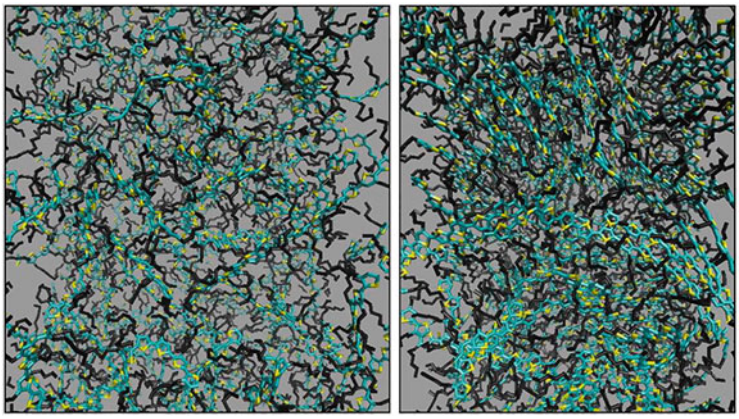

Fig. 3 Typical configuration of the amorphous system after annealing the crystal at high temperatures (*left*). Onset of crystallization at 300 K acquired at the end of the gradual cooling process that was started from the amorphous melt (*right*). Adapted with permission from Alexiadis and Mavrantzas [42]. Copyright (2013) American Chemical Society

[40]. One should note that even on this classical level of description, only highly crystalline morphologies and high-temperature amorphous melts can be studied. Still, some indications of local-chain ordering upon cooling of amorphous high-temperature melts (see Fig. 3) have been observed [42].

2.3 Amorphous Melts and Blends

Early simulations of amorphous systems considered thiophene oligomers as a model for P3HT. Alignment of polymer chains and thiophene units within chains have for instance been studied in a Monte-Carlo approach [43]. The authors were able to reproduce the density of the amorphous mesophase (an estimate of 1.06 g cm^{-3} was given) and concluded that chains tend to align parallel to each other, while thiophene rings of neighboring chains tend to adopt parallel or anti-parallel π-stacked arrangements. Systems with much shorter chains had significantly denser packing (predicted density 1.4 g cm^{-3}) and stronger alignment, a result obtained using molecular dynamics simulations [44].

Amorphous melts of oligomers of P3HT were also simulated in order to calculate the glass transition temperature (300 K) and, hence, validate the atomistic force field [40] and to develop coarse-grained models of P3HT in a liquid state approaching 500–600 K [45, 46]. Simulations of free-standing films of P3HT melts have been used to estimate the room-temperature value of surface tension (21–36 mN m^{-1}) [47]. Amorphous melts of P3HT are, however, of only moderate interest because the conductive abilities of this polymer are related to its high degree of lamellar ordering.

In order to understand molecular ordering and electronic processes in bulk heterojunction devices, blends of P3HT oligomers with fullerene and PCBM have been simulated at different levels of resolution. Atomistic simulations showed that bulk oligothiophenes (five chains of 20 repeat units each) tend to cluster better than oligothiophene/fullerene systems [48]. Prototypical model interfaces have been used to evaluate energetic profiles for electrons and holes [49]. Coarse-grained simulations could observe the onset of phase separation [45], distributions of domain sizes, and interface-to-volume ratios [50] in P3HT/PCBM mixtures. Nevertheless, the field of coarse-grained modeling of conjugated polymers is still in its infancy. Complications reside in the large persistence length and anisotropic nonbonded interactions that promote π–π stacking. We will discuss various strategies for developing coarse-grained models of conjugated polymers in Sect. 3.

3 Coarse-Grained Models

Apart from the local molecular packing discussed so far, mesoscopic ordering of conjugated polymers is equally important for the functionality of organic semiconducting devices. In a bulk heterojunction solar cell, for example, domain sizes of the donor and acceptor mesophases have considerable impact on cell efficiency. To predict and analyze such effects, modeling strategies that target the morphology on length scales reaching several hundreds of nanometers, the typical thickness of the active layer in a polymer-based solar cell, are required. With the currently available computational power, such system sizes can only be addressed on a coarse-grained level.

The idea of coarse-graining relies on the separation of time and length scales. For many polymeric systems, especially polymer melts, the chemical details, although strongly affecting material behavior on the microscopic level, become less important on the mesoscale, where simplified representations of polymer architecture and interactions can be used. In conjugated polymers, however, the mesoscale features of the morphology couple across many length scales: π–π stacking for instance promotes the formation of lamellae, which in turn self-assemble into supralamellar structures. Predicting this hierarchical self-assembly is the main target (and challenge) of coarse-grained modeling of conjugated polymers.

Coarse-graining strategies can be subdivided into bottom-up and top-down approaches [51, 52]. In bottom-up coarse-graining, the model is constructed to reproduce physical quantities known from a more detailed description of the system [53]. In other words, a fine-grained representation of the system is projected onto a representation with fewer degrees of freedom. This projection is not unique, and various techniques have been suggested, including structure-based coarse-graining [53, 54], force-matching [55, 56], and relative entropy frameworks [57]. Top-down

approaches, on the contrary, derive the coarse-grained model from macroscopic observables (e.g., the phase behavior). These are often based on experimental measurements [51, 52, 58] but can also incorporate elements of bottom-up coarse-graining. In the following sections, we review the results obtained using structure-based coarse-grained models and also introduce a coarse-graining technique based on soft interaction potentials.

3.1 Structure-Based Coarse-Graining

The idea of structure-based coarse-graining is to match structural properties, such as radial distribution functions, of the fine- and coarse-grained systems. Structure-based coarse-grained models have been developed for melts [45, 46], high-temperature (liquid) mixtures of P3HT/PCBM [45, 50, 59], and solutions of P3HT [60]. The P3HT monomers are normally coarse-grained into three interaction sites placed at the center of mass of the thiophene rings, then on the first and last three methyl groups of the hexyl side-chain, as shown in Fig. 4. The bonded and nonbonded interaction parameters are optimized using the iterative Boltzmann inversion method [54, 61], although phenomenological refinement is also used [59].

The three-site models allow for self-assembling polymer backbones into lamellar arrangements [59, 60]. They have also been used to study the morphology of phase-separated P3HT/PCBM blends, where explicit incorporation of side chains helped to understand penetration of acceptor molecules into side chains as a function of their grafting density along the backbone. No intercalation was found for P3HT, in contrast to poly(bithiophene-alt-thienothiophene) (PBTTT), which has a lower grafting density of side chains [59]. A further advantage of coarse-graining is that solvent-mediated interactions can be incorporated into coarse-grained interactions, leading to a dramatic decrease in the number of degrees of freedom. Simulations of P3HT aggregation in solutions with anisole could reproduce the experimentally observed aggregation of P3HT as a function of temperature with the back-folded hairpins of stacked P3HT molecules [60]. The spacing between P3HT lamellae was found to be 1.7 nm, which is comparable to experimental observations [9].

Three-site coarse-grained models normally employ orientationally *isotropic* nonbonded interactions and are parametrized either on high-temperature P3HT melts or solutions. Thus, by construction, they cannot capture the directionality of π–π interactions between thiophenes. The backbones of the P3HT chains within the same lamella are also less correlated, leading to smectic-like ordering [59, 60]. In fact, this type of ordering has been reported experimentally, although in a narrow temperature window, prior to melting [10].

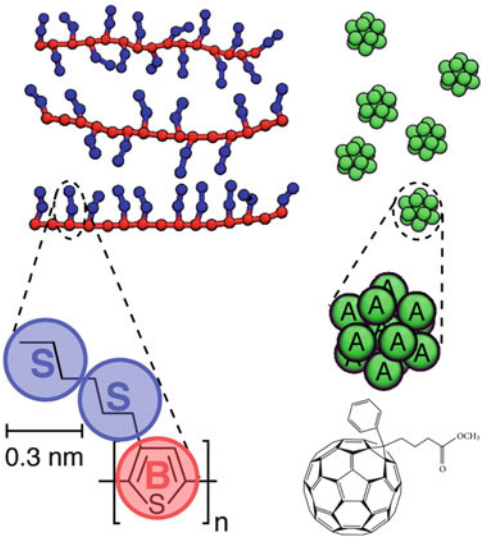

Fig. 4 *Left*: Three-site coarse-grained model of polythiophene derivatives with different side chain grafting densities. *Right*: PCBM modeled by a collection of 13 coarse-grained beads. Bead types are labeled by letters A (buckyball), B (backbone), and S (side chain). Adapted with permission from Jankowski et al. [59]. Copyright (2013) American Chemical Society

3.2 Soft Models

The three-site models with explicit beads for side chains are too complex for simulations of dense systems and long chains. For homopolymer melts, oligomers of 15 repeat units have been used [59], whereas simulations of P3HT/PCBM blends employed chains of 48 repeat units [45]. Further reducing the number of degrees of freedom, e.g., by removing coarse-grained side chains, necessitates orientationally anisotropic interaction potentials, otherwise even the lamellar order is no longer produced. In other words, anisotropic interactions are needed to account for the conformational frustration of side chains and the energetically favorable stacking of backbones. In this sense, they incorporate entropic and enthalpic contributions to the free energy of the system.

As the model becomes cruder and cruder, the number of microscopic states that correspond to the same coarse-grained state increases. As a result, the coarse-grained interaction potentials become softer. This, in combination with the reduction in the degrees of freedom, boosts computational efficiency. At the same time, the thermodynamic nature of the coarse-grained potentials becomes more prominent and transferability is gradually lost [62]. To remedy the situation, thermodynamic properties of the system can be incorporated into the coarse-grained model by using (phenomenological) top-down approaches. For conjugated polymers, the symmetry of the mesophase can be directly included into the anisotropic interaction potential, as has been shown for liquid crystalline mesophases [63, 64] observed experimentally in poly[3-(2′-ethyl)hexylthiophene] and poly(3-dodecylthiophene) [65, 66].

In such coarse-grained models, nonbonded interactions are chosen such that the system possesses a desired phase behavior, e.g., a nematic to isotropic transition. In practice, one starts with an appropriate density functional, in the spirit of

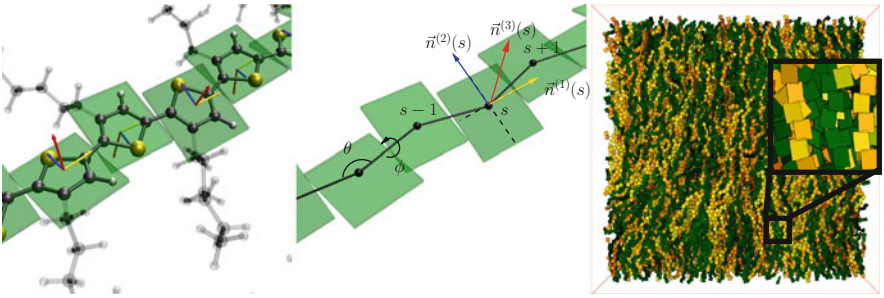

Fig. 5 Atomistic and coarse-grained representation of a P3HT chain (*left*), including coarse-grained angular (θ) and dihedral (ϕ) degrees of freedom (center). Biaxial nematic alignment in a melt of P3HT chains (*right*). Adapted with permission from Gemünden et al. [64]. Copyright (2013) American Chemical Society

field-theoretical descriptions of polymeric liquid crystals [67–71]. Each s-th coarse-grained thiophene of the i-th molecule with coordinate $\mathbf{r}_i(s)$ is assigned an orthonormal set of vectors $\{\mathbf{n}_i^{(1)}(s), \mathbf{n}_i^{(2)}(s), \mathbf{n}_i^{(3)}(s)\}$ as illustrated in Fig. 5. A repeat unit is smeared into a density distribution $\omega(\mathbf{r} - \mathbf{r}_i(s))$, which allows for collective degrees of freedom:

$$\begin{aligned}
\hat{\rho}(\mathbf{r}) &= \sum_{i=1}^{n}\sum_{s=1}^{N}\omega(\mathbf{r} - \mathbf{r}_i(s)) \\
\hat{Q}_{\alpha\beta}(\mathbf{r}) &= \rho_0^{-1}\sum_{i=1}^{n}\sum_{s=1}^{N}\omega(\mathbf{r} - \mathbf{r}_i(s))q_{i,\alpha\beta}(s) \\
\hat{B}_{\alpha\beta}(\mathbf{r}) &= \rho_0^{-1}\sum_{i=1}^{n}\sum_{s=1}^{N}\omega(\mathbf{r} - \mathbf{r}_i(s))b_{i,\alpha\beta}(s)
\end{aligned} \tag{1}$$

where $\alpha, \beta = x, y, z$, and

$$q_{i,\alpha\beta}(s) = \left[\frac{3}{2}n_{i,\alpha}^{(1)}(s)n_{i,\beta}^{(1)}(s) - \frac{\delta_{\alpha\beta}}{2}\right] \tag{2}$$

$$b_{i,\alpha\beta}(s) = \left[n_{i,\alpha}^{(2)}(s)n_{i,\beta}^{(2)}(s) - n_{i,\alpha}^{(3)}(s), n_{i,\beta}^{(3)}(s)\right] \tag{3}$$

are the orientational order parameters. The density cloud $\omega(\mathbf{r} - \mathbf{r}_i(s))$ represents, to some extent, the distribution of the underlying microscopic degrees of freedom [72]. Because molecules in a nematic phase are orientationally ordered but positionally disordered and side chain conformations strongly fluctuate, the average spatial distribution of monomers can be approximated by a spherical uniform density cloud, $\omega(\mathbf{r}) = \frac{3}{4\pi\sigma^3}$ if $r \leq \sigma$, zero otherwise. For P3HT, for example, $\sigma = 0.6$ nm, which is close to the length of a hexyl chain in the all-*trans* configuration, ~0.76 nm.

The nonbonded interactions are then defined through a free-energy functional of the collective variables [64]:

$$\begin{aligned} H_{\mathrm{nm}}\left[,\hat{\rho},\hat{\boldsymbol{Q}},\hat{\boldsymbol{B}}\right] = & \int \mathrm{d}\mathbf{r}\frac{\hat{\kappa}\rho_0}{2}\left(\frac{\hat{\rho}(\mathbf{r})}{\rho_0}-1\right)^2 \\ & -\frac{\hat{\nu}\rho_0}{3}\int \mathrm{d}\mathbf{r}\hat{\boldsymbol{Q}}(\mathbf{r}):\hat{\boldsymbol{Q}}(\mathbf{r}) \\ & -\frac{\hat{\mu}\rho_0}{3}\int \mathrm{d}\mathbf{r}\left\{\hat{\boldsymbol{Q}}(\mathbf{r}):\hat{\boldsymbol{B}}(\mathbf{r})+\hat{\boldsymbol{B}}(\mathbf{r}):\hat{\boldsymbol{Q}}(\mathbf{r})\right\} \\ & -\frac{\hat{\lambda}\rho_0}{4}\int \mathrm{d}\mathbf{r}\hat{\boldsymbol{B}}(\mathbf{r}):\hat{\boldsymbol{B}}(\mathbf{r}) \end{aligned} \tag{4}$$

Here the first term suppresses local density fluctuations [73, 74] and the rest is an analog of the Ginzburg–Landau free energy associated with the instantaneous tensorial fields $\hat{\boldsymbol{Q}}$ and $\hat{\boldsymbol{B}}$. Phenomenological parameters $\overline{\nu},\overline{\mu}$ and $\overline{\lambda}$ entering this functional are normally chosen such that the thermodynamic state of interest, e.g., a biaxial–nematic mesophase, is reproduced. In this respect, mean-field estimates can help to limit the physically adequate parameter ranges. Positive isothermal compressibility, for example, requires $\overline{\kappa} > \overline{\nu}+\overline{\mu}+\overline{\lambda}$ [64].

Following similar studies with scalar collective degrees of freedom [51, 75], one can then write the effective Hamiltonian of nonbonded interactions as:

$$\begin{aligned} H_{\mathrm{nb}} = \frac{1}{2}\sum_{i,j=1}^{n}\sum_{s,t=1}^{N} u\left(r_{ij}(s,t)\right)\Bigg[& \overline{\kappa}-\frac{2\overline{\nu}}{3}\boldsymbol{q}_i(s):\boldsymbol{q}_j(t)- \\ & -\frac{2\overline{\mu}}{3}\left(\boldsymbol{q}_i(s):\boldsymbol{b}_j(t)+\boldsymbol{b}_i(s):\boldsymbol{q}_j(t)\right)-\frac{\overline{\lambda}}{2}\boldsymbol{b}_i(s):\boldsymbol{b}_j(s)\Bigg] \end{aligned} \tag{5}$$

where $u(r_{ij}(s,t)) = \rho_0^{-1}\int \mathrm{d}\mathbf{r}\omega(|\mathbf{r}-\mathbf{r}_i(s)|)\omega(|\mathbf{r}-\mathbf{r}_j(t)|)$ is the soft repulsion core expressing the overlap of the density clouds [51, 64]:

$$u\left(r_{ij}(s,t)\right) = \frac{3}{8\pi\rho_0\sigma^3}\left(2+\frac{r_{ij}(s,t)}{2\sigma}\right)\left(1-\frac{r_{ij}(s,t)}{2\sigma}\right)^2 \tag{6}$$

Thus, the free-energy functional is transformed into a sum over pairwise, orientation-dependent interactions. Note that bonded interaction potentials are taken into account separately and can be parametrized using atomistic simulations of a single isolated chain in θ–solvent conditions. Here bond lengths are kept fixed and harmonic angular and Ryckaert–Bellemans torsion potentials are used to reproduce the corresponding distributions [64].

Once the Hamiltonian is fully parametrized, standard sampling techniques (e.g. Monte Carlo, molecular dynamics, or dissipative particle dynamics) can be used to explore the phase space and to evaluate macroscopic observables. Note that the coarse-grained hexylthiophenes interact even at a distance of $2\sigma = 1.2$ nm, which is almost twice the average separation of their centers of mass, estimated as $\rho_0^{-1/3} \approx 0.63$ nm. In order to obtain realistic values for the effective excluded volume, the interactions for strong overlaps of the density clouds must be weak, i.e., $\overline{\kappa} u(0) \sim k_B T$. This results in soft potentials and boosts the efficiency of phase-space sampling, especially if the Monte Carlo algorithm is used.

Simulations using the reptation algorithm [76, 77] showed that one can equilibrate systems on the scale of $\approx 50 \times 50 \times 50$ nm^3, containing around 5×10^{-5} hexylthiophenes with up to 32 monomers per chain. Depending on the coupling strength $\overline{\lambda}$ and the degree of polymerization, plate-like nematic mesophases (with normals of the thiophene rings parallel to the director) as well as biaxial phases (see Fig. 5 for a representative snapshot) have been observed. It has also been shown that the model predicts reasonable values for the persistence length and Frank elastic constants [64].

With the large-scale morphology at hand, some insights can be obtained on how the collective orientation of chains affects the energetic landscape for drift-diffusing charges. This has been done by splitting polymer segments onto conjugated segments (using a simple criterion for the torsion angle [78]; see, however, Sect. 5.1) and evaluating gas-phase ionization energies of these segments. Even this crude model predicts that isotropic melts consist of short conjugated segments with defects uniformly distributed along the chains. In the biaxial nematic case, the average segment length increases significantly, and the collective orientation of these segments leads to a spatially correlated energetic landscape, even without accounting for long-range Coulomb interactions [64].

4 Rate-Based Description of Charge Transport

We will now discuss the semiconducting properties of P3HT. When choosing an appropriate model for charge transport in this polymer, we have to rely on the experimentally observed increase in mobility with increasing temperature. This is interpreted as a sign for temperature-activated hopping transport. In other words, charges (charged states) are localized and charge transfer reactions that propagate the localized states are thermally activated. Localization can occur on single molecules (typically observed in amorphous small-molecule-based organic semiconductors) or molecular assemblies (crystalline materials). In polymers, charge localizes on molecular, or conjugated, segments, as discussed in Sect. 5.1.

If charge transfer rates are known, the resulting master equation for occupation probabilities of these localized states describes charge dynamics in the system. Hence, the solution of the master equation provides information about charge

distribution, currents, and eventually mobility, all as a function of temperature, external field, charge density, and, importantly, morphology. Here we will start with the charge transfer rate and introduce microscopic quantities that affect charge dynamics.

4.1 Rates

The simplest rate expression can be derived for a system with classical harmonic vibrational degrees of freedom (semiclassical high-temperature limit) [79, 80]:

$$k_{\mathrm{A}\to\mathrm{B}} = \frac{2\pi}{\hbar}\frac{\left|J_{\mathrm{AB}}\right|^2}{\sqrt{4\pi\lambda kT}}\exp\left[-\frac{\left(\Delta U_{\mathrm{AB}}-\lambda\right)^2}{4\lambda kT}\right]. \tag{7}$$

This so-called Marcus rate depends on only three microscopic parameters: reorganization energy λ, electronic coupling J_{AB}, and driving force $\Delta U_{\mathrm{AB}} = U_{\mathrm{A}} - U_{\mathrm{B}}$, all of which can be evaluated using quantum-chemical methods, classical polarizable force-fields, or quantum-classical hybrids as discussed in the following sections. Various generalizations of this expression to quantum-mechanical modes have been derived [81–84].

4.2 Reorganization Energy

The internal reorganization energy is a measure of how much the geometry of the charge transfer complex adapts as the charge is transferred. The reorganization energy can be estimated from four points on the diabatic potential energy surfaces (PES) shown in Fig. 6:

$$\begin{aligned}\lambda_{\mathrm{A}\to\mathrm{B}} &= U_a(\xi_{\mathrm{A}}) - U_a(\xi_a) + U_{\mathrm{B}}(\xi_b) - U_{\mathrm{B}}(\xi_{\mathrm{B}}),\\ \lambda_{\mathrm{B}\to\mathrm{A}} &= U_b(\xi_{\mathrm{B}}) - U_b(\xi_b) + U_{\mathrm{A}}(\xi_a) - U_{\mathrm{A}}(\xi_{\mathrm{A}}).\end{aligned} \tag{8}$$

Here, $U_{a,b}$ and $U_{\mathrm{A,B}}$ refer to the diabatic states of molecules A and B in their neutral and charged states, respectively. Treatments that do not approximate the PES in terms of a single shared normal mode are also available [85].

An additional contribution to the overall λ results from the reorganization of the environment in which the charge transfer takes place, giving rise to λ^{out}. This outer-sphere reorganization energy contributes to the exponent in the rate expression in the same fashion as its internal counterpart. We note however that, in organic semiconductors, λ^{out} is small (~0.01 eV) and becomes important primarily for charge transfer in polar solvents.

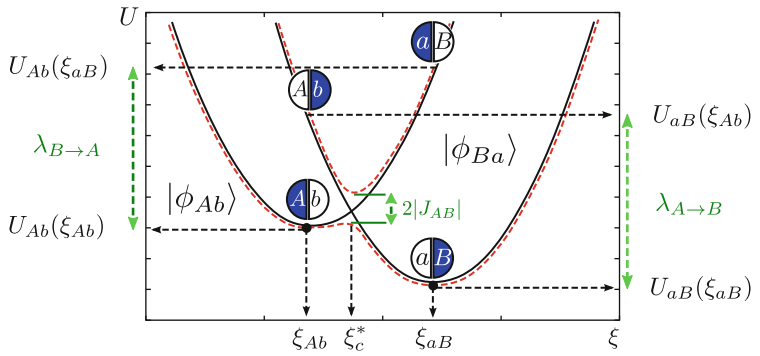

Fig. 6 Diabatic (*solid black line*) and adiabatic (*dashed red line*) potential energy surfaces of two electronic dimer states $|\phi_{Ab}\rangle$ and $|\phi_{aB}\rangle$ participating in the charge transfer reaction along the reaction coordinate ξ. Reorganization energies $\lambda_{A\to B}, \lambda_{B\to A}$

For P3HT, the reorganization energy decreases to ~0.1 eV for a chain length of 20 monomers, which is small compared to ~0.2–0.4 eV observed in many small-molecule-based organic semiconductors due to better delocalization of the charge. Additionally, steric hindrance prevents conformational changes of the polymer chain upon charging if embedded in a π-stacked crystal. The resulting constraint on the backbone planarity helps lower the reorganization energy.

4.3 Electronic Coupling Elements

Electronic coupling elements, or transfer integrals, between molecules i and j are given by the off-diagonal matrix elements [80, 86]:

$$J_{ij} = \langle \phi_i | \hat{\mathrm{H}} | \phi_j \rangle, \tag{9}$$

where $\phi_{i,j}$ are diabatic states, often approximated by the frontier orbitals of the molecules, and $\hat{\mathrm{H}}$ is the dimer Hamiltonian. These quantities are normally evaluated using electronic structure methods. Expanding the adiabatic states of the dimer in monomer states, we obtain the following secular equation:

$$(\mathbf{H} - E\mathbf{S})\mathbf{C} = 0, \tag{10}$$

where $\mathbf{H}$ and $\mathbf{S}$ are the Hamiltonian and overlap matrices of the system:

$$\mathbf{H} = \begin{pmatrix} e_i & H_{ij} \\ H_{ij}^* & e_j \end{pmatrix}, \quad \mathbf{S} = \begin{pmatrix} 1 & S_{ij} \\ S_{ij}^* & 1, \end{pmatrix} \tag{11}$$

and $e_i = \langle \phi_i | \hat{\mathrm{H}} | \phi_i \rangle$, $e_j = \langle \phi_j | \hat{\mathrm{H}} | \phi_j \rangle$, $H_{ij} = \langle \phi_i | \hat{\mathrm{H}} | \phi_j \rangle$, and $S_{ij} = \langle \phi_i |, \phi_j \rangle$

In the basis of its eigenfunctions, the Hamiltonian operator is diagonal, $\langle \phi_n^D | \mathbf{H} | \phi_m^D \rangle = E_n \delta_{nm}$. Hence, Eq. (10) can be rewritten as:

$$H_{ij} = \sum_n \langle \phi_i | \phi_n^D \rangle E_n \langle \phi_n^D | \phi_j \rangle. \tag{12}$$

Expanding the monomer and dimer functions into a basis set of atom-centered orbitals, $|\phi_k\rangle = \sum_\alpha M_\alpha^{(k)} |\varphi_\alpha\rangle$, $|\phi_n^D\rangle = \sum_\alpha D_\alpha^{(n)} |\varphi_\alpha\rangle$, the projections read:

$$\langle \phi_k | \phi_n^D \rangle = \sum_\alpha M_\alpha^{(k)} \langle \alpha | \sum_\beta D_\beta^{(n)} | \beta \rangle = \overline{\boldsymbol{M}}_{(k)}^\dagger S \overline{\mathbf{D}}_{(n)} \tag{13}$$

where $\mathbf{S}$ is the overlap matrix of the atomic basis functions. The Hamiltonian and overlap then take the form:

$$H_{ij} = \overline{\boldsymbol{M}}_{(i)}^\dagger S \mathbf{D} \mathbf{E} \mathbf{D}^\dagger S^\dagger \overline{\boldsymbol{M}}_{(j)} \tag{14}$$

$$S_{ij} = \overline{\boldsymbol{M}}_{(i)}^\dagger S \mathbf{D} \mathbf{D}^\dagger S^\dagger \overline{\boldsymbol{M}}_{(j)} \tag{15}$$

The final required transformation is the diagonalization of the diabatic states imposed by the charge-transfer Hamiltonian [87]. An orthonormal basis set that retains the local character of the monomer orbitals can be obtained by using the Lödwin transformation, $\mathbf{H}^{\mathrm{eff}} = \mathbf{S}^{-1/2} \mathbf{H} \mathbf{S}^{-1/2}$, yielding an effective Hamiltonian with entries directly related to site energies ε_i and transfer integrals J_{ij}:

$$\mathbf{H}^{\mathrm{eff}} = \begin{pmatrix} \varepsilon_i & J_{ij} \\ J_{ij}^* & \varepsilon_j \end{pmatrix}. \tag{16}$$

The projection method can be significantly simplified if semi-empirical methods are used for the dimer Hamiltonian [88–90] and made computationally more efficient by avoiding self-consistent dimer calculations [91].

4.3.1 Crystalline P3HT Couplings

As an illustration, we review the distribution of electronic couplings in P3HT crystals, molecular-dynamics snapshots of which are shown in Fig. 2. The diabatic states are constructed from the highest occupied molecular orbital of an optimized (B3LYP functional, 6-311 g(d,p) basis set) P3HT 20-mer. We account for the variation in dihedral angles along the polymer backbone by rotating the orbitals

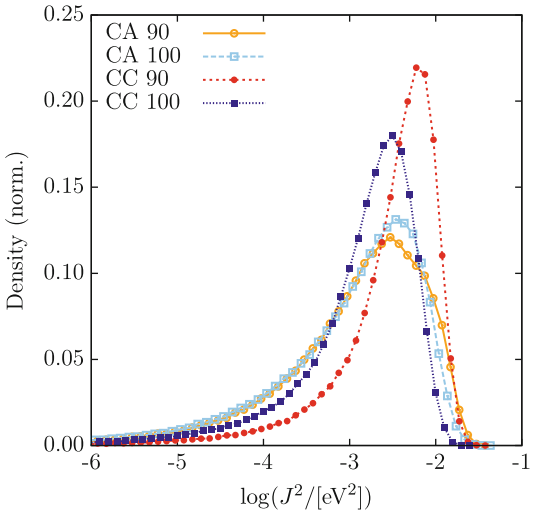

Fig. 7 Distributions of squared electronic couplings for CC-100, CA-100, CC-90, and CA-90. CA-100 corresponds to a system with a crystalline arrangement of backbones, amorphous packing of side-chains, and regioregularity of 100%. CC-100 corresponds to a system with crystalline side chains and 100% regioregularity. Adapted with permission from Poelking et al. [13]. Copyright (2013) American Chemical Society

into the respective coordinate frames of the thiophenes. The electronic coupling elements are calculated for each molecular pair (ij) from the neighbor list using the semi-empirical ZINDO method [88–90]. A pair of molecules is added to the list of neighbors if the distance between the centers-of-mass of any of the thiophene groups is below a cut-off of 0.5 nm. This small, fragment-based cut-off ensures that only nearest neighbors are added to the neighbor list.

The distribution of electronic coupling elements is shown in Fig. 7. Note that we use CA to denote crystalline (amorphous) packing, i.e., CA-100 corresponds to a system with a crystalline arrangement of backbones, amorphous packing of side-chains, and regioregularity of 100%. Unexpectedly, the 100% regioregular P3HT with crystalline side chains (CC-100) has (on average) lower electronic couplings than the corresponding 90% regioregular phase (CC-90). This peculiar effect is most probably due to the different interlevel shift observed for the two regioregularities. Transfer integrals tend to be very sensitive to this structural mode [92]. For two perfectly aligned and optimized chains, the coupling element $|J_{ij}|^2$ can vary between 0 and 10^{-2} eV as the backbones are shifted with respect to each other along the polymer's long axis by one repeat unit, thus yielding a $\sin^2$-type variation of $|J_{ij}|^2$ with interlevel shift.

Side-chain melting leads to a broadening of the distributions and a tail of very small couplings, down to 10^{-6} eV (even though only nearest neighbors are present in the neighbor list). This would obviously result in rather small average mobility values [93]. This conclusion is, however, valid only if (one-dimensional) charge-carrier transport were to occur within a static snapshot of the system; in reality, both transfer integrals and site energies are time-dependent. In order to understand whether such a static picture can be used in the case of P3HT, we compare the distributions of relaxation times of the electronic coupling elements and site energies to the distribution of escape times of a charge carrier (see Sect. 4.6).

4.4 Site Energies

The driving force, ΔU_{AB}, is given by the difference in site energy $U_{\mathrm{A}} - U_{\mathrm{B}}$, i.e., the energy separation between the diabatic PES minima shown in Fig. 6. U_{A} and U_{B} include both internal contributions U^{int}, i.e., the electron affinities for electrons and ionization potentials for holes of isolated molecules, and external contributions from the electrostatic (U^{est}) and induction (U^{ind}) interactions with surrounding molecules:

$$\begin{aligned} U_{\mathrm{A}} &= U_{\mathrm{A}b}(\xi_{\mathrm{A}b}) - U_{ab}(\xi_{ab}) = \\ &= \left(U^{\mathrm{int}}_{\mathrm{A}b} - U^{\mathrm{int}}_{ab}\right) + \left(U^{\mathrm{est}}_{\mathrm{A}b} - U^{\mathrm{est}}_{ab}\right) + \left(U^{\mathrm{ind}}_{\mathrm{A}b} - U^{\mathrm{ind}}_{ab}\right) \\ U_{\mathrm{B}} &= U_{a\mathrm{B}}(\xi_{a\mathrm{B}}) - U_{ab}(\xi_{ab}) = \\ &= \left(U^{\mathrm{int}}_{a\mathrm{B}} - U^{\mathrm{int}}_{ab}\right) + \left(U^{\mathrm{est}}_{a\mathrm{B}} - U^{\mathrm{est}}_{ab}\right) + \left(U^{\mathrm{ind}}_{a\mathrm{B}} - U^{\mathrm{ind}}_{ab}\right) \end{aligned} \tag{17}$$

Here, the subscript *ab* denotes the reference (neutral) state of the system, with all molecules in their ground states.

4.4.1 Electrostatic Contribution

The electrostatic interaction energy in the site-energy calculation can be evaluated as the first-order energy correction term that results when treating an external field as a perturbing term in the molecular Hamiltonian. This term is normally evaluated using atomic distributed multipoles, where the interaction energy U_{AB} of two molecules A and B, located at positions $\mathbf{X}$ and $\mathbf{Y}$ reads:

$$U_{\mathrm{AB}} = \frac{1}{4\pi\varepsilon_0} \iint \mathrm{d}^3x \mathrm{d}^3y \frac{\rho_{\mathrm{A}}(\mathrm{x})\rho_{\mathrm{B}}(\mathbf{y})}{|\mathbf{Y} + \mathbf{y} - \mathbf{X} - \mathbf{x}|}. \tag{18}$$

Here ρ_{A} and ρ_{B} are the charge densities of molecules A and B, respectively.

Using the spherical-harmonic addition theorem [94], this energy can be rewritten in terms of the molecular multipole moments defined with respect to the molecule's local frame:

$$\begin{aligned} U_{\mathrm{AB}} = \frac{1}{4\pi\varepsilon_0} \sum_{l_1,l_2} \sum_{k_1,k_2} \binom{l_1 + l_2}{l_1} \hat{Q}^{\,\mathrm{A}}_{l_1k_1} \hat{Q}^{\,\mathrm{B}}_{l_2k_2} \times \\ \times S^{k_1k_2}_{l_1l_2l_1+l_2} \left|\mathbf{X} - \mathbf{Y}\right|^{-l_1-l_2-1} \end{aligned} \tag{19}$$

These moments, $\hat{Q}^{\,\mathrm{A}}_{lm} = \int \mathrm{d}^3x \rho_{\mathrm{A}}(\mathrm{x}) R_{lm}(x)$, interact with each other via a tensor that contains the distance and orientation dependence. Note that here we have used $|x-y| < |\mathbf{X}-\mathbf{Y}|$ (i.e., the molecular charge densities must not interpenetrate). In this expression, the so-called S-function [95] has absorbed the orientation dependence, comprising a linear combination of products of Wigner rotation matrices and $3j$-coefficients: The latter result from re-centering the spherical harmonics in the expansion around the molecular centers $\mathbf{X}$ and $\mathbf{Y}$.

Due to the spherical-tensor formalism, the molecular multipole moments can be easily converted between two coordinate frames Σ_1 and Σ_2 according to $Q_{lk}^{(\Sigma_1)} = \sum_m Q_{lk}^{(\Sigma_2)} D^l_{mk}(\varphi,\theta,\psi)$. Here, ϕ,θ,ψ are Euler angles and $[D^l_{mk}]$ is a Wigner rotation matrix. This conversion allows us to perform the electrostatic parametrization of a molecule within a conveniently chosen local frame, and to include the transformation from the local to the global interaction frame in a tensor that takes care of both the distance and orientation dependence:

$$T^{\mathrm{A,B}}_{l_1k_1l_2k_2} = \frac{1}{4\pi\varepsilon_0} \begin{pmatrix} l_1+l_2 \\ l_1 \end{pmatrix} S^{k_1k_2}_{l_1l_2l_1+l_2} |\mathbf{X}-\mathbf{Y}|^{-l_1-l_2-1} \tag{20}$$

This way, the interaction energy reduces to a compact expression, comprising only molecular multipole moments defined with respect to the molecular local frame and generic interaction tensors $T^{\mathrm{A,B}}_{l_1k_1l_2k_2}$ (tabulated up to $l_1+l_2=5$ in [96]):

$$U_{\mathrm{AB}} = \hat{Q}^{\,\mathrm{A}}_{l_1k_1} T^{\mathrm{A,B}}_{l_1k_1l_2k_2} \hat{Q}^{\,\mathrm{B}}_{l_2k_2}, \tag{21}$$

where we have used the Einstein sum convention for the multipole-moment components l_ik_i. The site-energy correction that enters exponentially in the Marcus rate expression for a charge localized on molecule A is then:

$$\Delta U^{\mathrm{cm}}_{\mathrm{A}} = \sum_{\mathrm{B}\neq\mathrm{A}} \left(\hat{Q}^{\,\mathrm{A},c}_{l_1k_1} - \hat{Q}^{\,\mathrm{A},n}_{l_1k_1} \right) T^{\mathrm{A,B}}_{l_1k_1l_2k_2} \hat{Q}^{\,\mathrm{B},n}_{l_2k_2}, \tag{22}$$

where superscripts c and n denote the molecular multipole moments in the neutral and charged states, respectively, and the sum runs over all external molecules B.

4.4.2 Distributed Multipoles

In Eq. (21), we have given an expression for the electrostatic interaction energy in terms of molecule-centered multipole moments. To arrive at this expression, we required the separation between the molecular centers, $|\mathbf{X}-\mathbf{Y}|$, to be larger than the separation of any of the respective charge-carrying volume elements of the two molecules, $|x-y|$. In a molecular solid, this demand can hardly be satisfied,

considering the dense packing and (also important) strongly anisotropic charge density. This inevitably leads to breakdown of the single-point expansion at small interseparations. It is possible to avoid this breakdown by choosing multiple expansion sites ("polar sites") per molecule in such a way as to accurately represent the molecular electrostatic potential, with a set of suitably chosen multipole moments $\{Q_{lk}^{a}\}$ allocated to each site. We then simply extend the expression for the interaction energy between two molecules A and B in the single-point expansion, Eq. (21), and include the sum over expansion sites $a \in \mathrm{A}$ and $b \in \mathrm{B}$:

$$U_{\mathrm{AB}} = \sum_{a \in \mathrm{A}} \sum_{b \in \mathrm{B}} \hat{Q}^{\,a}_{l_1 k_1} T^{a,b}_{l_1 k_1 l_2 k_2} \hat{Q}^{\,b}_{l_2 k_2} \equiv \hat{Q}^{\,a}_{l_1 k_1} T^{a,b}_{l_1 k_1 l_2 k_2} \hat{Q}^{\,b}_{l_2 k_2}, \tag{23}$$

where we have used the Einstein sum convention for the site indices a and b on the right-hand side of the equation, in addition to the sum convention that is already in place for the multipole-moment components.

There are a number of strategies for arriving at such a collection of distributed multipoles [94, 97–101]. They can be classified according to whether the multipoles are derived from the electrostatic potential generated by the self-consistent field (SCF) charge density or from a decomposition of the wavefunction itself. For example, the CHELPG (charges from electrostatic potentials, grid-based) method relies on performing a least-squares fit of atom-placed charges to reproduce the electrostatic potential as evaluated from the SCF density on a regularly spaced grid [98, 102]. The distributed-multipole-analysis (DMA) approach [99, 100], developed by A. Stone, operates directly on the quantum-mechanical density matrix, expanded in terms of atom- and bond-centered Gaussian functions.

4.4.3 Induction Interaction

Similar to the distributed-multipole expansion of molecular electrostatic fields, one can derive a distributed-polarizability expansion of the molecular field response. We can start by including the multipole-expansion in the perturbing Hamiltonian term $\hat{W} = \hat{Q}^{\,a}_{t} \phi^{a}_{t}$, where we again use the Einstein sum convention for both superscripts a, referencing an expansion site, and subscripts t, which summarize the multipole components (l, k) in just one index. Using this approximation for the intermolecular electrostatic interaction, the second-order energy correction now reads:

$$W^{(2)} = -\sum_{n \neq 0} \frac{\left|\langle 0 | \hat{Q}^{\,a}_{t} \phi^{a}_{t} | n \rangle\right|^2}{W_n - W_0}. \tag{24}$$

We absorb the quantum-mechanical response into a set of intramolecular site–site polarizabilites, where $-\alpha_{tt'}^{aa'}\phi_{t'}^{a'}$ yields the induced multipole moment Q_t^a at site a that results from a field component $\phi_{t'}^{a'}$ at site a' [94]:

$$\alpha_{tt'}^{aa'}\phi_{t'}^{a'} = \sum_{n\neq 0}\frac{\left|\langle 0|\hat{Q}_t^{\,a}|n\rangle\langle n|\hat{Q}_{t'}^{\,a'}|0\rangle\right|}{W_n - W_0} + h.c. \tag{25}$$

With this set of higher-order polarizabilities at hand, we obtain the induction stabilization in a distributed formulation as $W^{(2)} = -\frac{1}{2}\phi_t^a\alpha_{tt'}^{aa'}\phi_{t'}^{a'}$. The derivatives of $W^{(2)}$ with respect to the components of the field ϕ_t^a at a polar site a then yield the correction to the permanent multipole moment Q_t^a at that site: $\Delta Q_t^a = \partial W^{(2)}/\partial\phi_t^a = -\alpha_{tt'}^{aa'}\phi_{t'}^{a'}$.

Using the multipole corrections ΔQ_t^a, we can extend the electrostatic interaction energy given by Eq. (23) to include the induction contribution in the field energy U_{ext}, while accounting for the induction work U_{int}:

$$U_{\text{ext}} = \frac{1}{2}\sum_{\text{A}}\sum_{\text{B}\neq\text{A}}\left(Q_t^a + \Delta Q_t^a\right)T_{tu}^{ab}\left(Q_u^b + \Delta Q_u^b\right) \tag{26}$$

$$U_{\text{int}} = \frac{1}{2}\sum_{\text{A}}\Delta Q_t^a\eta_{tt'}^{aa'}\Delta Q_{t'}^{a'} \tag{27}$$

Here, the inverse of the positive-definite tensor $\eta_{tt'}^{aa'}$ is given simply by the distributed polarizabilities tensor $\alpha_{tt'}^{aa'}$, and we have included explicit sums over molecules A and B.

We now use a variational approach to calculate the multipole corrections ΔQ_t^a based on the total energy $\mathcal{L} = U_{\text{ext}} + U_{\text{int}}$. Variation of this function with respect to ΔQ_t^a:

$$\delta(U_{\text{ext}} + U_{\text{int}}) = \delta Q_t^a\left[\sum_{\text{B}\neq\text{A}}T_{tu}^{ab}\left(Q_u^b + \Delta Q_u^b\right) + \eta_{tt'}^{aa'}\Delta Q_{t'}^{a'}\right] \tag{28}$$

leads to a set of self-consistent equations for the induced moments, which for large systems are best solved by iteration:

$$\Delta Q_t^a = -\sum_{\text{B}\neq\text{A}}\alpha_{tt'}^{aa'}T_{t'u}^{a'b}\left(Q_u^b + \Delta Q_u^b\right). \tag{29}$$

Reinserting ΔQ_t^a into $\mathcal{L}$ yields a total energy that can be decomposed according to three energy terms:

$$U_{pp} = \sum_{\mathrm{A}} \sum_{\mathrm{B>A}} Q_t^a T_{tu}^{ab} Q_u^b$$

$$U_{pu} = \frac{1}{2} \sum_{\mathrm{A}} \sum_{\mathrm{B>A}} \left[\Delta Q_t^a T_{tu}^{ab} Q_u^b + \Delta Q_t^b T_{tu}^{ab} Q_u^b \right]$$

$$U_{uu} = 0 \tag{30}$$

Here, $U_{pp} \leftrightarrow W^{(1)}$ is the electrostatic interaction energy, i.e., the first order correction due to the interaction of permanent multipole moments. $U_{pu} \leftrightarrow W^{(2)}$ is the sought-after induction energy associated with the interaction of the induced moments on one molecule with the permanent moments on surrounding molecules. Strikingly, the interaction between induced moments on different molecules, contributing to U_{uu}, is cancelled by the induction work, as is a consequence of the self-consistent nature of the induction process, see Eq. (29).

4.4.4 The Thole Model

Equations (29) and (30) allow us to compute the electrostatic and induction energy contribution to site energies in a self-consistent manner based on a set of molecular distributed multipoles $\{Q_t^a\}$ and polarizabilities $\left\{\alpha_{tt'}^{aa'}\right\}$, which can be obtained from a wavefunction decomposition or fitting schemes, as discussed in Sect. 4.4.2. The $\left\{\alpha_{tt'}^{aa'}\right\}$ are formally given by Eq. (25). This expression is somewhat impractical (although possible, see [99]) to evaluate and various empirical methods have been developed. One of these, the Thole model [103, 104], treats polarizabilities α^a in the local dipole approximation.

The Thole model is based on a modified dipole–dipole interaction, which can be reformulated in terms of the interaction of smeared charge densities. This eliminates the divergence of the head-to-tail dipole–dipole interaction at small interseparations (Ångstrom scale) [103–105]. Smearing out the charge distribution mimics the nature of the quantum mechanical wavefunction, which effectively guards against this unphysical polarization catastrophe.

The smearing of the nuclei-centered multipole moments is obtained via a fractional charge density $\rho_f(\mathbf{u})$, which should be normalized to unity and fall off rapidly at a certain radius $\mathbf{u} = \mathbf{u}(\mathbf{R})$. This radius relates to the distance vector $\mathbf{R}$ connecting two interacting sites via a linear scaling factor that takes into account the magnitude of the isotropic site polarizabilities α^a. This isotropic fractional charge density gives rise to a modified potential:

$$\phi(u) = -\frac{1}{4\pi\varepsilon_0} \int_0^u 4\pi u' \rho(u') \mathrm{d}u' \tag{31}$$

The multipole interaction tensor $T_{ij\ldots}$ (this time in Cartesian coordinates) can be related to the fractional charge density in two steps. First, it is rewritten in terms of the scaled distance vector $\mathbf{u}$:

$$T_{ij\ldots}(\mathbf{R}) = f\left(\alpha^a\alpha^b\right)t_{ij\ldots}\left(\mathbf{u}\left(\mathbf{R},\alpha^a\alpha^b\right)\right), \tag{32}$$

where the specific form of $f(\alpha^a\alpha^b)$ results from the choice of $u(\mathbf{R},\alpha^a\alpha^b)$. Second, the smeared interaction tensor $t_{ij\ldots}$ is given by the appropriate derivative of the potential in Eq. (31):

$$t_{ij\ldots}(\mathbf{u}) = -\partial_{u_i}\partial_{u_j}\ldots\phi(\mathbf{u}). \tag{33}$$

It turns out that for a suitable choice of $\rho_f(\mathbf{u})$, the modified interaction tensors can be rewritten in such a way that powers n of the distance $R = |\mathbf{R}|$ are damped with a damping function $\lambda_n(\mathbf{u}(\mathbf{R}))$ [106].

There are a large number of fractional charge densities $\rho_f(\mathbf{u})$ that have been tested for the purpose of giving the best results for the molecular polarizability as well as interaction energies. For most organic molecules, a fixed set of atomic polarizabilities ($\alpha_C = 1.334, \alpha_H = 0.496, \alpha_N = 1.073, \alpha_O = 0.873, \alpha_S = 2.926\,\text{Å}^3$) based on atomic elements yields satisfactory results [104] although reparametrizations are advised for ions and molecules with extended conjugated systems.

One of the common approaches used, e.g., in the AMOEBA force field [106], employs an exponentially decaying fractional charge density:

$$\rho(u) = \frac{3a}{4\pi}\exp\left(-au^3\right), \tag{34}$$

where $\mathbf{u}(\mathbf{R},\alpha^a\alpha^b) = \mathbf{R}/(\alpha^a\alpha^b)^{1/6}$ and the smearing exponent $a = 0.39$. The distance at which the charge–dipole interaction is reduced by a factor γ is then given by:

$$R_\gamma = \left[\frac{1}{a}\text{In}\left(\frac{1}{1-\lambda}\right)\right]^{1/3}\left(\alpha_i\alpha_j\right)^{1/6}. \tag{35}$$

The interaction damping radius associated with $\gamma = 1/2$ ranges around an interaction distance of 2 Å. A half-interaction distance on this range indicates how damping is primarily important for the intramolecular field interaction of induced dipoles.

4.4.5 Crystalline P3HT Site Energies

The expansion of the molecular field and field response in terms of distributed multipoles and polarizabilities is an efficient approach for solving for the first- and second-order corrections to the molecular Hamiltonian that result from a

perturbation by the molecular environment. Only a few studies have discussed the influence of this perturbation on the transport behavior of P3HT. Usually requiring atomistic resolution, systems of up 10^4 thiophenes have been treated in this fashion, for example, in order to explore the density of states of P3HT in dependence on the polymorph and regioregularity or at interfaces [13, 49].

In amorphous systems, localization of charge carriers has been reported to result from fluctuations of the electrostatic potential rather than from breaks in conjugation [107]. Furthermore, an exponentially decaying tail of the density of states was found.

In crystalline systems, P3HT backbones are fully conjugated and a charge can be assumed to delocalize over an entire oligomer [108] (for a more detailed discussion see Sect. 5.1). The internal contribution to the ionization potential does not change from segment to segment and the energetic disorder is mostly due to a locally varying electrostatic potential.

The distributions in hole site energies, i.e., the differences between the energies of the system when a selected molecule is in the cationic or neutral state excluding the constant internal contribution related to the gas-phase ionization potential, are reproduced in Fig. 8 according to [13], together with the fits to a Gaussian function.

It was shown that both the width σ and the mean $\langle U \rangle$ of the distribution depend on the side-chain packing and polymer regioregularity. As expected, 100% regioregular P3HT always has narrower site energy distributions than the 90% P3HT. Interestingly, the hole becomes less stable upon side-chain melting in the 100% regioregular P3HT (the distribution shifts to more negative numbers by 0.1 eV), whereas it is stabilized by side chain melting in the 90% regioregular P3HT.

One can attribute the changes in the energetic density of states (DOS) to specific structural features [13]. The width in the distributions is governed by regioregularity, with CC-100 and CA-100 having virtually identical widths of $\sigma = 45$ and 51 meV, respectively. CC-90 and CA-90 are energetically more disordered with $\sigma = 74$ and 75 meV, respectively. The magnitude of the disorder compares well with the width of the DOS as extracted from time-of-flight experiments [16, 17], where values for σ of 56 and 71 meV, respectively, have been proposed from a fit of the field-dependence of the mobility as obtained within the Gaussian disorder model [109]. In [16], σ did not vary significantly between 94% and 98% regioregular P3HT. However, an increase in DOS width of around 30 meV can drastically impact charge mobility in the case of a one-dimensional connected hopping network, which can be assumed to appropriately reflect conditions in crystalline lamellae.

On the level of chain ordering, the increase in energetic disorder can also be related to the increase in paracrystallinity along the π-stacking direction [13]. Considering that the hole–quadrupole interactions associated with thiophene dimers are the leading contributors to site energies here, this origin for the increase in σ is fully justified and explains the similar energetic disorder computed for CC-100 and

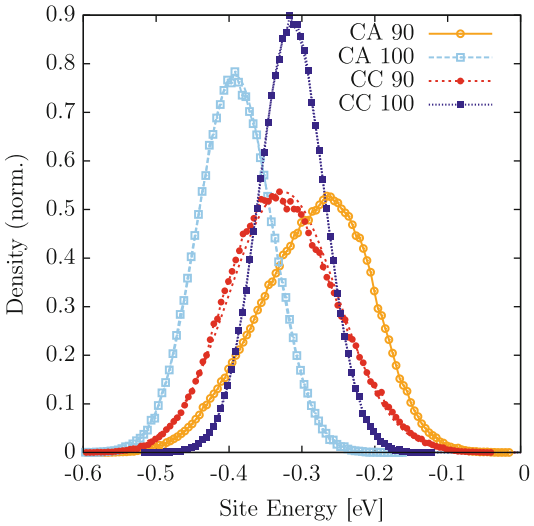

Fig. 8 Densities of state together with Gaussians fitted to CC-100, CA-100, and CC-90. Note the aberration from a Gaussian lineshape found for CA-90, which results from slipping defects in the lamellar stack. CA-100 corresponds to a system with a crystalline arrangement of backbones, amorphous packing of side-chains, and regioregularity of 100%. CC-100 corresponds to a system with crystalline side chains and 100% regioregularity. Adapted with permission from Poelking et al. [13]. Copyright (2013) American Chemical Society

CA-100. Notably, gliding-type paracrystallinity, measured along the c axis, does not strongly affect the electrostatic interactions between charged conjugated planes.

Shifts of the mean $\langle U \rangle$ of the site-energy distributions have been linked to the negative quadrupole moment of thiophene dimers: A hole localized on a polymer chain will be stabilized on an electrostatic level due to the quadrupole moment of the neighboring chains, even without including polarization. This means that better geometrical overlap of the backbones leads to a larger stabilization of holes. During the transition from a staggered to a coplanar stacking, the reduction in tilt angle leads to enhanced hole–quadrupole interactions. These are responsible for the lower $\langle U \rangle$ in CA-100 compared to CC-100. For the systems of lower regioregularity, the transition in backbone stacking is less pronounced because side-chain defects lead to a slight planarization of the backbone and, hence, lowered ionization potentials (compare the site-energy mean of CC-90 in Fig. 8 to that of CC-100). As the backbone stacking becomes entirely coplanar, side-chain defects lead to a high degree of slipping-type paracrystallinity. This implies a weakening of the energetically favorable hole–quadrupole interaction, and therefore an increase in the mean of the site-energy distribution when comparing CC-90 to CA-90. In addition to this shift of the mean, the slipping defects in CA-90 lead to a slight deviation from a Gaussian shape of the DOS.

Summing up, the external contribution to the energetic density of states in P3HT was shown to be intimately connected to paracrystallinity along the π-stacking direction, with the energetic disorder σ linearly related to the amplitude of backbone–backbone distance fluctuations, and the mean of the backbone–backbone distance distribution analogously related to the average site energy $\langle U \rangle$.

4.5 Charge Mobility

With the site energies and electronic couplings at hand, one can calculate charge transfer rates (see Sect. 4) for the set of electronically coupled pairs of conjugated segments. The directed graph that describes charge transport in the system is then fully parametrized and charge dynamics can be described via a master equation of the form:

$$\frac{\partial P_\alpha}{\partial t} = \sum_\beta \left[P_\beta K_{\beta \to \alpha} - P_\alpha K_{\alpha \to \beta} \right], \tag{36}$$

where P_α is the probability of finding the systems in state α. The rates $K_{\alpha \to \beta}$ are the transition rates from a state α to state β. For single-carrier dynamics, the number of available states α is the number of conjugated segments in the system, with each state associated with a molecule A being singly occupied. Using the single-site occupation probability p_A and transfer rates $k_{\mathrm{A} \to \mathrm{B}}$, Eq. (36) simplifies to:

$$\frac{\partial p_\mathrm{A}}{\partial t} = \sum_\mathrm{B} \left[p_\beta k_{\mathrm{B} \to \mathrm{A}} - p_\mathrm{A} k_{\mathrm{A} \to \mathrm{B}} \right]. \tag{37}$$

This equation, valid in the limit of low charge densities, has the form $\partial_t \mathbf{p} = \tilde{k}\,\mathbf{p}$ and can be solved using either linear solvers or a kinetic Monte Carlo (KMC) algorithm. A variable timestep size implementation of KMC is often used due to the broad distribution of rates $k_{\mathrm{A} \to \mathrm{B}}$, which easily spans many orders of magnitude.

The stationary solution of Eq. (37) can be used to evaluate a number of macroscopic observables. For comparison with TOF measurements, impedance spectroscopy, or similar, the charge-carrier mobility tensor $\tilde{\mu}$ at the electric field $\mathbf{E}$ is calculated as:

$$\tilde{\mu}\,\mathbf{E} = \sum_{\mathrm{A},\mathrm{B}} p_\mathrm{A} k_{\mathrm{A} \to \mathrm{B}} (\mathbf{R}_\mathrm{A} - \mathbf{R}_\mathrm{B}). \tag{38}$$

Alternatively, when using KMC, the charge-carrier mobility along the direction of the external field **E** can be obtained simply by:

$$\mu = \left\langle \frac{\Delta \mathbf{R} \cdot \mathbf{E}}{\Delta t |\mathbf{E}|^2} \right\rangle, \tag{39}$$

where $\langle \ldots \rangle$ denotes averaging over all trajectories, Δt is the total run time of a trajectory, and $\Delta \mathbf{R}$ denotes the net displacement of the charge.

4.5.1 Charge-Carrier Mobility in P3HT Lamellae

Transport studies of different levels of complexity have been performed to study hole transport along the π-stacking direction of P3HT lamellae [13, 110]. Since the transport has a one-dimensional character, it can be anticipated that a broad and static distribution of electronic couplings (see also Sect. 4.6) limits charge mobility along lamellae [93, 111–117]. This is illustrated in Fig. 9, which shows that the mobility values, evaluated for 5,000 lamellae, each consisting of 40 stacked chains, are broadly distributed, with small mobilities as low as 10^{-7} cm^2/V s.

It is important to relate the distribution of mobilities to those of electronic couplings and site energies. It has been found by comparing materials of different regioregularity that the associated mobility distributions are fundamentally different from those expected solely on the grounds of electronic couplings (see Fig. 7). The distribution of transfer integrals is determined by the polymorph at hand (I′ or I) and not sensitive to a small decrease in regioregularity, whereas energetic disorder is governed by regioregularity defects and, as such, is polymorph-independent. Aiming for high mobilities, one should hence prefer high regioregularity over medium regioregularity due to the smaller energetic disorder, and prefer P3HT form I′ over P3HT form I due to higher electronic couplings. The mobility implicitly depends on both quantities and as such mirrors a clear trend, with the average mobility decreasing in the order CC-100>CA-100>CC-90>CA-90 [13]. These averages are indicated by vertical bars in Fig. 9. In the case of 100% regioregular P3HT, simulation results are in excellent agreement with field-effect mobilities in P3HT nanofibers (devoid of grain boundaries) extracted from experimental transistor I–V curves on P3HT nanofibers [14, 24, 118]. The range of experimental values ($\mu = 0.01 - 0.06$ cm^2/V s) obtained for different solvent and processing conditions is shown as the gray bar in Fig. 9.

The effect of regioregularity on charge transport has been studied experimentally in the context of time-of-flight experiments [16], where a reduction in regioregularity by 5% led to a decrease in mobility by a factor of five. In simulations, a reduction in regioregularity by 10% translates into a factor of ten decrease in mobility, indicating that the decrease in mobility is due to intradomain instead of interdomain transport. According to [13], where the authors studied the intermolecular contribution to the DOS, the regioregularity effect is exclusively

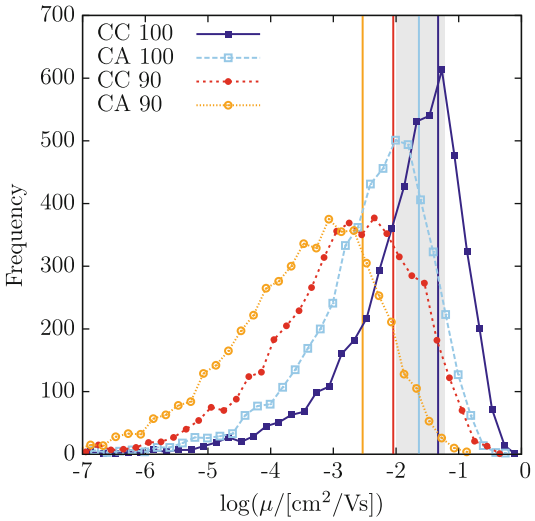

Fig. 9 Distributions of mobilities for CC-100, CA-100, CC-90, and CA-90. *Vertical lines* indicate averages. The *gray bar* includes the range of mobilities measured in P3HT nanofibers [14, 24, 118]. CA-100 corresponds to a system with a crystalline arrangement of backbones, amorphous packing of side-chains, and regioregularity of 100%. CC-100 corresponds to a system with crystalline side chains and 100% regioregularity. Adapted with permission from Poelking et al. [13]. Copyright (2013) American Chemical Society

due to increased energetic disorder. Additionally, the intramolecular contribution to the DOS was found to only have a negligible effect on localization length and, hence, transport in the high-regioregularity regime [108]. The conclusion is that the higher mobility in the more regioregular material is entirely attributable to a narrowing of the DOS that results from increased order in hole–quadrupole interaction distances.

The effect of energetic disorder is further amplified in the case of P3HT due to the one-dimensional character of transport, since a single energetic trap can impede transport through the entire lamella [93]. This effect is visualized in Fig. 10 [13], where the energetic landscape is exemplified for five different simulation times and four materials. Here, the widths of the bonds connecting the hopping sites are proportional to the logarithm of squared electronic coupling elements, while the heights of the vertical bars are proportional to the occupation probability of a specific site. The gray scale indicates the average mobility of a particular lamella, with darker colors corresponding to lower mobilities. One can see that site-energy profiles are highly corrugated and spatially correlated, with weaker correlations in the case of reduced regioregularity. Note also that the deep energetic traps found in CC-90 and CA-90 persist throughout the entire time range shown here, as expected from the associated time autocorrelation functions. Studying the landscape-mobility correlation more closely, it becomes apparent that transport in CC-100 and CA-100 is strongly dominated by weak links (small transfer integrals) that

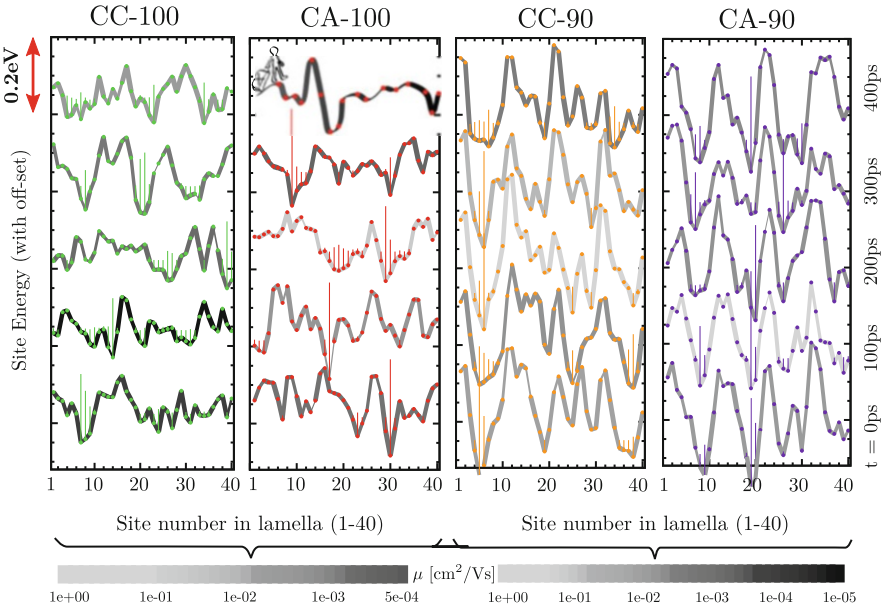

Fig. 10 The charge transport network for hole transport in polymeric lamellar crystals for four material systems from computer simulations: P3HT polymorphs CC (form I′) and CA (form I), with regioregularities of 100 and 90%. Widths of *connecting lines* between neighboring sites and heights of *vertical lines* are proportional to the logarithm of squared transfer integrals and occupation probabilities, respectively. Mobilities are color-coded as indicated. Adapted with permission from Poelking et al. [13]. Copyright (2013) American Chemical Society

adversely affect the lamellar mobility, whereas transport in CC-90 and CA-90 suffers mostly from energetic disorder, as already suspected from the shape of the mobility distribution in Fig. 9.

To summarize, a small concentration of defects in side-chain attachment (90% regioregular P3HT) was shown to lead to a significant (factor of ten) decrease in charge-carrier mobility. This reduction is due to an increase in the intermolecular part of the energetic disorder and can be traced back to the amplified fluctuations in backbone–backbone distances, i.e., paracrystallinity.

4.6 Autocorrelation of Electronic Couplings and Site Energies

In the hopping picture, understanding the factors that limit charge-carrier mobility in polymers not only demands knowledge of the distribution of transport parameters, but also their time dependence. The latter is an important hint as to whether or not the hopping picture is justified to begin with, since there is no theoretical

technique currently available that can predict the regime of charge transport for a given material system. To explore the limitations associated with simulating charge transfer in a frozen morphology, Poelking et al. [13] have compared charge escape times τ_{esc} with relaxation times of the backbone, as reflected both in the electronic coupling elements and in site energies. The escape time (i.e., the average time a charge spends localized on a given site) is the inverse of the escape rate, $\tau_{\mathrm{esc}}^{(i)} = 1/\Gamma_{\mathrm{esc}}^{(i)}$, where $\Gamma_{\mathrm{esc}}^{(i)} = \sum_{j(i)} \Gamma_{ij}$, Γ_{ij} is the hole-transfer rate from site i to site j, and the sum is evaluated for all nearest neighbors j of site i. From the resulting distribution of escape times, $p(t)$, one can calculate the distribution (exceedence, or complementary cumulative distribution function), $P(\tau) = \int_{\tau}^{\infty} p(t)\mathrm{d}t$, which is proportional to the number of sites with an escape time larger than τ.

Backbone dynamics can be estimated from the time autocorrelation functions $R_U(\tau)$ for site energies $U^{(i)}$ and $R_J(\tau)$ for couplings $|J_{ij}|^2$:

$$R_U(\tau) = \frac{\left\langle \left(U_t^{(i)} - \langle U \rangle\right)\left(U_{t+\tau}^{(i)} - \langle U \rangle\right)\right\rangle}{\sigma^2}, \tag{40}$$

where the outer $\langle \ldots \rangle$ denotes the ensemble average. The width σ and average $\langle U \rangle$ have the same meaning as in the electronic density of states (see Sect. 4.4). An analogous expression is used for the transfer integrals.

The autocorrelation function and the distribution of escape times for P3HT are summarized in Fig. 11. Relaxation of the electronic coupling elements and of the site energies occur on similar time scales in spite of their dissimilar physical origins: Site energies are related to long-range electrostatic interactions where averaging occurs over a large number of nearest neighbors and leads to spatial correlations. On the other hand, the electronic coupling elements (to a first approximation) only depend on the geometries of pairs of molecules, which results in increased sensitivity to thermal motion of the internal degrees of freedom. The reason for similar time scales is the chemical structure of P3HT: Every thiophene unit is linked to an alkyl side chain with slow dynamics both in the crystalline and amorphous phases. This overdamps the backbone dynamics, particularly torsional motions of thiophene units, and results in slow variations of electronic couplings. Interestingly, for the similar conjugated polymer PBTTT, where the thienothiophene unit is not linked to a side chain (implying a lower side-chain density and better crystallinity), the significantly faster dynamics of electronic couplings can boost the charge-carrier mobility [119].

Comparing the 100% and 90% regioregular materials, we can see how the defects in side-chain attachment lead to slower dynamics, with decorrelation times significantly increased over the defect-free case. More quantitatively, for intermediate delay times in the range of tenths of picoseconds, the time evolution is in all cases governed by a logarithmic diffusion-driven decorrelation of both site energies and electronic couplings. Regarding site energies, the dimensionless exponent that characterizes this decorrelation for CA-100 assumes a value three times larger than for CA-90. This again highlights how defects in regioregularity

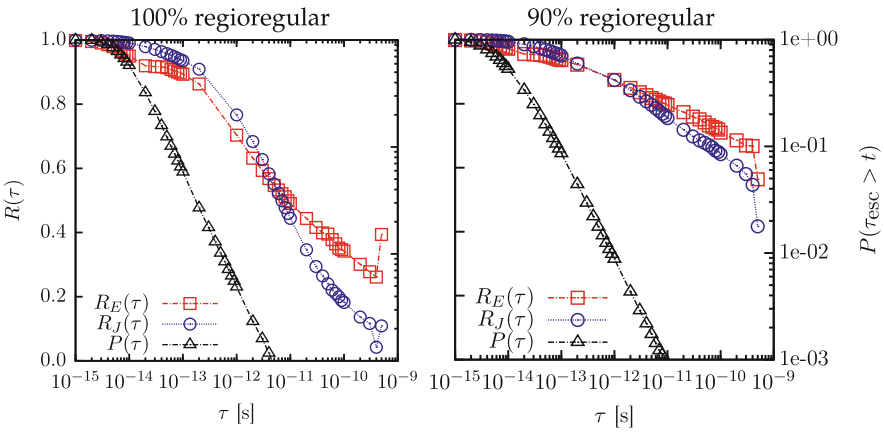

Fig. 11 The time scales of transport parameters in material systems of different regioregularity, estimated via the time autocorrelation function of transfer integrals (*blue circles*), site energies (*red squares*) and the tail distribution of escape times (*black triangles*). Adapted with permission from Poelking et al. [13]. Copyright (2013) American Chemical Society

induce glass-like features in structure and dynamics. Analyzing the de-correlation in polymorphs I′ and I, this exponent remains the same. There is, however, an offset between the two time characteristics that persists up to delay times in the nanosecond range. This offset is a consequence of structural decorrelations within the first few femtoseconds: Side chains in form I are in a dynamically disordered state and, hence, damp backbone dynamics more effectively than the hexyl groups in form I′. This damping apparently dominates dynamics on this short time scale.

For P3HT, even the slowest escape times for holes do not extend into the decorrelation regime. Charge-carrier dynamics is therefore limited by the static disorder of electronic couplings and site energies, since their relaxation times exceed the typical time scales for hopping transport. Hence, it is possible to resort to a single charge-transfer rate to describe transport, Eq. (7), without time-averaging of electronic couplings of a pair of molecules, as needed for columnar discotic liquid crystals [120] or PBTTT [119].

5 First-Principles-Based Calculations for Large Models of Polymer

5.1 The Charge Localization–Length Problem

As we have seen in the previous sections, the definition of a reasonably accurate kinetic master equation from the microscopic structure can be achieved by combining atomistic simulations, quantum chemical calculations, and microelectrostatic

corrections. These methodologies require the definition of a 'unit of transport', i.e., a region of the polymer where the charge is assumed to reside. For transport in small molecules, liquid crystals, and some relatively short polymers it is straightforward to consider the full molecular unit as the unit of transport. It is also reasonable to consider long oligomers when studying transport in the direction perpendicular to the π–π stacking in semicrystalline phases. For amorphous regions in fully amorphous polymers, or if one is interested in the transport along the π-conjugated backbone, further approximations are needed. In the case of amorphous polymers like poly(*p*-phenylene vinylene) (PPV), the structure determined by classical simulations [121–123] contains regions where there is a strong deviation from planarity and it was proposed that the polymeric chain can be divided into conjugated portions defined as the regions between these conjugation-breaking distortions [124]. This idea has been used to interpret spectroscopic data but it is very difficult to apply it to computational systems. First of all, it is not clear how one can rigorously define a sharp threshold separating the complete conjugation breaking from the full conjugation between monomers. Moreover, there are many interesting polymers (including P3HT) that form crystalline domains so extended that no conjugation breaks are found for hundreds of nanometers [125]. The charge is certainly more localized than that, either by the disorder present in the semicrystalline phase or by electron–phonon coupling (evidence of charge localization can be found for example from charge-modulated spectroscopy [126, 127]). Determination of the localization characteristic of charge carriers in polymers is another important area of computational investigation that has been pursued by several groups over the past few years.

To determine the charge localization in a large system there is no other alternative than computing the electronic wavefunction of a large model system. The model systems are generated by classical simulation of polymers containing thousands of atoms, so it is not practical to study them in a charged state using quantum-mechanical methods. A calculation of the electronic structure of such a large model with an electron less than the neutral state would only yield the ground state, whereas one is generally interested in the energy distribution and localization of many charged states. The excited state of the charged simulation box cannot be computed with modern computational methods and therefore one cannot even evaluate the nuclear relaxation (reorganization energy) for the hopping between two states by starting with a large model system. For these reasons, all attempts to evaluate the wavefunction of a large model of polymers have focused on neutral systems and have interpreted the one-electron states (the orbitals) as the possible sites where the excess charge can be localized [107, 108]. Results are normally presented in terms of a density of states (DOS) and localization length but it should be noted that these two quantities are computed for systems with orbitals fully filled and empty above and below the band gap, respectively. Therefore, they cannot be directly compared with the models in Sect. 4, which include electron and nuclear polarization but have to make assumptions regarding the localization length.

For the one-electron states to be representative of the actual localization of the charge carrier, a further condition needs to be satisfied. The charge needs to be localized predominantly by the conformational disorder of the polymer and not by

the electron–phonon coupling. If this coupling is particularly strong, the frontier orbitals may be delocalized over many monomers. However, when an excess charge is added, the nuclear polarization localizes the charge, completely modifying the electronic wavefunction with respect to the neutral calculation. There is some general consensus [128, 129] that the localization of the wavefunction in P3HT largely originates from disorder and not from electron–phonon coupling because there is a correlation between increased order of P3HT and increased mobility [20]. Alternatively, one can be convinced that the conformational disorder is stronger than the electron–phonon coupling by comparing the polaron size of a perfectly ordered polymer chain with the localization of the orbitals computed from calculation of large realistic models of disordered chains. If the polaron size of the perfectly ordered system is much larger than the orbital in the disordered model, it is acceptable to determine the charge localization from calculations that neglect the electron–phonon coupling as a first approximation. Calculations for P3HT support this approximation [108, 130] but it should be noticed that polaron sizes are strongly dependent on the DFT methodology [131] and that the same assumption may not hold for the new families of semiconducting polymers [132], where large conjugated units are more weakly coupled by smaller conjugated linkers.

5.2 *Strategies for Large-Scale Electronic-Structure Calculations of Polymer Models*

Under the conditions that the calculation of a ground state wavefunction of a polymer model yields information about the charge localization for the carrier states, it is still not trivial to carry out such calculations. It is not obvious to know in advance how large a model of bulk polymer should be in order to reproduce the DOS and localization length without the results being affected by finite-size effects. The experience of available calculations with P3HT and PPV suggests that a model containing several chains of 20–40 monomers displays electronic properties that do not depend appreciably on the chain length [133] (it should not be forgotten that the morphology depends on the chain length up to much larger molecular weights [134]). Such models contain tens of thousands of atoms, a number that is still one order of magnitude larger than that normally achievable by current software specialized in linear scaling ab initio calculations, like SIESTA [135] or ONETEP [136]. It is certainly possible that such methods can be employed in the near future in benchmark calculations, but it is important to remember that what is needed is a methodology able to evaluate the wavefunction for many replicas of the equilibrated systems in order to provide statistically meaningful results.

However, ideas from linear scaling methodologies can be used to develop ad hoc methods that are able to compute in a more approximate fashion the wavefunction for large systems. Essentially, all linear scaling methods are based on the definition of a very localized basis set that reduces the number of matrix elements to be

evaluated to a value that scales linearly with the size of the system [135–137]. For organic polymers, it seems natural to describe the polymer orbitals as a linear combination of monomer orbitals. It is possible to reduce the number of orbitals per monomer to be considered (e.g., from HOMO-1 to LUMO+1 in P3HT), thus reducing the size of the one-electron effective Hamiltonian. Different schemes have been proposed for evaluating the diagonal and off-diagonal elements of such a reduced Hamiltonian, including a fragment molecular orbital approach [138] and a charge patching method [107, 139, 140]. Their calculation of the matrix elements shares many points with the methodology described in Sect. 4.3, except that the calculations are always performed for the neutral state. A general formalism for such methods has been developed by the quantum chemistry community [137, 141–143] and has the obvious advantage of being very intuitive: All matrix elements entering in the Hamiltonian have a clear physical meaning.

The various partitioning schemes proposed for polymer systems are very often complemented by further approximations that take into account the chemical structure of the investigated system. As the frontier orbitals are invariably localized on the conjugated fragment of the monomer, while a large fraction of the molecular weight is taken up by the polymer side chains that do not contribute to the charge transport states, it is customary to remove the side chains from the calculation, sometimes substituting them with effective point charges that simulate the missing electrostatic effects [133]. For lamellar systems such as P3HT and PBTTT, it is an excellent approximation to neglect completely the electronic coupling between lamellae, therefore describing a system that is essentially two-dimensional [108, 144].

A relatively simple approach that can be considered the simplest possible Hamiltonian partitioning technique has been proposed recently for the calculation of the electronic properties of MEH-PPV [133]. Here the amorphous-polymer model is simply partitioned into subsystems containing single chains (surrounded by point charges reproducing the local electrostatic potential and with shortened side chains). The full wavefunction of each single chain can be computed with routine DFT calculations and the electronic couplings between chains can be evaluated similarly. The coupling between polymer orbitals localized on different chains is very small because only a few atoms localized on different chains are in contact while the orbitals are typically localized over several monomers. A further reduction in computational cost can be achieved using a small basis set, which, at least for this type of polymer, does not seem to affect the shape of the DOS or the localization length.

An alternative approach to full or ad hoc linear scaling DFT methods is calculation through approximate DFT methods such as the tight binding DFT (DFTB) [145]. This family of methods has been developed over the past few years and the most convenient version of the methodology is the self-consistent charge-density functional tight binding (SCC-DFTB) [146], as implemented for example in the software DFTB+. An acceleration of one to two orders of magnitudes for the electronic structure calculation is achieved by an approximate evaluation of the Kohn–Sham–Fock matrix elements in the atomic-orbital basis. A very broad range

of applications apart from organic semiconductors have been proposed [143], but relatively few results have been reported for semiconducting polymers [147] even though great success has been achieved in the study of charge transfer processes in biophysical systems [148, 149], which provide a similar level of computational challenge.

Finally, an obvious choice for calculation of the large-scale electronic structure would be via semi-empirical methods. These have been the methods of choice for many years for exploring charge [150] and exciton [151] dynamics in single-chain polymers containing only carbon and hydrogen (e.g., PPV, polyethylene). However, there are very few systematic studies of their reliability for polymers containing heteroatoms such as S, F, Se, and Ge, which are featured in a large number of new polymers.

Although there seems to be no lack of options for the calculation of the wavefunction of large models of polymeric systems, these calculations have been attempted on a very limited number of systems. One of the main objectives of future computational studies is to perform calibration of these methodologies, whereby the results obtained with different approximate electronic structure methods on the same structural models are compared.

5.3 *Results from the Computation of the Wavefunction for Large-Scale Polymer Models*

The calculations performed on models of polymers, according to any of the methodologies described in the previous section, provide in the first instance the DOS and a measure of the localization length of the states relevant for transport, i.e., those located at the edge of the valence (or conduction) band for holes (or electrons). For all polymers considered (amorphous and semicrystalline), the states deep in the tail of the DOS are more localized and the localization length increases as states deeper in the band are considered (see Fig. 12), as predicted by simplified generic polymer models [152]. The chemical description of these states in the tail is potentially very useful because it may suggest possible routes for increasing the charge mobility by reducing the number of trap states.

Calculations suggest that hole trap states (high-energy occupied orbitals) are found in regions of P3HT where the conjugated backbone is more planar than on average [108, 153]. The possibility of different degrees of planarity generates regions where the HOMO–LUMO gap is smaller, coinciding with the more planar segments of P3HT. Not surprisingly, when regioregularity defects are introduced, the trap states become localized far away from the regioregularity defect and, for this reason, the total number of trap states is not much affected by the regioregularity. This has also been found experimentally [108].

By adopting fast methods for calculation of the electronic structure, it is possible to monitor the lifetime of these trap states by repeating the electronic structure

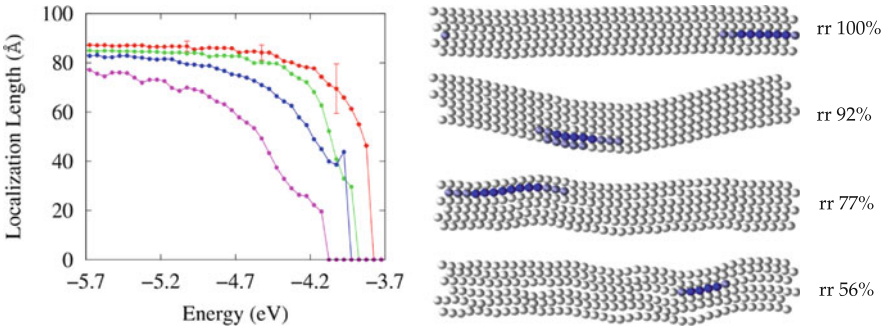

Fig. 12 *Left*: Average localization length in an ordered region of P3HT with regioregularities of 56% (*magenta*, *lowest curve*), 77% (*blue*), 92% (*green*) and 100% (*red*, *uppermost curve*). The error bars of a few selected points are larger in the tail region, indicating the coexistence of localized and delocalized states in that region. *Right*: Localization of the orbital density for the state at the band edge (*dark blue* regions correspond to higher density) on each P3HT monomer (represented as a *sphere*) for different polymer regioregularities. Adapted with permission from McMahon et al. [108]. Copyright (2013) American Chemical Society

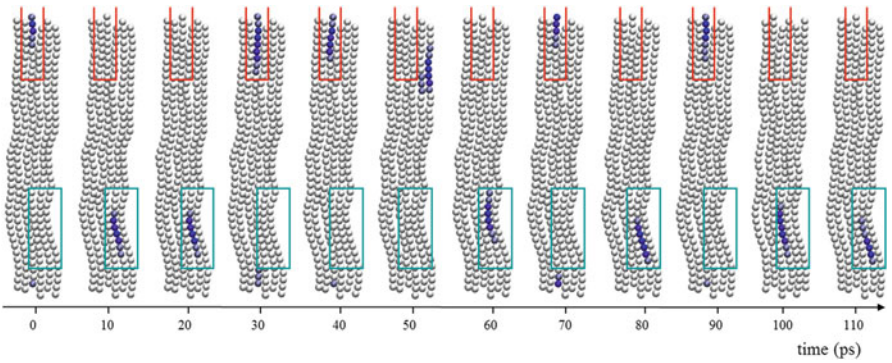

Fig. 13 Localization of the HOMO orbital density on each monomer in a P3HT lamella with low regioregularity during part of the molecular dynamics trajectory. The orbital density (*dark* regions correspond to higher density) is localized (except at 50 ps) in one of the two regions indicated by *rectangles*. Adapted with permission from McMahon et al. [108]. Copyright (2013) American Chemical Society

calculation for different snapshots obtained via classical molecular dynamics (see Fig. 13). For P3HT, the most stable trap states are stable for many tens of picoseconds, i.e., it is possible to think that these trap states are static defects from the point of view of the moving charge carrier [153]. Further analysis shows that these local deformations within the semicrystalline domain are stabilized by gauche conformations in the side chain. A similar analysis on PBTTT shows instead that the trap states appear and disappear in different parts of the chain within a few tens of picoseconds, i.e., there are no long-lived trap states in PBTTT

[147]. Considering that it was not possible to find a clear correlation between the geometry of the chain and the existence of trap states, it was argued that the excellent charge mobility in PBTTT could be due to the limited number of trap states that are supported by the PBTTT morphology.

The attempt to correlate the local structure of the polymer with the localization of the orbitals also yielded some interesting and counterintuitive results [133]. In amorphous PPV, a significant number of high-energy occupied orbitals was found in highly bent regions of the polymer spanning two fragments that, by considering the shape of the polymer, ought to be considered belonging to two separate conjugated units. Considering all the available studies together, it seems that simple intuitive arguments are not sufficient to qualitatively predict the relation between the local geometric structure of a polymer and the localization of its orbitals.

Once the one-electron states of a large system have been evaluated, it is very challenging to derive a fully satisfactory master equation like Eq. (36) that describes the hopping rate between these approximate states. Vukmirović and Wang have proposed a perturbative expression assuming that these states are coupled by nonadiabatic coupling terms that can be evaluated explicitly [107] or can be approximated using the overlap between the absolute value of the wavefunction [154]. Remarkably, the proposed expression does not contain the effect of nuclear polarization in the presence of an additional charge (reorganization energy) and so it is strictly valid in the limit of vanishing reorganization energy like Miller–Abrahams rates [155]. Using this approach it was highlighted that the DOS does not contain all the information needed to evaluate the mobility and that it is possible to have reduced broadening of the DOS due to increased order, but still have low mobility because the coupling between states is reduced [156]. Alternative methods for combining nuclear polarization and disorder effects have been proposed but they have so far only been applied to highly simplified model systems [157, 158].

Ideally, such large-scale calculations should be able to incorporate the effect of nuclear and electronic polarization but, as outlined in Sect. 5.2, it is not clear how such generalizations could be introduced within the available methodologies.

6 Outlook

To conclude, substantial method development is still required in order to achieve parameter-free modeling of organic semiconductors. Imperative for predicting large-scale morphologies are accurate polarizable force fields and computationally efficient coarse-grained models. These models should be capable of describing backbone crystallization and allow for reintroduction of atomistic details. Essential for charge transport are extensions of large-scale, first-principles methods to charged states. Challenges are the incorporation of polaronic effects and a unified description of charge transfer along a single chain and between conjugated segments located on different chains. Last but not least, molecular charge transfer

parameters must be included into a hybrid kinetic Monte–Carlo scheme, with transfer rates updated on the fly to account for long-range electrostatic and polarization effects.

Acknowledgments This work was partly supported by the DFG program IRTG 1404, DFG grant SPP 1355, and BMBF grants MEDOS (FKZ 03EK3503B), MESOMERIE (FKZ 13N10723), and MORPHEUS (FKZ 13N11704). We thank Patrick Gemünden for fruitful collaborations and discussions. We are grateful to Jeroen van der Holst, Mara Jochum and Kurt Kremer for critical reading of the manuscript.

References

1. McCullough RD (1998) Adv Mater 10(2):93–116
2. McCullough RD, Lowe RD (1992) Chem Commun 1992(1):70
3. Meyer V (1883) Berichte der deutschen chemischen Gesellschaft 16(1):1465
4. Yamamoto T, Sanechika K, Yamamoto A (1980) J Polym Sci Polym Lett Ed 18(1):9
5. Lin JWP, Dudek LP (1980) J Polym Sci Polym Chem Ed 18(9):2869
6. Elsenbaumer R, Jen K, Oboodi R (1986) Synth Met 15(2–3):169
7. Perepichka IF, Perepichka DF, Meng H (2009) Thiophene-based materials for electroluminescent applications. In: Perepichka IF, Perepichka DF (ed), Handbook of thiophene-based materials. Wiley, Hoboken, p 695–756
8. Prosa TJ, Winokur MJ, McCullough RD (1996) Macromolecules 29(10):3654
9. Brinkmann M (2011) J Polym Sci B Polym Phys 49(17):1218
10. Wu Z, Petzold A, Henze T, Thurn-Albrecht T, Lohwasser RH, Sommer M, Thelakkat M (2010) Macromolecules 43(10):4646
11. Yuan Y, Zhang J, Sun J, Hu J, Zhang T, Duan Y (2011) Macromolecules 44(23):9341
12. Dudenko D, Kiersnowski A, Shu J, Pisula W, Sebastiani D, Spiess HW, Hansen MR (2012) Angew Chem Int Ed 51(44):11068
13. Poelking C, Andrienko D (2013) Macromolecules 46(22):8941
14. Shimomura T, Takahashi T, Ichimura Y, Nakagawa S, Noguchi K, Heike S, Hashizume T (2011) Phys Rev B 83(11):115314
15. Li G, Shrotriya V, Huang J, Yao Y, Moriarty T, Emery K, Yang Y (2005) Nat Mater 4 (11):864
16. Mauer R, Kastler M, Laquai F (2010) Adv Funct Mater 20(13):2085
17. Ballantyne AM, Chen L, Dane J, Hammant T, Braun FM, Heeney M, Duffy W, McCulloch I, Bradley DDC, Nelson J (2008) Adv Funct Mater 18(16):2373–2380
18. Tsumura A, Koezuka H, Ando T (1986) Appl Phys Lett 49(18):1210
19. Bao Z, Dodabalapur A, Lovinger AJ (1996) Appl Phys Lett 69(26):4108
20. Chang JF, Clark J, Zhao N, Sirringhaus H, Breiby DW, An-dreasen JW, Nielsen MM, Giles M, Heeney M, McCulloch I (2006) Phys Rev B 74(11):115318
21. Kline RJ, McGehee MD, Kadnikova EN, Liu J, Fréchet JMJ, Toney MF (2005) Macromolecules 38(8):3312
22. Zen A, Paum J, Hirschmann S, Zhuang W, Jaiser F, Asawapirom U, Rabe JP, Scherf U, Neher D (2004) Adv Funct Mater 14(8):757–764
23. Merlo JA, Frisbie CD (2003) J Polym Sci B Polym Phys 41(21):2674–2680
24. Bolsée JC, Oosterbaan WD, Lutsen L, Vanderzande D, Manca J (2011) Org Electron 12 (12):2084
25. Raos G, Famulari A, Marcon V (2003) Chem Phys Lett 379(3–4):364
26. Darling SB, Sternberg M (2009) J Phys Chem B 113(18):6215, PMID: 19290596
27. Marchiori C, Koehler M (2010) Synth Met 160(7–8):643

28. Bhatta RS, Yimer YY, Tsige M, Perry DS (2012) Comput Theor Chem 995:36
29. Tsuzuki S, Honda K, Azumi R (2002) J Am Chem Soc 124(41):12200
30. Bhatta RS, Perry DS (2013) Comput Theor Chem 1008:90
31. Baggioli A, Famulari A (2014) Phys Chem Chem Phys 16:3983-3994
32. Maillard A, Rochefort A (2009) Phys Rev B 79(11):115207
33. Colle R, Grosso G, Ronzani A, Zicovich-Wilson CM (2011) Physica Status Solidi B 248 (6):1360–1368
34. Xie W, Sun YY, Zhang SB, Northrup JE (2011) Phys Rev B 83(18):184117
35. Famulari A, Raos G, Baggioli A, Casalegno M, Po R, Meille SV (2012) J Phys Chem B 116 (49):14504
36. Dag S, Wang LW (2010) J Phys Chem B 114(18):5997
37. Marcon V, Raos G (2004) J Phys Chem B 108(46):18053
38. Moreno M, Casalegno M, Raos G, Meille SV, Po R (2010) J Phys Chem B 114(4):1591
39. To TT, Adams S (2012) Nanosci Nanotechnol Lett 4(7):703
40. Bhatta RS, Yimer YY, Perry DS, Tsige M (2013) J Phys Chem B 117(34):10035
41. Melis C, Colombo L, Mattoni A (2011) J Phys Chem C 115(2):576
42. Alexiadis O, Mavrantzas VG (2013) Macromolecules 46(6):2450
43. Curcó D, Alemán C (2007) J Comput Chem 28(10):1743–1749
44. Zhang G, Pei Y, Ma J, Yin K, Chen CL (2004) J Phys Chem B 108(22):6988
45. Huang DM, Faller R, Do K, Moulé AJ (2010) J Chem Theory Comput 6(2):526
46. Do K, Huang DM, Faller R, Moulé AJ (2010) Phys Chem Chem Phys 12(44):14735
47. Yimer YY, Dhinojwala A, Tsige M (2012) J Chem Phys 137(4):044703
48. Reddy S, Kuppa VK (2012) Synth Met 162(23):2117
49. D'Avino G, Mothy S, Muccioli L, Zannoni C, Wang L, Cornil J, Beljonne D, Castet F (2013) J Phys Chem C 117(25):12981
50. Lee CK, Pao CW, Chu CW (2011) Energ Environ Sci 4(10):4124
51. Müller M (2011) J Stat Phys 145(4):967
52. Noid WG (2013) J Chem Phys 139(9):090901
53. Kremer K, Müller-Plathe F (2002) Mol Simulat 28(8–9):729
54. Lyubartsev AP, Laaksonen A (1995) Phys Rev E 52(4):3730
55. Izvekov S, Voth GA (2005) J Phys Chem B 109(7):2469
56. Noid WG, Chu J, Ayton GS, Krishna V, Izvekov S, Voth GA, Das A, Andersen HC (2008) J Chem Phys 128:244114
57. Shell MS (2008) J Chem Phys 129(14):144108
58. Daoulas KC, Müller M (2010) Comparison of simulations of lipid membranes with membranes of block copolymers. In: Meier WP, Knoll W (eds) Polymer membranes/biomembranes. Advances in Polymer Science, vol 224. Springer, Berlin Heidelberg, pp 43–85
59. Jankowski E, Marsh HS, Jayaraman A (2013) Macromolecules 46(14):5775
60. Schwarz KN, Kee TW, Huang DM (2013) Nanoscale 5(5):2017
61. Reith D, Pütz M, Müller-Plathe F (2003) J Comput Chem 24(13):1624–1636
62. Carbone P, Varzaneh HAK, Chen X, Müller-Plathe F (2008) J Chem Phys 128(6):064904
63. Daoulas KC, Rühle V, Kremer K (2012) J Phys Condens Mat 24(28):284121
64. Gemünden P, Poelking C, Kremer K, Andrienko D, Daoulas KC (2013) Macromolecules 46 (14):5762
65. Stingelin N (2012) Polym Int 61(6):866–873
66. Ho V, Boudouris BW, Segalman RA (2010) Macromolecules 43(19):7895
67. Holyst R, Vilgis TA (1996) Macromol Theor Simulat 5(4):573–643
68. Hamm M, Goldbeck-Wood G, Zvelindovsky AV, Sevink GJA, Fraaije JGEM (2002) J Chem Phys 116(7):3152
69. Wang Q (2011) Soft Matter 7(8):3711
70. Pryamitsyn V, Ganesan V (2004) J Chem Phys 120(12):5824
71. Kumar NA, Ganesan V (2012) J Chem Phys 136(10):101101

72. Vettorel T, Besold G, Kremer K (2010) Soft Matter 6(10):2282
73. Helfand E, Tagami Y (2003) J Chem Phys 56(7):3592
74. Daoulas KC, Müller M (2006) J Chem Phys 125(18):184904
75. Detcheverry FA, Pike DQ, Nealey PF, Müller M, Pablo JJD (2009) Faraday Discuss 144:111
76. Kron AK (1965) Polym Sci USSR 7(7):1361
77. Wall FT, Mandel F (2008) J Chem Phys 63(11):4592
78. Rühle V, Kirkpatrick J, Andrienko D (2010) J Chem Phys 132(13):134103
79. Marcus RA (1993) Rev Mod Phys 65(3):599
80. May V, Kühn O (2011) Charge and energy transfer dynamics in molecular systems, 3rd edn. Wiley-VCH, Weinheim
81. Grabert H, Weiss U (1985) Phys Rev Lett 54(15):1605
82. Fisher MPA, Dorsey AT (1985) Phys Rev Lett 54(15):1609
83. Rühle V, Lukyanov A, May F, Schrader M, Vehoff T, Kirkpatrick J, Baumeier B, Andrienko D (2011) J Chem Theory Comput 7(10):3335
84. Asadi K, Kronemeijer AJ, Cramer T, Jan Anton Koster L, Blom PWM, de Leeuw DM (2013) Nat Commun 4:1710
85. Reimers JR (2001) J Chem Phys 115(20):9103
86. Hsu CP (2009) Accounts Chem Res 42(4):509
87. Valeev EF, Coropceanu V, da Silva Filho DA, Salman S, Brédas JL (2006) J Am Chem Soc 128(30):9882
88. Brédas JL, Calbert JP, Filho DADS, Cornil J (2002) Proc Natl Acad Sci USA 99(9):5804
89. Coropceanu V, Cornil J, da Silva Filho DA, Olivier Y, Silbey R, Brédas JL (2007) Chem Rev 107(4):926
90. Kirkpatrick J (2008) Int J Quantum Chem 108(1):51, Bibtex: Kirkpatrick 2008
91. Baumeier B, Kirkpatrick J, Andrienko D (2010) Phys Chem Chem Phys 12(36):11103
92. Fogel Y, Zhi L, Rouhanipour A, Andrienko D, Räder HJ, Müllen K (2009) Macromolecules 42(18):6878
93. Scher H, Alexander S, Montroll EW (1980) Proc Natl Acad Sci U S A 77(7):3758
94. Stone AJ (1997) The theory of intermolecular forces. Clarendon, Oxford
95. Hättig C (1996) Chem Phys Lett 260(3–4):341
96. Hättig C, Heß BA (1994) Mol Phys 81(4):813
97. Verstraelen T, Pauwels E, De Proft F, Van Speybroeck V, Geer-lings P, Waroquier M (2012) J ChemTheory Comput 8(2):661
98. Breneman CM, Wiberg KB (1990) J Comput Chem 11(3):361–373
99. Stone A, Alderton M (1985) Mol Phys 56(5):1047
100. Stone AJ (2005) J Chem Theory Comput 1(6):1128
101. Kramer C, Bereau T, Spinn A, Liedl KR, Gedeck P, Meuwly M (2013) J Chem Inf Model 53 (12):3410
102. Chirlian LE, Francl MM (1987) J Comput Chem 8(6):894
103. Thole B (1981) Chem Phys 59(3):341
104. van Duijnen PT, Swart M (1998) J Phys Chem A 102(14):2399
105. Applequist J, Carl JR, Fung KK (1972) J Am Chem Soc 94(9):2952
106. Ren P, Ponder JW (2003) J Phys Chem B 107(24):5933
107. Vukmirović N, Wang LW (2011) J Phys Chem B 115(8):1792
108. McMahon DP, Cheung DL, Goris L, Dacuna J, Salleo A, Troisi A (2011) J Phys Chem C 115 (39):19386
109. Baessler H (1993) Phys Status Solidi B 175(1):15
110. Lan YK, Yang CH, Yang HC (2010) Polym Int 59(1):16
111. Kirkpatrick J, Marcon V, Nelson J, Kremer K, Andrienko D (2007) Phys Rev Lett 98 (22):227402
112. Marcon V, Kirkpatrick J, Pisula W, Andrienko D (2008) Phys Status Solidi B 245(5): 820–824

113. Andrienko D, Kirkpatrick J, Marcon V, Nelson J, Kremer K (2008) Phys Status Solidi B 245 (5):830
114. Nelson J, Kwiatkowski JJ, Kirkpatrick J, Frost JM (2009) Accounts Chem Res 42(11):1768
115. May F, Marcon V, Hansen MR, Grozema F, Andrienko D (2011) J Mater Chem 21(26):9538
116. Schrader M, Fitzner R, Hein M, Elschner C, Baumeier B, Leo K, Riede M, Bäuerle P, Andrienko D (2012) J Am Chem Soc 134(13):6052
117. Schrader M, Körner C, Elschner C, Andrienko D (2012) J Mater Chem 22(41):22258
118. Mas-Torrent M, Boer DD, Durkut M, Hadley P, Schenning APHJ (2004) Nanotechnology 15 (4):S265
119. Poelking C, Ivanov V, Kremer K, Risko C, Brédas JL, Andrienko D, Eunkyung C (2013) J Phys Chem C 117(4):1633
120. Olivier Y, Muccioli L, Lemaur V, Geerts YH, Zannoni C, Cornil J (2009) J Phys Chem B 113 (43):14102
121. De Leener C, Hennebicq E, Sancho-Garcia JC, Beljonne D (2009) J Phys Chem B 113 (5):1311
122. DuBay KH, Hall ML, Hughes TF, Wu C, Reichman DR, Friesner RA (2012) J Chem Theory Comput 8(11):4556
123. Kumar P, Mehta A, Mahurin SM, Dai S, Dadmun MD, Sumpter BG, Barnes MD (2004) Macromolecules 37(16):6132
124. Collini E, Scholes GD (2009) Science 323(5912):369, PMID: 19150843
125. Salleo A, Kline RJ, DeLongchamp DM, Chabinyc ML (2010) Adv Mater 22(34):3812–3838
126. Beljonne D, Cornil J, Sirringhaus H, Brown PJ, Shkunov M, Friend RH, Brédas JL (2001) Adv Funct Mater 11(3):229–234
127. Brown PJ, Sirringhaus H, Harrison M, Shkunov M, Friend RH (2001) Phys Rev B 63 (12):125204
128. Magin EH, Borsenberger PM (1993) J Appl Phys 73(2):787
129. Van der Auweraer M, De Schryver FC, Borsenberger PM, Bässler H (1994) Adv Mater 6 (3):199–213
130. Zade SS, Zamoshchik N, Bendikov M (2011) Accounts Chem Res 44(1):14
131. Nayyar IH, Batista ER, Tretiak S, Saxena A, Smith DL, Martin RL (2013) J Chem Theory Comput 9(2):1144
132. Bronstein H, Chen Z, Ashraf RS, Zhang W, Du J, Durrant JR, Shakya Tuladhar P, Song K, Watkins SE, Geerts Y, Wienk MM, Janssen RAJ, Anthopoulos T, Sirringhaus H, Heeney M, McCul-loch I (2011) J Am Chem Soc 133(10):3272
133. Qin T, Troisi A (2013) J Am Chem Soc 135(30):11247
134. Shaked S, Tal S, Roichman Y, Razin A, Xiao S, Eichen Y, Tessler N (2003) Adv Mater 15 (11):913–916
135. Soler JM, Artacho E, Gale JD, García A, Junquera J, Ordejón P, Sánchez-Portal D (2002) J Phys Condens Mat 14(11):2745
136. Skylaris CK, Haynes PD, Mostofi AA, Payne MC (2005) J Chem Phys 122(8):084119
137. Gordon MS, Mullin JM, Pruitt SR, Roskop LB, Slipchenko LV, Boatz JA (2009) J Phys Chem B 113(29):9646
138. McMahon DP, Troisi A (2009) Chem Phys Lett 480(4–6):210
139. Vukmirović N, Wang LW (2009) J Phys Chem B 113(2):409
140. Vukmirović N, Wang LW (2009) Nano Lett 9(12):3996
141. Fedorov DG, Kitaura K (2007) J Phys Chem A 111(30):6904
142. Kitaura K, Ikeo E, Asada T, Nakano T, Uebayasi M (1999) Chem PhysLett 313(3–4):701
143. Kubař T, Elstner M (2013) J R Soc Interface 10(87):20130415, PMID: 23883952
144. Liu J, Sun Y, Gao X, Xing R, Zheng L, Wu S, Geng Y, Han Y (2011) Langmuir 27(7):4212
145. Porezag D, Frauenheim T, Köhler T, Seifert G, Kaschner R (1995) Phys Rev B 51(19):12947
146. Elstner M, Porezag D, Jungnickel G, Elsner J, Haugk M, Frauen-heim T, Suhai S, Seifert G (1998) Phys Rev B 58(11):7260
147. Liu T, Troisi A (2014) Adv Funct Mater 24(7):925-933

148. Kubař T, Elstner M (2010) J Phys Chem B 114(34):11221
149. Kubař T, Kleinekathöfer U, Elstner M (2009) J Phys Chem B 113(39):13107
150. Johansson Å, Stafström S (2001) Phys Rev Lett 86(16):3602
151. Barford W, Trembath D (2009) Phys Rev B 80(16):165418
152. Noriega R, Rivnay J, Vandewal K, Koch FPV, Stingelin N, Smith P, Toney MF, Salleo A (2013) Nat Mater 12(11):1038
153. Cheung DL, McMahon DP, Troisi A (2009) J Am Chem Soc 131(31):11179
154. Vukmirović N, Wang LW (2010) Appl Phys Lett 97(4):043305
155. Miller A, Abrahams E (1960) Phys Rev 120(3):745
156. Vukmirović N (2013) Phys Chem Chem Phys 15(10):3543
157. Bronold FX, Alvermann A, Fehske H (2004) Phil Mag 84(7):673
158. Fornari RP, Troisi A (2014) Phys Chem Chem Phys 16(21):9997

Adv Polym Sci (2014) 265: 181–232
DOI: 10.1007/12_2014_289

Published online: 13 September 2014

P3HT-Based Solar Cells: Structural Properties and Photovoltaic Performance

Adam J. Moulé, Dieter Neher, and Sarah T. Turner

Abstract Each year we are bombarded with B.Sc. and Ph.D. applications from students that want to improve the world. They have learned that their future depends on changing the type of fuel we use and that solar energy is our future. The hope and energy of these young people will transform future energy technologies, but it will not happen quickly. Organic photovoltaic devices are easy to sketch, but the materials, processing steps, and ways of measuring the properties of the materials are very complicated. It is not trivial to make a systematic measurement that will change the way other research groups think or practice. In approaching this chapter, we thought about what a new researcher would need to know about organic photovoltaic devices and materials in order to have a good start in the subject. Then, we simplified that to focus on what a new researcher would need to know about poly-3-hexylthiophene:phenyl-C61-butyric acid methyl ester blends (P3HT:PCBM) to make research progress with these materials. This chapter is by no means authoritative or a compendium of all things on P3HT:PCBM. We have selected to explain how the sample fabrication techniques lead to control of morphology and structural features and how these morphological features have specific optical and electronic consequences for organic photovoltaic device applications.

Keywords Free carrier generation · Non-geminate recombination · Organic solar cells

A.J. Moulé (✉)
Department of Chemical Engineering and Material Science, University of California – Davis, Davis, CA 95616, USA
e-mail: amoule@ucdavis.edu

D. Neher (✉) and S.T. Turner
Institute of Physics and Astronomy, University of Potsdam, Karl-Liebknecht-Str. 24-25, 14476 Potsdam-Golm, Germany
e-mail: neher@uni-potsdam.de

Contents

1 Introduction

Increasing signs of global warming such as recent atmospheric CO_2 levels measured above 400 ppm, polar ice sheet loss, and super-storms, have recently focused attention on short- and long-term solutions to combat climate change [1–4]. Similar to the gold rush in the 1800s and the oil boom in the 1900s, intellectual property on new technologies is now the boom industry for innovative people to become rich and influential fast. In the twenty-first century, scientists and engineers are the pioneers and our ideas are the prize. One of the most alluring energy technologies of the past decade has been organic photovoltaics (OPV). This technology is alluring because it could potentially reduce the cost of producing photovoltaic (PV) modules and thereby make solar energy cost-competitive with fossil fuels. As can be seen in Fig. 1, the allure of OPV brought thousands of scientists and engineers into this new field, generating an exponential increase in scientific knowledge (as measured by the number of scientific articles) in this area. The sharp focus on OPV technology has led to an explosion of interest in enabling technologies such as polymer synthesis, polymer physics, microstructural measurement techniques, multiscale modeling, photophysics, organic electronics, organic–inorganic hybrid materials, etc. All of this intense focus into one research area has also created intense competition between research groups. With so many new scientific articles published yearly, it is impossible to read them all, and repeat or redundant articles have become unfortunately and unavoidably common. Even review articles and books about OPV have proliferated, making production of an original perspective difficult and a complete literature review impractical. We apologize in advance if any important work is not cited here.

Under this backdrop, we have decided to produce an article that is designed to be helpful to students and postdocs who are entering this field. Rather than focusing on the efficiency of devices or the morphology of materials (subjects that are covered very well elsewhere), we instead focus some attention on how to approach OPV research from a more practical (laboratory-based) perspective. Section 1 introduces

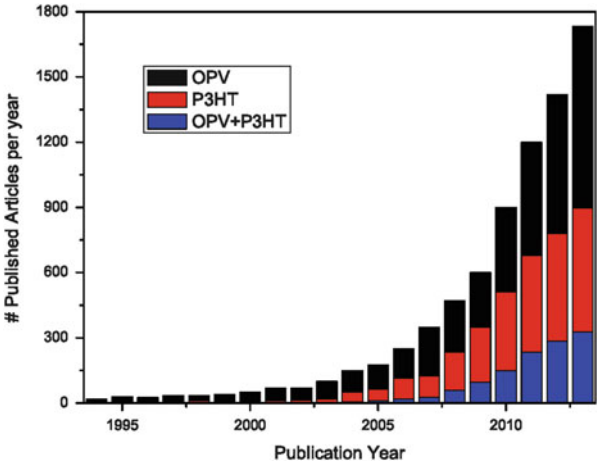

Fig. 1 Number of articles that are found on Web of Science when searching under the topics "Organic photovoltaic", "P3HT", and "OPV + P3HT"

OPV devices, modules, and scale-up. Section 2 discusses fabrication of poly-3-hexylthiophene (P3HT)-based OPV layers, with a focus on practical aspects like how to choose a solvent and how this choice affects other aspects of fabrication. Essentially, this chapter addresses the experimental process of controlling morphology in a P3HT:PCBM blend film, without dwelling on a discussion of the actual morphology of any particular film. Section 3 describes how optical absorption spectra provide detailed information on the crystallization of P3HT in blends with PCBM. Finally, Sect. 4 contains a detailed discussion on the elementary processes involved in photocurrent generation, and how photocurrent losses are related to blend morphology.

1.1 Device Characteristics

A photodiode or PV device converts light energy into electrical energy. The energy of a photon can be expressed by the simple formula:

$$E = hv = \frac{hc}{\lambda}, \tag{1}$$

where E is energy, h is Planck's constant, v is frequency, c is the speed of light, and λ is wavelength. The sun emits photons over a wide energy range in a spectrum that is close to a black body spectrum of ~6,000 K when measured in space. Some of the light is absorbed by the atmosphere by molecules such as O_3, O_2, H_2O, CH_4, and CO_2 or scattered by dust, clouds or pollution. The light spectrum that reaches the earth's surface is for these reasons somewhat different at every place and, due to weather and the rotation of the planet, changes constantly. For the sake of settling arguments, scientists have agreed to test PV devices using an approximate spectrum

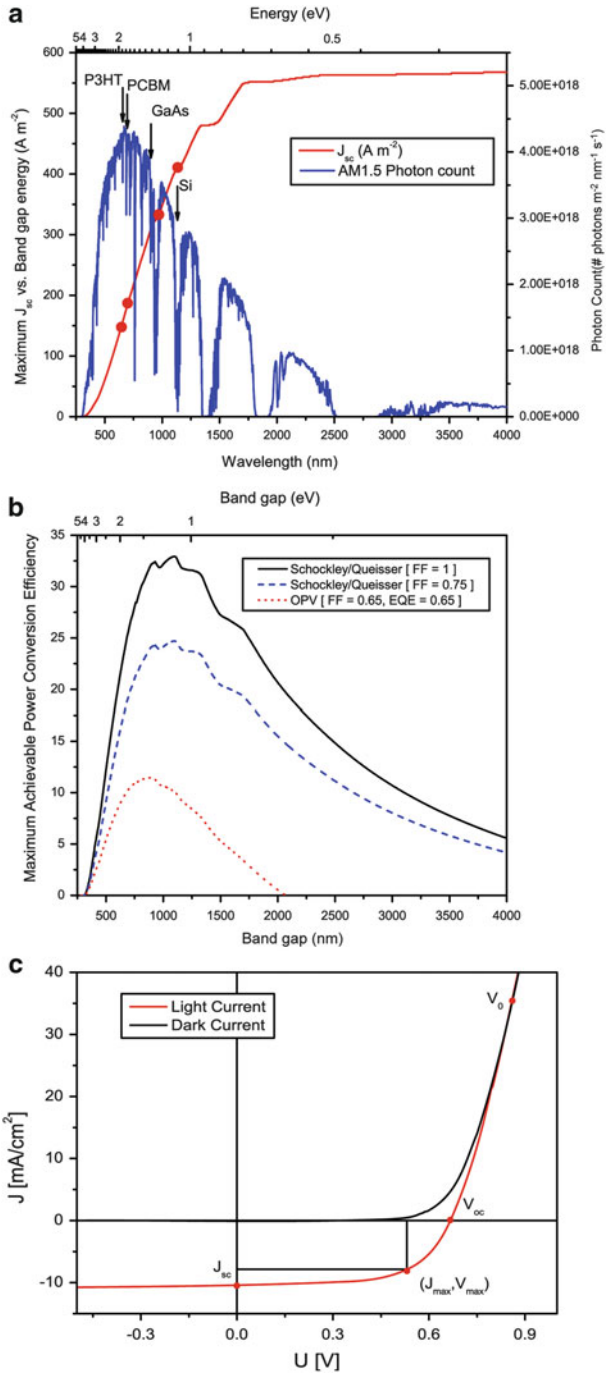

Fig. 2 (**a**) AM1.5G spectrum and calculated maximum J_{sc} as a function of band gap energy. (**b**) Calculated maximum PCE versus band gap energy of a PV device assuming detailed balance

called AM1.5G (Fig. 2a). This spectrum is equivalent to the sun's spectrum at a tilt of 48.2°, which increases the path length through the atmosphere by 150% with respect to 0° incidence. On a sunny day, the total sun power is approximately 930 W/m^2 and includes scattered light from clouds and pollution. This spectrum is approximated using a Xe arc lamp and an optical filter. The Xe lamp solar-simulated spectrum is relatively accurate throughout the visible range but does not have full spectral coverage in the near infrared. Usually solar simulator lamps are calibrated to 1,000 W/m^2 and direct incidence (0°) is used to simplify the experiment. A detailed (and worth reading) description of how to properly measure the mismatch factor for a simulated solar spectrum can be found in a publication by Shrotriya et al. [5]. The standard PCE measurement and testing protocol has also been published [6].

A PV device is made from a semiconductor with an optical band gap (E_g). This E_g is the minimum energy at which electromagnetic energy absorbed within the semiconductor promotes an electron from the valence band to the conduction band. In the case of an OPV device, the excited states are localized onto one or more molecular species, so extended energy bands do not exist. Instead, E_g is the minimum energy needed to promote an electron from the highest occupied molecular orbital (HOMO) to the lowest unoccupied molecular orbital (LUMO) of the molecules or polymers in the film. The band gap sets the maximum short-circuit photocurrent (J_{sc}) and power conversion efficiency (PCE) that any PV device can attain. Photons with energy below E_g do not contribute to photocurrent production. The maximum J_{sc} is shown in Fig. 2a. Due to the principle of detailed balance, the E_g also sets the maximum possible potential at which a photocurrent can be extracted [7]. The combination of these two limitations means that, at best, only ~33% of the total solar power $P(E)$ in the solar spectrum could be collected and converted to electricity by a single junction PV device. Practical considerations like the necessity of a p/n junction, finite area, recombination, reflection, imperfect materials, and series resistance mean that record laboratory scale efficiencies are ~25 and ~28% for single crystalline Si and GaAs, respectively. Figure 2b shows the relationship between band gap and maximum attainable PV efficiency at one sun power given several different assumptions.

The PCE is commonly obtained by measuring the current density (J) versus the applied potential (V) for a PV device under AM1.5G illumination. Figure 2c shows a typical J/V curve for an OPV device based on the donor P3HT and the acceptor phenyl-C61-butyric acid methyl ester (PCBM). The current density measured at zero applied potential is the short-circuit current density (J_{sc}). The applied voltage necessary to drive the current to zero is the open-circuit voltage (V_{oc}). The PCE is determined by calculating the maximum power produced, which is the maximum product of $J \times V$ and is denoted by J_{max} and V_{max}:

Fig. 2 (continued) (*black*), detailed balance and a FF of 0.75 (*blue*), and OPV conditions of 0.6 V energy loss, 0.65 EQE and 0.65 FF. (**c**) J/V curve for a P3HT:PCBM OPV device

$$\mathrm{PCE} = \frac{J_{\max} \cdot V_{\max}}{P_{\mathrm{in}}} = \frac{J_{\mathrm{sc}} \cdot V_{\mathrm{oc}} \cdot \mathrm{FF}}{P_{\mathrm{in}}} \tag{2}$$

and the fill factor (FF) is:

$$\mathrm{FF} = \frac{J_{\max} \cdot V_{\max}}{J_{\mathrm{sc}} \cdot V_{\mathrm{oc}}} \tag{3}$$

The device PCE can therefore be increased by increasing the J_{sc} through capture of more photons or reduced recombination, by increasing V_{oc} to approach E_{g}, and by increasing FF. The *J*/*V* curve for OPV devices has been interpreted in a number of ways and with numerous and sometimes contradictory models. We will discuss fundamental aspects of these models in Sects. 3 and 4.

A second measure of efficiency is the external quantum efficiency (EQE), which is the probability that a photon, incident on a PV device, with a wavelength λ will produce a quantum of photocurrent. The EQE can be broken into two components. The optical component is the probability with which a photon is absorbed into the active layer of the PV device η_{abs} and the electrical component is the probability with which the absorbed energy produces photocurrent η_{elec} at the measured bias. Component η_{elec} has been broken into various substeps, each with a particular meaning in several well-cited publications [8]. For this section, we will simply state that η_{elec} is also written as the internal quantum efficiency (IQE):

$$\mathrm{EQE}(\lambda) = \eta_{\mathrm{abs}}(\lambda) \cdot \eta_{\mathrm{elec}}(\lambda) = \eta_{\mathrm{abs}}(\lambda) \cdot \mathrm{IQE}(\lambda) \tag{4}$$

OPV materials that can operate with a band gap of 1.1–1.3 eV have, so far, not been made. Several successful donor polymers have been synthesized that absorb light to energies as low as 1.3 eV. But the most commonly used acceptor, PCBM, has a band gap of 1.75 eV, which is ultimately the limiting factor for efficiency [9]. Several different electrical device models have been used to calculate the maximum possible PCE of an OPV device [9–11]. All three models give a maximum PCE for a single junction device of 10–11%. The model by Veldman et al. predicts the maximum possible V_{oc} to be [9]:

$$V_{\mathrm{oc}}(\mathrm{maximum}) \; = \; E_{\mathrm{g}}(\mathrm{PCBM}) \; - \; 0.6\ \mathrm{V}. \tag{5}$$

To our knowledge, a higher V_{oc} has never been recorded. The device models predicting 10–11% PCE all assume that the FF would be 0.6–0.65 and that the EQE is 60–65% for photons above E_{g}. These are quite reasonable assumptions with "hero" devices regularly showing EQE of ~70% and FF of 70%. Considering that the current world record efficiency for an OPV device is 9.1% for a single bulk-heterojunction (BHJ) layer [12], it is reasonable to expect further device records with new materials that approach and exceed 11% PCE.

1.2 Scale-Up and Other Challenges

One exciting aspect of OPV research is the knowledge that there is a direct link between increasing basic science knowledge and progress towards a marketable product. But what does this product look like? What makes it marketable? The goal is to fabricate a PV module with 10–15% PCE that is printed from solution onto a flexible support in a continuous manner, similarly to printing newspapers. This OPV device needs to be inexpensive, lightweight, flexible, and must last for more than 5 years.

The most thorough publication to address the scale-up of OPV is a book by Frederick Krebs [13]. In this book and in follow-up articles, Krebs explores the use of several reel-to-reel printing methods with OPV materials [14–19]. Several other groups are working on continuous coating methods for OPV [20–29]. One of the more pressing problems for the OPV field is that most laboratory work is carried out using spin-coaters and rigid substrates, whereas any expected application of the research will use reel-to-reel coating and flexible substrates [30]. For this reason, future research work should focus on blends prepared by blade coating, which can more easily be compared to a reel-to-reel coated device. Also, blade coaters are more efficient in the use of material, so new polymers can be investigated more efficiently. Another issue is that flexible substrates such as PET–ITO (polyethylene terephthalate coated with indium tin oxide) tend to crack and degrade when bent, which defeats the advantage of flexibility. Flexible substrates are also not as well sealed to prevent O_2 and H_2O penetration of the device. All of these issues show that more studies on OPV device longevity for more device geometries, and the causes of degradation for each geometry, are needed.

1.3 A (Very) Brief History of P3HT:PCBM Solar Cells

Unlike traditional inorganic semiconductors, conjugated organic materials have tightly bound excited states. As a result, light excitation does not result in separated charges, but instead tightly bound exciton states are formed with photoexcitation above the band gap. These excitons recombine quickly (picoseconds to milliseconds), making single-component conjugated organics very inefficient PV materials. In 1986, Tang demonstrated that excitons could be effectively split into separated holes and electrons at a bilayer interface between electron-rich (donor) and electron-poor (acceptor) materials [31]. It was later shown that fullerenes make ideal electron acceptors, but the device efficiencies that could be reached were limited by the short exciton diffusion length [32]. The real breakthrough for OPV applications was the discovery that fullerenes and conjugated polymers could be mixed together to form a mixed bulk-heterojunction (BHJ) layer in which donors and acceptors are in intimate contact and separated charges must navigate through a disordered (mixed) material to

reach the electrodes [33, 34]. All OPV efficiency records since have come from BHJ style devices.

In 2003, Padinger and Sariciftci published a paper reporting a record OPV PCE of 3.5% [35]. This was a huge improvement over the previous record of 2.5% [36], but that was not what made the paper exciting. The exciting pieces of information were:

1. More than one polymer (P3HT instead of MDMO-PPV) made effective OPV devices
2. Choice of solvent and post-processing annealing conditions could greatly affect the device efficiency
3. This improvement was most probably related to the microstructure

The first piece of information spurred a creative explosion in conjugated polymer synthesis that has produced numerous polymers yielding higher OPV efficiencies than P3HT [37–39]. The realization that morphology and device efficiency are intimately related resulted in rapid advances in the use of new instrumentation to study organic nanostructure [40, 41]. At the same time, further OPV device efficiency increases were realized by the use of optimized morphology-controlling strategies including the use of thermal annealing [42], solvent annealing [43], and the application of various co-solvent additives [44, 45]. The most cited paper in all of OPV research (>2,900 total) was published by Li et al. [43]. It demonstrated the change in morphology associated with thermal and solvent annealing and was the first published and certified efficiency record of over 4% for an OPV device. Figure 3 shows *J*/*V* curves of P3HT:PCBM OPV devices from this seminal paper. In the same month, two other groups also published >4% efficiency with P3HT:PCBM but with different composition ratio, layer thickness, and annealing treatment [42, 46]. Although the OPV field has expanded widely beyond the P3HT:PCBM system, P3HT:PCBM remains the "fruit fly" of OPV because the materials are widely available with sufficient purity, and because all manner of new processing techniques can be tested with the knowledge that small changes to the microstructure yield large changes in OPV device PCE.

To demonstrate the pervasive study of P3HT as a model polymer for OPV, we tracked the number of articles published about P3HT and OPV. In Fig. 1 we show the number of scientific papers (as counted by Web of Knowledge) published per year under the search terms "organic photovoltaic", "P3HT", and "organic photovoltaic + P3HT". This search shows that in 2013, more than 300 out of almost 1,700 OPV papers were searchable with P3HT as the OPV polymer, although P3HT has not been a record polymer since 2006. Many of the other more than 500 P3HT articles involve microstructural or photophysical studies that inform the OPV field.

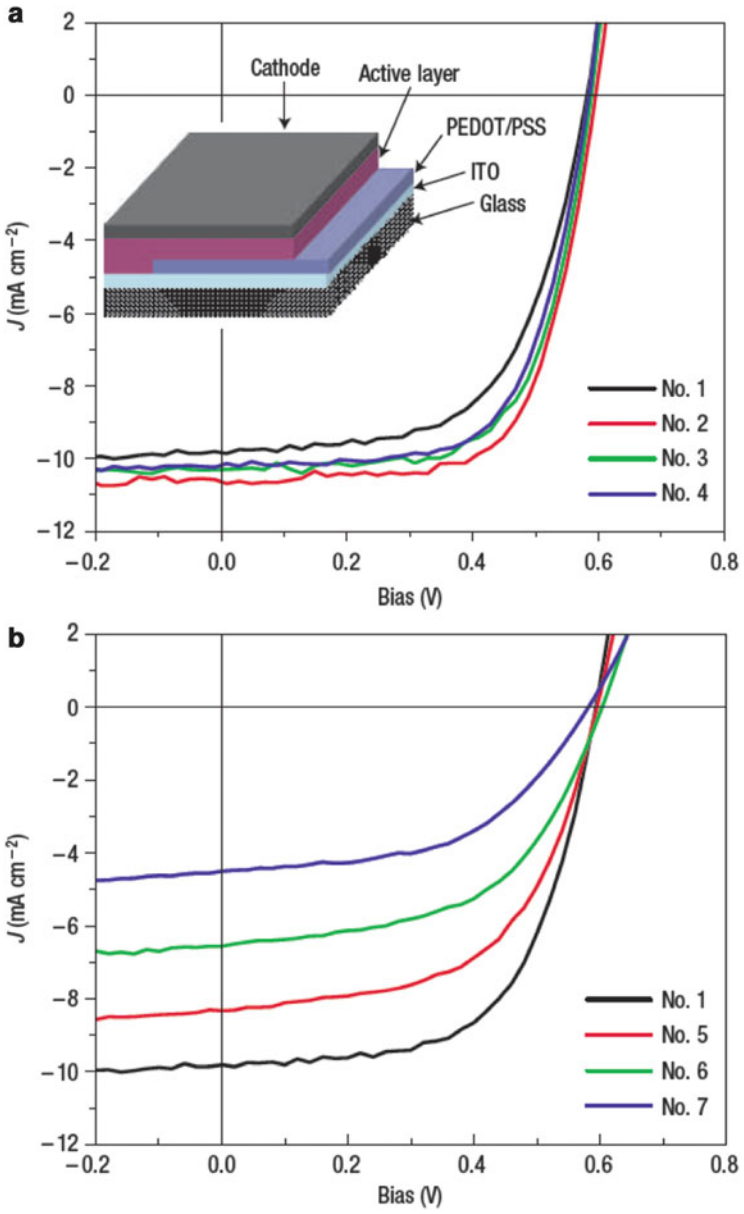

Fig. 3 (**a**) Different *J*/*V* curves of P3HT:PCBM cells corresponding to devices with active layers before (*no. 1*) and after thermal annealing at 110°C for 10 min (*no. 2*), 20 min (*no. 3*), and 30 min (*no. 4*). The active layer thickness was ∼210 nm and the film growth time was ∼20 min. (**b**) *J*/*V* characteristics under illumination for devices with different film growth rates by varying the solvent evaporation time, t_{evp}. The t_{evp} for different films were 20 min (*no. 1*), 3 min (*no. 5*), 40 s (*no. 6*), and 20 s (*no. 7*). Reprinted with permission from [43]. Copyright© 2005, Rights Managed by Nature Publishing Group

2 Relating Processing Conditions to Bulk-Heterojunction Morphology

One of the stranger lessons to be gleaned from the study of P3HT:PCBM is that the keys to understanding and controlling P3HT:PCBM BHJ morphology were published in 1993 [47] and 1994 [48], before the BHJ concept had been introduced [32–34]. The 1993 paper showed a transmission electron microscopy (TEM) image and crystal structure for a self-assembled P3HT nanoribbon. The 1994 paper reported on the solvatochromic and thermochromic properties of P3HT and related the folding of P3HT, due to reduced temperature or poor solvent, to the strong red shift in the absorption spectrum.

It is very instructive that in 1993 the strong tendency for P3HT to form ribbon-like nanostructures was known. Also, the solvents necessary to crystallize P3HT, the techniques to measure the fibers, and the technique to separate and coat the fibers were all known. In 1994 the research community knew that poor solvents caused P3HT to form supramolecular structures with coplanar P3HT chains and that this resulted in a red shift of the absorption spectrum and formation of vibronic structure. It was known that the same structures result from cooling a P3HT melt. But nevertheless, the research community did not start using these ideas to control P3HT:PCBM morphology until a decade later.

Why not?

The P3HT:PCBM processing conditions did not create a linear and obvious change in morphology and so the relationship between processing conditions and morphology to OPV performance was not obvious. The rest of this section points out the various relationships between processing conditions and the final film morphology. Many new OPV polymers exist that have higher efficiency than P3HT:PCBM. In terms of processability, these newer polymers may be more or less soluble, have lower or higher tendency to crystallize, or have differing mutual solubility with the fullerene of choice. The discussion focuses on the processing lessons that can be broadly applied to a variety of OPV materials.

2.1 The Fabrication Toolkit

This section was written from the perspective of a device physicist and is designed to help graduate students with new OPV materials. From this perspective, polymers and fullerenes arrive at the laboratory in small quantities and one wishes to learn whether this new material might be a good candidate for OPV devices. Usually, the synthesis group supplies basic information about a polymer, such as the band gap of the dissolved polymer determined using a UV/vis spectrometer, the molecular weight (M_W), and the oxidation/reduction levels of the polymer measured using cyclic voltammetry (CV).

At this point the researcher needs to learn how to produce uniform films of the new polymer mixed with the chosen fullerene without using too much of the valuable polymer. With the mixture of P3HT:PCBM, the PCE can increase tenfold with no change in layer thickness, concentration ratio, or deposition solvent [42]. This means that even if wise coating choices are made about the polymer solution and a highly uniform film is coated, the resulting PCE may still be much lower than that for an optimized morphology. The PCE increase for P3HT:PCBM comes from briefly annealing the film at 150°C, which causes a change in the nanoscale morphology and the altered morphology leads to an increase in PCE. The fabrication toolkit can therefore be further subdivided into fabrication steps that occur before, during, and after coating. The following sections attempt to describe the many interrelated but independently controlled fabrication parameters that affect morphology formation. We focus on how fabrication choices affect device morphology and thus efficiency.

2.1.1 Molecular Weight

Unlike small molecules, polymers do not have a well-defined M_W and a polymer sample contains a distribution of molecular weights so it is difficult to compare the molar ratio with a small molecule such as C_{60} or PCBM. Instead, one typically reports a weight ratio or wt%, so the molar ratio of polymer repeat units with respect to PCBM is fixed. However, the polymer M_W has a large effect on the solubility of the polymer and the miscibility of the polymer with the fullerene. Smaller M_W polymers or oligomers are in general more soluble and so can be processed with a wider variety of solvents. However, the smaller M_W means that the polymer chains are less entangled and that all species in both solution and melt phases can diffuse more quickly. As a result, low M_W polymers and oligomers tend to make less viscous solutions, phase separate on a larger length scale, and low M_W films are more likely to de-wet or form voids.

The relationship between polymer M_W and PCE has been exhaustively studied in P3HT and mixtures with PCBM [49–61]. We will attempt to briefly summarize the lessons here. First, a lower M_W polymer is more soluble and more miscible with PCBM. Also, in pure P3HT samples, it has been shown that aggregated domain content (for a given solvent and temperature) increases with M_W up to ~20 kDa as a result of increased regioregularity and reduced sample entropy [54, 62]. Even higher M_W (~70 kDa) P3HT has been shown to form highly crystalline nanofibers that can be solution processed [63, 64]. In mixed samples, the PCBM interferes with the formation of pure P3HT domains, so the P3HT is less crystalline. The P3HT crystallinity can be reintroduced by annealing the sample to allow phase separation. For a high regioregularity and M_W, the solubility of PCBM in P3HT is ~30% [65].

Another important result was the realization that charge mobility did not necessarily scale with crystallinity [58]. Kline et al. and others showed that for pure P3HT, lower M_W polymer formed samples with higher apparent crystalline content but that the crystals had few connecting polymer strands leading to poor

macroscopic charge mobility due to a high activation barrier to charge hopping. In contrast, in high M_W P3HT the crystalline domains were well connected to adjoining crystalline domains by individual polymer chains, and so the activation barrier for charge hopping is much lower [54, 58]. A more detailed discussion of the morphology of P3HT thin films can be found in the chapter "Morphology of P3HT in Thin Films" by Kim Tremel and Sabine Ludwigs in this book [66]. Various studies have shown that a M_W of less than 20,000 kD is too low for high efficiency OPV devices [52, 54, 57]. High M_W P3HT is also undesirable because it requires higher boiling point solvents and longer equilibration times for morphology formation [52]. The "Goldilocks" region for M_W for P3HT used for OPV is 20,000–75,000 kD with a maximum possible regioregularity [67, 68].

2.1.2 Solvent Choice

The choice of casting solvents became a clear issue in 2001 when Shaheen et al. published an article showing a PCE increase from 1.1 to 2.5 % for MDMO-PPV:PCBM OPV devices cast from toluene and chlorobenzene, respectively [36]. Subsequent studies showed that toluene was a better solvent for the MDMO-PPV than PCBM, so the PCBM crystallized out of solution with large domain sizes (>1 μm) that reduced the device quality [69]. However, chlorobenzene and dichlorobenzene are equally good solvents for both polymer and fullerene so the polymer and fullerene remain miscible to higher concentrations and the resulting domain sizes are much smaller (tens of nanometers) [69].

A zero-order statement about solvent choice is that the solvent must be equally good for each component to avoid large-scale phase separation. The next thing to consider is the absolute solubility of the polymer and fullerene. Polythiophene and C_{60} have negligible solubility in any solvent, whereas P3HT and PCBM have side chains that greatly increase their solubility. Nevertheless, concentrations of at least 10 mg/mL are necessary to obtain highly planar films of >80 nm thickness without defects using spin-coating. In general, a higher solubility is desired so that more concentrated solutions can be made and a wider variety of coating techniques can be employed. P3HT and PCBM have shown the highest solubility in polar aromatic solvents such as chlorobenzene, 1,2 dichlorobenzene, and 1-chloronaphthalene.

Another important consideration is the boiling point (BP) of the solvents. The BP determines how quickly the solvent evaporates and thereby the formation rate for polymer and fullerene domains. Polymer domains that equilibrate slowly in high BP solvents tend to be more crystalline (thermodynamic product) whereas low BP solvents evaporate quickly and yield mixed amorphous films (kinetic product). When spin-coating at 1,000 rpm, a 20 mg/mL solution of 1:1 P3HT:PCBM condenses to a film in 1–3 s when processed with $CHCl_3$ (BP = 61°C), 5–10 s when processed in chlorobenzene (BP = 132°C), and the film remains wet after 60 s when processed with 1,2 dichlorobenzene (BP = 182°C) (Moulé, personal observation) [70]. The change in structural order in P3HT is observed in a red shift of the absorption spectrum and formation of a clearly defined vibronic structure [71].

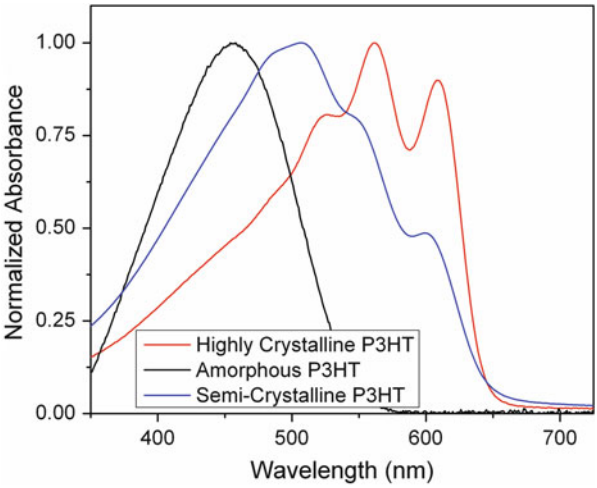

Fig. 4 Solution absorption spectra for P3HT dissolved in $CHCl_3$ (*black*) and anisole (*blue*), and for P3HT nanofibers slowly cooled, filtered, and re-dispersed into toluene (*red*) [63]

The idea to increase crystallinity of the P3HT with slower solvent evaporation was used by Li et al. to achieve the first record PCE over 4% for OPV [43].

With the introduction of semicrystalline polymers like P3HT, it became clear that the solvent could affect the formation of P3HT aggregated or crystalline structures in solution as well as in films. Figure 4 shows three liquid state UV/vis absorption spectra of P3HT dissolved in $CHCl_3$, anisole, and toluene, which result in the formation of ground state structures that are amorphous, somewhat crystalline H-aggregates, and highly crystalline J-aggregates, respectively [72]. The red shift of P3HT with increased order and (to the eye) very obvious color shift makes it an easy polymer to work with. Without any device measurement, one can look at the film and learn a lot about the nanoscopic order by observing the color.

2.1.3 Weight Ratio

The weight ratio between the donor polymer and acceptor fullerene in the final film has a large effect on the PCE of an OPV device. The ideal or correct weight ratio is usually defined as the ratio that achieves the highest PCE. However, there is a strong correlation between weight ratio, layer thickness, and domain size that makes clear that weight ratio, while easy to control, is not easily understood.

One highly useful generalization for OPV device function is that layers with matched hole and electron mobilities have higher FF and that devices with mismatched charge mobilities develop space-charge-limited current (SCLC) layers, particularly with increased light intensity [73]. We can clearly state that one reason to adjust the donor/acceptor weight ratio is to increase or decrease the relative mobilities of the hole and electron carrying materials [74]. One particular example of this relationship showed that for both P3HT:PCBM and OC_1C_{10}-PPV:PCBM, thicker layers perform better with increased PCBM content whereas thinner devices

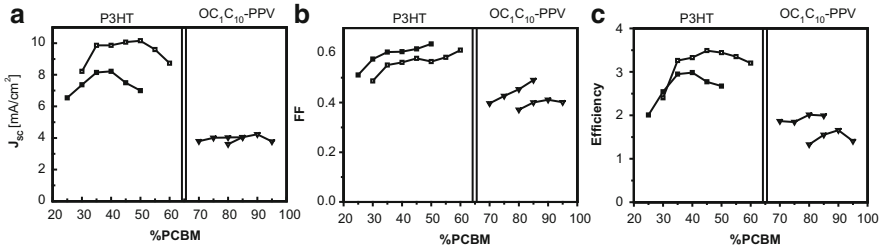

Fig. 5 (**a**) J_{sc}, (**b**) FF, and (**c**) PCE as a function of weight percentage of PCBM for P3HT:PCBM devices with thickness $L = 215$ nm (*open squares*) and $L = 105$ nm (*closed squares*), and for OC_1C_{10}-PPV:PCBM devices with $L = 190$ nm (*open triangles)* and $L = 80$ nm (*closed triangles*)

perform better with reduced PCBM (Fig. 5). The explanation is that the polymer absorbs more light than the fullerene in the visible range, so the absorption density and thereby J_{sc} is higher with increased polymer content. However, as the layer thickness increases, the FF is reduced because of the increased path length, which yields increased recombination and greater series resistance. An increased PCBM content in the layer balances the charge mobilities for thicker devices, yielding an increase in FF. For P3HT:PCBM, the total charge mobility is higher and well matched, so 200–400 nm OPV devices still function well [70]. In contrast, the hole mobility (μ_h) is 100 times lower in OC_1C_{10}-PPV than in P3HT, so balanced charge mobility is not possible for any device, and devices thicker than 100 nm suffer from greatly reduced FF [70].

Early in the OPV literature, it was common to publish a concentration and thickness dependence of the *J*/*V* characteristics for new polymer/fullerene mixtures [70, 75–81]. This information is very interesting, but ultimately was not as useful as desired because each group had slight differences in fabrication procedure and polymer batch that led to large differences in morphology and ultimately in PCE [82]. The difficulty in comparing samples between different research groups has led to a tendency for many groups to publish the "hero" efficiency result without properly reporting all of the fabrication steps necessary to repeat the result. This tendency to focus on PCE without reporting the details of fabrication has led to a great redundancy in OPV literature. We recommend that fabrication data still be published (even if only in the supplemental section) to reduce repeated studies. Accurately representing the data can be difficult. Figure 6 shows the optimization of BHJ layer thickness, and wt% PCBM with respect to PCE for a mixture of poly [4,4-bis(2-ethylhexyl)-4*H*-cyclopenta[2,1-b;3,4-b]dithiophene-2,6-diyl-alt-4,7-bis (2-thienyl)-(2,1,3-benzothiadiazole)-5′,5″-diyl] (PCPDTTBTT) with PCBM [83]. The color of the points indicates different solvents. The complexity (difficult readability) of this plot is meant to show that it is difficult to display fabrication information in a sufficiently dense format. Tables are popular but often fail to present the trend in the data. Nevertheless, publishing detailed fabrication information will reduce redundancy and confusion in the literature.

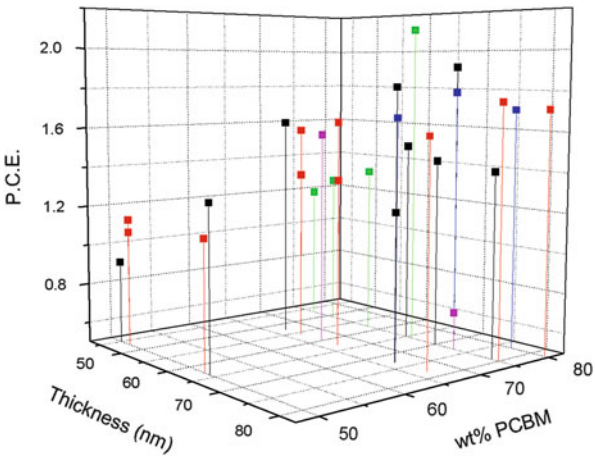

Fig. 6 Optimization of PCE data with respect to BHJ layer thickness, wt% PCBM, and casting solvent for a mixture of PCDTTBTT with PCBM. The *colors* indicate different solvents: chlorobenzene (*black*), *o*-xylene (*red*), chlorobenzene + anisole (*green*), *o*-xylene + anisol (*blue*), and chlorobenzene + nitrobenzene (*magenta*) [83]

2.1.4 BHJ Layer Thickness

As indicated in Figs. 5 and 6, the BHJ layer thickness and PCBM concentration ratio are not independently optimized fabrication parameters. This is because an increase in the BHJ layer thickness increases both the total light absorbance and the transport distance to the electrode. Several articles and reviews describe how light absorbance into BHJ layers increases nonlinearly as a result of interference between incident and reflected radiation [8, 84–86]. This interference pattern means that more light is absorbed into a BHJ layer that is 70–100 nm thick than into a layer that is 120–150 nm thick. Peumans et al. pointed out that constructive interference is maximized in a BHJ layer with thickness near $\lambda/4n$ and minimized at a thickness near $\lambda/2n$, where n is the refractive index of the active layer. Peaks in simulated sunlight absorbance occur at 80, 210, and 330 nm for a thermally annealed mixture of 1:1 P3HT:PCBM and at 110 and 230 nm for a solvent-annealed 1:1 P3HT:PCBM device [84, 85]. There are differences between thermally annealed and solvent-annealed samples in both the internal morphology [87, 88] and thermally induced mixing between the BHJ layer and poly(3,4-ethylenedioxythiophene):poly(styrene sulfonate) (PEDOT:PSS) [85, 89]. When PSS mixes with P3HT, the P3HT is oxidized and bleaches, which reduces the effective thickness of the active layer [85, 89].

Figure 7 shows J_{sc}, FF, and PCE for P3HT:PCBM and OC_1C_{10}-PPV:PCBM devices as a function of layer thickness [70]. Both device types show a peak–dip–peak in J_{sc} with increasing layer thickness. However, the first peak (~70 nm) in the J_{sc} of OC_1C_{10}-PPV:PCBM devices is much higher than the second peak, indicating that the electrical quality of the layer decreases with increasing thickness. As indicated above, the charge carrier mobilities in the hole-carrying and electron-carrying domains must be matched for high J_{sc} or PCE. Because the μ_h of OC_1C_{10}-PPV is much lower than μ_e of PCBM, this device type builds up a space charge layer and thicker devices show reduced performance. In contrast, the thicker

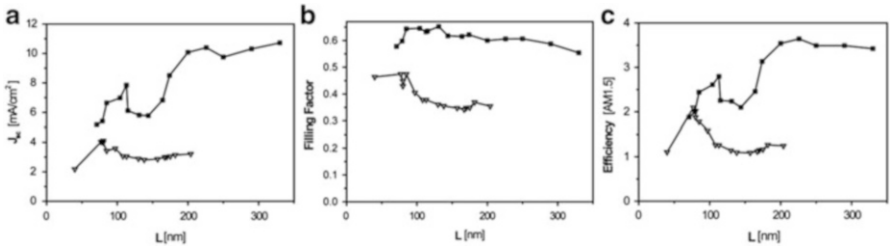

Fig. 7 Thickness dependence of (**a**) J_{sc}, (**b**) FF, and (**c**) PCE for 1:1 P3HT:PCBM (*squares*) and 1:4 OC_1C_{10}-PPV:PCBM (*triangles*) OPV devices illuminated by AM1.5 source at 100 mW/cm^2 intensity [70]

~210 nm P3HT devices have higher J_{sc} and PCE than devices with lower thickness. P3HT is able to make good thicker devices with PCBM because the μ_h of P3HT and μ_e of PCBM are comparable [74, 90].

Comparison of the peaks in J_{sc} between devices based on P3HT and OC_1C_{10}-PPV shows a second systematic difference. The PCE maxima shown in Fig. 7 for OC_1C_{10}-PPV devices are at ~70 and ~190 nm, whereas for P3HT-based devices the maxima occur at 110 and 230 nm. This shift in the position of the maxima comes because P3HT absorbs a red-shifted radiation compared to OC_1C_{10}-PPV (band gap = 1.9 eV rather than 2.2 eV). Because low energy photons have a longer wavelength, the interference pattern selects for maximum absorbance at a greater thickness than for higher energy photons [84].

2.2 The Post-deposition Toolkit

2.2.1 Solvent Annealing

Solvent-coating is a process whereby external forces are used to deliver a thin, uniform wet film. Spin-coating produces wet films by wicking excess solution off the substrate using centrifugal forces. Figure 8 shows a plot of wet layer thickness versus spinning time at 1,500 rpm for a 2:1 mixture of P3HT:PCBM in a chlorobenzene solvent [91]. Formation of the initial wet film and wicking of excess solution occurs in the first step (Fig. 8, step a). The wet film contains all of the polymer that will be in the final film plus solvent. The wet film (Fig. 8, step b) thins rapidly due to evaporation of the solvent and collapses to the final dry thickness after ~6 s (Fig. 8, step c) (note that the time of ~10 s mentioned in Sect. 2.1.2 corresponds to a lower spinning speed). The final stage is evaporation of solvent from the collapsed film (Fig. 8, step d). The order of the polymer as measured using grazing incidence x-ray scattering shows that crystal ordering occurs slowly in the wet film and that domain sizes form quickly during solidification.

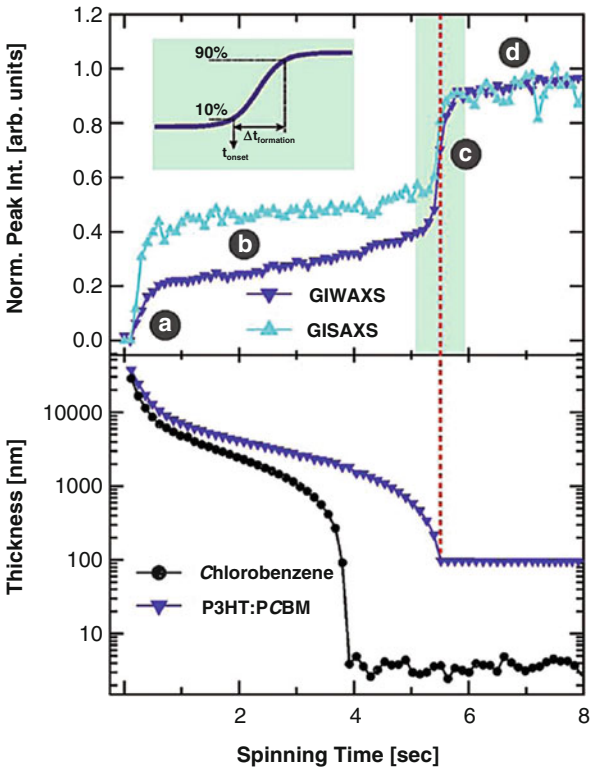

Fig. 8 Quantitative timeline of the spin-coating process of a P3HT:PCBM blended solution. The *upper graph* shows the normalized crystallization and aggregation peak intensities as a function of the spinning time during the spin-coating of P3HT:PCBM (62.5:37.5 wt%). The *light green box* indicates the time range where crystallization and phase separation occur. The onset of film formation t_{onset} and its duration $\Delta t_{formation}$ are defined in the *green inset*. The *lower graph* shows the thickness versus time evolution during the spin-coating process of the pure solvent and the P3HT:PCBM solution, respectively. Reprinted (adapted) with permission from [91]. Copyright © 2013 Wiley-VCH Verlag GmbH & Co. KGaA, Weinheim

As discussed above, high BP solvents evaporate slowly (10 s–10 h), leaving the polymer a long time to relax into unstrained and, depending on the polymer, crystalline domains. In contrast, low BP solvents evaporate quickly (<10 s), leaving the polymer in an amorphous form with strain that can cause dewetting.

In the OPV field, the drying time for a film was not purposefully controlled until solvent annealing experiments were published by the Yang group in 2005 [43]. The process of solvent annealing involves covering the wet film (with a petri dish or other cover), which keeps the atmosphere above the sample rich in solvent and prevents evaporation. In this way, the sample can be allowed to relax over hours instead of seconds [88, 92]. Solvent annealing for OPV blends has been widely reported. The Yang group also showed that the solvent annealing effect could be realized with any solvent if a high solvent partial pressure above the sample could be maintained [92]. A simple method for doing this is to spin-coat a wet film and then to cover the wet film and substrate with an up-turned petri dish. Assuming negligible mass transfer of solvent to outside of the petri dish, the film remains solvent-swollen for an arbitrary time period. Several review articles have detailed the change in morphology with solvent annealing [87, 88, 92]. In general, the longer relaxation times afforded by high boiling point solvents leads to increased crystallinity in P3HT films [88]. The crystallization of P3HT forces PCBM out into a

mixed amorphous P3HT:PCBM phase [93]. With increased PCBM density, the PCBM also starts to form pure amorphous and crystalline domains [94, 95]. Solvent annealing causes greater phase separation between P3HT and PCBM than thermal annealing [96].

2.2.2 Thermal Annealing

A more commonly used method for causing phase separation between P3HT and PCBM is thermal annealing. Thermal annealing of P3HT and mixtures of P3HT with PCBM has been studied in great detail [42, 56, 59, 70, 76, 97–117]. Optimized thermally annealed devices are spin-coated from a chlorobenzene solution in a ratio that contains 35–45% PCBM by weight. After spin-coating, the metal electrode is evaporated and then the device is heated for 5–30 min at ~150°C [42]. PCE as high as 5% for this device type have been reported [42] but 3.5–4.5% PCE is more common.

Moulé and Meerholz published two articles that described measurement of EQE as a function of BHJ layer thickness. Several thousand individual P3HT:PCBM OPV devices were fabricated to establish these data sets [70, 85]. We found that OPV devices with PCE of ~4% could regularly and repeatably be fabricated using the thermal annealing method with BHJ thicknesses of 80–350 nm. The solvent annealing method occasionally brought "hero" devices, but in general was less easy to control because the trace solvent atmosphere in the glove-box had a large effect on the final morphology [118]. During the fabrication of so many devices we found three issues that were likely to reduce device quality (without changing substrates or metal type):

1. Occasionally, there is a PEDOT:PSS batch supplied that produces exclusively S-shaped *J*/*V* curves with low FF [119, 120] This problem could only be solved by ordering new PEDOT:PSS and is attributed to slight changes in the doping level of the PEDOT:PSS itself.
2. The quality of P3HT varies widely between batches, which mostly has an effect on the FF. Average FF > 0.6 is an indication of "good" P3HT. Typically, a graduate student can achieve "good" results with a year of practice and with ~50% of the P3HT batches received. Cleaning the P3HT by dissolving and then dripping into a solution of CH_3OH:H_2O improves the FF by an average of 0.05. The improvement most probably comes from the removal of metals.
3. We have also informally found that evaporation of metal electrodes at a high rate can reduce the FF because the hot metal damages the polymer. We use an initial evaporation rate of 0.02 nm s^{-1}.

Two different two-component nonequilibrium phase diagrams have been made for P3HT:PCBM [121, 122]. Figure 9 shows the expected phase behavior of P3HT:PCBM in a melt or solidifying melt [121]. Thermal analysis is able to show the mixing ratio of P3HT:PCBM as a function of temperature. All investigations agree that PCBM has ~30% miscibility with P3HT and that with higher PCBM content,

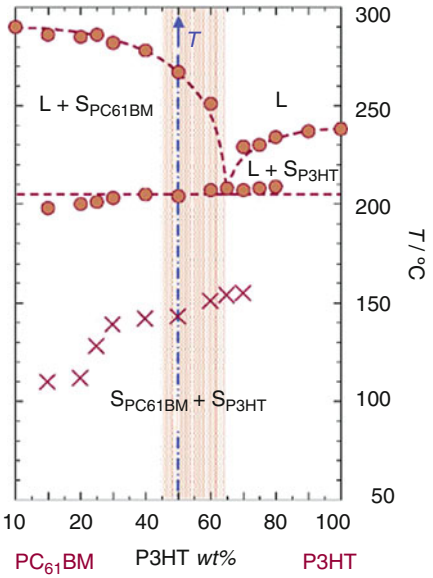

Fig. 9 Two component nonequilibrium phase diagram for P3HT:PCBM measured using differential scanning calorimetry. Reprinted (adapted) with permission from [121]. Copyright © 2008 WILEY-VCH Verlag GmbH & Co. KGaA, Weinheim

phase separation occurs. In addition, it has been widely reported that with heating, PCBM diffuses through the P3HT and forms extended crystals that are detrimental to OPV device function [118, 121, 123–125]. Some recent attempts have been made to generate fullerenes that do not crystallize in order to improve the device longevity [126].

Although thermal analysis can show the mixing ratio of P3HT:PCBM in a volume and the melting temperatures of crystals in the melt, it does not specify the miscibility between the amorphous P3HT and PCBM. Recent bilayer device investigations [127], neutron reflectometry [65, 128, 129], soft X-ray spectroscopy [95, 125], and 3D electron tomography images of P3HT:fullerene [96] have revealed that a mixed domain always exists between P3HT-rich and fullerene-rich domains. This means that P3HT:PCBM forms four separate domain types: P3HT and PCBM can each crystallize to form pure domains, P3HT and PCBM mix in a ~3:7 ratio in a mixed amorphous P3HT:PCBM domain, and amorphous PCBM with ~10% amorphous P3HT is also commonly found [130]. Spin-coating results in the rapid formation of a film and the most common phase is the mixed 3:7 amorphous domain type. With either solvent annealing or a short period of thermal annealing, the mixed domain phase separates into pure P3HT domains and amorphous PCBM domains with low P3HT content. With thermal annealing for longer times, PCBM seed crystals form and Oswald ripening occurs, which leads to increasingly large pure PCBM domains. Large PCBM domains result in a reduction of OPV device quality.

2.2.3 Co-solvent Additives

Examining solvent and thermal annealing as industrial processes showed that there were clear disadvantages to both post-deposition annealing methods. Solvent annealing utilizes long times with partially solvent-swollen films to allow the morphology to develop towards a more equilibrium-like configuration. By more equilibrium-like we mean a more crystalline, more phase-separated, and more relaxed structure. However, long annealing times and long solvent removal times are incompatible with rapid reel-to-reel coating.

There are also disadvantages to thermal annealing as a process in OPV manufacture. Thermal annealing also allows the BHJ layer morphology to develop towards a more equilibrium-like configuration. However, because the whole substrate must be heated, there is a possibility that other layers are affected. For example, it was shown that with heating to 150°C, P3HT reacts with PEDOT:PSS to make a mixed doped layer via the following reaction [89]:

$$2\ \mathrm{P3HT} + 2\ \mathrm{PEDOT{:}PSS} + \Delta \rightarrow 2\ \mathrm{P3HT^{+}PEDOT{:}PSS^{-}} + \mathrm{H_2}$$

Also, heating to elevated temperatures increases the diffusion rate of PCBM in P3HT, which leads to the formation of extended PCBM crystals and reduced device quality [102, 118, 131–134].

Given these considerations, it was clear that another method for the development of OPV morphology needed to be invented. In 2006, Zhang et al. published an article showing that if mixed solvents are used as a casting solution, the higher BP solvent would remain in the film longer and the film morphology would develop as if the entire solvent was the higher BP solvent [135]. This result gave rise to several useful ideas. First, halogenated solvents have always been an issue for scale-up of OPV because laws governing their release to the atmosphere are quite strict. It would be much less expensive if non-halogenated solvents could be used or if much smaller quantities of halogenated solvents could be used [50, 136]. Second, if high BP solvent-additives can be used to better solubilize both the donor and acceptor components, a different additive could be used that selectively affects one component or the other. Peet et al. published the use of a solvent additive that selectively solvated PCBM while acting as a nonsolvent for the donor polymer [44]. In subsequent research that compared several PCBM selective additives, it was determined that 1,8-di-iodo-octane (DIO) produced BHJ layers with the highest PCE [137]. Moulé et al. published the use of nitrobenzene (NB) as a nonsolvent additive for both P3HT and PCBM [45]. Both DIO and NB produce unannealed P3HT:PCBM devices with PCE near 4% [45, 138]. DIO has been shown to be an essential solvent additive for many copolymer donors in mixtures with PCBM and $PC_{71}BM$.

A solvent additive for OPV can be either a good solvent, selective solvent, or a nonsolvent for both species. The solvent additive must have a higher BP than the carrier solvent so that as the carrier solvent evaporates off, the co-solvent additive concentration increases. This means that the wet film thickness and concentration is created with the main solvent, but the morphology forms under the thermodynamic

conditions established by the co-solvent. DIO is by far the most popular co-solvent in terms of citation frequency. It has been used with most of the new low band gap alternating push–pull copolymers and often yields a superior PCE than films cast without DIO.

2.2.4 Pre-formed Polymer Particles

A further fabrication technique that has been used for OPV devices is the use of preformed polymer nanoparticles. Berson et al. published an article that examined the formation of P3HT nanofibers in solution, followed by coating the nanofibers with PCBM to form a BHJ layer [64, 139]. The idea behind the experiment was that highly crystalline P3HT fibers could be formed in solution that would have fewer defects than P3HT domains in a typical BHJ film. The principle is correct and the spectrum of P3HT fibers shows considerably more vibronic character than P3HT films [64, 139]. Subsequent work on P3HT fibers showed that P3HT forms highly fluorescent J-aggregates in solution under slow cooling conditions [63, 72, 140]. However, OPV devices cast from P3HT fibers have lower PCE than normal BHJ devices of the same thickness [64, 141]. It is known that the P3HT fibers lie within the plane of the film, so it is possible that the fibers are poor conductors of holes. In this case, we expect the J_{sc} to be lower due to increased recombination at unattached fibers. Also, the FF is expected to be lower because it probably requires an activation potential for a hole to hop from one fiber to the next. This activation barrier would appear as a series resistance and reduce the FF.

The mechanism was tested by adding a small amount of amorphous P3HT to the P3HT fibers and re-fabricating OPV devices [64]. The OPV devices with some amorphous P3HT had increased J_{sc} and FF. The authors concluded that the P3HT fibers lacked connectivity and that addition of some amorphous P3HT reestablished the connectivity between P3HT domains [64]. Several other thiophenes were tested for polymer nanoparticle-based OPV devices. It was found that poly (quaterthiophene) (PQ12T) was too insoluble and that polymer domains with extended sizes formed in solution [141]. Oosterbaan et al. fabricated nanofibers from a series of thiophenes with side chain length from 3 to 9 [139]. They concluded that P3HT has the ideal side chain length for polymer nanofiber OPV. Shorter side chains leave a less-soluble polymer that is immiscible with PCBM so OPV device layers do not have enough donor–acceptor interface, which reduces the charge separation probability. Longer side chains destabilize the polymer fibers and allow defects within the fiber to form. For long side chains, the miscibility with PCBM is too high and too much intermixed donor–acceptor phase forms, leading to increased recombination [139]. Another study of polymer nanofiber OPV was published by Xin et al., who worked on characterization of P3BT:$PC_{71}BM$ nanofiber OPV devices (Fig. 10) [142]. P3BT:$PC_{71}BM$ formed OPV devices with high EQE and increased efficiency compared with the Oosterbaan study. Analysis of the fabrication method shows that a combination of nanofiber formation (solvent

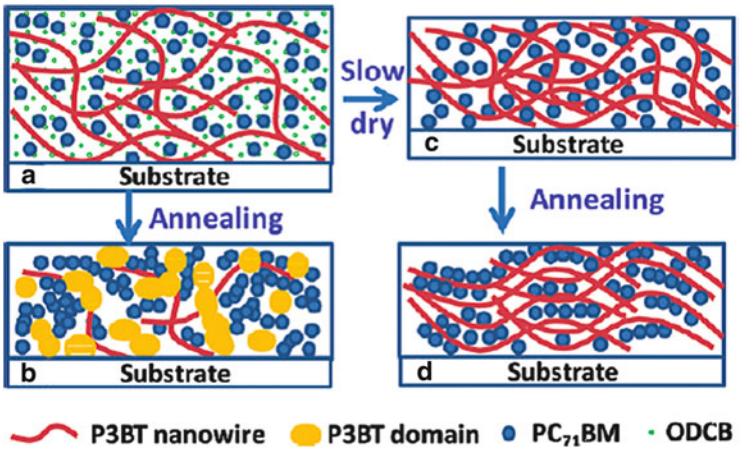

Fig. 10 Solvent annealing followed by thermal annealing yields a morphology for P3BT:$PC_{71}BM$ that cannot be reached by another fabrication pathway. Reprinted (adapted) with permission from [142]. Copyright 2010 American Chemical Society

annealing) and thermal annealing was used to create the optimized morphology film [142].

All of the experiments described above were designed to create more crystalline P3HT domains, and the domain size was controlled by the self-assembly of the P3HT fibers. An alternative need is to control the domain size between two noncrystalline polymers. In this case, the domain size can be set by fabricating polymer nanoparticles in solution [143]. One strategy for fabrication of mixed polymer nanoparticles is shown in Fig. 11. Here the polymer concentration, surfactant concentration, and surfactant strength all affect the size of the final polymer domain [143].

3 Optical Properties

One remarkable feature of solid P3HT:PCBM blends is that their optical properties depend largely on the preparation conditions [73, 144, 145]. Because absorption and emission spectra are easier to record than, for example, X-ray scans and TEM images, the quantitative analysis of optical data with regard to morphology is of great interest. Figure 12 shows exemplary optical absorption spectra of as-prepared and annealed P3HT:PCBM measured at room temperature, together with the corresponding *J*/*V* device characteristics. Here, the films were cast from chloroform, a low-boiling point solvent, and were annealed at the given temperatures for 10 min each. With annealing at higher temperatures, the long wavelength features at 560 and 610 nm attributed to absorption of planarized P3HT chains in polymer

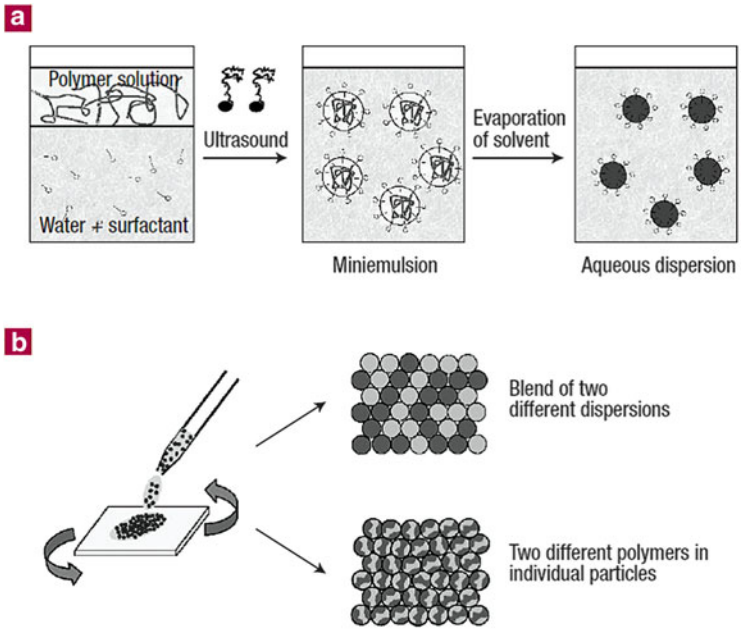

Fig. 11 (**a**) Preparation of a dispersion of solid polymer nanoparticles in water. First, a solution of the polymer in an organic solvent is mixed with water containing an appropriate surfactant. A miniemulsion is then formed upon stirring and ultrasonication. Finally, the solvent is evaporated, resulting in solid polymer nanoparticles dispersed in water. (**b**) Strategies for preparation of binary polymer blends using polymer nanospheres. Phase-separated structures at the nanometer scale can be prepared either by coating a layer from a dispersion containing nanoparticles of two different polymers, or by using dispersions that contain both polymers in each individual nanoparticle [143]

crystallites become more prominent. At the same time, the short-circuit current and the fill factor of the device both increase continuously.

A recent model by Spano enables a quantitative analysis of regioregular P3HT absorption spectra in relation to the morphology [147, 148]. This model was developed to describe the absorption of and the emission from H-aggregates comprising parallel-aligned cofacially packed conjugated chains in the case of weak exciton coupling. In this limit, the splitting of the electronic levels due to Coulombic interactions is considerably smaller than the vibrational energy. As a result, interchain coupling leads to the formation of vibronic bands with their width essentially determined by the exciton bandwidth W. It was shown later that W is inversely related to the length of the interacting chain segments in a P3HT aggregate [149]. An important prediction of Spano's model is that the exciton bandwidth affects the relative intensities of the individual transitions of the vibronic progression in the absorption. Clark et al. successfully applied this model to optical spectra of pure P3HT films with a variation in the solvent type used. Higher solvent boiling points led to smaller W values, which was attributed to an increase in the P3HT aggregate size [71, 150].

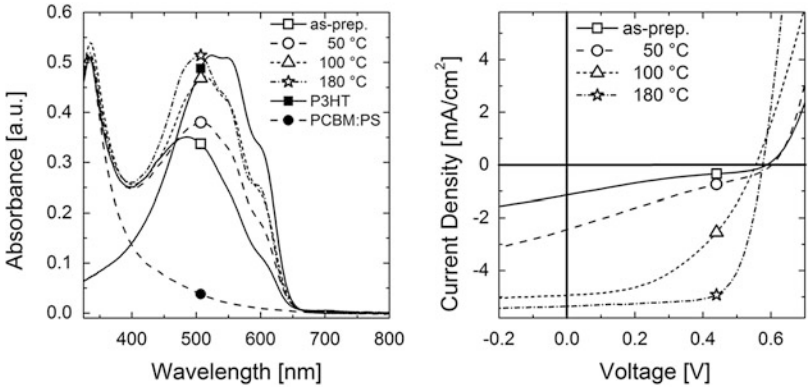

Fig. 12 Optical absorption spectra of P3HT:PCBM photoactive layers and the corresponding *J*/*V* characteristics of solar cells prepared with the same photoactive layer. The as-prepared film is the condition directly after spin-coating. The given annealing temperatures were applied for 10 min each, directly from the state after spin-coating. Also shown are the absorption spectra of a film of pure P3HT and a film comprising PCBM:PS, where the latter was used to determine the PCBM contribution to the P3HT:PCBM absorption spectra [146]. The active layer thickness was only 100 nm, which causes less absorption in the active layer and a lower photocurrent compared with optimized devices

This model has been successfully applied to understand the morphological changes of the P3HT phase in a 50:50 wt% P3HT:PCBM blend, where information about the crystallinity and interchain ordering of the polymer phase was determined [146]. A low and a high boiling point solvent were investigated with the use of different annealing temperatures. The absorption spectra analysis was compared with the solar cell performance in devices with identical active layers (Fig. 13). The low boiling point solvent, chloroform, led to a non-optimized initial film morphology. Compared to the as-prepared blend prepared from the high boiling point solvent dichlorobenzene, the chloroform-cast layer exhibited smaller aggregates, a lower degree of crystallinity, and a larger absorption bandwidth. Upon annealing, the degree of crystallinity of the P3HT component increased up to a temperature of ca. 70°C, with a correlated increase in the aggregate width from ca. 7 to 10 nm. The glass transition of a 1:1 blend of P3HT:PCBM has been observed to range from ca. 10 to 70°C [151–153]. It has, therefore, been concluded that annealing above the glass transition provides the chains with sufficient mobility to allow for the growth of existing polymer crystallites. Beyond the glass transition range, annealing had a surprisingly weak effect on the further changes to the degree of crystallinity. Neither the percentage of aggregated P3HT chains nor the aggregate width of annealed chloroform-cast layers reached the same level as found in the pristine P3HT layer cast from chloroform or as found in any of the dichlorobenzene-cast blends. It is plausible to assume that a further growth of P3HT crystallites in the chloroform-cast layers upon annealing at higher temperatures is prevented by an already-existing network of agglomerated PCBM molecules [154]. The Gaussian line width σ in the absorption spectra, however, decreased throughout the entire

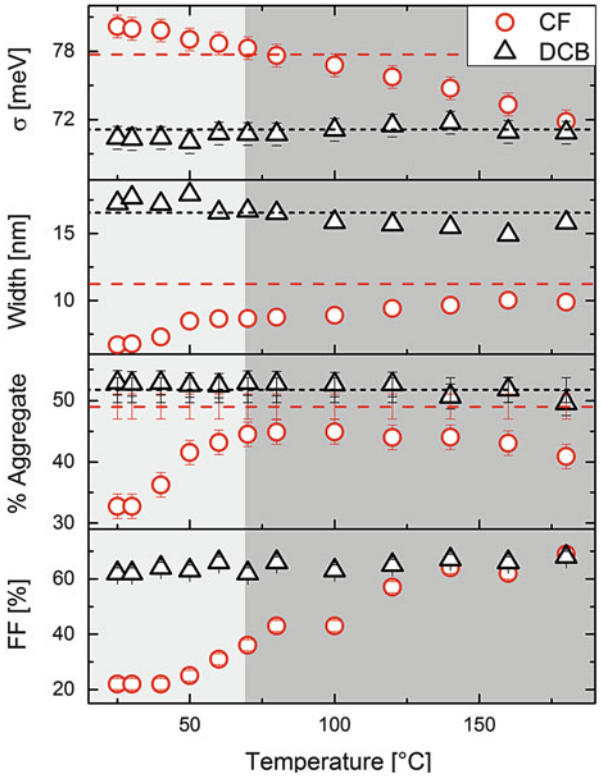

Fig. 13 Best-fit parameter of the aggregate P3HT component in the absorption spectra of P3HT:PCBM blends coated from chloroform (CF) and dichlorobenzene (DCB), with subsequent thermal annealing of the as-prepared film for 10 min at the indicated temperature. σ the Gaussian line width, *Width* aggregate width of the P3HT crystalline component, *% Aggregate* crystalline percentage of the P3HT component versus the total amount of P3HT, *FF* fill factor of the photovoltaic device with the same photoactive layer used in the optical absorption investigation. *Red* and *black dashed lines* show corresponding values measured on as-prepared layers of pristine P3HT, cast from CF and from DCB, respectively. The glass transition of P3HT:PCBM is shown by the change from *light* to *dark grey* background, with a glass transition temperature of around 60–70 °C [146]

range of annealing temperatures used. This decrease in the absorption line width is indicative that the intra- and/or interchain disorder is reduced. It was then shown that the decrease in σ goes along with a prominent increase in the hole mobility, enabling more rapid extraction of the photogenerated charges to the electrodes. As a consequence, non-geminate recombination becomes less efficient for higher annealing temperatures, which revealed itself in a prominent increase in the fill factor. As an important conclusion, we find that consideration of only the percentage of crystallinity and/or of the aggregate size is not sufficient to explain the overall effect of annealing on device properties.

Nevertheless, as efficient hole transport necessitates the existence of a percolation pathway of crystalline P3HT throughout the entire layer, knowledge about the degree of crystallinity and also about the 3D distribution of the different phases forming the P3HT:fullerene blend are highly important. A well-established method for obtaining information on these properties is electron tomography (ET) [79, 96, 155]. For example, Loos and coworkers applied ET to determine the amount and distribution of the crystalline P3HT component in P3HT:PCBM blends [79]. These samples were investigated directly after spin-coating or after thermal annealing for 20 min at 130°C. The overall degree of crystallinity (DoC) in the annealed samples was between 40 and 55%, depending on layer thickness. The DoC from ET compares nicely with the range of values given in Fig. 13 for annealed blends. Notably, ET on thin layers (50–100 nm) revealed an enrichment of the crystalline P3HT content close to the bottom side where hole extraction occurs [79]. On the other hand, 200 nm thick layers had a homogeneous distribution of P3HT crystallites, which is highly beneficial for the efficient collection of holes throughout the entire active blend.

Raman spectroscopy is another successful optical technique for study of the degree of molecular ordering in the P3HT phase of the P3HT:PCBM blend. The in-plane skeleton Raman modes of C=C and C–C stretching were studied by Tsoi et al. under excitation wavelengths ranging from resonant to nonresonant [156]. Although direct electronic excitations in the resonant range could lead to a strong fluorescent background that can cover Raman signals, this is still an important measurement technique because the resonant conditions provide information about the molecular structure. In order to better understand the changes in the morphology of the P3HT component, Raman spectra of regiorandom and regioregular P3HT were compared where the regioregular polymer is known to have a higher degree of ordering. These results were then compared with the Raman spectra from a blend of regioregular P3HT with PCBM. The C=C stretching mode was found to be the superposition of the ordered and disordered P3HT characteristics and this was used to quantitatively estimate the degree of molecular ordering in the blend. The degree of molecular ordering in the nonannealed blend compared with the annealed blend was found to increase from 42 to 94%, relative to the ordering of pristine regioregular P3HT. The percentage of crystallinity can then be estimated based on a known percentage of crystallinity in the pristine P3HT. Tsoi et al. assumes a crystallinity in the regioregular P3HT of 15% and hence a percentage crystallinity of 6 and 14% in the P3HT phase of the annealed and nonannealed blends, respectively. However, optical spectroscopy on pristine P3HT layers consistently showed a degree of chain aggregation of approximately 40–50% [62, 150], and even higher degrees of crystallinity were reported in bulk samples [157]. Using 50% as a reference value, the degree of aggregation as estimated from the Raman spectra is 21 and 47% in the nonannealed and annealed blends, respectively. This approximation seems to be more reliable, based on the results of previous studies. Therefore, with an accurate method for determining the percentage crystallinity in the pristine regioregular P3HT, the analysis of Raman

spectra provides a simple way to determine the percentage crystallinity in the P3HT:PCBM blend films.

In conclusion, optical spectroscopy is capable of quantifying some important morphological parameters of P3HT:PCBM blends. Annealing clearly enlarges the P3HT crystallites in the composites, but also improves intra- and interchain order within the polymer domains. It is documented that this improvement assists charge extraction via a higher hole mobility. Structural disorder was recently proposed to be one origin of gap states in semicrystalline polymer domains [158]. Although as-prepared chloroform-cast layers are less crystalline, they contain a noticeable number of aggregated chains. It has been postulated that free carrier generation in P3HT:PCBM cells is assisted by the delocalization of holes on fully conjugated chains [159]. It is, therefore, concluded that the number of aggregated P3HT chains in as-prepared blends is sufficiently high for the efficient photogeneration of free carriers (as documented in the next section), while the poor structural order in these layers prevents the efficient extraction of free carriers to the external circuit [146].

4 Geminate and Non-geminate Recombination

As described in the previous section, optimized samples of P3HT:PCBM exhibit high fill factors, meaning that the photogenerated current is independent of bias over a wide range. On the other hand, samples with non-optimum morphology suffer from low fill factors. In this case, the photocurrent becomes continuously smaller with increasing bias (decreasing internal electric field), which points to photocurrent losses that are most prominent at low internal electric field. Clearly, the identification of these loss processes in relation to morphology is of interest, not only with regard to an overall understanding of these complex devices but particularly when targeting the knowledge-based optimization of BHJ devices.

The elementary steps that lead to charge generation and extraction in BHJ solar cells are shown in Fig. 14. Free carrier formation from photogenerated excitons (created in either the donor or acceptor phase) involves formation and split-up of interfacial electron hole pairs (often called geminate pairs because they originate from the same photoexcited exciton). As these pairs can be generated directly via optical sub-bandgap excitation, they are commonly denoted as charge transfer states. Geminate pairs may either split up into free carriers or recombine geminately to the ground state. Clearly, the competition between these two processes sets the upper limit for the efficiency of the internal photon-to-charge conversion. The second important step is the extraction of photogenerated charge to the electrodes. The efficiency of this process is, in general, not unity because these charges might recombine with carriers of opposite sign (either free or trapped, photogenerated or injected) on their way to the electrodes. This recombination is called “non-geminate” or “free carrier recombination”. Therefore, the efficiency of an organic donor/acceptor blend is determined by the fate of three elementary states (see Fig. 15): the photogenerated exciton (mostly singlet excitons) with energy E_{S1}, the charge

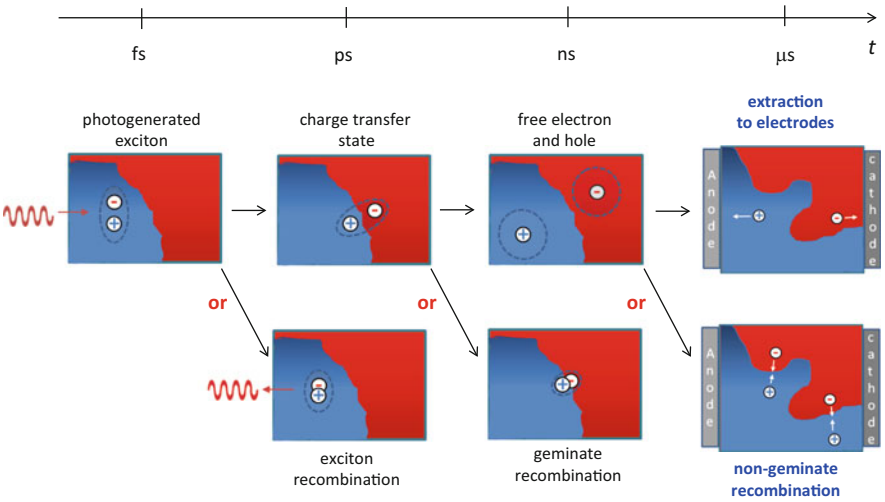

Fig. 14 Processes leading to free carrier generation and extraction. Absorption of light leads to the generation of a tightly bound intramolecular exciton (in P3HT:PCBM, the absorption in the visible spectrum is dominated by the polymer). This exciton decays to the ground state within its fluorescence lifetime or it diffuses to the donor–acceptor heterojunction where it dissociates into an interfacial electron–hole pair (charge transfer state). Due to the low permittivity of organic media, the interfacial polaron pair is bound by its mutual Coulomb potential. The charges forming this pair either overcome this potential to form free carriers, or they recombine geminately. Then, the free electron and the hole become extracted at the electrodes or they recombine non-geminately with other charges. The time scale for exciton dissociation, free carrier formation, and charge extraction is plotted at the *top*. Numbers should be taken with care because the charge carrier dynamics in blends depends very much on the chemical structure and morphology of the donor–acceptor mixture

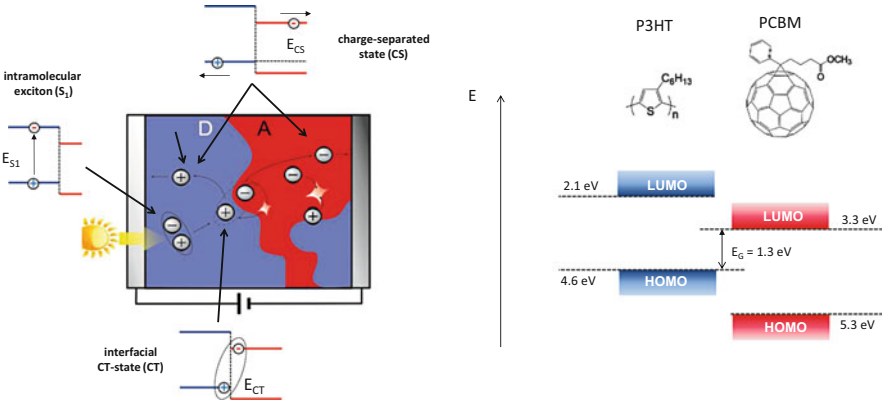

Fig. 15 *Left*: Donor–acceptor bulk heterojunction device and the relevant elementary states. *Right*: HOMO and LUMO energies of P3HT and PCBM in the 1:1 blend as determined by photoelectron spectroscopy (values taken from [160])

Table 1 Energies of the relevant states and excitations in blends of P3HT with PCBM

Blend	Energy (eV)	Reference
P3HT LUMO[a,b]	2.13	[160]
P3HT HOMO[a,b]	4.65	[160]
$PC_{61}BM$ LUMO[a,c]	3.80	[160]
$PC_{61}BM$ HOMO[a,c]	5.80	[160]
P3HT:$PC_{61}BM$ LUMO[a,d]	3.29	[160]
P3HT:$PC_{61}BM$ HOMO[a,d]	4.63	[160]
P3HT:$PC_{61}BM$ charge separated state[e]	1.34	
P3HT absorption onset[f]	1.68	
$PC_{61}BM$ absorption onset[f]	1.61	
Charge transfer state[g]	1.14	[161]

[a]Measured by photoelectron spectroscopy (PES) and inverse photoelectron spectroscopy (IPES)
[b]Pure P3HT layer, coated from chlorobenzene on either Si or Au
[c]Pure $PC_{61}BM$ layer, coated from chlorobenzene on either Si or Au
[d]P3HT:$PC_{61}BM$ (1:1) blend coated from chlorobenzene on Au, once buried interface. Similar values are seen for as-prepared and annealed samples
[e]Calculated from the P3HT:$PC_{61}BM$ (1:1) HOMO and LUMO energies given in the rows above
[f]From the extrapolation of the absorption onsets of the pure materials in Fig. 18b
[g]P3HT:$PC_{61}BM$ (1:1) on PEDOT:PSS, room temperature

transfer (CT) state with energy E_{CT}, and the charge separated (CS) state with energy E_{CS}. The CS state is different from the CT state in having overcome any mutual electron–hole interactions.

Because of the low dielectric constant of organic materials, the interfacial electron–hole pair is bound by Coulombic forces. Consequently, the energy of the CT state is expected to be smaller than that of the free electron–hole pair $E_{CT} < E_{CS}$. On the other hand, efficient photon-to-electron conversion is energetically favored only if the energy of the primary excitation is larger than that of the final product, meaning that $E_{S1} > E_{CS}$. Energies of the relevant species are listed in Table 1 for P3HT:PCBM. HOMO and LUMO energies in the blend are depicted in Fig. 15. The energy of the charge separated state was taken as the difference between the P3HT HOMO and the PCBM LUMO in the blend. The values suggest that the CT state has indeed the lowest energy, meaning that its split-up into free carriers is hampered by a potential barrier. However, note that the simple energy scheme drawn in Fig. 15 does not account for the heterogeneity of the P3HT:PCBM blend films, which has a large impact on the photovoltaic performance (see next section).

4.1 Free Carrier Generation Versus Geminate Recombination

A well-established model to describe free charge generation in isotropic media via split-up of Coulombically bound geminate pairs is the Braun–Onsager theory [164] (see also [165] for a detailed discussion on the accuracy of the model). Carriers are

considered to be free if their distance exceeds the Coulomb capture radius, meaning that the thermal energy is larger than the mutual Coulombic binding energy of the geminate pair. Free carrier formation involves a Brownian-type random walk that is well described by the Onsager theory. In general, the photogeneration efficiency P is a function of both the internal electric field and temperature:

$$P(E,T) = \frac{k_d(E,T)}{k_d(E,T) + k_f}, \tag{6}$$

where k_d is the field- and temperature-dependent rate for charge separation and k_f is the inverse lifetime of the bound e–h pair. Although the Braun–Onsager model was originally developed for homogeneous media, it has been applied to model BHJ cells made of poly[2-methoxy-5-(3′,7′-dimethyloctyloxy)-*p*-phenylene vinylene] (OC_1C_{10}-PPV) blended with $PC_{60}BM$ [166]. For nonzero k_f, the field-dependence of k_d causes P to vary with the internal electric field and therefore with the external bias. If non-geminate recombination is weak, this field-dependence determines the course of the photocurrent as a function of applied voltage. Based on this assumption, Mihailetchi et al. concluded that in OC_1C_{10}-PPV:$PC_{60}BM$ only 60% of the bound CT states dissociate into free carriers at short-circuit conditions and room temperature. Field-assisted generation in PPV-based blends was recently confirmed by Mingebach et al. [167]. The Braun–Onsager model was also applied to describe the *J*/*V* characteristics of P3HT:PCBM solar cells [73, 168], but this analysis yielded long CT lifetimes of at least 100 ns [159].

The application of the model to P3HT:PCBM blends was challenged by the observation of efficient ultrafast free carrier generation in as-prepared and annealed P3HT:$PC_{60}BM$ thin films using transient absorption spectroscopy (TAS) with a subpicosecond time resolution [100, 169, 170]. Quenching of the excitons in the P3HT phase, accompanied by the appearance of a photoinduced absorption signal assigned to polarons, was shown to occur within 100 fs for as-prepared blends and within a few picoseconds in annealed blends. The slower build-up of the polaron population in the annealed sample was attributed to the dynamics of exciton diffusion to the BHJ. Figure 16 shows exemplary TAS traces for as-prepared and annealed P3HT:PCBM blends as a function of illumination fluence. Detailed analysis of the TAS experiments as a function of the pulse fluence suggested that exciton dissociation leads to two populations, free charges and bound polaron pairs, with the latter recombining geminately within only 2 ns [169]. These experiments ruled out the possibility that photogeneration in P3HT:PCBM blends involves a long-lived CT state and suggested that free carrier formation may not necessarily be assisted by the electric field. Interestingly, the thermal treatment of these chlorobenzene-cast blends had a rather small effect on the fraction of generated free carriers, which was 68 and 85% for the as-prepared and thermally annealed layers, respectively. Thus, despite a large difference in the PV performance, exciton-to-polaron conversion proceeds with comparable efficiency in both of these samples. In contrast, regiorandom P3HT blended with PCBM yielded a much smaller free carrier formation efficiency of only about 20%, while most

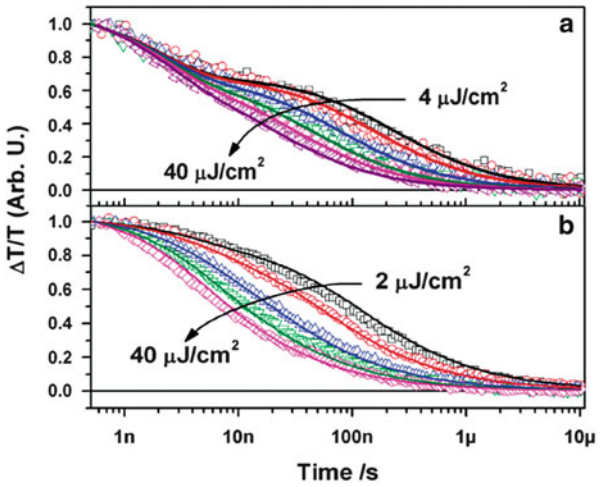

Fig. 16 Charge induced absorption decay (750–850 nm) for (**a**) as-prepared and (**b**) annealed 1:1 blends of regioregular P3HT and PCBM coated from chlorobenzene. The transients of the as-prepared device show a fluence-independent decay attributed to geminate recombination of strongly bound CT states at early times. The dynamics of both blends at longer times is entirely determined by the recombination of free polarons. *Lines* show global fits to a non-geminate recombination model including a density-dependent recombination coefficient. The data show conclusively that free carrier formation is rapid and that geminate recombination is completed within few nanoseconds. Reprinted (adapted) with permission from [169]. Copyright 2010 American Chemical Society

excitons formed strongly bound CT states that decayed geminately to the ground state within 2 ns.

Field-independent photogeneration in solvent-annealed P3HT:PCBM was unambiguously proven by Kniepert et al. using time-delayed collection field (TDCF) experiments [171]. In a TDCF measurement, as schematically shown in Fig. 17a, the sample is illuminated by a short laser pulse while being kept at a constant pre-bias voltage V_{pre}. After the delay time, t_d, a rectangular pulse with voltage V_{coll} is applied to sweep out all remaining free carriers. Therefore, TDCF is analogous to TAS with an electrical probe instead of an optical probe. In contrast to steady-state current–voltage measurements, classical time-of-flight experiments, or the photo-CELIV (charge extraction by a linearly increasing voltage upon photogeneration) technique, TDCF allows application of different biases during generation and collection of the charge carriers. To measure the field dependence of free carrier formation, TDCF experiments are performed with variable pre-bias, a short delay time, and a large collection field. Thereby, the delay time must be carefully chosen to ensure that geminate recombination is completed within the delay time. Also, the pulse fluence must be kept low to avoid non-geminate recombination prior to application of the collection bias. Provided that these conditions are safely met, the total collected charge as a function of the pre-bias

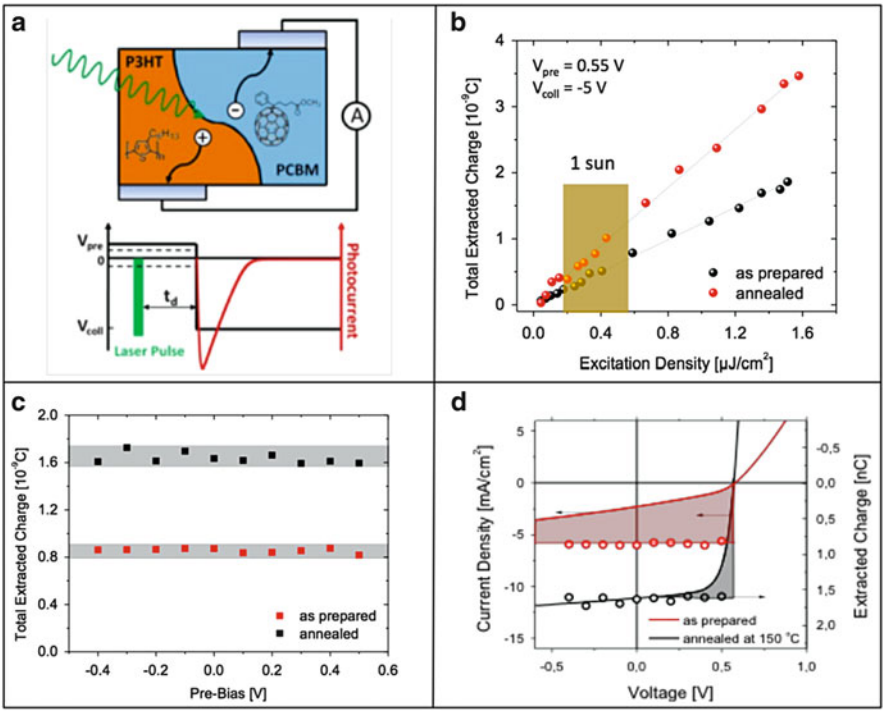

Fig. 17 (**a**) The TDCF experiment. A pre-bias V_{pre} is applied during illumination with a nanosecond laser pulse. After a given delay, rapid charge extraction is ensured by applying a large reverse bias V_{coll} [171]. (**b**) Total extracted charge Q_{tot} as a function of pulse fluence for as-prepared and annealed P3HT:PCBM. The time delay was 20 ns and the collection field was −5 V. Q_{tot} is perfectly linear in the fluence for both samples over the entire intensity range, ruling out losses due to non-geminate recombination. (**c**) Q_{tot} as a function of pre-bias for a pulse fluence of 0.7 μJ/cm^2. The generated charge is found to be independent of bias within an error of 10% (*grey areas*). (**d**) Comparison of the bias-dependent extracted charge and the steady-state *J*/*V* characteristics of the as-cast and annealed blend. In contrast to $Q_{tot}(V)$, the shape of the *J*/*V* characteristics of the two devices differs greatly, with the as-prepared device exhibiting a much lower fill factor. Therefore, incomplete charge extraction rather than field-dependent charge generation must be the main cause for the much poorer performance of the as-prepared device [172]. The shaded areas indicate the extraction losses

measures the field-dependence of free charge generation in competition with geminate recombination.

Field-independent free charge generation was also seen for P3HT:PCBM blends coated from chloroform, which had either been dried at room temperature (as-prepared) or annealed at 150°C for 15 min directly after spin-coating. These measurements were performed with a delay time of 20 ns, which is well above the lifetime of the CT state (as determined from TAS experiments, as described above). For such a short delay, the total collected charge Q_{tot} is perfectly linear over a wide range of pulse fluences, meaning that non-geminate recombination losses are

insignificant for the chosen parameters (Fig. 17b). The dependence of Q_{tot} versus V_{pre} measured for a moderate pulse fluence of 0.7 μJ/cm^2 is shown in Fig. 17c. The extracted free charge is independent of pre-bias (within 10%, see grey area in Fig. 17c) for both as-cast and thermally annealed blends, implying field-independent charge carrier generation. A very weak dependence of free carrier generation on the electric field was also seen in TDCF experiments performed on chlorobenzene-cast P3HT:PCBM, with and without thermal annealing [167, 173]. Further evidence for field-independent free carrier formation in thermally annealed P3HT:PCBM came from transient photoconductivity experiments [174, 175].

To summarize, field-independent generation is shown to be common to blends of regioregular P3HT with PCBM. The importance of this finding becomes evident when considering that the studied devices were processed under a variety of conditions (different solvents, thermal annealing, solvent annealing, different layer thicknesses), which resulted in different morphologies and, consequently, in a wide range of PV performance parameters.

Before discussing possible morphological pictures to explain these findings, we turn to the involvement of CT states in the exciton-to-polaron conversion in P3HT:PCBM blends. The observed insensitivity of free carrier generation to the internal electric field suggests that this process does not involve split-up of bound CT states. It has been proposed that the dissociation of P3HT excitons at the heterojunction generates "hot" CT states (Fig. 18a), which possess a sufficient amount of energy to overcome the Coulomb barrier without the aid of an electric field [169]. Interestingly, "colder" CT states in P3HT:PCBM can be directly excited by using photon energies of between 1.2 and 1.6 eV, which is below the energy of the vibronically relaxed S_1 exciton of P3HT. Lee and coworkers measured the external quantum efficiency and the absorption of annealed P3HT:PCBM over a wide range of photon energies [163]. The main result of these experiments is displayed in Fig. 18b. The EQE spectrum was fully reproduced by considering only the wavelength-dependent absorption of the organic layer in the device while keeping the internal quantum efficiency constant at around 80%. It was concluded that efficient free charge generation in P3HT:PCBM does not require the split-up of hot CT states, which is in contrast to the hot CT model outlined above. In accordance with the interpretation by Lee and coworkers, it was reported that the incident photon energy has no effect on the charge generation and recombination in either as-prepared or thermally annealed P3HT:PCBM blends [162]. These authors also showed that the shape of the EQE does not change with bias. Because free carrier generation is known to be independent of bias upon excitonic excitation, the dissociation of CT states must also be unaffected by the internal electric field.

An important observation by Lee et al. is that free charge generation is efficient, even when directly exciting the sub-bandgap CT state. Therefore, a driving force must exist that counterbalances the mutual Coulomb attraction of these geminate polaron pairs. One possible cause of this force is the energy landscape in these blends, arising from its particular three-phase morphology. As pointed out above, these blends consist of three phases: intermixed regions of P3HT and PCBM, domains of crystallized P3HT chains, and almost pure agglomerates of PCBM

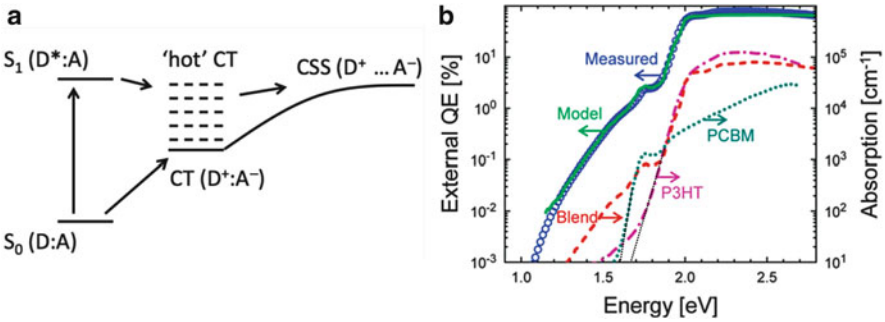

Fig. 18 (**a**) Generation of free charges either via a "hot" charge transfer (CT) state formed by S_1 exciton split-up or via a "cooler" CT state that is generated by direct excitation. Reprinted with permission from [162]. Copyright © 2012 Wiley-VCH Verlag GmbH & Co. KGaA, Weinheim. (**b**) Experimental EQE spectrum under short-circuit conditions (*circles*) compared with the absorption coefficient of solid P3HT, PCBM, and the 1:1 P3HT:PCBM blend. Also shown is the modeled EQE spectrum that assumed a constant IQE of 80% but a wavelength-dependent absorption (A) of the blend layer according to $A = A_0(1 - \exp(-2\alpha d))$, with α being the absorption coefficient and d the active layer thickness. Reprinted (adapted) with permission from [163]. Copyright 2010 American Chemical Society

molecules. P3HT chains within the mixed domains are believed to exhibit a twisted conformation, similar to chains in solution or in a solid sample of regiorandom P3HT. As these twisted chains exhibit lower HOMO energies than those in crystallites of planar P3HT [176], an energy gradient is established that drives holes out of the intermixed regions [177]. Similarly, Jamieson et al. pointed out recently that the larger electron affinity of PCBM molecules in pure fullerene aggregates compared to the intermixed domain assists free charge generation [178]. Polaron pairs generated in the intermixed regions are therefore prone to rapid dissociation into spatially separated charges, with the hole and electron residing on domains of the pure donor and acceptor, respectively (Fig. 19a). This model of a morphology-related driving force is consistent with the observation of efficient dissociation of even relaxed CT states, and it also provides a reasonable explanation for the inefficient non-geminate recombination of electrons and holes in annealed P3HT:PCBM blends.

The situation is different when considering excitons that are formed within ordered P3HT domains. Troisi and coworkers pointed out that because of the lower band gap of chain segments within the crystallites, these excitons are repelled by the more disordered donor–acceptor interface [179]. The authors therefore proposed that these excitons split via tunneling of the electron through layers of more distorted polymer chains at the interface into higher and partially delocalized states on the PCBM aggregates (see Fig. 19b). This long-range exciton dissociation results in a spatially separated electron–hole pair, stabilized by a more disordered interfacial region. In a subsequent publication, Caruso and Troisi considered the

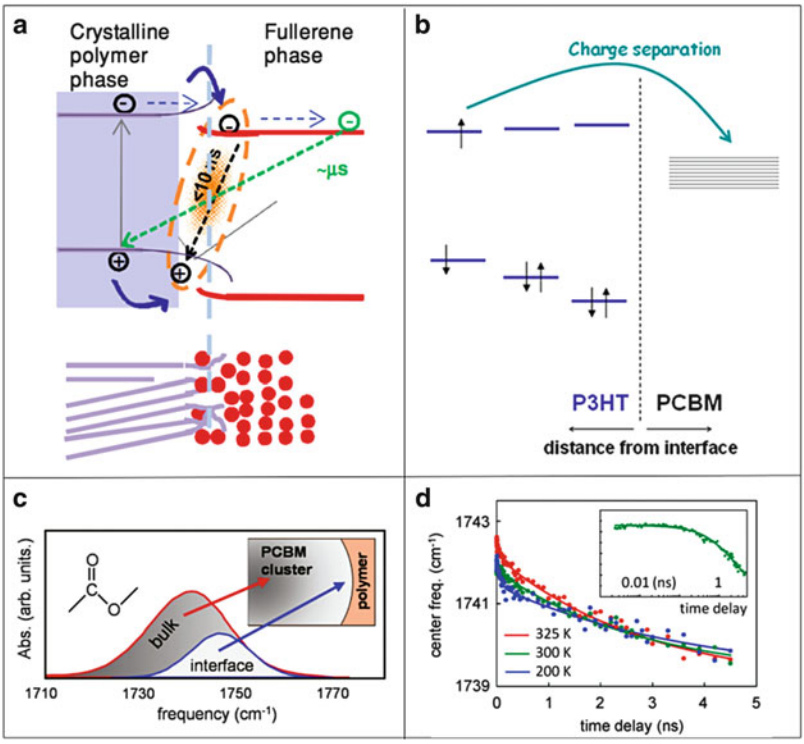

Fig. 19 (**a**) Split-up of geminate electron–hole pairs formed in the intermixed region between polymer-rich and fullerene-rich domains. Backbone twisting and disruption of intermolecular interactions raise the energies of electrons and holes in the intermixed region. Therefore, a morphological driving force is established that counterbalances the mutual Coulombic interaction of the geminate pair. Reprinted (adapted) with permission from [177]. Copyright © 2013 Wiley-VCH Verlag GmbH & Co. KGaA, Weinheim. (**b**) An exciton formed within the P3HT crystallite is repelled from the interface because chains at the boundary to PCBM exhibit a higher band gap. Exciton split-up can, however, occur via electron tunneling into partially delocalized states in the PCBM aggregates. Reprinted (adapted) with permission from [179]. Copyright 2011 American Chemical Society. (**c**) The frequency of the carbonyl stretch vibration of the PCBM is higher at the interfaces with conjugated polymers than of PCBM molecules in the interior of fullerene aggregates. Therefore, the dynamics of charge transfer spit-up in polymer:fullerene blends can be followed through the time dependence of the carbonyl vibration frequency after excitation in a transient visible/infrared experiment. Reprinted (adapted) with permission from [180]. Copyright 2010 American Chemical Society. (**d**) Time-dependence of the center frequency of the PCBM carbonyl stretch recorded at three different temperatures after pulsed excitation of a P3HT:PCBM blend film with 550 nm light. The independence of the transient on temperature is interpreted in terms of an activationless split-up of interfacial electron–hole pairs. Reprinted (adapted) with permission from [181]. Copyright 2012 American Chemical Society. The inset demonstrates that charge separation occurs on the nanosecond time scale in the P3HT:PCBM blend

kinetics and energetics of the proposed process in greater detail [182]. For long-range transfer, the electron transfer rate k_{ET} scales approximately like $k_{ET}(R) = k_0 \exp(-\beta R)$ with distance R, where β is an attenuation factor. It is shown that tunneling through conjugated chains results in values of β as small as 0.2 $Å^{-1}$.

Under these conditions, k_{ET} for an exciton formed 23 Å from the interface (corresponding to six chains in the π-stacking direction) is on the order of 10^{12} s^{-1}, which leads to polaron formation on a time scale comparable with that found experimentally in annealed P3HT:PCBM.

In P3HT:PCBM, both mechanisms described above may contribute to free charge photogeneration. Tunneling, as proposed by Troisi and coworkers, is important when exciting the blend at 500–650 nm, where aggregated P3HT absorbs. On the other hand, sub-bandgap absorption excites CT states predominately in the intermixed region, and the split-up of these coulombically interacting electron–hole pairs benefits from the morphology-related driving force. One might, therefore, expect the IQE to depend on the excitation energy, which is apparently not the case in P3HT:PCBM. In a very recent work, Vandewal et al. demonstrated the IQE to be insensitive to excitation energy for various organic donor–acceptor BHJ systems [183]. It is proposed that photogeneration proceeds via the split-up of thermalized (electronically and vibronically relaxed) CT states at all illumination conditions, even if illumination primarily excites the donor or acceptor component. This situation was encountered in an inefficient blend with a pronounced field dependence of generation, but also for a highly efficient blend with field-independent generation. Accordingly, we propose that photogeneration in P3HT:PCBM is entirely governed by the efficient split-up of low-energy CT states.

We note that activationless free charge generation in P3HT:PCBM was unambiguously proven with ultrafast vibrational spectroscopy [180, 181]. It had previously been shown that the frequency of the carbonyl group in PCBM depends on the local environment: the vibration frequency of a PCBM molecule located in the interior of a fullerene cluster is lower than that of a PCBM molecule at the interface to the donor polymer [184] (see Fig. 19c). Therefore, the motion of the electron away from the heterojunction during charge separation can be monitored through a decrease in the carbonyl frequency. For P3HT mixed with PCBM, the time-dependence of the carbonyl center frequency was independent of the temperature, meaning that free charge formation via CT split-up does not require thermal activation (Fig. 19d) [181]. In agreement with this, TAS experiments presented by Mauer et al. showed free carrier generation in annealed regioregular (rr)-P3HT:PCBM blends to be independent of temperature [185], indicating again activationless geminate pair separation.

In conclusion, free charge generation in blends of regioregular P3HT with PCBM is independent of electric field and possibly temperature for a wide range of preparation conditions and efficiencies. Carrier formation seems to be equally efficient when CT states are formed via the split-up of singlet excitons at the BHJ or when they are generated directly via sub-bandgap excitation. The findings are explained by the complex morphology of these layers, which comprise pure and intermixed regions. The answer to the question of why the exciton-to-polaron conversion in rr-P3HT:PCBM blends is rather insensitive to the preparation conditions might lie in the fact that even samples as-cast from chloroform with very

poor performance exhibit a considerable concentration of P3HT aggregates, which guarantee efficient CT split-up at the local scale.

4.2 Charge Extraction Versus Non-geminate Recombination

As pointed out in the previous section, free carrier generation in P3HT:PCBM blends proceeds at the picosecond time scale, unassisted by the applied electric field. It must, therefore, be the free carrier recombination (non-geminate recombination) in competition with charge extraction that accounts for most of the photocurrent loss within the working regime of P3HT:PCBM blends.

The influence of non-geminate recombination on the J/V characteristics can be best understood by considering the current flowing through the device under steady-state illumination, $J_{\text{light}}(V)$, in terms of current densities of generation and of non-geminate loss:

$$J_{\text{light}}(V) = J_{\text{gen}}(V) - J_{\text{NG}}(V), \tag{7}$$

where J_{gen} is the generation current density (the generated free charge per unit area and time) and J_{NG} the loss current density including non-geminate recombination in the bulk and carrier extraction at the wrong contact (electrons leaving the device via the anode or holes via the cathode). J_{NG} can be written as [186]:

$$J_{\text{NG}}(V) = ed\frac{n}{\tau(n)}, \tag{8}$$

with $\tau(n)$ being the inverse recombination rate parametric in the carrier density n as given by:

$$\frac{1}{\tau(n)} = \gamma n^{\lambda}. \tag{9}$$

Here, γ is the non-geminate recombination coefficient and $\lambda + 1$ the order of recombination. Clearly, non-geminate losses become more significant at higher carrier density n, e.g., at low fields or as a result of low mobilities, and for a high γ. In the ideal case, free carriers recombine either with trapped charges (Schottky–Reed–Hall recombination; SRH) or with free carriers of the opposite sign (bimolecular recombination). In the first case, $\lambda + 1 = 1$ and the lifetime of the free carrier does not depend on carrier density. In contrast, for bimolecular recombination, $\lambda + 1 = 2$ and an increased density of photogenerated charge accelerates recombination. Although there is some evidence that the SRH process cannot be neglected in P3HT:PCBM devices [175, 187], the consensus is now that the non-geminate photocurrent loss is mainly due to bimolecular recombination.

Various methods have been applied to P3HT:PCBM in order to quantify the parameters that describe non-geminate recombination (see, e.g., [187–194]). Knowledge about γ and $\lambda+1$ was mostly derived from transient pump-probe measurements (see, e.g., [169, 189, 195]). In these experiments, a short laser pulse excites the sample and the fate of the photogenerated charge is followed by measuring the transient polaron-induced absorption signal. In a homogenous medium with low carrier mobility, the decrease in carrier density via non-geminate recombination is predicted to follow Langevin-type bimolecular recombination:

$$\frac{\mathrm{d}n}{\mathrm{d}t} = -\frac{n}{\tau(n)} = -\gamma_{\mathrm{L}} n^2 \tag{10}$$

with $\lambda+1=2$ and the Langevin recombination coefficient $\gamma_{\mathrm{L}} = e(\mu_{\mathrm{e}}+\mu_{\mathrm{h}})/\varepsilon_0\varepsilon_{\mathrm{r}}$. However, most publications show that the free carrier dynamics in bulk heterojunction devices is not guided by simple Langevin-type recombination. TAS transients of annealed P3HT:PCBM could be described only when assuming a higher order recombination process with $\frac{dn}{dt} \propto -n^3$. This finding was explained by bimolecular recombination $\frac{dn}{dt} \propto -\gamma(n)n^2$ with a recombination coefficient that itself depends on charge density [189]. Earlier work by Nelson suggested that charge recombination in polymer:fullerene blends occurs via diffusive motion of polarons in the presence of an exponential density of traps [196]. Increasing the density of photogenerated charge fills these traps and thus accelerates non-geminate recombination. Carrier-dependent mobilities in P3HT:PCBM blends were independently proven by two groups [197, 198]. TAS experiments performed by Shuttle et al. also showed that bimolecular recombination in annealed P3HT:PCBM blends is severely slowed down compared with the Langevin limit, with values of $\gamma/\gamma_{\mathrm{L}}$ of the order of 10^{-2}–10^{-3}. This finding is in agreement with earlier work by Pivrikas et al. [188]. Suppressed recombination was attributed to the particular nanomorphology of these blends that consists of an interpenetrating network of spatially separated (and energetically separated) pathways for electrons and holes. The basic finding of a higher order but suppressed recombination, compared with the Langevin limit, was consistently seen in follow-up TAS experiments on both as-prepared and annealed P3HT:PCBM blends [169, 185, 195, 199], and was confirmed by flash photolysis and time resolved microwave conductivity experiments [191].

One disadvantage of these all-optical pump-probe techniques is that they require high excitation densities and thus do not provide information on the fraction of charge surviving recombination under different bias conditions. An elegant approach to quantify these processes is to perform TDCF measurements with increasing delay time. Integration of the transients during delay and during collection yields the quantities $Q_{\mathrm{pre}}(t_{\mathrm{d}})$ and $Q_{\mathrm{coll}}(t_{\mathrm{d}})$, respectively, from which the total collected charge can be calculated via $Q_{\mathrm{tot}}(t_{\mathrm{d}}) = Q_{\mathrm{pre}}(t_{\mathrm{d}}) + Q_{\mathrm{coll}}(t_{\mathrm{d}})$. The example shown in Fig. 20 is the dependence of these quantities as a function of delay time for

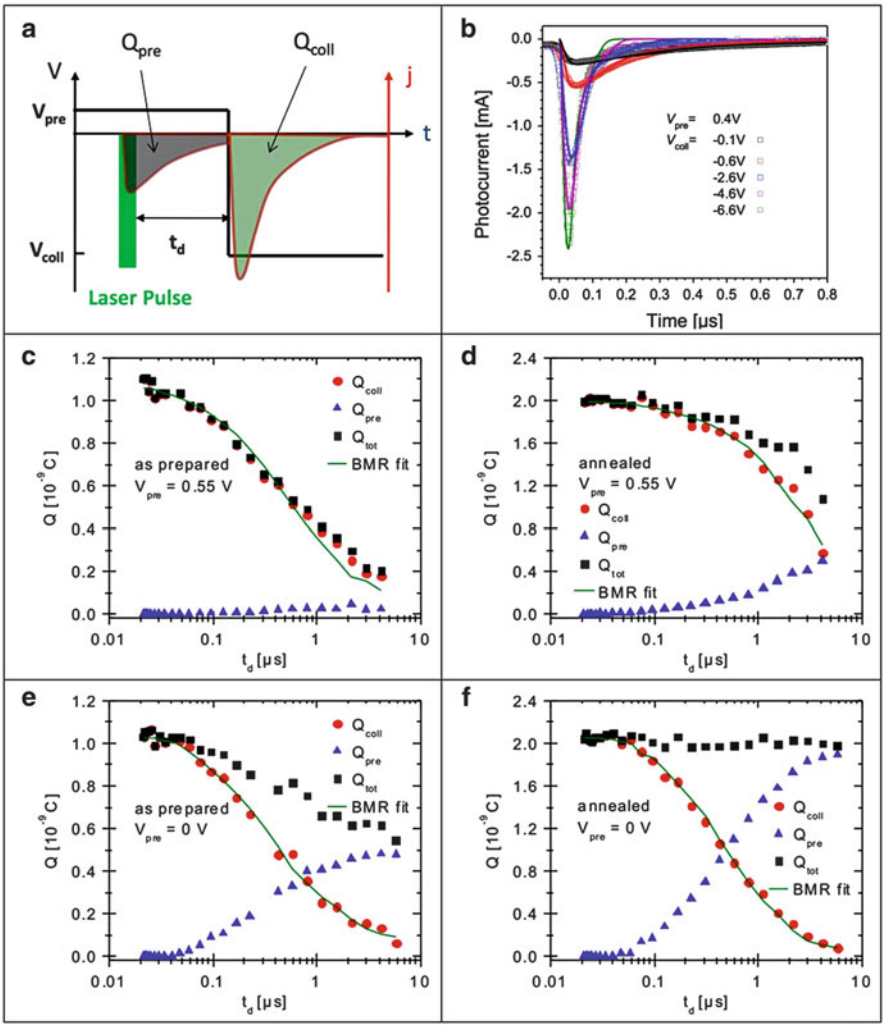

Fig. 20 Determination of the coefficient of bimolecular recombination by performing TDCF experiments with variable delay between the excitation pulse and application of the collection bias. (**a**) Scheme of the experiment. (**b**) Experimental TDCF photocurrent transients (*open squares*) measured on a 200 nm thick layer of slow-dried P3HT:PCBM (1:1) during application of different collection biases V_{coll}. The collection bias was applied 150 ns after the laser pulse ($t = 0$ in this graph). *Solid lines* show fits to the data using a numerical drift diffusion model with constant electron and hole mobilities. A noteworthy observation is that charges can be fully extracted from these layers within a few hundreds of nanoseconds for a sufficiently high collection bias [171]. (**c–f**) Q_{pre}, Q_{coll}, and Q_{tot} plotted as a function of the delay time t_d for as-prepared and thermally annealed chloroform-cast P3HT:PCBM, and with the pre-bias V_{pre} set either to 0.55 V (near open circuit) or to 0 V (short-circuit conditions) [172]. *Solid lines* show fits with an iterative model that considers bimolecular recombination of free charges in competition with their extraction

chloroform as-cast and annealed P3HT:PCBM for a pre-bias of 0.55 and 0 V. In all cases, the increase in Q_{pre} with t_d is due to field-induced extraction of photogenerated carriers, leaving less charge available when the collection bias is switched on. Decreasing the pre-bias, and thereby increasing the internal field, accelerates the sweep-out of carriers, reducing the amount of available charge upon starting collection after the delay time t_d. If V_{coll} is chosen to be sufficiently high to avoid recombination during collection, the course of Q_{tot} (t_d) is a measure of the total non-geminate recombination loss during delay.

This set of data displays some important differences between the as-prepared and annealed samples. First, the extraction of charges from the annealed layers is faster and far more efficient. For example, half of the initially photogenerated carriers are swept out of the device at 0 V within 1 ms and non-geminate recombination is almost absent at short-circuit conditions (Q_{tot} is essentially independent of t_d). When raising the bias close to $V_{oc,}$ extraction is slowed down and the carrier density in the sample declines as a result of non-geminate recombination. For the as-prepared layer, non-geminate recombination is seen for both short-circuit and open-circuit conditions, rendering extraction inefficient for both bias conditions. Also, extraction is considerably slower and recombination is more efficient in these samples.

Because Q_{coll} is a direct measure of the charge present in the layer at a delay time t_d, the recombination dynamics can be determined via an iterative procedure [171]. For the data shown in Fig. 20, this analysis yields $\gamma = 3.5 \times 10^{-17}$ m^3 s^{-1} and $\gamma = 1.2 \times 10^{-18}$ m^3 s^{-1} for the chloroform as-cast and the annealed P3HT:PCBM layer, respectively. The value for the annealed sample agrees very well with the bimolecular recombination coefficient measured by TAS at carrier densities typical for steady-state AM1.5 illumination (see, e.g., [189, 195]). To compare these values to the Langevin limit, the mobilities of the electrons and the holes in the blend must be known. Information on these quantities can be gained from drift-diffusion simulations of the photocurrent transients with different collection biases (see Fig. 20b). This yields mobilities of 1.2×10^{-7} m^2 V^{-1} s^{-1} and 1.7×10^{-7} m^2 V^{-1} s^{-1} for the faster carrier in the as-prepared and annealed blends, respectively. Assuming that the faster carrier determines non-geminate recombination dynamics, recombination is reduced by three orders of magnitude compared with the Langevin limit in the annealed layer whereas it is still suppressed by a factor of 20 in the as-cast blend.

Although suppressed bimolecular recombination in P3HT:PCBM blends has been seen in numerous experimental studies, there is still no consistent model to explain values of the Langevin reduction factor γ/γ_L as low as 10^{-4}. Koster et al. pointed out that if electrons and holes move in separate regions and recombination takes place only at the donor–acceptor interface, non-geminate recombination kinetics will be determined not by the faster but by the slower carrier: $\gamma = \frac{e}{\varepsilon}\min(\mu_e, \mu_h)$ [200]. The analysis of space-charge-limited currents (SCLC) in chloroform-cast P3HT:PCBM blends revealed holes to be less mobile than electrons, particularly for low annealing temperatures [73, 171]. This view has been

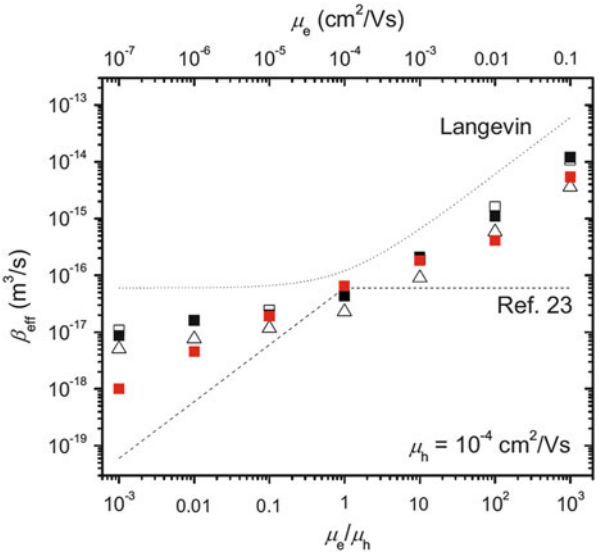

Fig. 21 Effective bimolecular recombination coefficient β_{eff} calculated by Monte Carlo modeling of a phase-separated blend with an average feature size of 4 (*black*) and 35 nm (*red*). Simulations were performed in the absence of energetic disorder (*squares*) or by assuming a Gaussian-type DOS with a width $\sigma = 75$ meV (*triangles*). *Open symbols* represent an electric field $F = 0$ and *closed symbols* are for $F = 10^7$ V/m. The Langevin limit is shown by the *dotted line* and the *dashed line* is for Langevin-type recombination limited by the slower carrier. *Ref 23* refers to the model in Shuttle et al. [202]. In all cases, the hole mobility was 10^{-4} cm^2/V s. Reprinted with permission from [201]. Copyright 2008 by the American Physical Society

challenged by Monte Carlo simulations of non-geminate recombination in phase-separated blends [201]. Although these calculations allowed carriers to recombine only at the interface, the non-geminate recombination coefficient was less affected by the slower carrier mobility than Koster and coworkers had proposed (see Fig. 21). The surprisingly weak effect of the slow carrier mobility on the recombination coefficient was attributed to the fact that carriers are distributed homogeneously in their respective phases, meaning that there is a population of the slower carriers close enough to the interface to be able to recombine with the faster carriers. It is, therefore, most likely that the reduced recombination originates mainly from the energetic barrier formed at the heterojunction due to increased morphological disorder in the interfacial region; however, other reasons such as an inhomogeneous distribution of electrons and holes in the device or unbalanced transport might also account for this effect [203, 204].

The strongly suppressed non-geminate recombination is highly beneficial for device performance as it prevents free charges from recombining prior to extraction to the electrodes. Quantitative information on the photocurrent loss due to non-geminate recombination, J_{NG}, can be obtained by combining transient photovoltage (TPV) with charge extraction (CE) measurements, as shown by

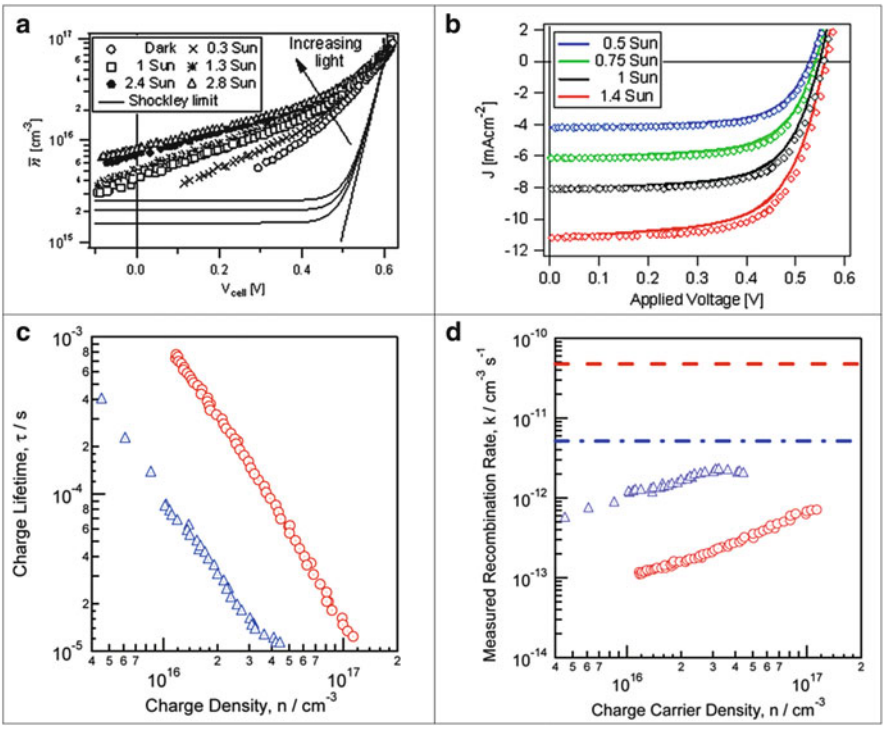

Fig. 22 (**a**) Average charge density in an annealed P3HT:PCBM layer (coated from xylene solution) as a function of cell voltage and illumination intensity as measured by charge extraction (CE). (**b**) Reconstruction of the measured current–voltage characteristics under steady-state illumination from Eqs. (7) and (8), with the carrier densities shown in (**a**) and carrier density-dependent recombination rates measured with TPV. (**c**) Charge carrier lifetimes and (**d**) bimolecular recombination coefficients as a function of carrier density as obtained by CE and TPV measurements on pristine (*blue triangles*) and thermally annealed (*red circles*) P3HT:PCBM blends. (**a**, **b**) reprinted (adapted) with permission from [207]. (**c**, **d**) reprinted (adapted) with permission from [205]. Copyright 2010 American Chemical Society

Shuttle and coworkers [205]. In TPV, the layer is under steady-state illumination with white light of appropriate intensity and the voltage across the device is measured with a large serial resistor. Therefore, the sample is under quasi-open-circuit conditions. The sample is then illuminated with a short and weak laser pulse, which increases the charge carrier density and thus causes the voltage across the device to increase. The decay of the transient photovoltage back to its steady-state value is, therefore, a direct measure of the non-geminate recombination rate [189]. To determine the charge within the illuminated blend layer by CE, the device is held under steady-state illumination at a certain bias and then is switched to short circuit (zero bias) while at the same time the light is switched off. The current transient after the switch to short-circuit conditions is integrated and corrected for the capacitive charge [206].

As shown in Fig. 22, the carrier density within the blend layer changes with illumination intensity I, cell voltage V, and temperature T. Combining $n(I, V, T)$ with charge carrier lifetime data determined with TPV at comparable carrier densities allows calculation of the loss current density J_{NG} via Eq. (8). Finally, the current characteristics under steady-state illumination are reconstructed with the assumption of a field-independent generation current density, $J_{gen} \cong J_{sc}$. This approach has been successfully applied to both as-prepared and annealed P3HT:PCBM layers [173, 205]. The data in Fig. 22c, d also show that the annealed device displays larger carrier lifetimes and lower recombination coefficients than the as-cast sample at comparable carrier densities. This has been quoted as the main cause for the superior performance of the thermally treated sample [173, 205].

We will, finally, comment briefly on the importance of establishing high electron and hole mobilities in P3HT:PCBM blends. Clearly, a high mobility of both types of carriers ensures rapid extraction of photogenerated charge out of the blend layers, rendering these carriers less vulnerable to recombination loss. Goodman and Rose [208] and later Mihailetchi et al. [209] stated that unequal carrier mobilities cause formation of space charge within the active layer, which renders part of the blend essentially field-free. As a consequence, the extracted current becomes significantly smaller than the photogenerated current:

$$J_{ph} = q\left(\frac{9\varepsilon_0\varepsilon_r\mu_{min}}{8q}\right)^{1/4} G^{0.75}V^{0.5}. \tag{11}$$

Here, G is the generation rate and μ_{min} the mobility of the slower carrier. A characteristic feature of space-charge-limited photocurrents is that they possess a sublinear dependence on generation rate (illumination intensity). As demonstrated in Fig. 23, as-cast blends of chloroform-coated P3HT:PCBM blends exhibit reasonable electron mobilities but very poor hole mobilities. As pointed out in Sect. 3, the poor hole transport in these as-prepared devices is a result of the low degree of crystallinity in combination with poor ordering within the polymer aggregates. As a consequence, the performance of this device is space-charge limited, as evidenced by the sublinear increase in photocurrent with light intensity. Annealing the device improves μ_h, thereby reducing the mobility imbalance, which concurrently results in a large improvement in device performance. Poor hole mobility was also identified as the main cause of the poor performance of devices made from low molecular weight P3HT [57, 210].

To conclude this section, non-geminate recombination is identified as the main loss channel in poorly performing as-prepared P3HT:PCBM blends. This is for two reasons: First, the coefficient for bimolecular recombination is larger in as-prepared blends, possibly caused by a higher degree of intermixing of the donor and acceptor component. Second and more important, as-prepared P3HT:PCBM blends exhibit lower mobilities, rendering free charges more vulnerable to non-geminate recombination and causing severe space–charge effects at solar illumination conditions.

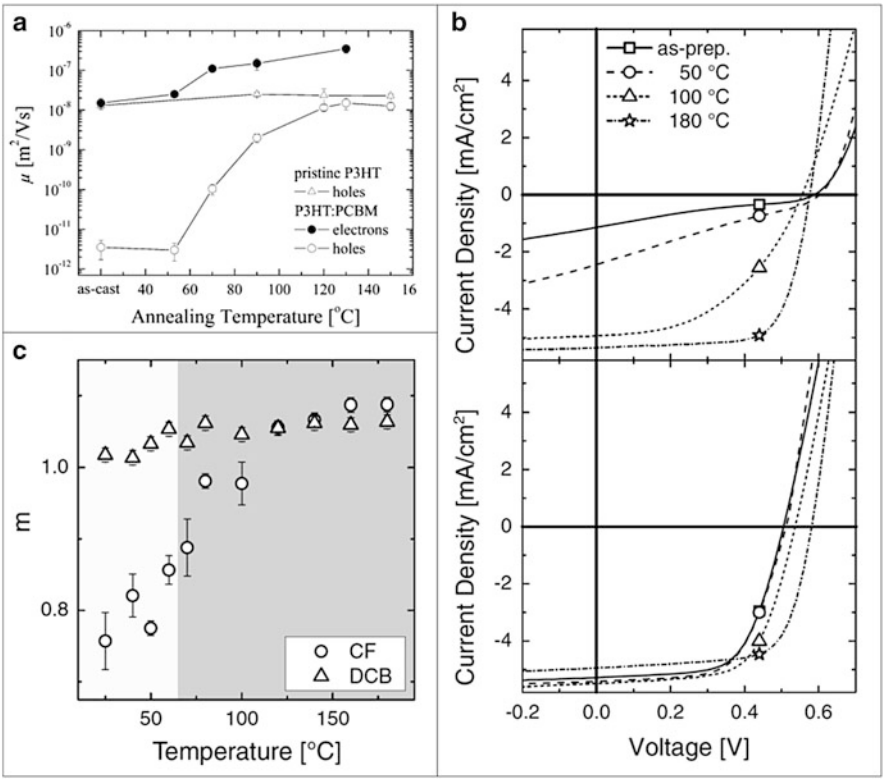

Fig. 23 (**a**) Zero-field mobilities for electrons (*closed circles*) and holes (*open circles*) at room temperature for chloroform-coated 1:1 P3HT:PCBM blends as a function of postproduction annealing temperature. Also shown is the hole mobility in pure P3HT (*triangles*). Mobilities were derived from space-charge-limited current measurements on the corresponding unipolar devices. Reprinted with permission from [73]. Copyright © 2006 Wiley-VCH Verlag GmbH & Co. KGaA, Weinheim. (**c**) Slope of the power-law increase *m* in the photocurrent as a function of illumination intensity in a log–log representation as a function of annealing temperature for a 100 nm thick P3HT:PCBM blend coated from chloroform (*CF*) or dichlorobenzene (*DCB*) [146]. (**b**) *J*/*V* characteristics under simulated AM1.5G illumination for the devices in (**c**) for selected annealing temperatures cast from chloroform (*top*) and dichlorobenzene (*bottom*) [146]

5 Summary, Conclusions, and Outlook

From 2003 to 2013, P3HT:PCBM was the "fruit fly" system to study for understanding organic photovoltaic properties. The understanding of these properties has not been straightforward because of the complex way that P3HT and PCBM interact with each other, with themselves, and with the substrates. In particular, mixed BHJ films, which self-assemble from solution in the length range from 10^{-10} to 10^{-5} m, have a hierarchical variety of film features. Because the film forms via self-assembly, changing the fabrication conditions that affect the solvation of

one component more than the other can lead to a dizzying variety of optical, electrical, and morphological features that are not particularly easy to measure and are difficult to interpret. Further complicating the literature are polymer samples with a variety of molecular weights and regioregularities. Mixtures have different mixing ratios, and are cast from different solvents.

Regarding charge carrier dynamics, charge generation in P3HT:PCBM was shown to be ultrafast and activationless, even when exciting low energy CT states. Therefore, formation of free charge must be driven by particular energetics at the mesoscale, which counterbalance the Coulomb attraction of the geminate pair forming the CT state. Recent quantum dynamic simulations suggest that delocalization of electrons and holes on well-ordered domains assists free charge generation by reducing the Coulomb binding of interfacial CT states [211]. Because most blends of regioregular P3HT with PCBM studied so far exhibit a significant fraction of crystallized P3HT chains, charge delocalization might explain why free charge generation is field-independent, irrespective of the exact preparation scheme. A second particularity of well-performing P3HT:PCBM devices is highly reduced non-geminate recombination. In comparison to the Langevin limit of electron–hole recombination in an isotropic homogeneous medium, free charge recombination in P3HT:PCBM is slowed down by a factor of 100–1,000. This vast reduction in recombination speed allows the use of thick and well-absorbing blend layers, without risking inefficient charge extraction and low fill factors.

In total, it took thousands of people 10 years, and more than 10^3 published articles, to reach this level of understanding about how P3HT:PCBM BHJ OPV devices really function, how the materials self-assemble, and how to alter the self-assembly process via fabrication conditions to achieve a desired morphology for efficient charge generation and extraction. The lessons learned from P3HT:PCBM are being applied to a variety of new polymers and fullerenes with the goal of making better OPV devices. Mixed solvents, a high level of synthesis control, and highly specialized methods to measure the morphology are now necessary to produce new insights into BHJ function. Thus, the low hanging fruit have been eaten.

Also, advanced electronic and optical measurements are needed to describe common features of BHJ OPV devices. Clear (although complicated) optical and electrical models have been developed that do a good job of predicting the efficiency and other *I*/*V* characteristics of a given donor–acceptor mixture.

So is OPV all figured out? If not, what is next? Now that the science of determining how to synthesize high efficiency materials, how to process the mixtures, how to fabricate the devices, how to characterize each step of the film formation, and how to measure the optical and electrical features of the device have been established, we still need to reliably engineer good devices. In particular, it is necessary to determine the following:

– How to coat BHJ layers quickly and without defects
– How to protect films against O_2 and UV light, which destroy device function

– What other impurities degrade BHJ function under the conditions of heat, light, electric field, and mechanical stress.
– What electrode materials are flexible, transparent, low resistance, and provide greater device longevity
– How to fabricate multiple BHJ layers in series (which is difficult due to the problem of dissolving previously deposited layers.)

The future of OPV research is bright and active, but the challenges that remain require continued increases in our understanding of the device complexity. Measurements will be even harder, because we will be searching for the low concentration impurity states (at 1 ppt to 1 ppm) that degrade device function, rather than assuming that these impurities either do not exist or are not important.

References

1. Allan RP, Soden BJ (2008) Science 321:1481–1484
2. Emanuel K (2005) Nature 436:686–688
3. Webster PJ, Holland GJ, Curry JA, Chang HR (2005) Science 309:1844–1846
4. Wentz FJ, Ricciardulli L, Hilburn K, Mears C (2007) Science 317:233–235
5. Shrotriya V, Li G, Yao Y, Moriarty T, Emery K, Yang Y (2006) Adv Funct Mater 16:2016–2023
6. Reese MO, Gevorgyan SA, Jorgensen M, Bundgaard E, Kurtz SR, Ginley DS, Olson DC, Lloyd MT, Moryillo P, Katz EA, Elschner A, Haillant O, Currier TR, Shrotriya V, Hermenau M, Riede M, Kirov KR, Trimmel G, Rath T, Inganas O, Zhang F, Andersson M, Tvingstedt K, Lira-Cantu M, Laird D, McGuiness C, Gowrisanker S, Pannone M, Xiao M, Hauch J, Steim R, DeLongchamp DM, Roesch R, Hoppe H, Espinosa N, Urbina A, Yaman-Uzunoglu G, Bonekamp J-B, van Breemen AJJM, Girotto C, Voroshazi E, Krebs FC (2011) Sol Energ Mat Sol C 95:1253–1267
7. Shockley W, Queisser HJ (1961) J Appl Phys 32:510–519
8. Peumans P, Yakimov A, Forrest SR (2003) J Appl Phys 93:3693–3723
9. Veldman D, Meskers SCJ, Janssen RAJ (2009) Adv Funct Mater 19:1939–1948
10. Scharber MC, Wuhlbacher D, Koppe M, Denk P, Waldauf C, Heeger AJ, Brabec CL (2006) Adv Mater 18:789–794
11. Koster LJA, Mihailetchi VD, Blom PWM (2006) Appl Phys Lett 88:093511
12. SolarServer.com (2012) Organic photovoltaics: Polyera reaches 9.1% efficiency with a polymer/fullerene cell. http://www.solarserver.com/solar-magazine/solar-news/archive-2012/2012/kw05/organic-photovoltaics-polyera-reaches-91-efficiency-with-a-polymerfullerene-cell.html (accessed 2 July 2014)
13. Krebs FC (2008) Polymer photovoltaics: a practical approach. SPIE, Bellingham
14. Krebs FC, Fyenbo J, Tanenbaum DM, Gevorgyan SA, Andriessen R, van Remoortere B, Galagan Y, Jorgensen M (2011) Energy Environ Sci 4:4116–4123
15. Krebs FC, Gevorgyan SA, Alstrup J (2009) J Mater Chem 19:5442–5451
16. Krebs FC (2009) Org Electron 10:761–768
17. Krebs FC (2009) Sol Energ Mat Sol C 93:394–412
18. Krebs FC (2009) Sol Energ Mat Sol C 93:465–475
19. Krebs FC, Jorgensen M, Norrman K, Hagemann O, Alstrup J, Nielsen TD, Fyenbo J, Larsen K, Kristensen J (2009) Sol Energ Mat Sol C 93:422–441
20. Shaheen SE, Radspinner R, Peyghambarian N, Jabbour GE (2001) Appl Phys Lett 79:2996–2998

21. Steirer KX, Reese MO, Rupert BL, Kopidakis N, Olson DC, Collins RT, Ginley DS (2009) Sol Energ Mat Sol C 93:447–453
22. Hoth CN, Steim R, Schilinsky P, Choulis SA, Tedde SF, Hayden O, Brabec CJ (2009) Org Electron 10:587–593
23. Hau SK, Yip H-L, Leong K, Jen AKY (2009) Org Electron 10:719–723
24. Girotto C, Rand BP, Genoe J, Heremans P (2009) Sol Energ Mat Sol C 93:454–458
25. Lim YF, Lee S, Herman DJ, Lloyd MT, Anthony JE, Malliaras GG (2008) Appl Phys Lett 93:193301
26. Green R, Morfa A, Ferguson AJ, Kopidakis N, Rumbles G, Shaheen SE (2008) Appl Phys Lett 92:033301
27. Vak D, Kim S-S, Jo J, Oh S-H, Na S-I, Kim J, Kim D-Y (2007) Appl Phys Lett 91:081102
28. Arias AC, MacKenzie JD, McCulloch I, Rivnay J, Salleo A (2010) Chem Rev 110:3–24
29. Mativetsky JM, Loo Y-L (2012) AIChE J 58:3280–3288
30. Moulé AJ (2010) Curr Opin Sol State Mat Sci 14:123–130
31. Tang CW (1986) Appl Phys Lett 48:183–185
32. Sariciftci NS, Smilowitz L, Heeger AJ, Wudl F (1992) Science 258:1474–1476
33. Halls JJM, Walsh CA, Greenham NC, Marseglia EA, Friend RH, Moratti SC, Holmes AB (1995) Nature 376:498–500
34. Yu G, Gao J, Hummelen JC, Wudl F, Heeger AJ (1995) Science 270:1789–1791
35. Padinger F, Rittberger RS, Sariciftci NS (2003) Adv Funct Mater 13:85–88
36. Shaheen SE, Brabec CJ, Sariciftci NS, Padinger F, Fromherz T, Hummelen JC (2001) Appl Phys Lett 78:841–843
37. Chen JW, Cao Y (2009) Acc Chem Res 42:1709–1718
38. Li G, Zhu R, Yang Y (2012) Nat Photon 6:153–161
39. Liang Y, Xu Z, Xia J, Tsai S-T, Wu Y, Li G, Ray C, Yu L (2010) Adv Mater 22:E135–E138
40. DeLongchamp DM, Kline RJ, Herzing A (2012) Energy Environ Sci 5:5980–5993
41. Chen W, Nikiforov MP, Darling SB (2012) Energy Environ Sci 5:8045–8074
42. Ma W, Yang C, Gong X, Lee K, Heeger AJ (2005) Adv Funct Mater 15:1617–1622
43. Li G, Shrotriya V, Huang J, Yao Y, Moriarty T, Emery K, Yang Y (2005) Nat Mater 4:864–868
44. Peet J, Kim JY, Coates NE, Ma WL, Moses D, Heeger AJ, Bazan GC (2007) Nat Mater 6:497–500
45. Moulé AJ, Meerholz K (2008) Adv Mater 20:240–245
46. Reyes-Reyes M, Kim K, Carroll DL (2005) Appl Phys Lett 87:083506
47. Ihn KJ, Moulton J, Smith P (1993) J Polym Sci B Polym Phys 31:735–742
48. Bouman MM, Havinga EE, Janssen RAJ, Meijer EW (1994) Mol Cryst Liquid Cryst Sci Technol A 256:439–448
49. Wu ZY, Petzold A, Henze T, Thurn-Albrecht T, Lohwasser RH, Sommer M, Thelakkat M (2010) Macromolecules 43:4646–4653
50. Koppe M, Brabec CJ, Heiml S, Schausberger A, Duffy W, Heeney M, McCulloch I (2009) Macromolecules 42:4661–4666
51. Brinkmann M, Rannou P (2009) Macromolecules 42:1125–1130
52. Ballantyne AM, Chen L, Dane J, Hammant T, Braun FM, Heeney M, Duffy W, McCulloch I, Bradley DDC, Nelson J (2008) Adv Funct Mater 18:2373–2380
53. Brinkmann M, Rannou P (2007) Adv Funct Mater 17:101–108
54. Zen A, Saphiannikova M, Neher D, Grenzer J, Grigorian S, Pietsch U, Asawapirom U, Janietz S, Scherf U, Lieberwirth I, Wegner G (2006) Macromolecules 39:2162–2171
55. Hiorns RC, de Bettignies R, Leroy J, Bailly S, Firon M, Sentein C, Preud'homme H, Dagron-Lartigau C (2006) Eur Phys J 36:295–300
56. Hiorns RC, De Bettignies R, Leroy J, Bailly S, Firon M, Sentein C, Khoukh A, Preud'homme H, Dagron-Lartigau C (2006) Adv Funct Mater 16:2263–2273
57. Schilinsky P, Asawapirom U, Scherf U, Biele M, Brabec CJ (2005) Chem Mater 17:2175–2180

58. Kline RJ, McGehee MD, Kadnikova EN, Liu JS, Frechet JMJ, Toney MF (2005) Macromolecules 38:3312–3319
59. Zen A, Pflaum J, Hirschmann S, Zhuang W, Jaiser F, Asawapirom U, Rabe JP, Scherf U, Neher D (2004) Adv Funct Mater 14:757–764
60. Kline RJ, McGehee MD, Kadnikova EN, Liu JS, Frechet JMJ (2003) Adv Mater 15:1519–1522
61. Trznadel M, Pron A, Zagorska M (1998) Macromolecules 31:5051–5058
62. Scharsich C, Lohwasser RH, Sommer M, Asawapirom U, Scherf U, Thelakkat M, Neher D, Koehler A (2012) J Polym Sci B Polym Phys 50:442–453
63. Roehling JD, Arslan I, Moulé AJ (2012) J Mater Chem 22:2498–2506
64. Berson S, De Bettignies R, Bailly S, Guillerez S (2007) Adv Funct Mater 17:1377–1384
65. Yin W, Dadmun M (2011) ACS Nano 5:4756–4768
66. Tremel K, Ludwigs S (2014) Morphology of P3HT in thin films in relation to optical and electrical properties. Adv Polym Sci doi: 10.1007/12_2014_288
67. Kim Y, Cook S, Tuladhar SM, Choulis SA, Nelson J, Durrant JR, Bradley DDC, Giles M, McCulloch I, Ha CS, Ree M (2006) Nat Mater 5:197–203
68. Hoth CN, Choulis SA, Schilinsky P, Brabec CJ (2009) J Mater Chem 19:5398–5404
69. Hoppe H, Sariciftci NS (2006) J Mater Chem 16:45–61
70. Moulé AJ, Bonekamp JB, Meerholz K (2006) J Appl Phys 100:094503
71. Clark J, Silva C, Friend RH, Spano FC (2007) Phys Rev Lett 98:206406
72. Niles ET, Roehling JD, Yamagata H, Wise AJ, Spano FC, Moulé AJ, Grey JK (2012) J Phys Chem Lett 3:259–263
73. Mihailetchi VD, Xie HX, de Boer B, Koster LJA, Blom PWM (2006) Adv Funct Mater 16:699–708
74. Blom PWM, Mihailetchi VD, Koster LJA, Markov DE (2007) Adv Mater 19:1551–1566
75. Drees M, Davis RM, Heflin JR (2004) Phys Rev B 69:165320
76. Li G, Shrotriya V, Yao Y, Yang Y (2005) J Appl Phys 98:043704
77. Lenes M, Koster LJA, Mihailetchi VD, Blom PWM (2006) Appl Phys Lett 88:243502
78. Hoppe H, Shokhovets S, Gobsch G (2007) Phys Status Solidi Rapid Res Lett 1:R40–R42
79. van Bavel S, Sourty E, de With G, Frolic K, Loos J (2009) Macromolecules 42:7396–7403
80. Jin H, Olkkonen J, Tuomikoski M, Kopola P, Maaninen A, Hast J (2010) Sol Energ Mat Sol C 94:465–470
81. Parmer JE, Mayer AC, Hardin BE, Scully SR, McGehee MD, Heeney M, McCulloch I (2008) Appl Phys Lett 92:113309
82. Dang MT, Hirsch L, Wantz G (2011) Adv Mater 23:3597–3602
83. Moulé AJ, Tsami A, Brunnagel TW, Forster M, Kronenberg NM, Scharber M, Koppe M, Morana M, Brabec CJ, Meerholz K, Scherf U (2008) Chem Mater 20:4045–4050
84. Moulé AJ, Meerholz K (2007) Appl Phys B 86:771–777
85. Moulé AJ, Meerholz K (2008) Appl Phys B 92:209–218
86. Pettersson LAA, Roman LS, Inganas O (1999) J Appl Phys 86:487–496
87. Chen LM, Hong ZR, Li G, Yang Y (2009) Adv Mater 21:1434–1449
88. Li G, Yao Y, Yang H, Shrotriya V, Yang G, Yang Y (2007) Adv Funct Mater 17:1636–1644
89. Huang DM, Mauger SA, Friedrich S, George SA, Dumitriu-LaGrange D, Yoon S, Moulé AJ (2011) Adv Funct Mater 21:1657–1665
90. Mihailetchi VD, Xie HX, de Boer B, Popescu LM, Hummelen JC, Blom PWM, Koster LJA (2006) Appl Phys Lett 89:012107
91. Chou KW, Yan BY, Li RP, Li EQ, Zhao K, Anjum DH, Alvarez S, Gassaway R, Biocca A, Thoroddsen ST, Hexemer A, Amassian A (2013) Adv Mater 25:1923–1929
92. Li G, Shrotriya V, Yao Y, Huang JS, Yang Y (2007) J Mater Chem 17:3126–3140
93. Yang XN, Loos J, Veenstra SC, Verhees WJH, Wienk MM, Kroon JM, Michels MAJ, Janssen RAJ (2005) Nano Lett 5:579–583
94. Chen D, Nakahara A, Wei D, Nordlund D, Russell TP (2010) Nano Lett 11:561–567

95. Collins BA, Gann E, Guignard L, He X, McNeill CR, Ade H (2010) J Phys Chem Lett 1:3160–3166
96. Roehling JD, Batenburg KJ, Swain FB, Moulé AJ, Arslan I (2013) Adv Funct Mater 23:2115–2122
97. Agostinelli T, Lilliu S, Labram JG, Campoy-Quiles M, Hampton M, Pires E, Rawle J, Bikondoa O, Bradley DDC, Anthopoulos TD, Nelson J, Macdonald JE (2011) Adv Funct Mater 21:1701–1708
98. Yan HP, Swaraj S, Wang C, Hwang I, Greenham NC, Groves C, Ade H, McNeill CR (2010) Adv Funct Mater 20:4329–4337
99. Shin M, Kim H, Park J, Nam S, Heo K, Ree M, Ha CS, Kim Y (2010) Adv Funct Mater 20:748–754
100. Marsh RA, Hodgkiss JM, Albert-Seifried S, Friend RH (2010) Nano Lett 10:923–930
101. Kim S-S, Na S-I, Kang S-J, Kim D-Y (2010) Sol Energ Mat Sol C 94:171–175
102. Watts B, Belcher WJ, Thomsen L, Ade H, Dastoor PC (2009) Macromolecules 42:8392–8397
103. Pingree LSC, Reid OG, Ginger DS (2009) Nano Lett 9:2946–2952
104. Kim HJ, Lee HH, Kim JJ (2009) Macromol Rapid Commun 30:1269–1273
105. Jo J, Kim SS, Na SI, Yu BK, Kim DY (2009) Adv Funct Mater 19:866–874
106. Yun J-J, Peet J, Cho N-S, Bazan GC, Lee SJ, Moskovits M (2008) Appl Phys Lett 92:251912
107. Clarke TM, Ballantyne AM, Nelson J, Bradley DDC, Durrant JR (2008) Adv Funct Mater 18:4029–4035
108. McNeill CR, Halls JJM, Wilson R, Whiting GL, Berkebile S, Ramsey MG, Friend RH, Greenham NC (2008) Adv Funct Mater 18:2309–2321
109. Ayzner AL, Wanger DD, Tassone CJ, Tolbert SH, Schwartz BJ (2008) J Phys Chem C 112:18711–18716
110. Nguyen LH, Hoppe H, Erb T, Gunes S, Gobsch G, Sariciftci NS (2007) Adv Funct Mater 17:1071–1078
111. Zhokhavets U, Erb T, Hoppe H, Gobsch G, Sariciftci NS (2006) Thin Solid Films 496:679–682
112. Warman JM, de Haas MP, Anthopoulos TD, de Leeuw DM (2006) Adv Mater 18:2294–2298
113. Cugola R, Giovanella U, Di Gianvincenzo P, Bertini F, Catellani M, Luzzati S (2006) Thin Solid Films 511:489–493
114. Cho S, Lee K, Yuen J, Wang GM, Moses D, Heeger AJ, Surin M, Lazzaroni R (2006) J Appl Phys 100:114503
115. Kim Y, Choulis SA, Nelson J, Bradley DDC, Cook S, Durrant JR (2005) J Mater Sci 40:1371–1376
116. Kim Y, Choulis SA, Nelson J, Bradley DDC, Cook S, Durrant JR (2005) Appl Phys Lett 86:063502
117. Al-Ibrahim M, Ambacher O, Sensfuss S, Gobsch G (2005) Appl Phys Lett 86:201120
118. Chang L, Lademann HWA, Bonekamp J-B, Meerholz K, Moulé AJ (2011) Adv Funct Mater 21:1779–1787
119. Kumar A, Sista S, Yang Y (2009) J Appl Phys 105:094512
120. Tress W, Leo K, Riede M (2011) Adv Funct Mater 21:2140–2149
121. Müller C, Ferenczi TAM, Campoy-Quiles M, Frost JM, Bradley DDC, Smith P, Stingelin-Stutzmann N, Nelson J (2008) Adv Mater 20:3510–3515
122. Kim JY, Frisbie D (2008) J Phys Chem C 112:17726–17736
123. Pientka M, Dyakonov V, Meissner D, Rogach A, Vanderzande D, Weller H, Lutsen L (2004) Nanotechnology 15:163–170
124. Yan HP, Collins BA, Gann E, Wang C, Ade H, McNeill CR (2012) ACS Nano 6:677–688
125. Collins BA, Ade H (2012) J Electron Spectros Relat Phenomena 185:119–128
126. Zhang Y, Yip HL, Acton O, Hau SK, Huang F, Jen AKY (2009) Chem Mater 21:2598–2600
127. Treat ND, Brady MA, Smith G, Toney MF, Kramer EJ, Hawker CJ, Chabinyc ML (2011) Adv Energy Mater 1:82–89

128. Ruderer MA, Meier R, Porcar L, Cubitt R, Müller-Buschbaum P (2012) J Phys Chem Lett 3:683–688
129. Mauger SA, Chang LL, Friedrich S, Rochester CW, Huang DM, Wang P, Moulé AJ (2013) Adv Funct Mater 23:1935–1946
130. Wodo O, Roehling JD, Moulé AJ, Ganapathysubramanian B (2013) Energy Environ Sci 6:3060–3070
131. He X, Collins BA, Watts B, Ade H, McNeill CR (2012) Small 12:1920–1927
132. Bartelt JA, Beiley ZM, Hoke ET, Mateker WR, Douglas JD, Collins BA, Tumbleston JR, Graham KR, Amassian A, Ade H, Fréchet JMJ, Toney MF, McGehee MD (2013) Adv Energy Mater 3:364–374
133. Collins BA, Tumbleston JR, Ade H (2011) J Phys Chem Lett 2:3135–3145
134. Chirvase D, Parisi J, Hummelen JC, Dyakonov V (2004) Nanotechnology 15:1317–1323
135. Zhang FL, Jespersen KG, Bjorstrom C, Svensson M, Andersson MR, Sundstrom V, Magnusson K, Moons E, Yartsev A, Inganas O (2006) Adv Funct Mater 16:667–674
136. Schmidt-Hansberg B, Sanyal M, Grossiord N, Galagan Y, Baunach M, Klein MFG, Colsmann A, Scharfer P, Lemmer U, Dosch H, Michels J, Barrena E, Schabel W (2012) Sol Energ Mat Sol C 96:195–201
137. Lee JK, Ma WL, Brabec CJ, Yuen J, Moon JS, Kim JY, Lee K, Bazan GC, Heeger AJ (2008) J Am Chem Soc 130:3619–3623
138. Yao Y, Hou JH, Xu Z, Li G, Yang Y (2008) Adv Funct Mater 18:1783–1789
139. Oosterbaan WD, Vrindts V, Berson S, Guillerez S, Douheret O, Ruttens B, D'Haen J, Adriaensens P, Manca J, Lutsen L, Vanderzande D (2009) J Mater Chem 19:5424–5435
140. Martin TP, Wise AJ, Busby E, Gao J, Roehling JD, Ford MJ, Larsen DS, Moulé AJ, Grey JK (2013) J Phys Chem B 117:4478–4487
141. Moulé AJ, Allard S, Kronenberg NM, Tsami A, Scherf U, Meerholz K (2008) J Phys Chem C 112:12583–12589
142. Xin H, Reid OG, Ren GQ, Kim FS, Ginger DS, Jenekhe SA (2010) ACS Nano 4:1861–1872
143. Kietzke T, Neher D, Landfester K, Montenegro R, Guntner R, Scherf U (2003) Nat Mater 2:408–412
144. Erb T, Zhokhavets U, Gobsch G, Raleva S, Stuhn B, Schilinsky P, Waldauf C, Brabec CJ (2005) Adv Funct Mater 15:1193–1196
145. Campoy-Quiles M, Ferenczi T, Agostinelli T, Etchegoin PG, Kim Y, Anthopoulos TD, Stavrinou PN, Bradley DDC, Nelson J (2008) Nat Mater 7:158–164
146. Turner ST, Pingel P, Steyrleuthner R, Crossland EJW, Ludwigs S, Neher D (2011) Adv Funct Mater 21:4640–4652
147. Spano FC (2005) J Chem Phys 122:234701
148. Spano FC (2006) Chem Phys 325:22–35
149. Gierschner J, Huang YS, Van Averbeke B, Cornil J, Friend RH, Beljonne D (2009) J Chem Phys 130:044105
150. Clark J, Chang JF, Spano FC, Friend RH, Silva C (2009) Appl Phys Lett 94:163306
151. Zhao J, Swinnen A, Van Assche G, Manca J, Vanderzande D, Van Mele B (2009) J Phys Chem B 113:1587–1591
152. Wang T, Pearson AJ, Lidzey DG, Jones RAL (2011) Adv Funct Mater 21:1383–1390
153. Pearson AJ, Wang T, Jones RAL, Lidzey DG, Staniec PA, Hopkinson PE, Donald AM (2012) Macromolecules 45:1499–1508
154. Beal RM, Stavrinadis A, Warner JH, Smith JM, Assender HE, Watt AAR (2010) Macromolecules 43:2343–2348
155. van Bavel SS, Barenklau M, de With G, Hoppe H, Loos J (2010) Adv Funct Mater 20:1458–1463
156. Tsoi WC, James DT, Kim JS, Nicholson PG, Murphy CE, Bradley DDC, Nelson J, Kim JS (2011) J Am Chem Soc 133:9834–9843
157. Pascui OF, Lohwasser R, Sommer M, Thelakkat M, Thurn-Albrecht T, Saalwächter K (2010) Macromolecules 43:9401–9410

158. Rivnay J, Noriega R, Northrup JE, Kline RJ, Toney MF, Salleo A (2011) Phys Rev B 83:121306
159. Deibel C, Strobel T, Dyakonov V (2009) Phys Rev Lett 103:036402
160. Guan ZL, Kim JB, Wang H, Jaye C, Fischer DA, Loo YL, Kahn A (2010) Org Electron 11:1779–1785
161. Vandewal K, Tvingstedt K, Gadisa A, Inganas O, Manca JV (2010) Phys Rev B 81:125204
162. van der Hofstad TGJ, Di Nuzzo D, van den Berg M, Janssen RAJ, Meskers SCJ (2012) Adv Energy Mater 2:1095–1099
163. Lee J, Vandewal K, Yost SR, Bahlke ME, Goris L, Baldo MA, Manca JV, Van Voorhis T (2010) J Am Chem Soc 132:11878–11880
164. Braun CL (1984) J Chem Phys 80:4157–4161
165. Wojcik M, Tachiya M (2009) J Chem Phys 130:104107
166. Mihailetchi VD, Koster LJA, Hummelen JC, Blom PWM (2004) Phys Rev Lett 93:216601
167. Mingebach M, Walter S, Dyakonov V, Deibel C (2012) Appl Phys Lett 100:193302
168. Limpinsel M, Wagenpfahl A, Mingebach M, Deibel C, Dyakonov V (2010) Phys Rev B 81:085203
169. Howard IA, Mauer R, Meister M, Laquai F (2010) J Am Chem Soc 132:14866–14876
170. Guo JM, Ohkita H, Benten H, Ito S (2010) J Am Chem Soc 132:6154–6164
171. Kniepert J, Schubert M, Blakesley JC, Neher D (2011) J Phys Chem Lett 2:700–705
172. Kniepert J, Lange I, van der Kaap NJ, Koster LAJ, Neher D (2014) Adv Energy Mater 4:1301401
173. Gluecker M, Foertig A, Dyakonov V, Deibel C (2012) Phys Status Solidi Rapid Res Lett 6:337–339
174. Street RA, Cowan S, Heeger AJ (2010) Phys Rev B 82:121301
175. Cowan SR, Street RA, Cho SN, Heeger AJ (2011) Phys Rev B 83:035205
176. Tsoi WC, Spencer SJ, Yang L, Ballantyne AM, Nicholson PG, Turnbull A, Shard AG, Murphy CE, Bradley DDC, Nelson J, Kim JS (2011) Macromolecules 44:2944–2952
177. Shoaee S, Subramaniyan S, Xin H, Keiderling C, Tuladhar PS, Jamieson F, Jenekhe SA, Durrant JR (2013) Adv Funct Mater 23:3286–3298
178. Jamieson FC, Domingo EB, McCarthy-Ward T, Heeney M, Stingelin N, Durrant JR (2012) Chem Sci 3:485–492
179. McMahon DP, Cheung DL, Troisi A (2011) J Phys Chem Lett 2:2737–2741
180. Pensack RD, Asbury JB (2010) J Phys Chem Lett 1:2255–2263
181. Pensack RD, Guo CH, Vakhshouri K, Gomez ED, Asbury JB (2012) J Phys Chem C 116:4824–4831
182. Caruso D, Troisi A (2012) Proc Natl Acad Sci USA 109:13498–13502
183. Vandewal K, Albrecht S, Hoke ET, Graham KR, Widmer J, Douglas JD, Schubert M, Mateker WR, Bloking JT, Burkhard GF, Sellinger A, Fréchet JMJ, Amassian A, Riede MK, McGehee MD, Neher D, Salleo A (2014) Nat Mater 13:63–68
184. Barbour LW, Hegadorn M, Asbury JB (2007) J Am Chem Soc 129:15884–15894
185. Mauer R, Howard IA, Laquai F (2010) J Phys Chem Lett 1:3500–3505
186. Credgington D, Durrant JR (2012) J Phys Chem Lett 3:1465–1478
187. Wetzelaer G, Kuik M, Blom PWM (2012) Adv Energy Mater 2:1232–1237
188. Pivrikas A, Juska G, Mozer AJ, Scharber M, Arlauskas K, Sariciftci NS, Stubb H, Osterbacka R (2005) Phys Rev Lett 94:176806
189. Shuttle CG, O'Regan B, Ballantyne AM, Nelson J, Bradley DDC, Durrant JR (2008) Phys Rev B 78:113201
190. Deibel C, Baumann A, Dyakonov V (2008) Appl Phys Lett 93:163303
191. Ferguson AJ, Kopidakis N, Shaheen SE, Rumbles G (2011) J Phys Chem C 115:23134–23148
192. Mauer R, Howard IA, Laquai F (2011) J Phys Chem Lett 2:1736–1741
193. Leong WL, Cowan SR, Heeger AJ (2011) Adv Energy Mater 1:517–522
194. Garcia-Belmonte G, Guerrero A, Bisquert J (2013) J Phys Chem Lett 4:877–886

195. Guo JM, Ohkita H, Yokoya S, Benten H, Ito S (2010) J Am Chem Soc 132:9631–9637
196. Nelson J (2003) Phys Rev B 67:155209
197. Shuttle CG, Hamilton R, Nelson J, O'Regan BC, Durrant JR (2010) Adv Funct Mater 20:698–702
198. Rauh D, Deibel C, Dyakonov V (2012) Adv Funct Mater 22:3371–3377
199. Clarke TM, Jamieson FC, Durrant JR (2009) J Phys Chem C 113:20934–20941
200. Koster LJA, Mihailetchi VD, Blom PWM (2006) Appl Phys Lett 88:052104
201. Groves C, Greenham NC (2008) Phys Rev B 78:155205
202. Shuttle CG, O'Regan B, Ballantyne AM, Nelson J, Bradley DDC, de Mello J, Durrant JR (2008) Appl Phys Lett 92:093311
203. Deibel C, Wagenpfahl A, Dyakonov V (2009) Phys Rev B 80:075203
204. Kirchartz T, Nelson J (2012) Phys Rev B 86:165201
205. Hamilton R, Shuttle CG, O'Regan B, Hammant TC, Nelson J, Durrant JR (2010) J Phys Chem Lett 1:1432–1436
206. Shuttle CG, Maurano A, Hamilton R, O'Regan B, de Mello JC, Durrant JR (2008) Appl Phys Lett 93:183501
207. Shuttle CG, Hamilton R, O'Regan BC, Nelson J, Durrant JR (2010) Proc Natl Acad Sci USA 107:16448–16452
208. Goodman AM, Rose A (1971) J Appl Phys 42:2823–2830
209. Mihailetchi VD, Wildeman J, Blom PWM (2005) Phys Rev Lett 94:126602
210. Ma W, Kim JY, Lee K, Heeger AJ (2007) Macromol Rapid Commun 28:1776–1780
211. Tamura H, Burghardt I (2013) J Am Chem Soc 135:16364–16367